

---

# The boundary between star clusters and dwarf galaxies: What is the nature of diffuse star clusters and ultra-compact dwarf galaxies?

Karina Voggel

---



München 2016



---

# The boundary between star clusters and dwarf galaxies: What is the nature of diffuse star clusters and ultra-compact dwarf galaxies?

Karina Voggel

---

Dissertation  
an der Fakultät für Physik  
der Ludwig-Maximilians-Universität  
München

vorgelegt von  
Karina Voggel  
aus Sigmaringen

München, den 19. August 2016

Erstgutachter: Prof. Dr. Andreas Burkert

Zweitgutachter: Prof. Dr. Hans Böhringer

Tag der mündlichen Prüfung: 17. Oktober 2016



# Contents

<b>Abstract</b>	<b>xiii</b>
<b>1 Introduction</b>	<b>1</b>
1.1 The "gap" between star clusters and dwarf galaxies . . . . .	1
1.1.1 How to define a galaxy? . . . . .	2
1.2 UCDs . . . . .	4
1.2.1 Formation channel of UCDs . . . . .	5
1.2.2 Dynamical friction and the formation of UCDs . . . . .	9
1.3 Ultra-faint dwarf galaxies and extended star clusters . . . . .	11
1.3.1 Dynamical signatures to distinguish dwarf galaxies from GCs . . . .	15
1.3.2 Spread in heavy element abundance of GCs and dwarf galaxies . . .	15
1.3.3 A controversial object in the boundary region: Crater/Laevens I . .	18
1.4 Open questions . . . . .	21
1.5 Structure of this thesis . . . . .	23
<b>2 GC clustering and tidal features around UCDs in NGC 1399</b>	<b>25</b>
2.1 Introduction . . . . .	25
2.2 Imaging . . . . .	27
2.3 UCD Analysis . . . . .	28
2.3.1 Surface brightness analysis . . . . .	28
2.3.2 Surface brightness profiles . . . . .	34
2.3.3 Color magnitude diagram . . . . .	36
2.3.4 Luminosity-effective-radius relation . . . . .	39
2.4 Tidal structures and globular clusters around UCDs . . . . .	42
2.4.1 Tidal structures . . . . .	42
2.4.2 Globular clusters around UCDs . . . . .	45
2.5 Spatial clustering of GCs around UCDs in the halo of NGC 1399 . . . . .	47
2.5.1 The globular cluster system around NGC 1399 . . . . .	47
2.5.2 Spatial correlation of GCs with UCDs . . . . .	52
2.6 Discussion . . . . .	57
2.6.1 Surface brightness profiles of UCDs and their scaling relations . . .	57
2.6.2 Tidal features . . . . .	60
2.6.3 Spatial correlation of UCDs with globular clusters . . . . .	61

<b>3</b>	<b>A MUSE view on the dynamics of Crater/Laevens I</b>	<b>65</b>
3.1	Introduction . . . . .	65
3.2	MUSE Observations . . . . .	68
3.2.1	Data reduction process . . . . .	68
3.2.2	Absolute velocity calibration . . . . .	70
3.2.3	Extraction of stellar spectra . . . . .	72
3.2.4	Radial velocity measurements . . . . .	74
3.2.5	Comparison to other velocity measurements of Crater stars . . . . .	78
3.3	Probability based analysis of membership . . . . .	80
3.3.1	Membership probability . . . . .	80
3.3.2	Likelihood analysis . . . . .	84
3.4	The kinematics of Crater . . . . .	85
3.4.1	Velocity dispersion and M/L . . . . .	85
3.4.2	Radial distribution of stellar velocities, cluster rotation and velocity gradient . . . . .	88
3.5	Discussion . . . . .	91
3.5.1	Dynamical state of Crater . . . . .	91
3.5.2	Is Crater a former member of a dwarf galaxy? . . . . .	93
3.5.3	Crater among Milky Way halo GCs and dwarf galaxies . . . . .	93
3.6	Summary . . . . .	94
<b>4</b>	<b>The metallicity of the stars in the outer halo globular cluster Crater</b>	<b>97</b>
4.1	Introduction . . . . .	97
4.2	Observation, reduction and extraction of spectra . . . . .	99
4.3	Analysis . . . . .	99
4.4	Results . . . . .	100
4.4.1	Stellar parameters . . . . .	100
4.4.2	Colour magnitude diagram and metallicity . . . . .	104
4.4.3	Iron spread . . . . .	109
4.4.4	Metallicity-velocity distribution . . . . .	112
4.4.5	Hertzsprung-Russel diagram . . . . .	112
4.4.6	The blue stars . . . . .	115
4.5	Discussion . . . . .	117
4.5.1	Metallicity and iron spread . . . . .	117
4.5.2	What is the nature of the blue stars? . . . . .	122
4.6	Conclusion . . . . .	123
<b>5</b>	<b>Summary and Outlook</b>	<b>125</b>
5.1	Future prospects . . . . .	126
5.1.1	Ultra-compact dwarf galaxies . . . . .	126
5.1.2	Ultra-faint dwarf galaxies and extended star clusters . . . . .	128
<b>A</b>	<b>Tables of UCD properties</b>	<b>131</b>

Table of Contents	vii
-------------------	-----

---

B Radial velocities and membership probabilities of Craters stars	137
---	-----

Acknowledgements	148
------------------	-----



# List of Figures

1.1	Size magnitude scaling relation . . . . .	3
1.2	Iron spread in GCs and dwarfs . . . . .	4
1.3	Mass-size plane with stripping simulations . . . . .	6
1.4	Size-magnitude scaling relation for faint objects . . . . .	13
1.5	All-sky plot of Milky Way satellite galaxies . . . . .	14
1.6	Luminosity to mass-to-light ratio of early-type systems . . . . .	16
1.7	Optical Image of Crater . . . . .	19
2.1	R-band wide field image of NGC 1399 . . . . .	29
2.2	R-band images, and residual of the extended UCDs with a Sérsic profile . .	32
2.3	Isophotal analysis of the R-band images of extended UCDs with GALFIT .	35
2.4	Color magnitude diagram for extended UCDs and UCDs with companions	37
2.5	Size-magnitude relation for early type systems, with extended UCD compo- nents . . . . .	40
2.6	R-band image of the tidal tails of UCD-FORS 2 with surface-brightness con- tours . . . . .	43
2.7	R-band image of UCD-FORS 94 and UCD-FORS 7 with possible tidal tails	44
2.8	Magnitude histogram of UCDs and clustered point sources . . . . .	46
2.9	Cutout images of UCDs that have companion point sources within $r < 300$ pc.	48
2.10	Projected surface density distribution of GCs and UCDs as a function of their galactocentric distance to NGC 1399. . . . .	50
2.11	Projected surface density distribution of blue and red globular clusters as function of their galactocentric distance to NGC 1399. . . . .	51
2.12	Spatial distribution of UCDs and GCs in the vicinity of NGC 1399 . . . . .	54
2.13	Average GC clustering depending on the radial distance from the UCD . .	55
2.14	GC around a UCD example object Y4289 . . . . .	58
3.1	White light image of the collapsed MUSE cube . . . . .	69
3.2	Sky emission spectrum and two-dimensional map of velocity offsets . . . .	71
3.3	The arc lamp spectrum model and velocity scatter histogram . . . . .	73
3.4	FWHM of the point-spread function for each wavelength slice of the MUSE cube . . . . .	74
3.5	Ca II region of the MUSE spectrum with best fit model and velocity his- togram of the Monte Carlo trials . . . . .	76
3.6	Position map of Craters stars with radial velocity measurements . . . . .	77
3.7	Radial velocity comparison with existing literature values . . . . .	79

3.8	Velocity histogram for Crater stars and foreground population . . . . .	82
3.9	Crater CMD with membership probabilities . . . . .	83
3.10	Two dimensional likelihood map of the systemic velocity and velocity dispersion, as well as the marginalised one dimensional distributions . . . . .	86
3.11	Radial velocity as a function of distance to Crater . . . . .	89
3.12	Velocity of Crater stars as a function of position angle . . . . .	90
4.1	Full spectrum, model and tellurics of star 5 . . . . .	101
4.2	Details in the spectrum of star 5 . . . . .	105
4.3	Details in the spectrum of star 8 . . . . .	106
4.4	Details in the spectrum of star 17 . . . . .	107
4.5	CMD comparison with metallicities for free and fixed $\log(g)$ values . . . . .	108
4.6	Histogram of the iron dispersion Monte Carlo realisations . . . . .	109
4.7	The iron abundance as a function of magnitude . . . . .	111
4.8	The metallicity distribution vs. stellar velocities . . . . .	113
4.9	Hertzsprung-Russel diagram of Craters stars . . . . .	114
4.10	Comparison of $\log(g)$ models for star 7 . . . . .	118
4.11	Comparison of $\log(g)$ models for star 13 . . . . .	119
4.12	Iron dispersion comparison to literature values . . . . .	121

# List of Tables

2.1	Sérsic for results for extended UCDs . . . . .	38
2.2	Double profile fits to the surface brightness profiles of the extended UCDs .	41
2.3	Clustering signals of GCs around UCDs . . . . .	56
3.1	Stellar radial velocities compared to those in the literature. . . . .	78
4.1	Surface gravity, effective temperatures and metallicity for Craters stars . .	103
4.2	Stellar parameters for different $\log(g)$ values for the two blue stars . . . . .	116
4.3	Literature comparison of metallicity of Crater stars . . . . .	120
A.1	UCD and companion properties of 19 objects with faint point sources . . .	132
A.2	Properties of all 97 UCDs in the FORS fields . . . . .	133
A.2	continued. . . . .	134
A.2	continued. . . . .	135
B.1	Radial velocities and membership probabilities of Craters stars . . . . .	137





# Zusammenfassung

In dieser Doktorarbeit werden die Eigenschaften von diffusen Kugelsternhaufen und ultrakompakten Zwerggalaxien (ultra-compact dwarf galaxies, UCDs) untersucht, um deren Beschaffenheit und Entstehungsmechanismen besser zu verstehen. Bezogen auf ihre Größen und Helligkeiten befinden sich beide im Bereich zwischen klassischen Zwerggalaxien und Kugelsternhaufen, was viele vorherige Definitionen von Kugelsternhaufen und Zwerggalaxien in Frage gestellt hat. Ihre Entstehung und Entwicklung ist noch nicht verstanden.

In dieser Arbeit habe ich tiefe photometrische Beobachtungen dazu benutzt, um die Eigenschaften von UCDs im Fornaxhaufen zu untersuchen. Das Aufteilen der Oberflächenhelligkeitsprofile in zwei Komponenten hat gezeigt, dass schwache stellare Hüllen die Kernkomponente umgeben, und zum ersten mal wurden signifikante Gezeitenarme um UCDs entdeckt. Die stellaren Hüllen sind wahrscheinlich die Überreste der Mutter-Zwerggalaxie, und die Gezeitenarme kennzeichnen die erste Beobachtung von UCDs während des Stripping Prozesses. Wenn zukünftige Beobachtungen UCDs mit Gezeitenarmen als ehemalige Kerne von Galaxien bestätigen, wären sie das fehlende Bindeglied zwischen Zwerggalaxien und UCDs.

Zudem habe ich eine neue statistische Methode entwickelt, um die Anteile verschiedener Entstehungsmechanismen zur gesamten UCD Population im Fornaxhaufen zu bestimmen. Die Methode überprüft, ob Kugelsternhaufen häufiger in der Nähe von UCDs vorkommen als was von ihrer globalen Verteilung im Halo von NGC 1399 erwartet wird. In der Tat wurde eine lokale Häufung von Sternhaufen innerhalb von 1 kpc um UCDs gefunden. Dieser Häufungseffekt ist stärker für die metallarmen blauen Kugelsternhaufen, und ist konsistent mit Rest-Kugelsternhaufensystemen um gestrippte Zwerggalaxien herum.

Am schwachen Ende der Zwerggalaxie-Sternhaufen Übergangsregion, habe ich Crater/Laevens I, ein Objekt im äußeren Halo der Milchstraße, studiert. Seine Eigenschaften sind sehr kontrovers, da es Hinweise dafür gibt, dass es eine Zwerggalaxie ist und andere, die die Interpretation als Kugelsternhaufen unterstützen. Um herauszufinden, ob Crater mehrere Sterngenerationen und/oder dunkle Materie beinhaltet, wurde es mit dem Integralfeldspektrographen MUSE am VLT beobachtet. Mit Radialgeschwindigkeitsmessungen konnten 26 Sterne als Mitglieder von Crater bestätigt werden. Dazu habe ich eine neue Methode entwickelt, um die positionsabhängige systematische Geschwindigkeitsunsicherheit für einen MUSE Beobachtung zu bestimmen, was die Genauigkeit der Geschwindigkeitsmessung verbessert hat. Mit einer Maximum-Likelihood Methode wurde ein Masse-Leuchtkraft Verhältnis gemessen, dass mit einem rein baryonischen Sternsystem übereinstimmt. Dieses Ergebnis bekräftigt, dass Crater ein schwacher Kugelsternhaufen im äußeren Halo ist, und keine Zwerggalaxie.

Im dritten Kapitel werden die MUSE Spektren mit synthetischen Sternmodellen verglichen, um die Metallizitäten von Craters Sternen zu bestimmen. Wir messen eine Dispersion der Eisenhäufigkeit von  $\sigma_{[\text{Fe}/\text{H}]} = 0.15 \pm 0.05$  dex. Diese stimmt innerhalb von  $2\sigma$  mit den typischen Dispersionen in Kugelsternhaufen überein und ist deutlich kleiner als

die in Zwerggalaxien. Auch dieses Resultat unterstützt die Interpretation von Crater als Kugelsternhafen. Zwei blaue Sterne außerhalb des Riesenastes haben überraschenderweise dieselben Elementhäufigkeiten und Radialgeschwindigkeiten wie die Mitgliedssterne von Crater und sind daher höchstwahrscheinlich Teil des Crater Systems. Beide Sterne können mit Modellen für post-Horizontalastentwicklung erklärt werden.

Diese Doktorarbeit hat gezeigt, dass man mit Detailstudien als auch mit globalen Studien die Entstehung und Beschaffenheit von Zwerggalaxien und Sternhaufen im Übergangsbereich herausfinden kann.

# Abstract

This thesis examines the properties of extended star clusters and ultra-compact dwarf galaxies (UCDs), and aims to establish their nature and provide insights into their formation mechanisms. In terms of their sizes and magnitudes, they are both located in the gap region between classical dwarf galaxies and globular clusters (GCs), which challenged many previous definitions of what constitutes a star cluster and what is the definition of a galaxy. Their formation and evolution is not yet understood.

In this thesis, I use deep imaging to study the properties of UCDs in the Fornax cluster. Decomposing the UCD surface brightness profiles in two components revealed the existence of faint stellar envelopes surrounding their compact cores, and for the first time the presence of significant tidal tails around some UCDs. The envelopes are the likely remnants of the former host dwarf galaxy, and the tails mark the first detection of UCDs caught during the stripping process. If future follow-up studies can confirm them as stripped nuclei, it would provide the missing evolutionary link between dwarf galaxies and UCDs. I also developed a new method to statistically constrain the contribution of different formation channels to the total UCD population in the Fornax cluster. This method tests if GCs are more abundant in the vicinity of UCDs than what is expected from their global distribution in the halo of the central Fornax galaxy NGC 1399. A local overabundance of GCs was found around UCDs within 1 kpc. This clustering effect is stronger for the metal-poor blue GCs, which would be consistent with a remnant GC systems of a stripped dwarf galaxy.

On the faint end of the dwarf galaxy-star cluster boundary region, I perform an observational study of Crater/ Laevens I, an object in the outer halo of the Milky Way, which has an ambiguous nature. To determine whether this object hosts multiple stellar populations and whether it contains dark matter, it was observed with the integral field spectrograph MUSE on the VLT. Using radial velocity measurements, 26 stars were confirmed as members of Crater. I developed a new method to quantify the spatially-dependent systematic velocity uncertainties in the MUSE cube which improved the velocity accuracy. Using a maximum likelihood analysis, the data reveal that Crater has a dynamical mass-to-light ratio that is consistent with a stellar system dominated by baryonic matter. These findings support that Crater is a faint outer halo globular cluster and not a dwarf galaxy.

Finally, I compare the MUSE spectra with synthetic stellar models, to determine the metallicities of Crater's stars. I identify an iron spread of  $\sigma_{[\text{Fe}/\text{H}]} = 0.15 \pm 0.05$  dex for the member stars, which is consistent within  $2\sigma$  with iron dispersions of GCs and much smaller than iron spreads in dwarf galaxies. This finding further supports that Crater is a GC and not a dwarf galaxy. Surprisingly, two blue stars offset from the red giant branch have similar metallicities and velocities as Crater's member stars, and thus are as well likely member stars of the system. They can be explained with evolution models of post-horizontal branch stars.

This thesis has shown that detailed as well as global studies can shed light on the nature and formation channels of dwarf galaxy-star cluster transition objects.



# Chapter 1

## Introduction

### 1.1 The "gap" between star clusters and dwarf galaxies

Since the discovery of the first globular clusters and galaxies their classification was an easy task using their physical sizes and magnitudes. Every object that has a half-light radius above 100 pc was catalogued as a galaxy and everything below a size of 10 pc was readily put into the globular cluster category. The sizes between 10-100 pc were not populated with any objects and served as obvious division line between those two classes of objects. This simple and intuitive classification scheme was substantially challenged by the discovery of dozens of intermediate objects that fell right into this gap region. The clear distinction line between galaxies and star clusters (e.g. [Gilmore et al. 2007](#)) in terms of their sizes but also masses and luminosities became blurred. The magnitude-size plane of early-type galaxies and GCs is shown in Fig. 1.1. The "galaxy branch" extends from giant elliptical galaxies (in blue), to dwarf galaxies (orange and dark green symbols), whereas the GCs are plotted as light grey dots. The other symbols mark objects that were only discovered in the last 20 years. These intermediate objects are in general more extended and brighter in size than the average globular cluster. However, they are considerably more compact than a dwarf galaxy of similar luminosity. This previously empty area in the mass-size plane of the early-type stellar systems (see Fig. 1.1) is gradually being filled with new objects.

At the faint end of the mass-size relation ( $M_V > -8$ ), these newly discovered intermediate objects were named ultra-faint dwarfs (UFDs) and extended star clusters (e.g. [McConnachie 2012](#); [Willman et al. 2005a](#); [Huxor et al. 2005](#); [Zucker et al. 2006b,a](#); [Belokurov et al. 2007, 2008](#); [Laevens et al. 2015a](#); [Martin et al. 2016b](#)). At the bright end between  $-14 \text{ mag} < M_V < -10 \text{ mag}$  ultra-compact dwarf galaxies (UCDs) were discovered ([Minniti et al. 1998](#); [Hilker et al. 1999](#); [Drinkwater et al. 2000](#)). The appearance of the latter wiped-out the simple dividing line between star clusters and galaxies, and raised many questions about their origin. It is especially under debate if they genuinely formed with their current physical properties (nature) as massive GCs, or if they have been subjected to extensive transformation processes by their environment, such as e.g. the tidal forces exerted by host galaxies, and were originally the nuclei of those. The formation channel of UFDs/extended star clusters is similarly unclear. They are either the smallest known dwarf galaxies that formed in the smallest dark matter halos, or they are pure stellar systems. The question remains, why extended clusters are much larger in size than normal star cluster. The first possibility is that these GCs were formed with smaller half-light

radii of  $\sim 4$  pc classical GCs and they are extended in size due to tidal transformation that expands them. Another theory is that there are two modes of GC formation, one normal mode which produces the compact 4 pc sized clusters and an extended mode when GCs form in the shallow gravitational potential of dwarf galaxies (Da Costa et al. 2009).

This thesis aims to improve the understanding of the formation channels and nature of objects in the boundary region between star clusters and dwarf galaxies. It is vital to understand these objects thoroughly, as it will enhance our knowledge of how galaxies form within the smallest dark matter halos and how the densest and most diffuse GCs form. Studying these objects will provide insights into questions such as: Is there a maximum stellar density for a globular cluster? Is there a smallest size for a dwarf galaxy? Are UCDs transition objects that pass the gap originating from nucleated dwarf galaxies? Is the gap region filled with stable objects that formed there, or are they in a transition phase crossing the gap region? And, if they intrinsically formed in the gap region, why is the specific frequency in it much lower than for galaxies/GCs?

### 1.1.1 How to define a galaxy?

There have been attempts in the literature to clarify the term galaxy when distinguishing them by mere morphological properties and size and magnitude is not feasible anymore (e.g. Willman & Strader 2012). The two proposed diagnostics to disentangle dwarfs from star clusters, is the presence of an unseen mass and a spread in iron abundance. The current cold-dark matter galaxy formation paradigm suggests that galaxies form at the centres of dark matter halos (White & Rees 1978). Since globular clusters do generally not show signatures of an unseen mass component (e.g. Jordi et al. 2009; Frank et al. 2012) they are expected to form independently of dark matter subhalos. A dynamical mass-to-light ratio that is elevated above the expected baryonic mass is considered a diagnostic for galaxies. However, this diagnostic assumes that the stellar system is in dynamical equilibrium.

In addition to dynamics, the chemical composition of the stellar population can also be used as a tracer of how the object has formed. Dwarf galaxies have assembled their stellar population during multiple epochs of star formation (Grebel & Gallagher 2004). A dwarf galaxy can have continuous star formation episodes spanning over many Gigayears. Globular clusters in contrast, formed in very short and intense bursts of star formation.

During multiple epochs of star-formation, the metals that are produced in supernova explosions of the first generations of stars can subsequently pollute the gas out of which later generations are formed. This will increase the metallicity of the younger generations of stars significantly. Thus in (dwarf-) galaxies with an extended star-formation history a high ( $>0.1$  dex) spread in the iron abundance  $[\text{Fe}/\text{H}]$  (see Fig. 1.2) can be detected, whereas no such spread is found in globular clusters, as they have no time to self-enrich in heavy elements (Kirby et al. 2008, 2010; Willman et al. 2011; Willman & Strader 2012).

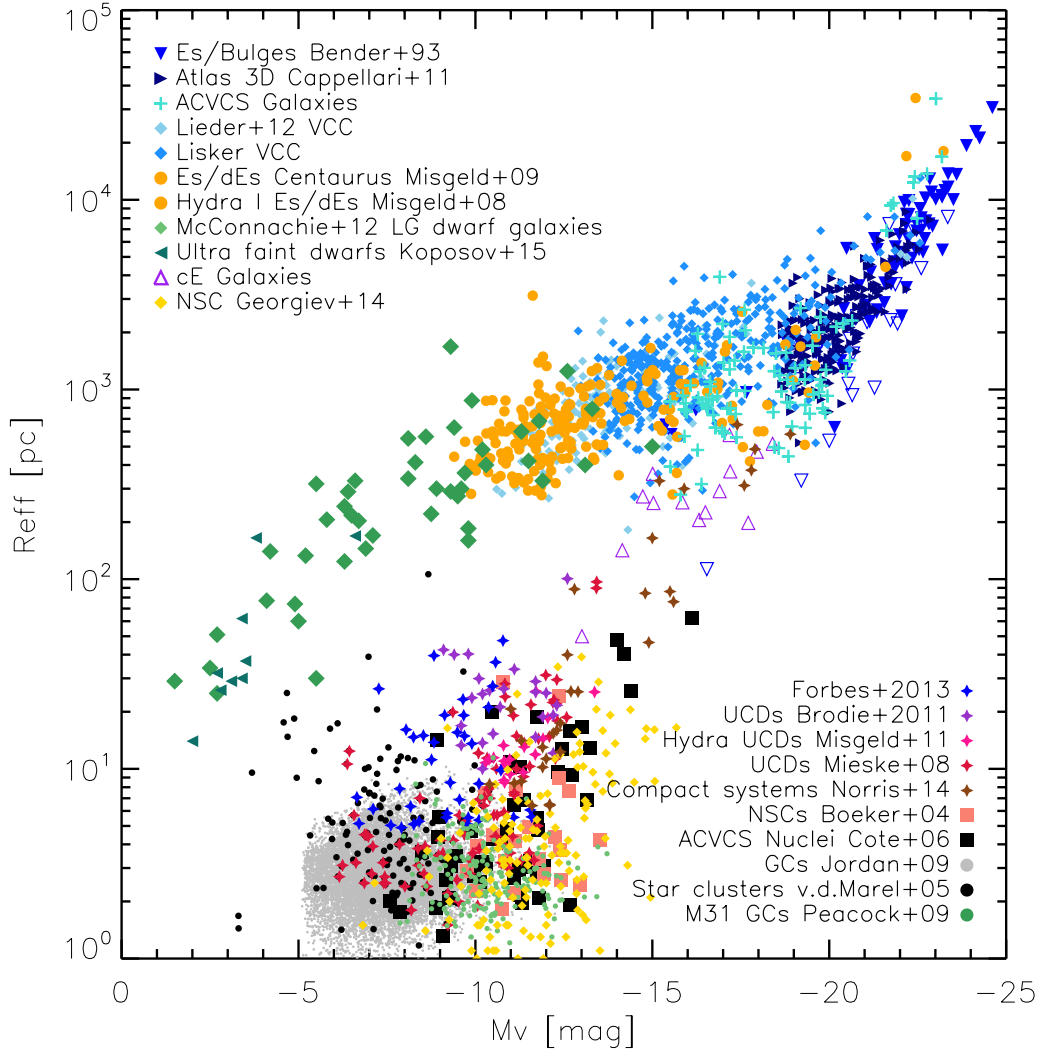


Figure 1.1: A compilation of early-type systems in the size-magnitude plane. Giant ellipticals, normal ellipticals, bulges and some bright dwarf ellipticals are shown with blue triangles (Bender et al. 1993), dark blue triangles (Cappellari et al. 2011), light blue plus signs (Ferrarese et al. 2006), light blue diamonds (Lieder et al. 2012), dark blue diamonds (Lisker et al. 2007) and compact ellipticals are denoted by open purple triangles (Price et al. 2009). Dwarf ellipticals and ultra-faint dwarfs are shown as orange circles (Misgeld et al. 2008a, 2009a), green diamonds (McConnachie 2012) and green triangles (Koposov et al. 2015). Ultra-compact dwarf galaxies are plotted as blue star symbols (Forbes et al. 2013), purple stars (Brodie et al. 2011), pink stars (Misgeld & Hilker 2011), red stars (Mieske et al. 2008) and brown stars (Norris et al. 2014). The nuclear star clusters are plotted as yellow diamonds (Georgiev & Böker 2014), orange squares (Böker et al. 2004), and black squares (Côté et al. 2006). The globular clusters are marked as grey dots (Jordán et al. 2009), black dots (McLaughlin & van der Marel 2005) and green dots (Peacock et al. 2009).

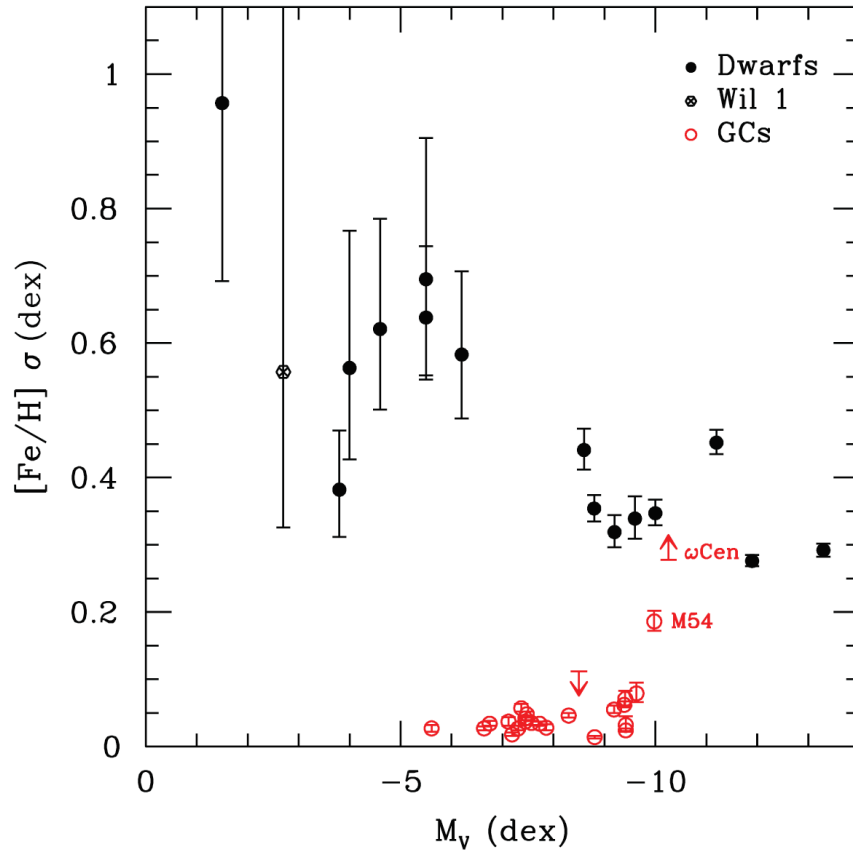


Figure 1.2: The iron spread is shown as a function of the absolute magnitudes of GCs and dwarf. GCs are marked in red, whereas dwarf galaxies are plotted in black. Figure taken from [Willman & Strader \(2012\)](#).

## 1.2 The bright end of the boundary region: Ultra-compact dwarf galaxies (UCDs)

Ultra-compact dwarf galaxies were first noticed in a spectroscopic survey of the central Fornax cluster galaxy NGC 1399 ([Minniti et al. 1998](#)). With radial velocity measurements, a compact object much brighter than a typical GC was unexpectedly confirmed to be a member of the galaxy. Another spectroscopic survey of the Fornax cluster ([Hilker et al. 1999](#)) confirmed these findings, and found a second bright compact member object. Already in this early work it was speculated that these objects might either be very compact elliptical galaxies, very bright globular clusters or the stripped nuclei of dwarf elliptical galaxies. The wide field 2dF spectroscopic Fornax survey discovered three further UCDs in addition to the two already discovered ones around NGC 1399 ([Drinkwater et al. 2000](#)). In [Phillipps et al. \(2001\)](#) the name ultra-compact dwarf galaxies was proposed. The general physical properties of this new class of UCD objects were then compiled by [Drinkwater et al. \(2003\)](#). Although their naming implies that they are intrinsically compact dwarf



galaxies, there is no consensus on their nature and their formation is still widely debated in the literature. As most of the literature has used the UCD naming convention, I will continue to use it throughout this thesis as well, but want to emphasise that this does not imply a conclusion about their nature.

UCDs make up a new class of objects. Their definition varies between different works, but the parameters all definitions have in common, place them at a brightness between  $-10 < M_V < -14$ , with sizes ranging from 10-100 pc. Hence they are generally more extended in size and significantly brighter than the normal globular clusters.

Before the discovery of UCDs, the location of GCs (grey dots, Fig. 1.1) and (dwarf-) galaxies (blue, orange symbols in Fig. 1.1) in the size-magnitude plane was well separated by one order of magnitude in size. UCDs have removed this size gap and effectively connected the "star cluster branch" from GCs, to UCDs, to compact ellipticals (purple triangles Fig. 1.1) all the way to normal elliptical galaxies (blue symbols). Understanding the composition of these intermediate objects and their physical formation mechanisms is key to understand dynamically hot stellar systems.

### 1.2.1 Formation channel of UCDs

In the literature two major scenarios considering the formation process of UCDs are discussed. One hypothesis suggests that UCDs are nuclei of (dwarf-) satellite galaxies that were tidally stripped by their host galaxy (Bekki et al. 2003). Simulations have shown that the stripping of a dwarf galaxy in a galaxy cluster can produce a UCD-like object where only the nucleus remains (Pfeffer & Baumgardt 2013). The path of an UCD in the mass-size plane, when subjected to the tidal forces of a galaxy cluster, is shown in Fig. 1.3. Three different simulations from Pfeffer & Baumgardt (2013) are shown as coloured tracks. The set-up of these simulations starts with nucleated dwarf galaxies placed in the tidal field of a galaxy cluster that is comparable to the Virgo cluster. The simulations demonstrate that repeated close pericenter passages of dwarf galaxies on elliptical orbits can produce UCD-like objects through tidal stripping. Their simulations also suggest that what is observed as 'extended' UCDs could be compact nuclear star clusters surrounded by a remnant stellar envelope. They could merely appear as one single extended object due to the superimposed envelope on the nuclei that we cannot discriminate with normal ground based seeing-limited observations. Extended, double light-profile objects are produced by orbits with only few close pericenter passages in the simulations. If UCDs are extended due to the residual light from a former dwarf elliptical envelope this would explain the 'nuclei-size' problem that UCDs face. If UCDs are stripped galaxy nuclei, why do they have sizes 2-20 times larger than what is measured for nuclei of dwarf galaxies? Nuclear star clusters are generally much smaller than UCDs with  $r_{\text{half}} \sim 4$  pc. Two-component light profiles are also observed for several of the brightest UCDs in Fornax and Virgo, using HST photometry (e.g. Evstigneeva et al. 2007, 2008).

Another straightforward interpretation of the existence of UCDs is that they are the natural bright tail of the globular cluster distribution and thus have formed in a similar fashion as their low luminosity globular cluster counterparts. In Mieske et al. (2004) a study

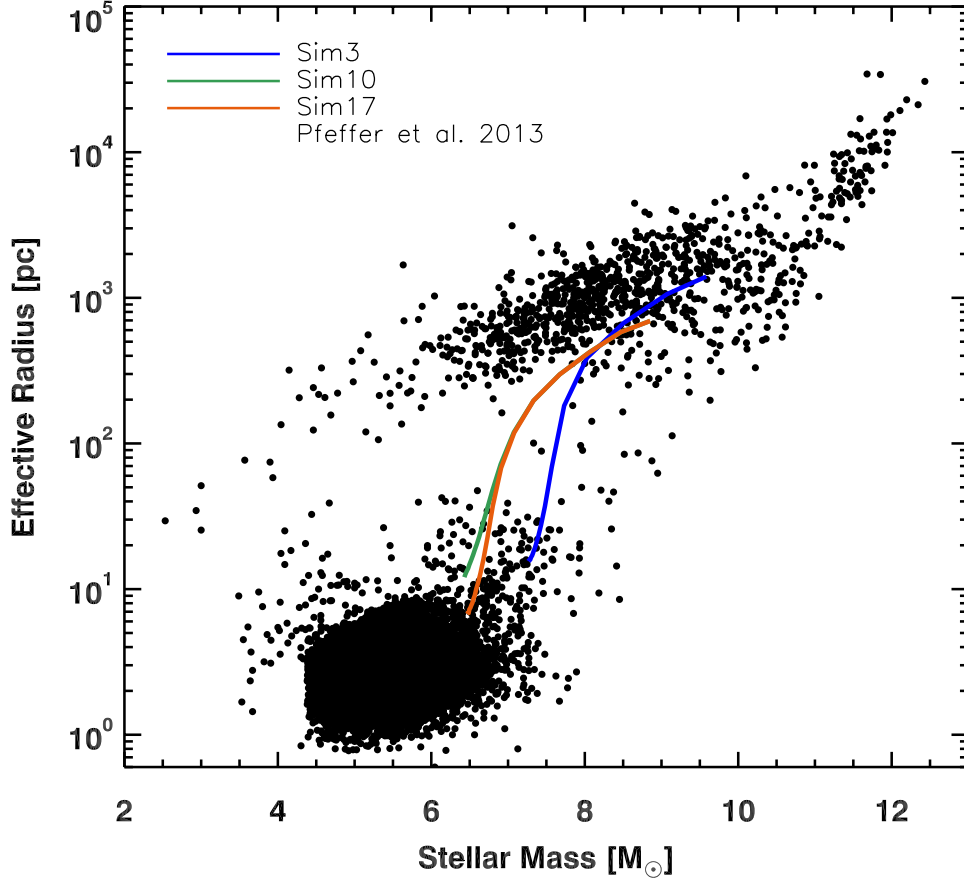


Figure 1.3: In this plot early-type systems from Fig. 1.1 are plotted as black points. Overlaid as coloured tracks are three different simulations from Pfeffer & Baumgardt (2013) of a dwarf elliptical being stripped in a galaxy cluster.

of UCDs in the Fornax cluster suggests that only objects brighter than  $M_V = -11.4$  are genuine UCDs and the fainter UCDs are compatible with the globular cluster luminosity function.

In Murray (2009) it was proposed that the observed increase of the size of UCDs with mass can be explained by star clusters becoming massive enough that they are optically thick to infrared radiation. If massive GCs are optically thick during their formation it would lead to a mass-size relation of  $r_{gc} = 0.3(\frac{M_{gc}}{10^6 M_\odot})^{3/5}$  pc when taking into account the equilibrium between radiation pressure and gravity. This transition between normal GC formation and optically thick GC formation is expected to set in for globular cluster masses of  $M_\odot > 10^6$ , which is similar to the mass where we observe the onset of the mass-size relation. This formation scenario of Murray (2009) also predicts that the mass-to-light ratios of old, massive UCDs should be elevated, compared to less-massive GCs.

Elevated mass-to-light ratios are observed for massive UCDs. Hasegan et al. (2005) reported six massive UCDs have mass-to-light ratios between  $M/L_V = 2.9 - 9.3$ . In

Evstigneeva et al. (2007), six UCDs in the Virgo cluster have the same range of elevated mass-to-light ratios. Five UCDs in the Fornax cluster also exhibit V-band mass-to-light ratios between 3-5 (Hilker et al. 2007). Although single UCDs with such M/L ratios can be compatible with stellar population models, the ensemble properties of UCDs with  $M_{\odot} > 2 \times 10^6 M_{\odot}$  have a significantly elevated M/L ratio. For higher dynamical masses of  $M > 10^7 M_{\odot}$  the average mass-to-light ratio is  $M/L \sim 5$  (see Fig.6 in Murray 2009), whereas  $M/L \sim 2$  is expected from their stellar population.

Other scenarios favour the theory that UCDs originate from massive star cluster complexes in merging galaxies, where many smaller clusters subsequently merge into a more massive UCD-like object. A highly concentrated ensemble of young massive clusters merge within several hundred Megayears into a single star cluster of  $10^6 M_{\odot}$  in the numerical simulations of Fellhauer & Kroupa (2002). The lower concentration star cluster complexes in the simulations are ripped apart by tidal forces and will not merge into one large cluster, but get distributed as single smaller star clusters in their host galaxy. Another simulation of star cluster complexes by Brüns et al. (2011) studies the final properties of the merged object. Their simulation covers a wide range of input masses for the star cluster complexes from  $10^{5.5} - 10^8 M_{\odot}$ . They find that the final structural parameters of the merged complexes are consistent with the values measured for both extended star clusters and UCDs. Star cluster complexes are fully merged into one smooth object without detectable GC substructure after 1 Gigayear.

Despite the fact that most UCD studies have tried to assign one origin to the whole category of UCDs, it is discussed that they might be objects with vastly different physical origins. Although they ended up with the same size and magnitude and occupy the same space in the size-magnitude scaling relations they might not have a common physical origin (Hilker 2006). Therefore, what is categorised commonly as UCDs could in fact be a mix of massive GCs and stripped nuclei of dwarf galaxies. The detailed study of an ensemble of UCDs in a compact group (Da Rocha et al. 2011) has shown that the majority of objects classified as UCDs are consistent with the bright end of the GC population. Nevertheless there is evidence that at least one of their UCDs a stripped nucleus. They detect an intermediate age stellar population which is not consistent with standard GC formation scenarios. However, such intermediate age GCs can be produced in galaxy mergers.

Assuming that the category of UCDs is made up of both, stripped nuclei and high mass GCs, new observables that go beyond size and magnitude are needed to disentangle the contribution of each formation channel to this class of objects.

UCD studies have mainly focussed on the photometric properties (size, magnitude, colour) of a large number of objects (e.g. Mieske et al. 2002; Hasegan et al. 2005; Evstigneeva et al. 2008; Price et al. 2009; Gregg et al. 2009; Zhang et al. 2015; Liu et al. 2015a) or on very detailed studies of a few individual objects (e.g. Hilker et al. 2007; Strader et al. 2013; Seth et al. 2014; Janz et al. 2015; Norris et al. 2015; Liu et al. 2015b). The former approach, i.e. gathering observational parameters for a large UCD ensembles cannot differentiate conclusively between both formations channels.

Identifying the origin of individual UCDs is observationally very expensive as most UCDs are at large distances and thus too faint for high signal-to-noise spectroscopy. It

typically requires several hours of observing on an 8 meter class telescope like the VLT to get high S/N spectroscopy. In addition, their small physical sizes make them barely resolved in ground-based imaging at distances of Fornax, Virgo or other nearby galaxy clusters. This makes dynamical and chemical studies of their internal resolved properties only feasible with space-based facilities such as HST or adaptive optics supported ground-based telescopes. Therefore, coherent large spectroscopic campaigns to get detailed internal properties of UCDs are very challenging. Currently, we are confined to determining the formation channels of individual UCDs piece by piece. Due to the different methods and different environments, our ability to derive general conclusions about the nature and contribution of each formation channel to the general population of UCDs, is severely limited.

There are several observables that are "smoking gun" properties for UCDs that are the former nuclei of dwarf galaxies. The presence of a super-massive black hole, an extended star-formation history over several Gyrs, or tidal tails as direct evidence for the stripping process, are such observables. The detection of a supermassive black hole (SMBH) in M60-UCD1 by [Seth et al. \(2014\)](#) is to date the most solid evidence for a UCD that formed as the stripped nucleus of a dwarf galaxy. [Norris et al. \(2015\)](#) discovered an extended star formation history over several Gyrs for NGC 4546-UCD1 from its integrated light spectrum. These signatures for stripped nuclei origins are still rare and limited to individual objects, as there is no observable that can discriminate the fraction of each formation channel for an entire UCD population.

One way of discriminating UCD formation scenarios is to search for low surface brightness envelopes as the remnants of the stripped dwarf galaxy host. To do this high spatial resolution imaging that also reaches low surface brightness levels are required to decompose its surface brightness profile into a core and the faint envelope component. At the distances of the Fornax cluster, the angular scale is given as 92 pc/arcsec. Thus even for a good ground-based seeing of 0.6 arcsec, most UCDs are only marginally resolved with physical sizes of 10-50 pc. This is equal to an angular extent of 0.1-0.55 arcsec at the distance of Fornax. However they can be spatially resolved by space telescopes such as HST, or JWST in the future, or by using adaptive optics on ground based imaging. A handful of light profiles of UCDs were studied using HST imaging ([Evstigneeva et al. 2007, 2008](#); [De Propris et al. 2005](#)).

For the most luminous and extended UCDs it was found that a single King profile does not fit their luminosity distribution well. Combining a King profile for the core and a Sérsic or exponential profile for the halo component can reproduce the surface brightness profiles of the most extended UCDs ([Evstigneeva et al. 2008](#); [Strader et al. 2013](#)). In particular the brightest UCDs require highly concentrated profiles in their centres and extended exponential profiles to model the wings of the light distribution. These envelope components can have effective sizes up to 100 pc (e.g. [Drinkwater et al. 2003](#); [Richtler et al. 2005](#)). Extended faint surface brightness envelopes around UCD-like objects were also observed by [Liu et al. \(2015a\)](#) in the Next Generation Virgo survey. UCDs with envelopes are more likely to be located further from the centre of the galaxy cluster in this study. This correlation of envelope fraction with the cluster-centric distance is compatible

with stripping as UCD formation channel.

There are six known UCDs that show a double surface brightness profile, VUCD 7 in the Virgo cluster and UCD 3 and UCD 5 in the Fornax cluster (Evstigneeva et al. 2008). The compact object M59cO (Chilingarian et al. 2008) and the densest known UCD, M60-UCD1 (Strader et al. 2013) are both located in the Virgo cluster, also show double light profiles. In section 2.3.2 we demonstrate the capability of very good seeing ground based imaging to find UCDs with extended envelopes. Using ground based instead of space-based imaging enables much larger areas to be surveyed for envelopes, and are not limited to preselected individual objects that require HST observations.

### 1.2.2 Dynamical friction and the formation of UCDs

It was suggested that the nuclear star clusters (NSCs) of galaxies are formed through the inspiraling and merging of globular clusters in the center (e.g. Tremaine et al. 1975; Capuzzo-Dolcetta 1993). The inspiraling of GCs that move through the stellar field of a host galaxy is caused by dynamical friction, which is a drag force that slows down stars passing through field stars. If UCDs are the stripped nuclei of former dwarf galaxies, they might form through the inspiraling of GCs into the nucleus.

The theory of the effects of dynamical friction on stars was first described by Chandrasekhar (1943). Energy and momentum is transferred from the test particle to the field stars via two-body encounters. This force leads to the loss of orbital energy for massive objects moving through the host system of smaller particles, and massive objects move closer to the centre. The decay of massive particle orbits is also the reason that mass-segregation in globular clusters exists, where more massive stars sink to the centre and become centrally concentrated. Dynamical friction also affects globular clusters on their orbits through the stellar field of a host galaxy, causing them to lose energy and finally decay into the galaxy nucleus in case the dynamical friction decay timescale is short enough.

The time it takes for the orbit of a globular cluster of the mass  $M$  to decay into the centre of an isothermal halo with a circular velocity  $v_c$  from an initial distance  $r_i$  was parameterized for example by Lotz et al. (2001) and is given as:

$$t_{\text{dyn}} = \frac{2.64 \cdot 10^2}{\ln \Lambda} \left( \frac{r_i}{2 \text{ kpc}} \right)^2 \left( \frac{v_c}{250 \text{ kms}^{-1}} \right) \left( \frac{10^6 M_\odot}{M} \right) \text{Gyr} \quad (1.1)$$

A first study with numerical methods to test the GC inspiraling scenario for nuclear star cluster formation was done by Capuzzo-Dolcetta (1993), where it was shown that dynamical friction is efficient enough to carry sufficient stellar mass to the centre of galaxies to form a compact nucleus.

Dwarf galaxies have smaller circular velocities  $v_c$  which result in shorter decay timescales, making this process more efficient. In Lotz et al. (2001) it is calculated that in a dwarf galaxy with a circular velocity  $v_c = 50 \text{ kms}^{-1}$  all globular clusters above a cluster mass of  $5 \times 10^5 M_\odot$  will have merged into the centre within 10 Gyrs, if they were originally within 1 kpc of the centre of the galaxy. Therefore, the dynamical friction decay timescale is less than a Hubble time.

In their observational study, [Lotz et al. \(2001\)](#) found a deficit of bright globular clusters in the central regions of nucleated dwarf ellipticals when comparing it to the outer regions of the galaxy. This is interpreted as direct observational evidence for the inward migration of massive GCs.

In [Arca-Sedda & Capuzzo-Dolcetta \(2014\)](#) a statistical approach was used to constrain the number of expected surviving globular clusters around a galaxy, as function of its mass, after a full Hubble time of dynamical friction at work. Their models predict on average 65% of the original globular cluster population has migrated to the centre within one Hubble time in a host galaxy with  $M = 10^{10} M_{\odot}$ . This fraction rises for smaller host masses. For a galaxy of  $M = 10^9 M_{\odot}$  one expects 80% of the original GCs to decay into the centre of the galaxy and merge there with the nucleus. If UCDs are the stripped nuclei of former dwarf galaxies with masses of  $M = 10^9 - 10^{10} M_{\odot}$ , who hosted their own globular cluster system, a large fraction of their GC population has merged into the nucleus and the remaining GCs are still on their way to merge into the nucleus.

In particular, we can test if there is a statistical overabundance of globular clusters in close proximity to UCDs, which is expected if inwards migration of GCs is still ongoing within the shrinking tidal radius of the disrupting dwarf galaxy. In addition, GCs clustered around UCDs within its tidal radius are much easier to detect than the low surface brightness envelopes from the progenitor galaxies, as they are bright point sources. In contrast, the low surface brightness envelopes from the progenitor galaxies require much deeper imaging to be detected.

As the dynamical friction decay timescale is shorter for massive test particles, massive GCs will merge into the nucleus faster and mainly lower mass GCs will survive around UCDs. This can be tested by sampling the luminosity function of the companion GCs and test if it is consistent with the faint-end globular cluster luminosity function (GCLF).

Super star cluster mergers also have substructure and non-merged companion GCs in their early stages of formation. [Brüns et al. \(2011\)](#) simulated a merging super star cluster complex. It has several surrounding close GC companions 70 Myrs after the start of the merging process and after 280 Myrs, only one non-merged GC is left. Finally, after 1.3 Gyrs, no more companions or substructure are visible and the merging process has finished. In a simulation of extended star cluster formation with a mass of  $10^5 M_{\odot}$  ('faint fuzzies') the substructure caused by non-merged star clusters can survive up to a post-merger age of 5 Gyr ([Brüns et al. 2009](#)). Also tidal tails are formed while the merged star cluster complex orbits in the gravitational field of its host galaxy. Therefore, companions and tidal tails around merged super star clusters are detectable up to a Gyr after their formation in massive complexes and several Gyrs in low-mass star cluster complexes.



### 1.3 The faint end of the boundary region: Ultra-faint dwarf galaxies and extended star clusters

At the very faint end of the scaling relations, until 2005 only the 11 "classical" dwarf galaxies of the Milky Way were known. Of these 11 classical satellites 8 are dwarf spheroidal galaxies with magnitudes between  $-13.1 < M_V < -8.9$ , and then there are the LMC ( $M_V = -18.5$ ), SMC ( $M_V = -17.1$ ) and Sagittarius as the brighter non-spheroidal companions of the Milky Way (magnitudes taken from [Grebel et al. 2003](#)). Then the faintest known dwarf spheroidal satellite galaxy was Ursa Minor with  $M_V = -8.9$ . At that time globular clusters and dwarf galaxies were well separated in the size-luminosity parameter space and thus could easily be distinguished from each other. In [Gilmore et al. \(2007\)](#) it was suggested that any stable star cluster always has an effective radius of  $r_{\text{eff}} < 30$  pc, whereas any stable dwarf galaxy would have a radius larger than  $r_{\text{eff}} = 120$  pc.

The advent of new wide-field surveys with unprecedented depths in surface brightness, have opened a completely new field of astrophysics with the discovery of dozens of ultra-faint dwarf satellite galaxies in the halo of the Milky Way. The first wide field survey that discovered many new faint satellites was the Sloan Digital Sky Survey ([York et al. 2000](#)), which doubled the number of known dwarf galaxies of the Milky Way.

The first two dwarfs that are much fainter than the classical dwarfs were discovered in 2005. Ursa Minor ([Willman et al. 2005a](#)) has a magnitude of  $M_V = -6.75$  and a half-light radius of 250 pc. The second dwarf was later named Willman I, with  $M_V = -3.0$  and a very small half-light radius of 23 pc, almost an order of magnitude smaller than previously known dwarf galaxies ([Willman et al. 2005b](#)). Due to its ambiguous properties it was not obvious if it was a dwarf galaxy or a globular cluster. Later it was confirmed to be the least-luminous ultra-faint dwarf galaxy known at that point. In the following years many more ultra-faint dwarf galaxies were discovered. Boötes I ([Belokurov et al. 2006](#)), Canes Venatici ([Zucker et al. 2006b](#)), Ursa Major ([Zucker et al. 2006a](#)), Canes Venatici II ([Sakamoto & Hasegawa 2006](#)), 5 new dwarf satellites by [Belokurov et al. \(2007\)](#): Leo T ([Irwin et al. 2007](#)), Boötes II ([Walsh et al. 2007](#)), Leo V ([Belokurov et al. 2008](#)), Boötes III ([Grillmair 2009](#)) and Segue II ([Belokurov et al. 2009](#)). Within a timespan of only 5 years, the number of known dwarf satellites of the Milky Way has increased significantly. These 15 new dwarf satellites were all discovered within the limited footprint of the SDSS survey area, which mainly covers the northern galactic pole, and many more are likely to be found in other regions of the sky. The revelation of ultra-faint dwarfs between  $-8 < M_V < -1.5$  has opened an entirely new field of "near-field" cosmology, devoted to study the faintest galaxies and their implications for galaxy formation and dark matter theories.

Many regions not included in the SDSS footprint are covered by new surveys, such as Pan-STARRS1, which already discovered five new MW companions. The first discovery was Crater/Laevens I ([Laevens et al. 2014](#)), which was also independently discovered in a second publication by [Belokurov et al. \(2014\)](#) at the same time. The second new dwarf satellite is Triangulum II ([Laevens et al. 2015a](#)). Furthermore, in [Laevens et al. \(2015b\)](#), three more dwarf companions were discovered in the Pan-STARRS1 footprint: Sagittar-

ius II, Draco II and Laevens 3. In addition, another ultra-faint dwarf, Hydra II (Martin et al. 2015) was revealed, using the Magellanic Stellar History Survey.

The publicly available data from the Dark Energy Survey (DES) have expanded the zoo of dwarf galaxies even further. A total of 9 new companion objects in the halo of the Milky Way were discovered, of which 8 are thought to be ultra-faint dwarf galaxies (Koposov et al. 2015). In the same dataset another ultra-faint dwarf, Horologium II was identified (Kim & Jerjen 2015), after having been overlooked previously.

Such faint satellite galaxies were also recognised in the vicinity of the Andromeda galaxy in recent years. For example, Zucker et al. (2004) observed a dwarf spheroidal satellite around Andromeda with  $M_V = -8.3$ . Three fainter dwarf satellites with absolute magnitudes from  $-7.3 < M_V < -6.4$  were found by Martin et al. (2006). In total there are 28 known dwarf satellite galaxies of Andromeda. In contrast to the Milky Way satellite system, due to the larger distance to Andromeda, only satellites down to a magnitude of  $M_V \sim -6$  are known.

The sizes and magnitudes of all these dwarf galaxies are plotted in the faint-end scaling relations in figure 1.4. The green points denote the objects that have been classified as dwarf galaxies, blue points the ultra-faint dwarf galaxies discovered in the last two years (see caption of the figure), whereas black dots mark objects that are classified as globular clusters. Crater that will be studied in further detail in this thesis, is marked with two red star symbols, represent the size and magnitude values from the two discovery papers. This figure visualises, how the formerly clear size division at the faint end of the size-magnitude scaling relations has been blurred by the discovery of a zoo of objects that fall right into this gap.

Within this blended parameter space, determining the nature of an object, becomes substantially more challenging. The current consensus on how to define a galaxy are the dynamical signs of the presence of dark matter and a prolonged star formation history (Willman & Strader 2012). Therefore, deducing the nature of ultra-faint objects requires spectroscopic follow-up, to analyse the detailed chemistry and dynamics of the individual stars (e.g. Martin et al. 2016a, 2015; Kirby et al. 2015).

It has been noted already many years ago that the distribution of dwarf galaxies is not random but several of the satellites are aligned in what was called the "Magellanic plane" (Lynden-Bell 1976). The satellites of the MW are located in a thin (20 kpc) disk-like structure (Kroupa et al. 2005), and 8 out of the 11 classical satellites co-rotate in the same direction (Metz et al. 2008). Many of the newly discovered ultra-faint dwarf galaxies, as well as young outer halo star clusters (e.g. Kim 1 or Crater I) also align with this plane (see Figure 1.5 from Pawlowski et al. 2015). This alignment was named the Vast Polar Structure of the Milky Way (VPOS) (Pawlowski et al. 2012). The members of the VPOS are aligned in a plane and co-rotating in the same direction, as visualised by the red arrows plotted in Figure 1.5.

The dwarf galaxies surrounding the Andromeda galaxy are similarly distributed in two planes of satellites (Ibata et al. 2013). Half the dwarf galaxies associated with Andromeda are located in a thinner plane than the MW with a thickness of merely 14 kpc, and they co-rotate in the same angular direction. That the dwarf galaxies surrounding the Milky



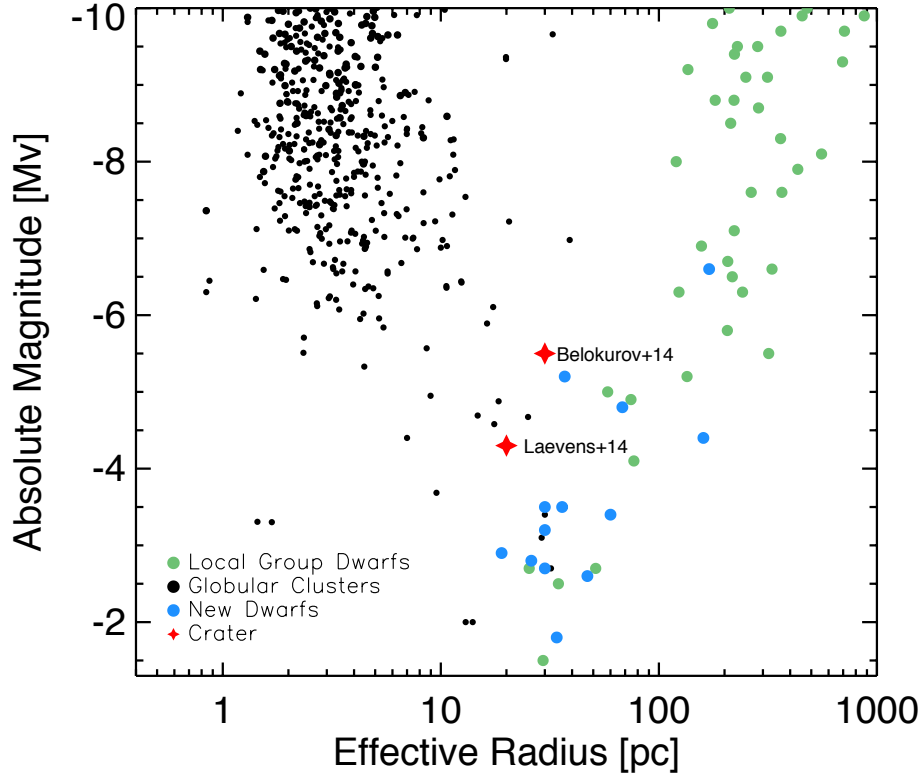


Figure 1.4: The faint end of the size-magnitude scaling relation for early-type systems. Green points mark the sizes and magnitudes of Local Group dwarf galaxies from [McConnachie \(2012\)](#), and black points mark the globular clusters. Blue circles are the ultra-faint dwarf galaxies discovered in the recent two years ([Laevens et al. 2015a,b](#); [Koposov et al. 2015](#); [Kim & Jerjen 2015](#); [Martin et al. 2015](#)). The red stars mark the size and magnitude of Crater as determined by the two discovery papers of [Belokurov et al. \(2014\)](#) and [Laevens et al. \(2014\)](#).

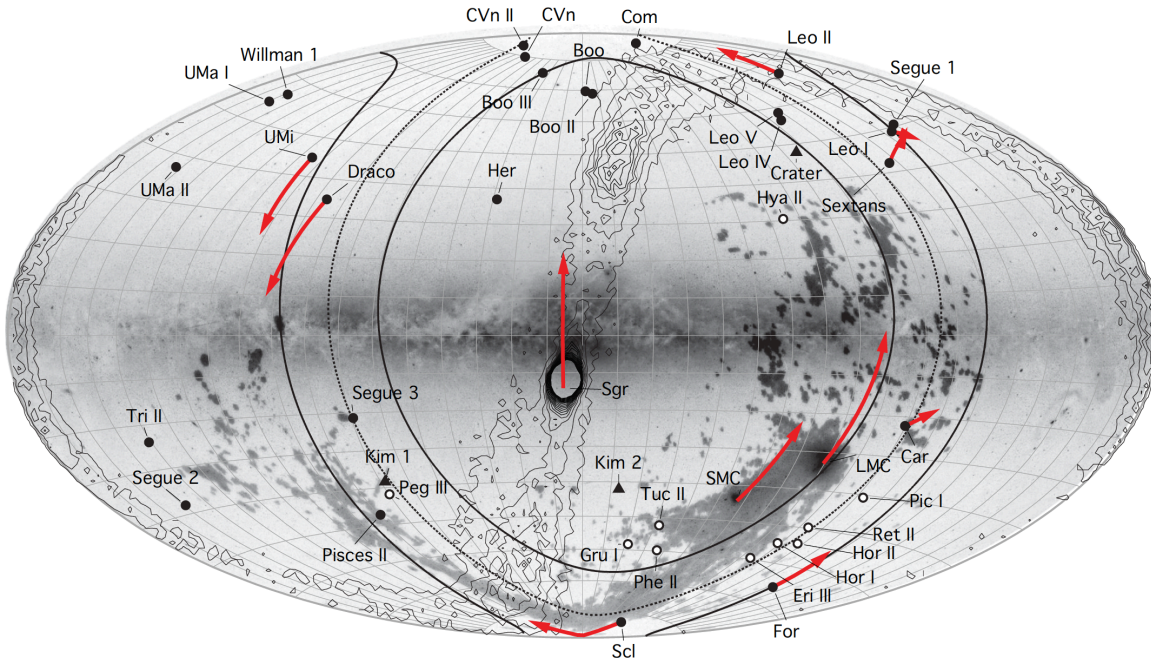


Figure 1.5: A full sky plot of the satellites of the Milky Way (filled and open circles), outer halo star clusters (triangles) and the Milky Way and the Magellan Stream are overlaid as background images. The red arrows mark the proper motion vectors for the satellite galaxies with available measurements. The dotted line shows the best-fit plane of satellites, whereas the solid lines mark the width of the plane structure. The plot is taken from [Pawlowski et al. \(2015\)](#).

Way and Andromeda are not isotropically distributed disagrees with cosmological predictions of an isotropic distribution of dark matter (sub-)halos (Pawlowski et al. 2014). The combined probability to find a thin *and* co-rotating plane of satellites similar to the MW or Andromeda is extremely small in most dark matter simulations, and has been computed to be on the order of  $10^{-5}$ . In other words, only 1 time out of 100.000 such an alignment occurs by chance in modern dark matter simulations, which would make the Local Group an extremely special and rare case.

As a solution to this tension, it was suggested that the planes of satellites have formed through a special event, such as the tidal interaction of two major gas-rich disk galaxies. In such an encounter the formation of dark matter free tidal dwarf galaxies can be triggered (Metz & Kroupa 2007). Tidal dwarf galaxies would be without dark matter in contrast to their dark matter dominated primordial counterparts. The tidal dwarf scenario could explain the phase space correlation of position and velocity of the dwarfs located in planes (Pawlowski et al. 2011).

But detailed studies of the satellites of the Andromeda galaxy do not find significant differences in the chemistry and dynamics of satellites on and off the plane (Collins et al. 2015). That on and off-plane satellites are not distinguishable from each other in terms

of internal properties indicates that they must have formed in a very similar manner, and not in separate events. The infall of a group of galaxies along a filament is also considered as an explanation for plane of satellite formation scenarios (Li & Helmi 2008). However, it was shown that dwarf galaxy groups are too wide in size to cause the very thin planes of satellites that are observed (Metz et al. 2009).

### 1.3.1 Dynamical signatures to distinguish dwarf galaxies from GCs

Dwarf galaxies are extremely dark matter dominated objects with small stellar densities. They generally possess highly elevated mass-to-light ratios ( $M/L_V$ ), which can be as high as  $10^3$  for the faintest dwarf galaxies (see red and blue data points in Fig. 1.6). The mass-to-light ratios of galaxies display a U-shaped distribution (see Fig. 1.6) with a minimum of  $M/L_V \sim 1 - 10$  for galaxies with stellar masses of  $10^{10} M_\odot$  (Wolf et al. 2010). For more massive galaxies,  $M/L_V$  rises, up to values of 100-500. The fact that dwarf spheroidal galaxies are so extremely dark matter dominated and have a very low stellar density has made them a prime target for the searches of direct dark matter annihilation  $\gamma$ -ray signals (e.g. Ackermann et al. 2015).

In the luminosity interval of  $10^4 - 10^6 L_\odot$  dwarf galaxies possess much lower M/L ratios than globular clusters (yellow and unfilled star symbols in Fig. 1.6), and are well separated from each other in terms of their dynamical M/L ratios. The low M/L ratios for globular clusters suggest that they are intrinsically dark-matter-free. Due to the physical sizes of GCs with half-light radii of  $\sim 4$  pc and the high stellar densities, dynamical signatures of an extended dark matter halo are harder to detect than for extended ( $>100$  pc) dwarf galaxies whose stellar dynamics are dominated by dark matter. In addition, the tidal field of a host galaxy can make the dynamical detection of dark matter more difficult, as they disturb the dynamical equilibrium, which has to be accounted for computing their dynamical masses. The globular clusters in the outer halo of the Milky Way are less affected by galactic tidal effects and for several of those objects it was found that in general the M/L ratios are consistent with stellar population models (e.g. Jordi et al. 2009; Frank et al. 2012).

### 1.3.2 Spread in heavy element abundance of GCs and dwarf galaxies

The heavy element abundances within classical globular clusters is very homogenous. Most GC do not have sufficient mass to retain much of the heavy elements ejected by supernova explosions (Gratton et al. 2004; Carretta et al. 2009a). The intrinsic spread in iron abundance within most globular clusters is very small. In Carretta et al. (2009a), a large high resolution spectroscopy study of 19 globular clusters measured an iron spread of 0.05 dex or less in each cluster (see red points in Fig. 1.2).

However, for several GCs brighter than  $M_V = -10$ , a larger spread than 0.05 dex was detected. For M 54, the central GC of the Sagittarius dwarf galaxy, Sarajedini & Layden

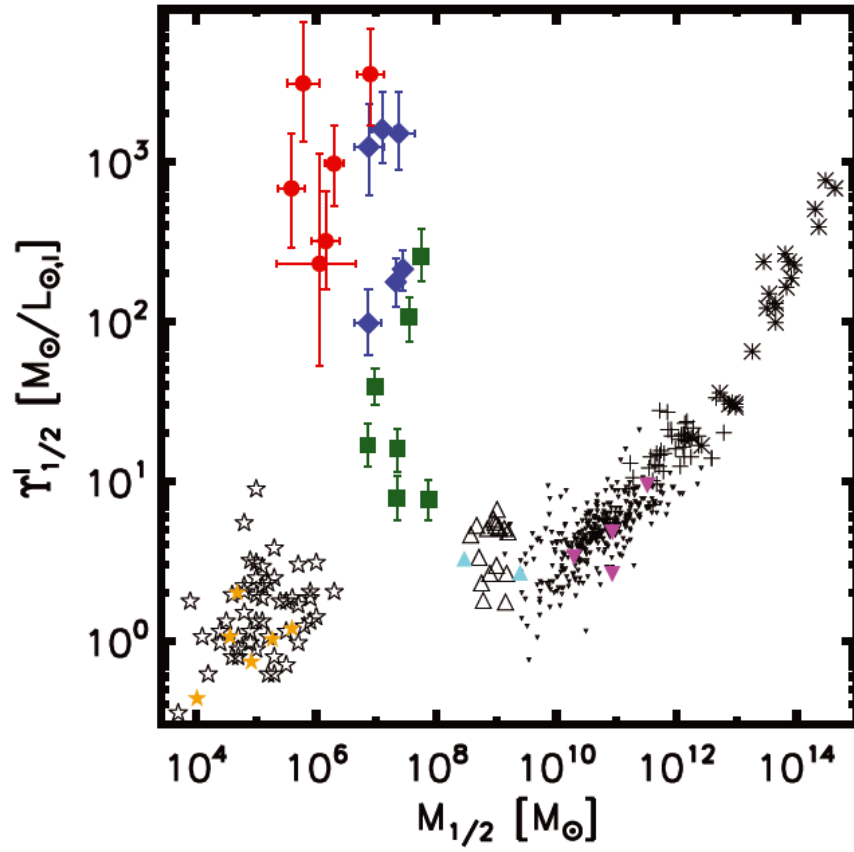


Figure 1.6: The mass-to-light ratios of early type systems is plotted against the luminosity of the systems. The yellow star symbols and unfilled star symbols are GCs from the literature. The rest of the coloured symbols are galaxies. Image taken from [Wolf et al. \(2010\)](#).

(1995) determined a spread in the  $[\text{Fe}/\text{H}]$  abundance of  $\sigma_{[\text{Fe}/\text{H}]} = 0.16$  dex. A similar spread of 0.14 dex in heavy elements within M 54 was also identified by Bellazzini et al. (2008), using a large spectroscopic study of 321 member stars of M 54. Due to the location of M 54 close to the centre of Sagittarius, it was proposed that it is its nuclear star cluster, which would explain its iron spread (Sarajedini & Layden 1995; Ibata et al. 1995).

The faintest cluster with a confirmed iron spread is M 22, with a magnitude of  $M_V = -8.5$ . A study of 41 RGB stars in M 22 by Da Costa et al. (2009) measured the spread in heavy elements to be 0.14 dex, which was confirmed by Marino et al. (2009). Another massive GC that has an intrinsic iron spread is  $\omega$  Cen. Many studies have revealed that the iron abundance of the stars in  $\omega$  Cen covers the range from  $-2.2 < [\text{Fe}/\text{H}] < -0.5$  with a clear intrinsic difference in abundances (e.g.: Norris & Da Costa 1995; Hilker & Richtler 2000; Sollima et al. 2005).

One explanation for the presence of multiple episodes of star formation is that these GCs have formed as nuclear star clusters of galaxies, which are known to host multiple generations of stars (e.g.: Seth et al. 2006; Walcher et al. 2006; Rossa et al. 2006). As these massive Galactic GCs with iron spreads are not embedded in a galaxy currently, they must have been stripped from a dwarf galaxy if they were formed as their nucleus (Freeman 1993). Dynamical models (e.g. Bekki & Freeman 2003) have shown that the dynamical evolution of a nuclear star cluster that is being stripped from its host galaxy is a viable formation scenario for a cluster like  $\omega$  Cen.

A different explanation for the spread in iron abundance within massive GCs is that they did not form as the nuclear star clusters, but have a spread in iron abundance due to self-enrichment (Ikuta & Arimoto 2000; Marcolini et al. 2007; Carretta et al. 2009b). For effective self-enrichment, GCs need to be massive, with a potential well that is deep enough, to keep the ejected heavy elements from supernova explosions within their gravitational potential.

The spread in iron abundance  $\sigma_{[\text{Fe}/\text{H}]}$  has been suggested as diagnostic to distinguish dwarf galaxies from globular clusters in cases where the dynamics of the objects give ambiguous results (Willman & Strader 2012). For the magnitude range of Crater there are several dwarf galaxies that have an iron dispersion larger than 0.55 dex.

For example, the Hercules dwarf galaxy with  $M_V = -6.2$ , has an intrinsic iron spread of  $\sigma_{[\text{Fe}/\text{H}]} = 0.51$  dex (Kirby et al. 2008), and the Ursa Major I dwarf galaxy ( $M_V = -5.5$ ) has  $\sigma_{[\text{Fe}/\text{H}]} = 0.54$  dex (Kirby et al. 2008). Similarly, the Leo IV dwarf galaxy, which has a magnitude of  $M_V = -5.5$ , has a spread of 0.75 dex (Kirby et al. 2008).

Thus, in Craters magnitude range of  $-7 < M_V < -4$ , an iron spread of  $\sigma_{[\text{Fe}/\text{H}]} > 0.55$  dex is a dwarf galaxy diagnostic, whereas spreads smaller than 0.1 dex is the abundance pattern associated with GCs. The repeating star formation episodes over a span of several Gyrs with self-enrichment from supernovae is the main reason for the abundance patterns observed in dwarf galaxies (Grebel et al. 2003). As dwarf galaxies continue to form stars, later populations of stars will be more metal-rich than the older populations. For objects fainter than  $M_V = -10$  the iron dispersion is used as a second diagnostic tool independently of dynamical measurements (e.g. Martin et al. 2007; Willman et al. 2011). For brighter objects the separation between dwarf galaxies and GCs in iron dispersion becomes less

clear and thus caution is needed for those cases.

### 1.3.3 A controversial object in the boundary region: Crater/Laevens I

Crater/Laevens I is an ultra faint object that was independently discovered by [Belokurov et al. \(2014\)](#) and [Laevens et al. \(2014\)](#). It is located in the outer Milky Way halo at 150 kpc distance. Before the discovery by professional astronomers the amateur astronomer Pascal Le Dû had already spotted Crater in his observations, and his findings were published in January 2014 in the magazine L’Astronomie <sup>1</sup>.

[Belokurov et al. \(2014\)](#) discovered Crater in observational data from the ESO VST ATLAS survey. A composite colour image taken with the William Herschel telescope with a  $4 \times 4'$  cutout around Crater is shown in Figure 1.7. In the image Crater is clearly visible as the central concentration of stars with many faint stars and a few bright giant stars among them. In [Belokurov et al. \(2014\)](#) they find that Crater’s half-light radius is  $r_h = 30$  pc when using an exponential profile to fit its surface brightness profile. Its absolute magnitude is found to be  $M_V = -5.5$  mag. As plotted in Figure 1.4, this places it right at the boundary between extended star clusters and the faintest dwarf galaxies in terms of size and magnitude. Therefore, its structural parameters cannot determine conclusively whether it is a dwarf galaxy or a globular cluster by nature. [Belokurov et al. \(2014\)](#) determined that Crater lies at a heliocentric distance of 170 kpc. At this distance Crater would be more distant than any other previously known Milky Way globular cluster, but comparable to the distances of other dwarf galaxies.

In a first analysis of the groundbased colour-magnitude diagram of Crater, [Belokurov et al. \(2014\)](#) fitted several isochrones to the CMD. They identify the stellar population has an age between 7 and 10 Gyrs and it must be metal-poor between  $-2.5 \text{ dex} < [\text{Fe}/\text{H}] < -2.0 \text{ dex}$ . In addition to the old metal poor population, their CMD also shows several stars that appear to be bluer than the RGB stars. They speculate that these might be bright and young “blue loop” stars, which is the stage in stellar evolution when intermediate mass stars are starting the core helium burning stage. These blue loop stars could be as young as 400 Myrs. If they were confirmed as young, second generation members, this would indicate a recent episode of star formation. Such extended star formation histories over several gigayears are usually a diagnostic of dwarf galaxies (e.g. [Willman & Strader 2012](#)). Due to the presence of these tentative young blue loop stars, [Belokurov et al. \(2014\)](#) concluded that this newly discovered object is probably one of the smallest dwarf galaxies known.

Simultaneously, this faint object was also discovered in the Pan-STARRS1 survey by [Laevens et al. \(2014\)](#), but they came to a vastly different conclusion about its nature. Their measurements revealed a fainter absolute magnitude of  $M_V = -4.3 \pm 0.2$  and a smaller heliocentric distance of  $145 \pm 17$  kpc, which also results in a smaller half-light radius of  $r_h = 20 \pm 2$  pc in their light profile fits. They concluded, that Crater consists of a stellar population that is 8-10 Gyr old and metal-poor with  $[\text{Fe}/\text{H}] \sim -1.5$  dex. In their work

<sup>1</sup>[http://www.cielocean.fr/uploads/images/FichiersPDF/L-Astronomie-\\_Janvier2014.pdf](http://www.cielocean.fr/uploads/images/FichiersPDF/L-Astronomie-_Janvier2014.pdf)



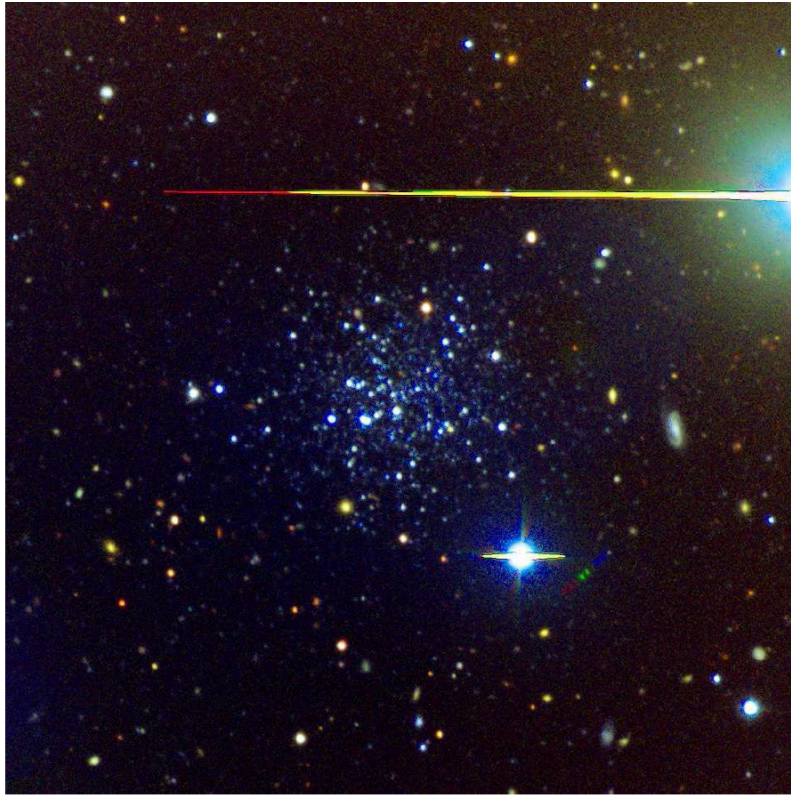


Figure 1.7: Colour composite (i-band, r-band, g-band) image of Crater taken with ACAM on the William Herschel Telescope. The image shows a cutout region of  $4' \times 4'$  centred on Crater. Image taken from [Belokurov et al. \(2014\)](#).

the tentative blue loop stars were detected as well. But in their work, it is argued, that these are likely not part of the system. Combined with their slightly smaller structural parameters (see the Laevens+14 red point in Figure 1.4) they concluded that this object has the typical properties of an extended young outer halo globular cluster. As a globular cluster they named it Laevens I consequently.

These two different interpretations of the same object triggered lots of debate about the nature of this intriguing object, that challenges our prior conceptions of what constitutes a galaxy and where a globular cluster starts. This controversy in the literature has triggered several spectroscopic follow-up works dedicated to this object. Crater’s nature can only be inferred from detailed studies of its internal dynamics and stellar population.

One such spectroscopic follow-up was carried out by Kirby et al. (2015), who presented spectra of 14 potential member stars of Crater, which were taken with DEIMOS on Keck II. In their analysis, they find a heliocentric velocity of  $v_{\text{sys}} = 149.3 \pm 1.2 \text{ km s}^{-1}$  for the 10 stars that they consider to be member stars. They derive a velocity dispersion of  $\sigma_v < 4.8 \text{ km s}^{-1}$  at a confidence level of 95%. Considering the membership status of the tentative blue loop stars, they find that two of them are not members and a third one is an ambiguous case. This blue star is within their  $2.58\sigma$  radial velocity membership criterion, but it is excluded as a member based only on its position in the CMD. They suggest that this star might be a Cepheid variable star if it were a member. Due to these findings, in this work it was also concluded that this object is most likely an outer halo GC.

Another attempt to clarify the nature of Crater was performed by Bonifacio et al. (2015) with X-SHOOTER spectra of two red giant stars in the system. They derived a radial velocity of  $v_1 = 144.3 \pm 4.0 \text{ km s}^{-1}$  for the first and  $v_2 = 134.1 \pm 4.0 \text{ km s}^{-1}$  for the second star. They conclude that both stars are probable members of the stellar system, and that their velocity difference implies a dispersion of  $\sigma_v > 3.7 \text{ km s}^{-1}$  at 95% confidence level, if one ignores the errors on the stellar velocities. If the errors are taken into account, their measurement is, however, consistent with a velocity dispersion of 0. They determined metallicities of  $[\text{Fe}/\text{H}] = -1.73 \text{ dex}$  and  $[\text{Fe}/\text{H}] = -1.67 \text{ dex}$  for the two stars. Their spectral and photometric data are consistent with an age of 7 Gyr for the majority of Crater’s stellar population, and the blue stars can be interpreted as a population with the same metallicity but an age of only 2.2 Gyr. Thus, in their work it was concluded that Crater is more likely to be a dwarf galaxy.

Recently, a new deep HST photometric study of Crater (Weisz et al. 2015) was published. The CMD revealed that Crater’s stellar population can be well described by a single age isochrone of 7.5 Gyr that has a metallicity of  $[\text{M}/\text{H}] \sim -1.65 \text{ dex}$ , and a total stellar mass of  $1 \times 10^4 M_{\odot}$ . Their CMD of Crater extends 4 magnitudes below the main-sequence-turnoff. They find that Crater has a second population of stars, above the turn-off, that is however very sparsely populated. The position of the blue stars is consistent with medium age stellar populations, as well as the position of blue straggler stars. For each giant star we expect a much larger number of main sequence faint counterparts which is not found in the CMD. Thus the sparse sampling of these faint blueish stars leads them to conclude that the most likely explanation for this sparse population are blue stragglers and not an intermediate age second generation of stars. This result would imply that Crater is a globular cluster,



although they note that the majority of intermediate-age star clusters are more metal-rich than Crater and it is in agreement with the age-metallicity relation of faint dwarf galaxies.

A similar object to Crater is the cluster Lindsay 38 in the SMC, which has comparable physical properties (Weisz et al. 2015). Lindsay 38 is an intermediate age star cluster (6.5 Gyr), with a metallicity of  $[\text{Fe}/\text{H}] = -1.59$  (Glatt et al. 2008). Lindsay 38 is also comparable in structural parameters to Crater. The half-light radius measured by Weisz et al. (2015) of Crater is  $r_h = 19.4 \text{ pc}$ , while Lindsay 38 has a half-light radius of  $r_h = 20.93 \text{ pc}$  (Glatt et al. 2009). In addition, the luminosity of Lindsay 38,  $M_V = -5.1$  is the same as Craters within the errorbars.

The ongoing controversy on the nature of Crater/Laevens I, even after spectroscopic follow-up, shows how unclear and blurry the distinction between dwarf galaxies and globular clusters is when we approach the boundary region where they are no longer distinguishable from each other by their structural parameters. The location of Crater in the outer Milky Way halo means that the presence of dark matter in this object can be tested, as the tidal field of the galaxy has a much reduced influence at such distances, minimising the tidal effects on the stellar velocities (Baumgardt et al. 2005). With seven times the physical size of a typical GC and at the largest galactocentric distance of any GC in the MW halo, it is a system that can serve to uncover the formation and evolution mechanisms of ultra-faint dwarfs or intermediate-age, extended globular clusters at low metallicities.

## 1.4 Open questions

- **If UCDs form via tidal stripping, where are those UCDs currently in the process of being stripped?**

We have evidence for UCDs that formed through the tidal stripping of a nucleus of a dwarf galaxy. The transitional process, which strips the nucleus away from its host dwarf galaxy is predicted to last for 1-2 Gyr according to simulations. However, a UCD observed during the tidal stripping process is the missing observational link between the end product and the starting point of the stripping formation process. Such a UCD-in-formation has not been observed yet at the beginning of this thesis. Therefore, one of the objectives of this thesis was to search for tidal features around UCDs in deep imaging data to provide this direct link between UCDs and tidal stripping.

- **What is the contribution of each formation channel to an ensemble of UCDs?**

Many photometric studies on the properties of a large ensemble of UCDs around galaxies have been carried out. But these large scale studies have not been able to conclusively pin down the fraction of UCDs that were formed as genuine large globular cluster and such that are stripped nuclei. Several results indicate that UCDs are originating from both formation channels, but few of them are able to give significant constraints on the contribution of each formation channel to the overall

number of UCDs. The studies that can identify the origin of UCDs with certainty are currently limited to observationally expensive spectroscopy of single objects.

Therefore it is one of the goals of this thesis to develop new alternative UCD observables that are able to discriminate their formation channels, based only on wide-field photometric studies of large UCD samples. Such new observables are necessary to enable us to eventually bridge the gap between single object spectroscopic studies and wide field photometry of an ensemble of UCDs.

- **Is Crater the smallest known dwarf galaxy or the most distant globular cluster of the Milky Way?**

Crater is an intriguing new discovered object that has challenged the clear distinction between galaxies and globular clusters. Even after several follow-up studies there is an ongoing debate about its origin in the literature, if it is either a diffuse star cluster or a dwarf galaxy. In this thesis, I analysed Crater based on new IFU observations with the new instrument MUSE on the VLT to study the internal chemistry and dynamical properties of this object in detail and settle the debate about its nature.

- **Is there a lower limit on the size of ultra-faint dwarf galaxies?**

In terms of the small scale dark matter distribution, the study of the smallest and faintest dwarf galaxies is of big interest as these objects are among the most dark matter dominated objects we know. If Crater were to be confirmed as a dwarf galaxy with an underlying dark matter halo, it would be the smallest known to date and would set new lower limits on dwarf galaxy formation and dark matter clustering on the smallest scales.

- **Are the dwarf satellites and GCs in the outer Milky Way halo the result of accretion events?**

It was suggested that Crater might have formed in another dwarf galaxy, which was subsequently accreted onto the Milky Way and then stripped from its host galaxy. If Crater is confirmed as an outer halo globular cluster it will be very interesting to probe the kinematics of its stellar population for signature of accretion events or tidal influences to study the hypothesis that it has not formed within the halo but was only accreted later on.

## 1.5 Structure of this thesis

The thesis is structured in the following way:

Chapter 2 is focussed on the introduction of new observables to distinguish the physical nature and the formation paths of UCDs. I am presenting the analysis of the UCD and GC population of NGC 1399 from wide-field FORS 2 imaging. In the first part of chapter 2 a detailed structural decomposition of the surface brightness profiles of the UCDs around NGC 1399 is carried out, using ground based imaging taken in very good seeing conditions. I examine their surface profiles by fitting single component models to them, as well as decomposing some of them into an envelope and core component. I compare how modelling UCDs with different light profiles affects the scaling relations of UCDs within the larger picture of early-type systems. In the same chapter, I examine a large sample of confirmed UCDs for tidal tails, as direct signature of ongoing tidal stripping. Such signatures are be direct observational “smoking gun evidence” for the tidal transformation of UCDs.

The third subsection of this chapter explains the newly developed analysis method using the spatial clustering of GCs around UCDs as a tracer of their formation channel. To do this I have put forward a new analysis method using the spatial clustering of wide-field ground-based data of GCs and UCDs in a cluster that can help us to understand the contribution of each formation channel. I search for associated companion star clusters in the distribution of GCs around UCDs. If UCDs are formed via the stripping of a nucleated dwarf galaxy, which previously had its own globular cluster system, we would expect some residual GCs that have not yet been stripped. I investigated how likely it is, that this clustering signal is coming from globulars which were originally part of the ancestor dE galaxy before it was stripped down to its nucleus. In this work I show how this new method enables us to potentially constrain the contribution of a formation channel to a full population of UCDs rather than just individual objects with time-intensive spectroscopy.

In Chapter 3 I describe the recently collected MUSE (Multi Unit Spectroscopic Explorer) observations on the ultra-faint object Crater and the dynamical analysis of this dataset. This object is very controversial, as there is evidence that supported that it is a dwarf galaxy and others that supported the GC interpretation. In this thesis, I present radial velocity measurements of stars in Crater using the new VLT instrument MUSE on UT4. This is an integral field unit instrument that has a field-of-view of  $1 \times 1'$  and a spatial sampling of  $0.02''$ , while covering the spectral range from 470-920 nm with medium resolution ( $R=2000-4000$ ) for each of the 90.000 spaxels. To study the dynamical and chemical properties of extended clusters with high precision, accurate radial velocities are needed. Therefore, I developed new methods to accurately model the two dimensional wavelength calibration and determined the systematics of the wavelength calibration. I performed a detailed study of Craters stellar dynamics by increasing the sample size of likely member stars to 26. The dynamical analysis revealed a velocity dispersion that is consistent with Crater being a GC, which essentially settles the debate in the literature.

In Chapter 4 I describe the spectroscopic analysis of the stellar population of Crater, using a full spectral fitting of the MUSE spectrum. We derive the effective temperatures and metallicities  $[\text{Fe}/\text{H}]$  for each extracted spectrum. It yields an average metallicity of

$[\text{Fe}/\text{H}] = -1.76 \pm 0.17 \text{ dex}$ . Craters stars between  $19 < M_{\text{I}} < 21$  have a dispersion in iron abundance of  $\sigma_{[\text{Fe}/\text{H}]} = 0.15 \pm 0.05$ . Thus, Crater is more similar to the homogenous abundance patterns found in GCs, in contrast to the very large dispersions found in dwarf galaxies. The two blue stars have metallicities that are consistent with the average metallicity of Craters stars, and can be explained by models of post horizontal branch stars. Thus, the two blue stars are likely members of Crater. Instead of their original explanation as young stars left over from a recent burst of star formation, they are likely post horizontal branch stars. The data supports our finding from chapter 3 that Crater is a globular cluster and not a dwarf galaxy.

In Chapter 5 I summarise the findings, draw my conclusions and discuss the future perspectives of this work.

# Chapter 2

## Globular cluster clustering and tidal features around ultra-compact dwarf galaxies in the halo of NGC 1399

This work has been published as Voggel, K., Hilker, M., Richtler, A&A, 2016, 586A, 102V;

*"Globular cluster clustering and tidal features around ultra-compact dwarf galaxies in the halo of NGC 1399"*

### 2.1 Introduction

Ultra-compact dwarf galaxies (UCDs) were first discovered in the Fornax cluster ([Minniti et al. 1998](#); [Hilker et al. 1999](#); [Drinkwater et al. 2000](#)). Although their name implies a galaxy origin, their nature and origin is still puzzling more than 15 years after their discovery. Their sizes (3-100 pc) and luminosities ( $-10 < M_V < -14$ ) have filled the void in the scaling relations of early-type stellar systems ([Misgeld & Hilker 2011](#); [Norris et al. 2014](#)). The size and magnitude gap in between classical globular clusters (GCs) and dwarf galaxies was not populated before the advent of UCDs.

Two main scenarios for the origin of UCDs have been discussed in the literature: 1) UCDs are the surviving nuclei of tidally stripped (dwarf) galaxies ([Bekki et al. 2003](#), [Pfeffer & Baumgardt 2013](#), [Zhang et al. 2015](#)); and 2) UCDs are the bright end extension of the globular cluster luminosity function, either formed as genuine GCs ([Murray 2009](#); [Mieske et al. 2004](#)), or are the result of a star cluster complex, where many clusters merge into a massive UCD-like object ([Fellhauer & Kroupa 2002](#); [Brüns et al. 2009, 2011](#)).

The view that UCDs are an inhomogeneous class of objects with different origins, i.e., made up of high mass GCs as well as stripped nuclei, has been emphasized ever since their discovery ([Hilker 2006](#); [Da Rocha et al. 2011](#); [Brodie et al. 2011](#); [Norris & Kannappan 2011](#)). The contribution of each formation channel is not well constrained yet and has been the subject of much debate. Identifying the origin of individual UCDs is observationally very difficult since most observed parameters do not differentiate between both formations channels. Smoking gun properties, such as a massive black hole, an extended star formation history, or massive tidal tails, are expensive to obtain for these barely resolved objects. One

of the most convincing proofs for a stripped nucleus-origin of an individual UCD is the detection of a supermassive black hole (SMBH) in M60-UCD1 in the Virgo cluster by [Seth et al. \(2014\)](#). Another very recent example is the detection of an extended star formation history in NGC 4546-UCD1 by [Norris et al. \(2015\)](#). However, for large ensembles of UCDs there is no estimator yet, which can distinguish between both UCD formation channels and thus constrain their fractions among a UCD population.

The Fornax cluster, in particular, its central galaxy NGC 1399, has a well-studied UCD and globular cluster population ([Dirsch et al. 2003](#); [Bassino et al. 2003](#); [Dirsch et al. 2004](#); [Bassino et al. 2006](#); [Schuberth et al. 2010](#)). NGC 1399 hosts  $\sim 6500$  globular clusters within 83 kpc (at a distance of 19 Mpc) with a specific frequency of  $S_N = 5.5$ , making it a good testing ground for GC/UCD populations.

At the distances of the Virgo and Fornax clusters most UCDs are barely resolved on ground-based images under regular seeing conditions. They can however be spatially resolved by space telescopes like HST or adaptive optics supported ground-based imaging. The light profiles of a few UCDs have been studied in detail via HST photometry ([Evstigneeva et al. 2007, 2008](#); [De Propris et al. 2005](#)). It has been found that a simple single King profile does not fit well the luminosity distribution of the most luminous and extended UCDs. A King core and a Sérsic or exponential halo component are needed to explain their surface brightness profiles ([Evstigneeva et al. 2008](#); [Strader et al. 2013](#)). Especially, the brightest UCDs exhibit compact and concentrated profiles in their centers and extended exponential wings with no signs of a sharp tidal truncation. Some UCDs exhibit envelope components with effective radii up to 100 pc (e.g., [Drinkwater et al. 2003](#); [Richtler et al. 2005](#); [Liu et al. 2015a](#)). There are six UCDs listed in the literature, which have double surface brightness profiles: VUCD 7 in the Virgo Cluster and UCD 3 and UCD 5 in Fornax ([Evstigneeva et al. 2008](#)); the compact object M59cO ([Chilingarian et al. 2008](#)); and the very compact, SMBH-harboring M60-UCD1 ([Strader et al. 2013](#)).

One of the scenarios suggested for the formation of nuclear star clusters (NSCs) is that massive globular clusters migrate toward the center of their host galaxy via dynamical friction and merge there in less than a Hubble time ([Tremaine et al. 1975](#); [Capuzzo-Dolcetta 1993](#)). This process is especially efficient in dwarf galaxies. [Lotz et al. \(2001\)](#) found a deficit of bright globular clusters in the central regions of nucleated dEs as compared to the outer regions, which can be the result of inward migration of massive GCs. Recently, [Arca-Sedda & Capuzzo-Dolcetta \(2014\)](#) derived, in a statistical approach, the number of surviving clusters around a galaxy as function of its mass, after a full Hubble time of dynamical friction at work. Their models predict that for a host galaxy with a stellar mass of  $M = 10^{10} M_\odot$ , on average, 65% of the original globular cluster population has migrated to the center within one Hubble time. This fraction rises for smaller host masses. At  $M = 10^9 M_\odot$  we already expect 80% of the original globular cluster population to have merged into the nucleus via dynamical friction. Assuming that UCDs are the stripped nuclei of progenitor dwarf galaxies in the mass range  $M = 10^9 - 10^{10} M_\odot$ , we can test whether observed UCDs show signatures of this process. In particular, we can test if there is a statistical overabundance of globular clusters in close proximity of UCDs, as we expect that inwards migration of GCs is still ongoing within the shrinking tidal radius of the

disrupting dwarf galaxy. And, as the most massive globular clusters have the shortest dynamical timescales, we only expect lower mass GCs to survive around UCDs. This can be tested by sampling the luminosity function of the companion objects to see if it agrees with a GC population that is skewed toward low masses in the globular cluster luminosity function (GCLF). Also, we would expect that small, low surface brightness envelopes from the progenitor galaxies are left within the present-day tidal radius of the stripped nuclei.

Merging super star cluster mergers are also expected to show substructure and non-merged companion GCs. In Brüns et al. (2011) it was shown that this kind of merging super star cluster complex has several surrounding close GC companions at 70 Myrs after the start of the merging process. After 280 Myrs of merging, it is left with one GC companion. Finally, after 1.3 Gyrs no more companions or substructure are visible in that particular simulation and the merging process is finished. In another simulation of merging star cluster complexes that leads to the formation of an extended star cluster of  $10^5 M_\odot$  ("faint fuzzies"), Brüns et al. (2009) showed that substructure in form of nonmerged star clusters can survive up to a merger age of 5 Gyr. Also tidal tails are formed while the merged star cluster complex orbits in the gravitational field of its host galaxy. Thus, we might expect to find companions around merged super star clusters up to several Gyrs after their formation.

In this work we present novel approaches to constrain the origin of UCDs in the Fornax Cluster. Firstly, we carry out a detailed structural decomposition of the surface brightness profiles of several UCDs around NGC 1399 using ground-based, very good seeing images (Sects. 2 and 3). We examine their surface profiles by fitting single component models to them, as well as decomposing some of them into an envelope and core component. We compare how modeling UCDs with different light profiles affects the scaling relations of UCDs within the larger picture of early-type systems. Secondly, we examine a large sample of confirmed UCDs for direct signatures of ongoing tidal stripping (Sect. 4). We look for direct, so-called, smoking gun evidence for the tidal transformation of UCDs by searching for tidal tails. Finally, we search for signatures of associated companion star clusters in the distribution of GCs around UCDs, which we expect if the UCD was a nucleated dwarf galaxy that previously had its own globular cluster system or originated from a super star cluster complex that still has substructure (Sect. 5). We investigate how likely it is that these clustered globulars were either originally part of the ancestor dE galaxy before it was stripped down to its nucleus, or originated from a super star cluster complex that has not yet fully merged. The main difference between the two scenarios is the age of the UCDs with substructure, since we do not expect a star cluster complex older than 5 Gyrs to retain substructure, but rather to be fully merged into one smooth object.

## 2.2 Imaging

To study UCDs within the Fornax cluster, we used data from ESO program 076.B-0520 (PI:Richtler). The imaging data were taken in the nights October 9th and 10th, 2005, with the high-resolution collimator mode of FORS2, which is mounted on UT1 of the



Very Large Telescope (VLT). Three separate fields were observed in the R-band. Fields 1 and 2 with 3x800s exposure time each and field 3 with 5x800s. Every single exposure was reduced separately with our own IDL routine. The reduction process included all standard procedures for image reduction. First, a master bias was created from five bias exposures, then a normalized master flatfield of five separate bias-subtracted flatfields was created. The original science exposures were then corrected for bias and flatfield effects and subsequently stacked together using the IDL routine MEDARR, creating a median stacked image of all three exposures. Before stacking we fitted Gaussian models to four bright stars in each exposure to determine their positions with subpixel accuracy. This was used to correct for small subpixel shifts in the astrometry before stacking the exposures, so that our psf size was not increased. The pixel scale of the observations is 0.126 arcsec/pixel, which corresponds to a physical scale of 92 pc arcsec<sup>-1</sup> at the distance of NGC 1399, which we assume throughout the paper as  $(m - M) = 31.39$  (Freedman et al. 2001), or 18.97 Mpc. For each final stacked image, we retrieved the psf using the GETPSF idl routine taken from the NASA IDL Astronomy Users Library (Landsman 1993)<sup>1</sup>. Mean FWHM values of the PSFs in the three fields are FWHM=0.53'', 0.55'', 0.53'' for pointings Nr.1, 2, and 3, respectively. The positions of the three pointings are shown in Fig. 2.1. The orientations of the fields were optimized to cover most objects presented in Richtler et al. (2005).

## 2.3 UCD Analysis

### 2.3.1 Surface brightness analysis

We compiled a sample of 313 UCDs and GCs in the Fornax cluster with stellar masses above  $M = 10^6 M_\odot$  (Firth et al. 2007; Mieske et al. 2002, 2004; Dirsch et al. 2004; Richtler et al. 2008; Schuberth et al. 2010), which all are confirmed Fornax members according to their radial velocities. To determine their stellar masses consistently for the full sample, we used their  $V$ -band magnitudes and  $(V - I)$  colors and calculated their  $V$ -band mass-to-light ratios from the simple stellar population models (SSP) of Maraston (2005). For the UCDs, we assume an age of 13 Gyr and a Kroupa (2001) initial mass function (IMF) with a red horizontal branch. A fit to the tabulated  $M/L_V$  and  $(V - I)$ , valid for the color range  $0.80 < (V - I) < 1.40$ , can be expressed as

$$\frac{M}{L_V} = 4.408 + 1.782 \cdot \arctan[11.367 \cdot ((V - I) - 1.162)]. \quad (2.1)$$

The root mean square of the fit is rms=0.101. In Fig. 2.1 a 20'x20' cutout DSS image is shown, centered on NGC 1399. The UCDs of the Fornax sample are labeled with red circles. The three FOVs of our FORS2 observations are shown as blue squares. 97 UCDs/GCs are located in those fields.

We analyzed the surface brightness profiles of these 97 UCDs with the two-dimensional fitting algorithm GALFIT (Peng et al. 2002). The GALFIT algorithm is a parametric

<sup>1</sup><http://idlastro.gsfc.nasa.gov/>



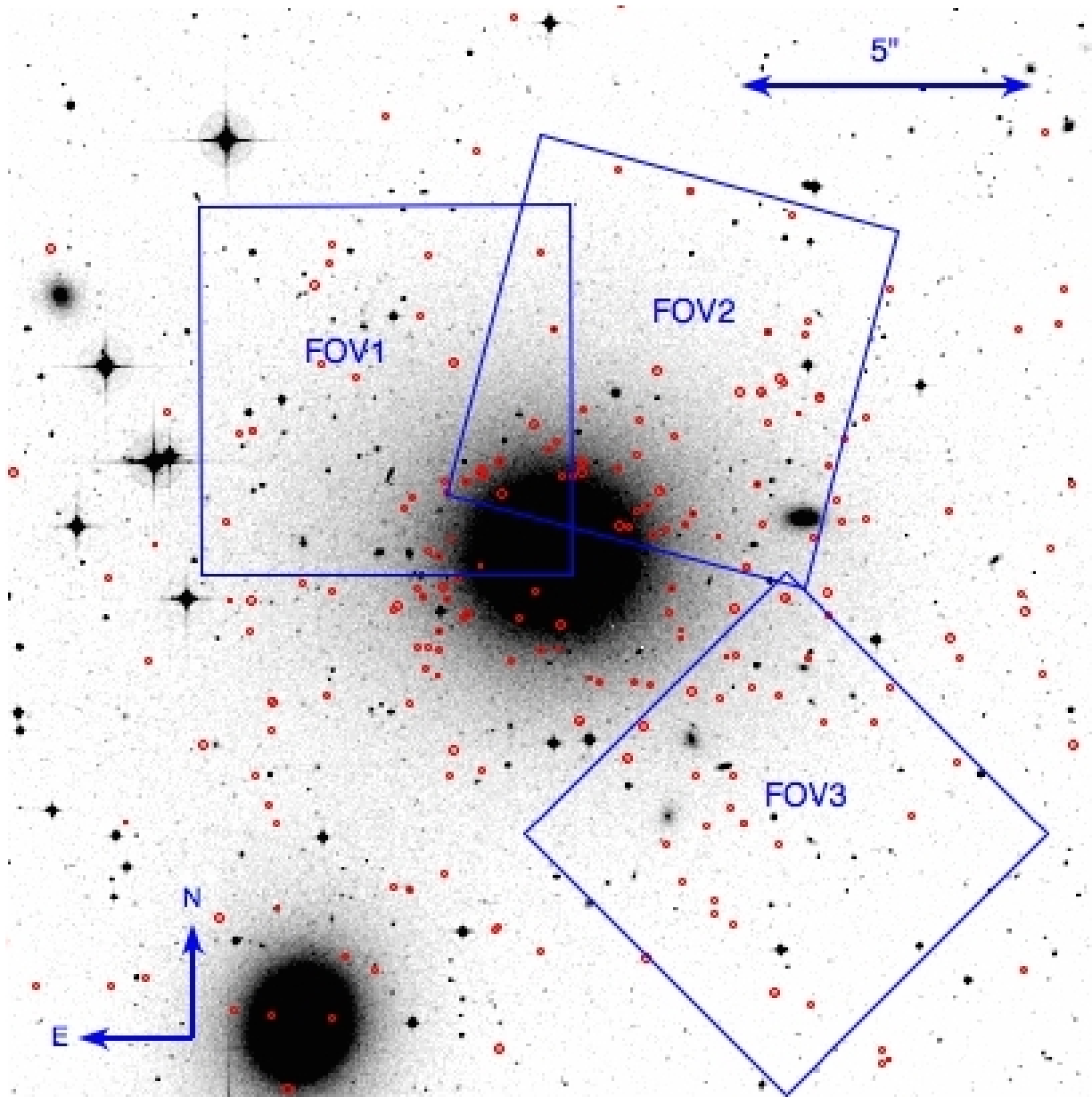


Figure 2.1: DSS cutout image of  $20' \times 20'$  around NGC 1399 (RA=03h38m29.0s DEC=-35d27m02s), the central galaxy of the Fornax cluster. The locations of the three FORS2 pointings with  $6.8' \times 6.8'$  size are shown as blue squares. The confirmed Fornax UCDs/GCs within this region are labeled with red circles.

approach to light profile fitting, which minimizes the residuals between the two-dimensional model and the image. The difference between model and original image is given as a residual map. As the diameters of the UCDs are very close to the spatial resolution of our images, it is crucial that we use a fitting technique that takes the smearing of the light profile by the PSF into account. GALFIT convolves each analytic profile with an input point-spread function (PSF). We derived the input PSFs using the GETPSF IDL routine for, on average, 20 bright stars in each observing field and each chip separately, as the PSF varies in each observation and also per chip. The average FWHM of our derived PSFs is 4.25 pixels, which corresponds to  $0.55''$ . For each UCD, a cutout of  $120 \times 120$  pixels, which corresponds to  $15'' \times 15''$ , was created from the large image as an input for GALFIT. We used GALFIT to fit two single and two double luminosity profile models to each UCD: a single Sérsic (S), a single King (K), a double King+Sérsic (KS), and a Sérsic+Sérsic (SS) model.

The Sérsic surface brightness function used to model galaxy luminosity profiles can be given as

$$I(R) = I(\text{eff}) \exp \left[ -b \left( \left( \frac{R}{R_{\text{eff}}} \right)^{\frac{1}{n}} - 1 \right) \right], \quad (2.2)$$

where  $R_{\text{eff}}$  is the half-light radius,  $I(\text{eff})$  is the surface brightness at the half-light radius,  $n$  is the shape parameter of the function, and  $b$  is a constant that depends on  $n$  with a good approximation as

$$b(n) = 2n - 0.324 \quad (2.3)$$

See [Ciotti \(1991\)](#) for exact values.

For  $n=1$  the profile is an exponential law, and for  $n=4$  it is a de Vaucouleurs profile.

The generalized King profile (in original form from [King 1962](#)) is given as

$$I(R) = I_0 \left[ \frac{1}{(1 + (R/R_c)^2)^{\frac{1}{\alpha}}} - \frac{1}{(1 + (R_t/R_c)^2)^{\frac{1}{\alpha}}} \right]^{\alpha}, \quad (2.4)$$

where  $R_c$  is the core radius,  $R_t$  is the tidal radius where the profile is truncated,  $I_0$  is the central surface brightness, and  $\alpha$  is the shape parameter of the King profile. The classical profile fixes  $\alpha = 2$ , but we use it in its generalized form where  $\alpha$  can vary. Often the concentration index  $c$  is used to characterize the profile, which is defined as  $c = \log(R_t/R_c)$ . The King profile is often a good fit to light profiles of globular clusters with their flat cores and truncated outer parts.

All model parameters of our fits were allowed to vary within GALFIT. In cases where a very close faint point source or an asymmetric tidal feature was visible in the image, we fixed the ellipticity to 1.0, providing a spherical model. When there is a nearby faint substructure GALFIT often tends to settle into a local  $\chi^2_{\nu}$  minimum with a very elliptical model, which results in a bad representation of the real object. For objects without faint substructure, we allowed the ellipticity to vary. The ellipticities of the UCDs is given by GALFIT as the ratio between semiminor and semimajor axis of the fitted model. For all UCDs where there were no faint tidal features nearby we allowed the ellipticity parameter

to vary. The ellipticities from the Sérsic fits were all larger than 0.75, which shows that UCDs are round objects with few deviations from their round shape in the inner light profile.

As many UCDs are located close to the very bright galaxy NGC 1399, the background level in the cutout images is not uniform but has a brightness level, which depends on the distance to the main galaxy. For each UCD fit we determined the individual sky background and allowed it to have an additional sky gradient in the x and y direction.

We only accept GALFIT parameters if the best fit converged with no runaway parameters, i.e., parameters whose values do not diverge with increasing radius, and if  $r_{\text{eff}}$  of the fitted profile is  $> 2\text{pix} = 23.18\text{ pc}$ , which corresponds to 45% of the size of the FWHM and  $0.252''$  in angular size. This is the resolution limit we adapted for all our fits. For the double component fits, the  $r_{\text{eff}}$  values of both components are also required to lie above this resolution limit.

Applying these cutoffs we find that 54 UCDs have a converged Sérsic fit, and of these 13 have a half-light radius above the resolution limit and no runaway parameters. The cutout images of these 13 extended UCDs and their residuals of the Sérsic fit are shown in Fig. 2.2. The structural parameters we derived from the Sérsic fits to these UCDs are given in Table 2.1.

The quality of the fits is shown as residuals in Fig. 2.2. These residual maps are the results from subtracting the best-fit Sérsic model from each observed object. As can be seen some larger residuals are left in the central parts for most UCDs. These are either due to an undersampled PSF determination in the centers or an imperfect description of the Sérsic profile to the very central parts of the UCDs. For several objects we see faint outer residuals (e.g., UCD-FORS 4, 32, 36, 45). This suggests the existence of a faint underlying second component, which we test with double profile fits. For UCD-FORS 81 (=Fornax UCD2), we find an effective radius of  $r_{\text{eff}} = 37.82 \pm 2.58\text{ pc}$  and a Sérsic index of  $n = 2.03$ . For this object, a much higher Sérsic index of  $n = 6.8$  and an effective radius of  $26.6\text{ pc}$  was derived in [Evstigneeva et al. \(2007\)](#) based on higher resolution HST photometry. High Sérsic indices are very sensitive to the determination of the sky level, and a slight underestimation already leads to a higher Sérsic index, which might cause this difference. Another explanation for this discrepancy is that an intrinsic double profile was fitted with a single component in their work.

The average Sérsic index of our 13 extended UCDs is  $n = 3.82$ . The objects with larger Sérsic indices are more centrally concentrated and have extended wings toward faint levels compared to those with lower Sérsic  $n$  values. As mentioned above, profile fits to extended wings can be sensitive to background determinations. Therefore, it is important to determine our background carefully, including the modeling of the gradient introduced by the central galaxy NGC 1399 to minimize these effects.

For the King profile fits, we have 47 UCDs, for which the fit returned results, but only three of them have no runaway parameters and effective radii above the resolution limit we adapted. These three objects above the resolution limit showed an extremely low alpha index of  $\alpha < 0.2$ , which is unphysical. Thus we consider none of the UCDs to be well fitted by a single generalized King law in contrast to previous HST results. None of the UCDs

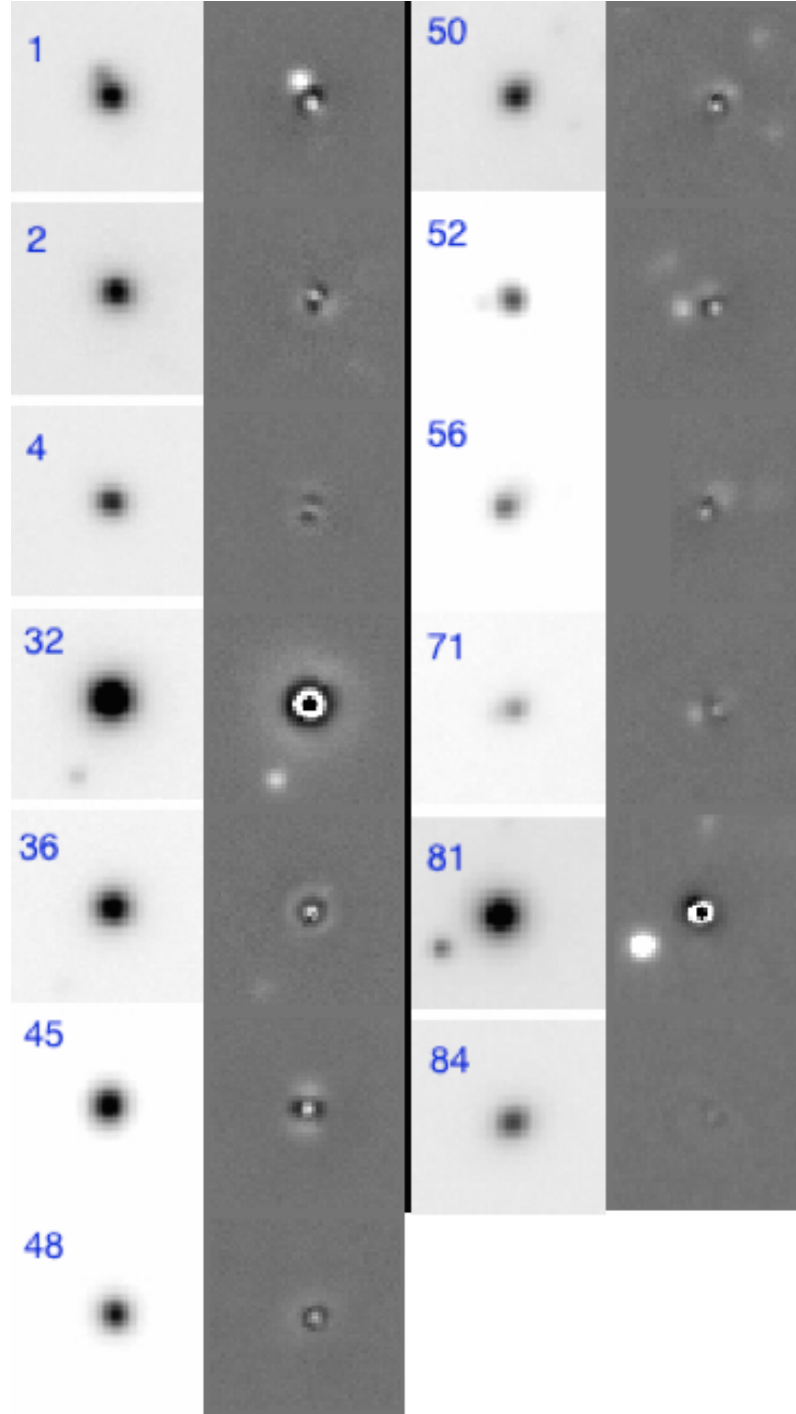


Figure 2.2: Left columns show the thumbnail images of the 13 UCDs that were found to have a half-light radius above 23 pc, which we adopted as limit for a reliable measurement. The right-hand column next to each UCD shows the residuals after subtracting the best-fit single Sérsic model from the observed image. Each UCD is labeled with its identifier number among the 97 UCDs in both FORS fields. Their properties are listed in detail in Table 2.1.

have either a flat cored light profile or a marked truncation radius, which we would both expect from typical King profiles.

We also attempted to fit the UCDs with double component profiles, King-Sérsic (K+S) and Sérsic-Sérsic (S+S). Many of these fits did not converge and had runaway parameters. And none of the fits that converged had effective radii for the inner component that were above our resolution limit when we allowed all parameters to vary. As we know from the five known double profile UCDs in the literature (Evstigneeva et al. 2007; Chilingarian et al. 2008; Strader et al. 2013), the inner component usually has  $r_{\text{eff}} < 15$  pc. Finding no UCD with an inner component larger than 23 pc was thus expected, within our seeing limited ground based dataset.

To test how it would affect the outer Sérsic component if we actually had an inner King component, we reran GALFIT on the 13 extended UCDs with a fixed size King component in the center. We held the King effective radius at  $r = 11.6$  pc with a concentration of  $c = 30$  and allowed the magnitude to vary. Also, the Sérsic envelope profile was allowed to vary in its parameters. All these fits converged except for the one of UCD-FORS 32 (UCD6). Instead, for this UCD, a double Sérsic profile is the best fit to the data. Notably this is the object with the lowest Sérsic index of  $n = 0.94$  and thus the most cored profile consistent with the profile shape derived by Evstigneeva et al. (2008).

In Table 2.2 the results of the K+S fits are shown, including the relative change in  $\chi^2$  between the Sérsic only and the K+S fit. For 11 out of the 13 UCDs the relative change of  $\chi^2$  is positive and thus the quality of the fits increased when using a double K+S profile. For UCD-FORS 4 and 52 these percentages are slightly negative, but with only a tenth of a percent the quality of the fit is almost unchanged. The average increase in the quality of the fits is  $\Delta\chi^2 = 10.59\%$ . The double profile fit is especially good for UCD-FORS 32, 45, and 81, for which a faint envelope is even visible by eye from the images in Fig. 2.2. To illustrate the improvement in residuals for the double component fits, those three objects have been included in the last three panels of Fig. 2.3 and all of them show significant improvement of the residuals when using a K+S profile instead of a single Sérsic. The asymmetric faint features around UCD-FORS 1, 52, and 71 are caused by faint background point sources, which is discussed further in Sect. 2.4.2.

The effective radii for the envelope Sérsic components are shown in Fig. 2.5 with dark blue circles with crosses. They are connected to the respective parameters derived by the single Sérsic fit with a solid line.

It is obvious from the plot that the effective radii of these so-called envelope components are larger than their single component counterparts. In the scaling relations some of these envelopes are located in the empty area between the branch of dwarf elliptical galaxies and star cluster-like objects (UCDs and GCs).

As expected, the Sérsic index for the envelope decreased because of its less concentrated profile. As many as six of our envelopes now have Sérsic indices of two or smaller, which is closer to the  $n = 1$  exponential profile that is usually measured for dEs.

### 2.3.2 Surface brightness profiles

For those 13 UCDs where we were able to measure the structural parameters directly, we show their one-dimensional, background-corrected radial light distributions in Fig. 2.3. The last three panels of the 4th column show the best-fit Sérsic+Sérsic fit for UCD=FORS 32 and the respective King+Sérsic fits for UCD-FORS 45 and 81. The best-fit convolved Sérsic profile is plotted in green. The background corrected observed surface brightness profile is shown in blue. To accomplish this, we used the IRAF ellipse task and analyzed the surface brightness level of the UCDs as a function of aperture radius. This non-parametric curve-of-growth analysis does not correct for the smearing of the light profile in the central parts by the PSF but shows the profile as observed. The errorbars for the blue profile denote the change in the profile when we vary the determined background value by 5%. The black dashed line illustrates the surface brightness profile of the PSF. The vertical green line shows the size of the effective radius  $R_{\text{eff}}$  of the best-fit Sérsic profile. Below each isophote plot the residuals between the model profile after convolution with the PSF and the observed profile is shown.

For the inner parts of most UCD isophote profiles ( $r < 50\text{pc}$ ) the residuals are small and scattered around zero. The residuals become positive for several objects at larger radius, meaning an excess of the observed light compared to the model. For UCD-FORS 1, 52, and 71 this can be accounted for by the very close second point sources we detected after subtracting the UCD profile (see Fig. 2.2). As also visible from the two-dimensional residuals plotted in Fig. 2.2, for several UCDs (e.g. 1, 71, 84) the two- and one-dimensional residuals both show a faint excess of light at radii  $r > 70\text{pc}$ , i.e. the Sérsic profile dropped too fast in surface brightness compared to the true light profile of the UCDs. A very interesting case is UCD-FORS 32 whose best-fit light profile has the smallest Sérsic index of the whole sample of  $n=0.93$ . The behavior of its residuals shows an excess of observed light between 30 and 50 pc compared to the profile, and between 70 and 100 pc the Sérsic profile has a higher surface brightness than the object. Profiles with Sérsic indices below 1 indicate a light distribution with a central flat (core) and a truncation at larger radii. In the second panel of the 4th column this object is shown with its best-fit Sérsic+Sérsic fit. The envelope component of this fit now has an even lower Sérsic index of 0.59 and a half-light radius of 88.69 pc, and the improvement in the quality of the fit is easily visible from the residuals. The double profile results from UCD-FORS 45 and 81 are plotted in the last two panels of the last column, and also show significant reduction in the amount of residual compared to their single-component counterpart.

All light profiles of the 13 extended UCDs lie significantly above the PSF profile (dashed black) and are clearly not compatible with a point source profile within their errorbars.

In Table 2.1 we summarize the structural parameters from the best-fit Sérsic models for the 13 UCDs that have half-light radii above the resolution limit of 23 pc. The  $(V - I)$  color and radial velocities are taken from their original sources described in detail in Sect. 2.3.1. The provided errors on the fit parameters, both in Tables 2.1 and 2.2, are those given by GALFIT and should be taken with caution, as these errors might be underestimated and do not take any systematic effects into account. For objects this close to the resolution

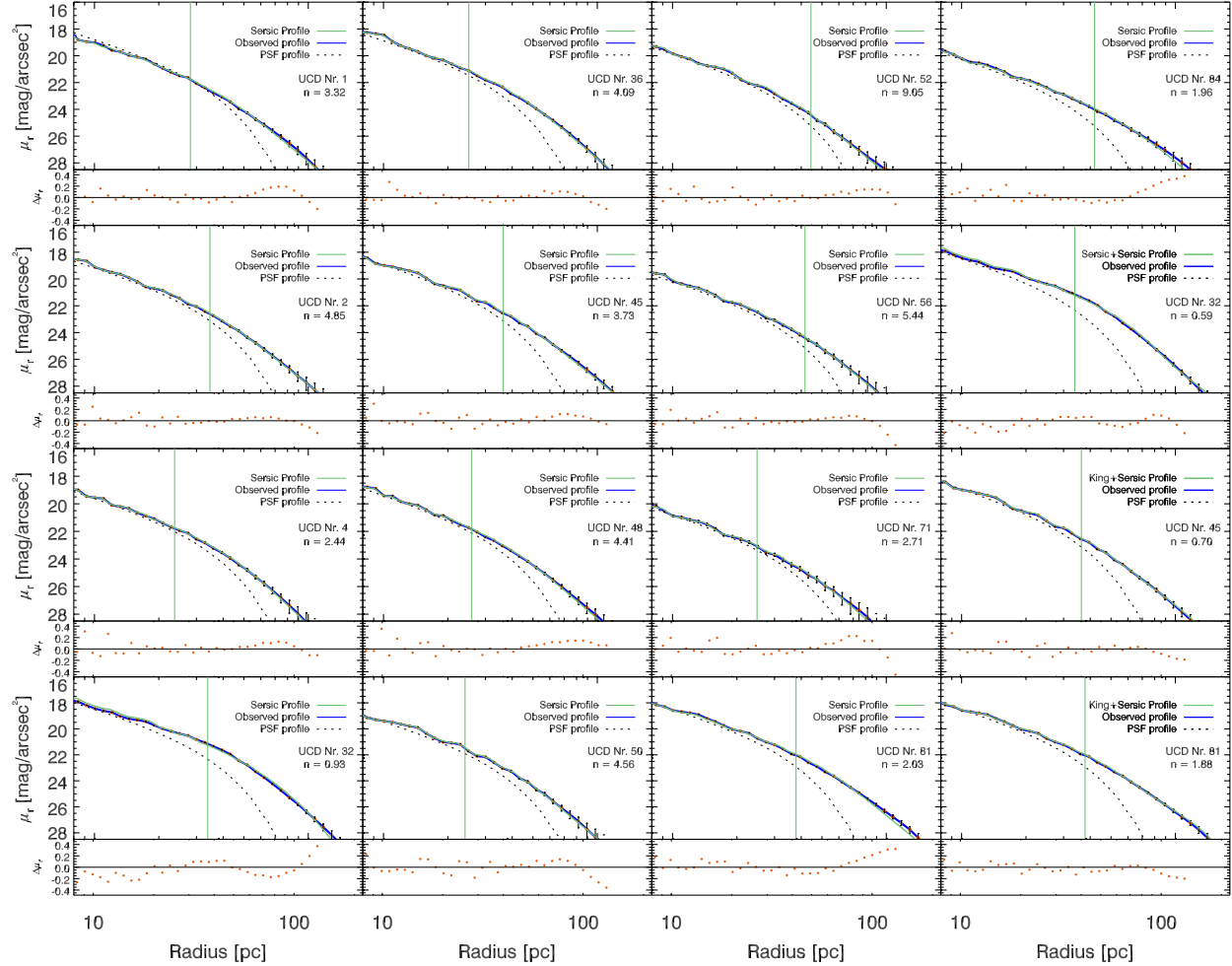


Figure 2.3: Isophotal analysis of the R-band images of 13 extended UCDs. For each UCD, the top panel in each plot shows the output of the GALFIT Sérsic model (green) compared to the observed background subtracted surface brightness profile (blue line, orange points). The shape of the PSF is also plotted as dashed black line. The Sérsic index  $n$  and the identification number of the UCD is indicated within each plot. The lower panel of each plot shows the residuals between the model profile after convolution with the PSF and the observed profile. The vertical green line is the effective radius of the best-fit Sérsic profile. The last three panels in the fourth column show the model results for the King+Sérsic fits for UCD FORS 45 and 81, respectively. For UCD-FORS 32, the Sérsic+Sérsic result is shown. The two-component models of these three UCDs show improved residuals compared with their single profile fits.



limit we expect the true total errors to be at least 10-20%.

### 2.3.3 Color magnitude diagram

In Fig. 3.9 we show the color-magnitude diagram (CMD) of our NGC 1399 UCDs compared to GCs in Fornax and UCD color data from other work. The dark blue points denote the extended UCDs with sizes above 23pc, whereas the light blue points denote all the other UCDs that are located in the three fields for which we have FORS data. The yellow diamonds show UCDs from [Evstigneeva et al. \(2008\)](#). We also include (purple triangles) data for the nuclei of dwarf elliptical galaxies, which are taken from [Lotz et al. \(2004\)](#). The GC data (light gray dots) include the GCs of NGC 1399, NGC 1404, and NGC 1389, which were taken from the Fornax ACS Survey ([Jordán et al. 2007](#)). The  $g'$  and  $z'$  AB magnitudes of the ACS Survey were transformed into the  $V$  and  $I$  system using the single stellar population models from [Bruzual & Charlot \(2003\)](#). We assumed a GC age of 11-13 Gyrs and a Chabrier IMF with a metallicity between -2.2 dex and -0.6 dex. The transformation equation for the magnitude and color is given as

$$V = g' - 0.004 - 0.301 \cdot (g' - z') \quad (2.5)$$

$$(V - I) = 0.445 + 0.518 \cdot (g' - z'). \quad (2.6)$$

The root mean square of Eq. 5 is rms=0.010 and that of Eq. 6 is rms=0.012. When we look at the location of the dwarf elliptical nuclei (purple) and the UCDs from [Evstigneeva et al. \(2008\)](#), we can see that the nuclei are on average ‘bluer’ than UCDs of comparable luminosity and their colors become redder with increasing nuclei luminosity. This trend toward redder color for brighter objects is also observed for the UCDs from the literature (yellow) but with a shallower slope than for the nuclei. A large fraction of our sample of extended UCDs (dark blue) falls close to this relation, which has been noted already by [Evstigneeva et al. \(2008\)](#) and [Brodie et al. \(2011\)](#). In contrast to their findings, we find several extended red UCDs, which are much fainter than that expected from the color-magnitude relation established by the nuclei.

Another feature in the CMD is the position of confirmed UCDs/GCs with half-light radii <23 pc. Their locations in the CMD (light blue) are compatible with those of GCs (gray dots) for luminosities fainter than  $M_V = -11$ . They also overlap in magnitude with the bright end of the GC population. In the very blue range of  $(V - I) < 0.9$  there is a lack of UCDs with magnitudes brighter than  $M_V < -11$ . This can be explained by the blue tilt found in various globular cluster systems (e.g. [Mieske et al. 2010](#); [Fensch et al. 2014](#)).



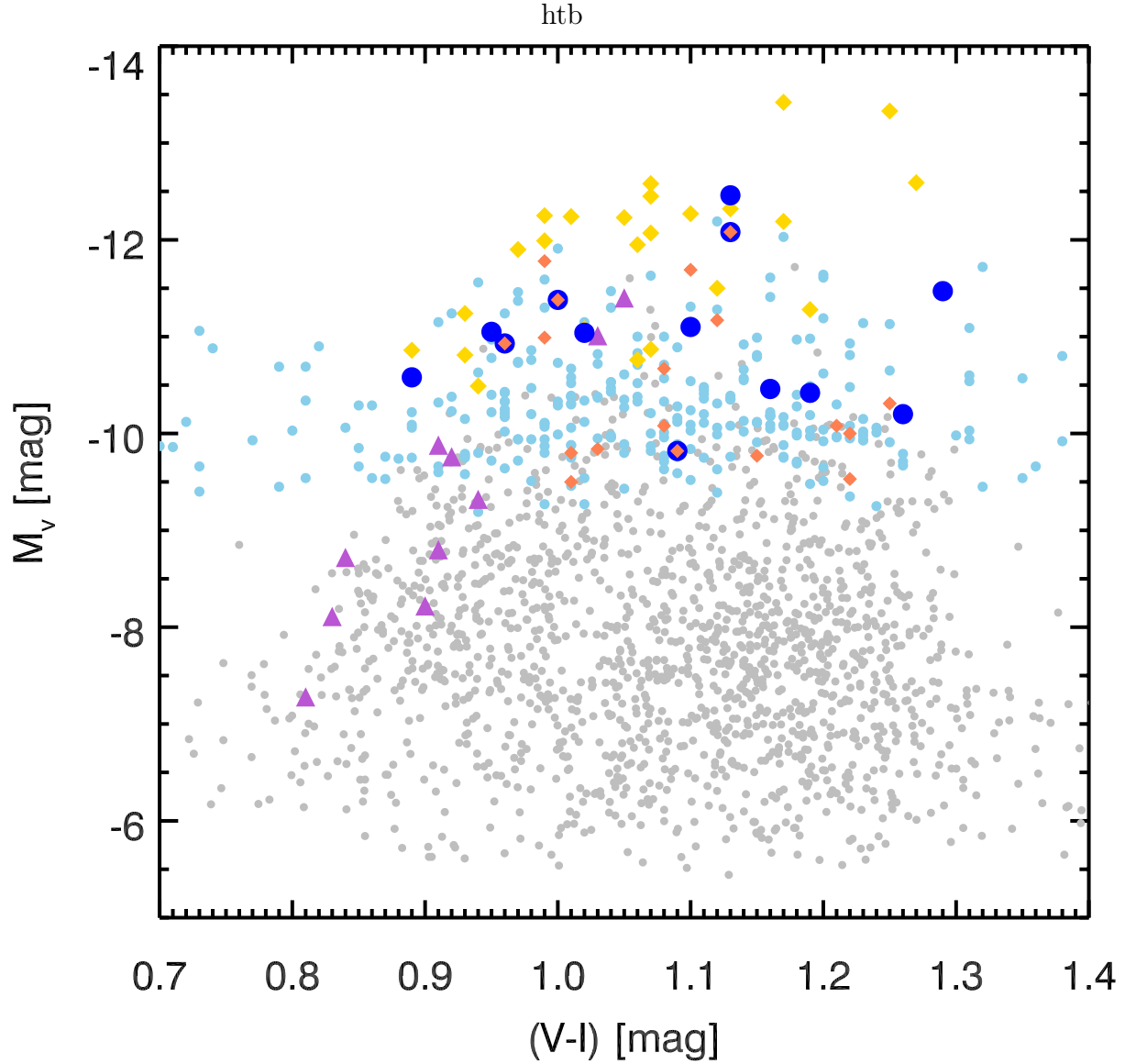


Figure 2.4: Color magnitude diagram for the extended UCDs (dark blue) and UCDs with companions as orange diamond symbols. These are compared to the parameters of the rest of our NGC 1399 UCD sample with  $M > 10^6 M_\odot$  in light blue. The yellow diamonds indicate UCDs from the work of [Evstigneeva et al. \(2008\)](#). The light gray dots are the NGC 1399, NGC 1404, and NGC 1389 GCs from the Fornax ACS Survey ([Jordán et al. 2007](#)). The purple triangles are nuclei from dE galaxies in the Fornax cluster taken from [Lotz et al. \(2004\)](#).

Table 2.1: Results from the Sérsic fits for those 13 UCDs that have half-light radii larger than the resolution limit of  $23pc$ . The  $(V - I)$  colors and radial velocities are taken from the respective original samples. The provided errors on  $R_{eff}$  and  $n$  are those given by GALFIT, which should be taken with caution because close to the resolution limit these errors might be underestimated. The alternative object names from the literature are from the following sources: for UCDx [Firth et al. \(2007\)](#), x – xxxx [Mieske et al. \(2002, 2004\)](#), Yxxx references [Richtler et al. \(2008\)](#). Some of these objects were also presented in [Richtler et al. \(2005\)](#) with the following names: <sup>a</sup> 78:12 <sup>b</sup> 91:93 <sup>c</sup> 90:12

Name	Name <sub>alt</sub>	R.A. (h:m:s)	DEC. (°:′:″)	V (mag)	R <sub>eff</sub> (pc)	n	(V – I) mag	v (km s <sup>-1</sup> )
UCD-FORS 1	1_0630	3:38:56.14	-35:24:49.0	20.31 ± 0.004	28.10 ± 0.16	3.32 ± 0.06	1.02 ± 0.07	666 ± 48
UCD-FORS 2	Y99025 <sup>a</sup>	3:38:58.55	-35:26:26.0	20.21 ± 0.012	34.68 ± 0.76	4.85 ± 0.17	0.96 ± 0.04	1070 ± 38
UCD-FORS 4	2_2115	3:38:49.18	-35:21:42.1	20.96 ± 0.003	23.70 ± 0.15	2.44 ± 0.05	1.19 ± 0.07	864 ± 79
UCD-FORS 32	UCD6	3:38:05.04	-35:24:09.7	19.15 ± 0.001	33.27 ± 0.07	0.94 ± 0.01	1.13 ± 0.11	1220 ± 45
UCD-FORS 36	UCDm	3:38:06.48	-35:23:03.8	20.00 ± 0.002	25.06 ± 0.08	4.09 ± 0.04	1.00 ± 0.04	1442 ± 123
UCD-FORS 45	UCD28	3:38:10.73	-35:25:46.2	19.97 ± 0.003	33.83 ± 0.14	3.81 ± 0.03	1.29 ± 0.04	1715 ± 90
UCD-FORS 48	UCD31	3:38:16.51	-35:26:19.3	20.60 ± 0.008	25.88 ± 0.29	4.41 ± 0.13	0.95 ± 0.05	899 ± 85
UCD-FORS 50	1_2095	3:38:33.82	-35:25:57.0	20.61 ± 0.007	24.05 ± 0.24	4.56 ± 0.13	1.10 ± 0.04	1223 ± 221
UCD-FORS 52	2_2127	3:38:11.69	-35:27:16.2	20.81 ± 0.02	44.41 ± 2.47	9.05 ± 0.38	1.16 ± 0.06	1443 ± 131
UCD-FORS 56	Y10056	3:38:38.77	-35:25:55.2	21.18 ± 0.033	36.72 ± 2.37	5.44 ± 0.42	1.26 ± 0.07	1062 ± 105
UCD-FORS 71	Y10048	3:38:35.23	-35:25:39.2	22.05 ± 0.015	24.85 ± 0.51	2.71 ± 0.20	1.09 ± 0.04	1601 ± 30
UCD-FORS 81	UCD2 <sup>b</sup>	3:38:06.29	-35:28:58.8	19.31 ± 0.048	37.82 ± 2.58	2.03 ± 0.33	1.13 ± 0.11	1249 ± 37
UCD-FORS 84	2_2072 <sup>c</sup>	3:38:14.69	-35:33:40.7	20.77 ± 0.001	41.85 ± 0.11	1.96 ± 0.01	0.89 ± 0.05	1448 ± 176

### 2.3.4 Luminosity-effective-radius relation

One of the main theories for UCD formation is that they are the isolated nuclei of larger dwarf ellipticals, being stripped of their stellar envelope through tidal interactions (e.g. [Bekki et al. 2003](#); [Drinkwater et al. 2003](#)). In [Pfeffer & Baumgardt \(2013\)](#) the trajectories from simulations in the luminosity-size plane of this kind of process were shown. During the tidal interaction dwarf galaxies lose their envelopes and, from their original position in the size-luminosity diagram as dwarf ellipticals (green points in Fig. 2.5), they end up with sizes and magnitudes of UCDs, effectively having to cross the empty region in between the galaxy and the star cluster branch. One could naively ask: If these objects are formed by tidal stripping, why do we not see more objects in between both branches being currently transformed? This is because the transformation timescale is rather short ([Pfeffer & Baumgardt 2013](#)) and dwarf galaxy destruction has happened in the early phases of cluster formation, i.e., several Gyr ago ([Pfeffer et al. 2014](#)). This makes objects in the transition phase between the two branches very rare at present time. Additionally, if the surface brightness of the stellar envelope component reaches faint levels very quickly, we miss them in observations because there have not been systematical or deep enough searches for low surface brightness features around a large sample of UCDs yet. Nevertheless, even today galaxy clusters still accrete substructures and some dwarf galaxies get disrupted. Therefore, we should be able to find some smoking gun evidence for the tidal nature of these objects at low surface brightness levels.

In Fig. 2.5 we plotted the effective size and magnitude of dwarf ellipticals and dwarf spheroidal (green and light green), globular clusters (light gray dots), UCDs (blue diamonds) and galaxy nuclei (dark gray diamonds). The five literature UCDs with double component profiles are shown in different colors (red, yellow, orange, brown, and purple) with a circle for the core component, square for the single component and a crossed circle for the envelope.

The structural parameters for UCDs from our sample, which could be fitted with a double profile, are shown in dark blue. The envelope component for each UCD from the two component decomposition is shown as circle with a cross. The single components are the dark blue points. Each single component UCD is connected with a line to its derived envelope component. We do not show the core component since it was artificially fixed to a size of 11.6 pc.

For the literature UCDs, as well as the new sample, the derived envelope parameters fall right in between the galaxy and star cluster branch. The core components from the literature UCDs all fall into a lower size UCD range close to the nuclear star cluster range. This might be a hint that UCDs with envelopes are actually transition objects in the stripping process of dwarf elliptical galaxies, or alternatively are merged super star cluster complexes with an extended envelope component, which is a result of the star cluster merging process (e.g., [Fellhauer & Kroupa 2002](#)).

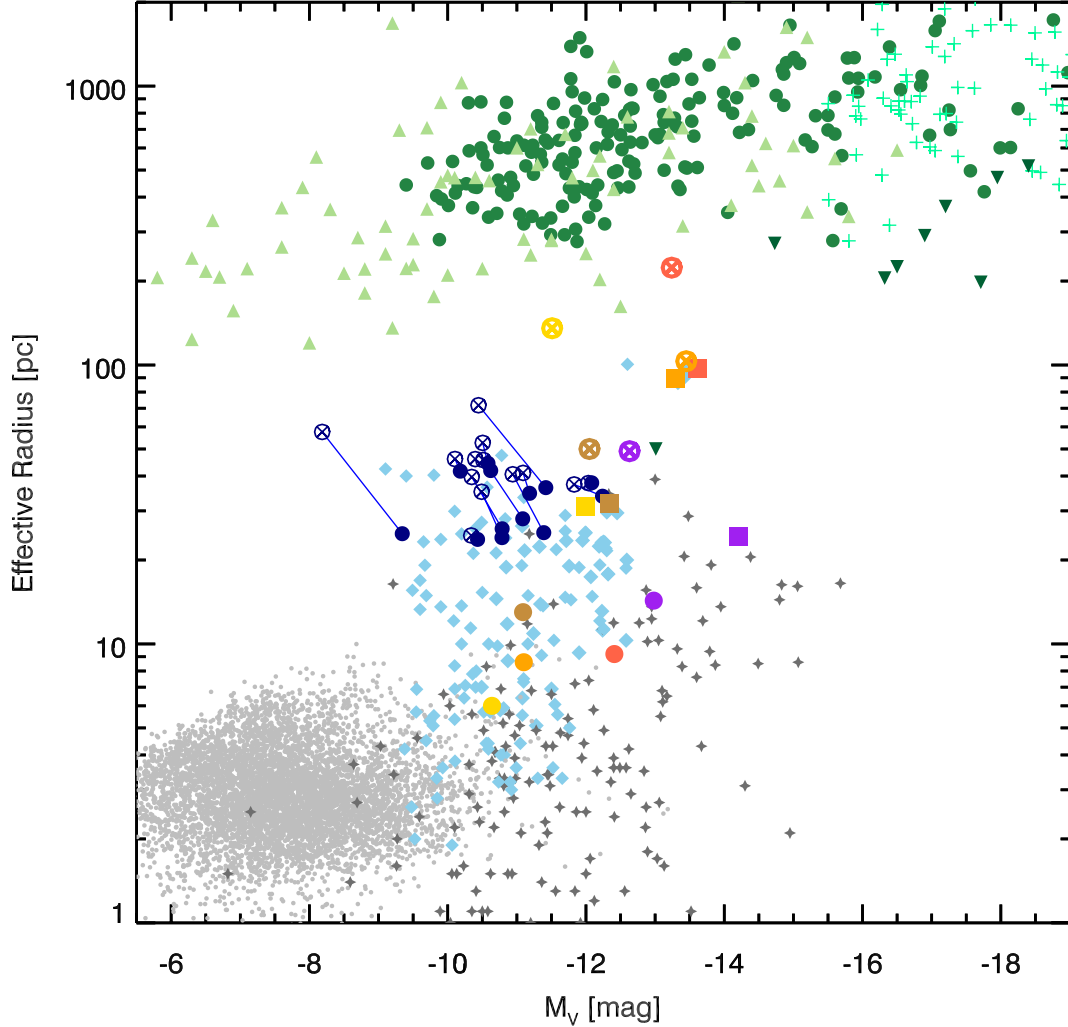


Figure 2.5: Relation between the effective radius and the absolute visual magnitude of several types of early-type systems are shown. We show in green dots dEs in the Hydra and Centaurus clusters taken from [Misgeld et al. 2008b, 2009b](#). The light green triangles are dSphs in the Local Group from [McConnachie \(2012\)](#). The inverted green triangles are compact ellipticals from [Price et al. \(2009\)](#). Light green plus signs represent early-type galaxies from [Ferrarese et al. \(2006\)](#). Light gray dots are the Fornax Cluster GCs from the ACVCS survey ([Jordán et al. 2007](#)). The dark gray star symbols are the nuclear star clusters from [Georgiev & Böker \(2014\)](#). In light blue, we show an assembly of UCDs with measured sizes taken from [Mieske et al. 2008; Brodie et al. 2011; Forbes et al. 2013; Evstigneeva et al. 2008; Haşegan et al. 2005](#). We plot in navy blue dots the effective radii from the Sérsic profile fit. The connected navy circles with a cross shows which sizes we derived for the envelopes of a two-component King+Sérsic model to each of our UCDs when we assume a 11.6 pc King component in their centers. The yellow, orange, red, and brown symbols show the five known decomposed UCDs with clear double profiles in the literature. Squares are the single component fits, dots the core component, and circles with crosses the envelope component. The red points denote (VUCD7), orange (UCD3) and yellow (UCD5), all taken from [Evstigneeva et al. \(2007\)](#). Purple symbols show M60-UCD1 taken from [Strader et al. \(2013\)](#) and the brown symbols are M59cO taken from [Chilingarian et al. \(2008\)](#).

Table 2.2: Results from the double profile fits to the surface brightness profiles of the UCDs. Here we used a profile consisting of a King core fixed at 11.6pc in effective radius and a variable Sérsic Envelope component. The second and third column show the magnitude of both components. The fourth column shows the effective radius of the Sérsic envelope and the fifth column the best-fit Sérsic index. The relative change in  $\chi^2$  between the K+S fit and the original Sérsic-only fit is shown in the second to last column. In the last column, the expected tidal radius for these objects according to Eq. 2.8 are shown. <sup>1</sup> For object UCD-FORS 32, the results for a double Sérsic fit are shown.

Name	$R_{\text{King}}$ (mag)	$R_{\text{Envelope}}$ (mag)	$R_{\text{Envelope}}$ (pc)	$n$	Rel. Change %	Change $\chi^2$	$r_{\text{tidal}}$ (pc)
UCD-FORS 1	21.28 $\pm$ 0.09	20.88 $\pm$ 0.06	45.67 $\pm$ 2.32	1.84 $\pm$ 0.15	3.08		590
UCD-FORS 2	22.96 $\pm$ 0.07	20.30 $\pm$ 0.09	41.04 $\pm$ 6.38	4.76 $\pm$ 0.31	1.57		444
UCD-FORS 4	23.71 $\pm$ 0.13	21.05 $\pm$ 0.28	24.45 $\pm$ 4.40	2.25 $\pm$ 0.19	-0.13		684
UCD-FORS 32 <sup>1</sup>	19.60 $\pm$ 0.04	20.32 $\pm$ 0.02	88.68 $\pm$ 1.39	0.59 $\pm$ 0.03	44.28		985
UCD-FORS 36	21.17 $\pm$ 0.10	20.45 $\pm$ 0.11	40.57 $\pm$ 5.22	3.33 $\pm$ 0.30	4.44		659
UCD-FORS 45	20.53 $\pm$ 0.03	20.95 $\pm$ 0.01	71.75 $\pm$ 0.35	0.70 $\pm$ 0.01	28.60		592
UCD-FORS 48	21.79 $\pm$ 0.22	21.04 $\pm$ 0.32	39.64 $\pm$ 16.11	3.46 $\pm$ 0.73	0.23		253
UCD-FORS 50	22.22 $\pm$ 0.09	20.89 $\pm$ 0.07	35.12 $\pm$ 5.22	5.36 $\pm$ 0.22	5.45		160
UCD-FORS 52	23.82 $\pm$ 0.03	20.88 $\pm$ 0.02	52.59 $\pm$ 12.50	8.88 $\pm$ 0.75	-0.14		349
UCD-FORS 56	23.72 $\pm$ 0.13	21.29 $\pm$ 0.09	46.02 $\pm$ 10.32	4.99 $\pm$ 0.30	0.9		229
UCD-FORS 71	22.50 $\pm$ 0.08	23.21 $\pm$ 0.05	57.50 $\pm$ 2.32	0.31 $\pm$ 0.08	0.85		136
UCD-FORS 81	22.68 $\pm$ 0.16	19.36 $\pm$ 0.41	37.74 $\pm$ 12.40	1.88 $\pm$ 0.86	42.90		776
UCD-FORS 84	22.61 $\pm$ 0.07	20.99 $\pm$ 0.02	46.02 $\pm$ 0.70	1.40 $\pm$ 0.05	7.05		587

## 2.4 Tidal structures and globular clusters around UCDs

### 2.4.1 Tidal structures

In our FORS sample of 97 UCDs we investigated all of them visually for signatures of tidal tails and general asymmetric features. We looked at the original images, as well as the residual images from our best-fit GALFIT models. Underlying faint features or tails are often only well visible when subtracting the light of a symmetric profile. We classify those UCDs as having tidal features when there was a coherent tidal feature above the background level identified. The background noise level was determined locally for each UCD, as the noise level significantly varies as a function of the distance to NGC 1399. In total, we found 11 out of the 97 UCDs exhibiting such tails and features.

We found the most striking features around UCD-FORS 2 (Y99025), as shown in Fig. 2.6. We detect three clear tidal tail-like structures around this UCD. Two narrow tidal features emerge from the UCD toward the east and the northwest (NW). A smaller but brighter feature is visible on the northern side of the UCD. The NW tidal feature is above the  $3\sigma$  level for almost all of its extension with a small  $5\sigma$  peak in its middle. The tidal feature extending toward the east is enclosed by the  $2\sigma$  isophote with a  $3\sigma$  peak in the middle. These two large tidal tails, measured from the center of the UCD, have an apparent extension of  $\sim 350$  pc, whereas the smaller tail in the northern direction is extended to  $\sim 250$  pc. Anisotropies in the isophotes are detected up to  $10 - \sigma$ . The significance of our detection combined with symmetric appearance of two collimated tails, makes it very unlikely that what we see is a projection or alignment effect. If this were faint background features overlaid on a normal UCD we would expect much rounder isophotes at 5 and  $10\sigma$  significance levels and there would be no multiple tails. In addition, the isophotes on the southern side of the UCD have a much steeper profile than those on the northern side, which extend to larger radii at the same level.

This UCD-FORS 2 is also among those that have a size above the resolution limit, with a Sérsic half-light radius of  $r_{\text{eff}} = 34.68 \pm 0.76$  pc, and a very blue ( $V - I$ ) color of 0.96. This object has been pointed out before by Richtler et al. (2005) for appearing to have two very faint features and potentially a faint envelope around it. They also found strong Balmer lines, which usually indicates the presence of a young stellar population. The alternative explanation of a very low metallicity is not supported because of its Washington color that points to a metallicity of  $> -1.3$  dex.

The  $R$ -band image of UCD-FORS94 is shown in Fig. 2.7 on the left-hand side, on the right panel UCD-FORS7 is shown. Overlaid on both images are the contour levels of constant surface brightness as green lines. We indicate the 2, 3, 5, 10, and  $30\sigma$  levels with respect to the background noise level for each image. The UCD in the left panel shows a strongly pronounced and extended feature toward the southeast. Compared to the tails of UCD-FORS 2 of image 2.6 this is a much brighter feature. Already the  $10\sigma$  contour level is clearly shaped like a tail-like extension. Measuring the full extent of the  $5\sigma$  contour level of this feature from the center of the UCD outward gives us an apparent size of 230 pc. The surface brightness level of this extension is higher than expected for a tidal tail. It

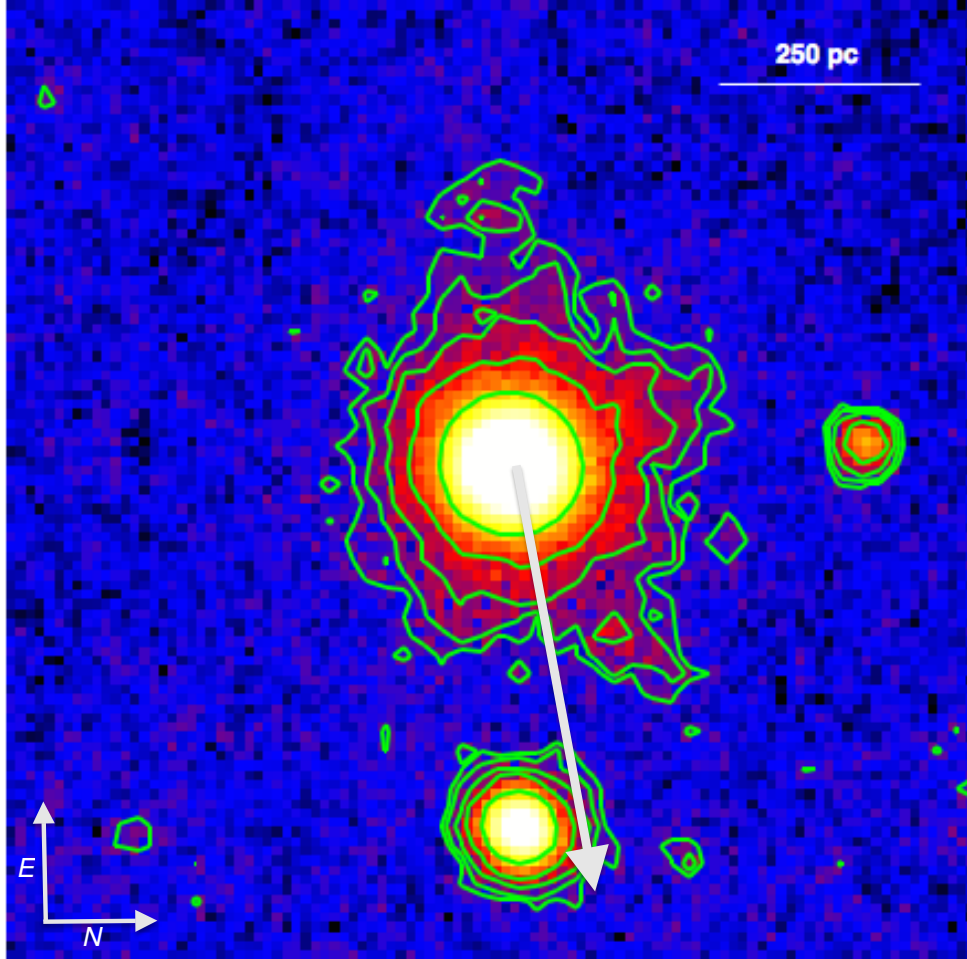


Figure 2.6: *R*-band image of UCD-FORS 2 (Y99025) overlaid with green contour lines of isophotes with constant surface brightness levels. The density levels correspond to  $2, 3, 5, 10$  and  $30\sigma$  above the background. The  $2\sigma$  contour corresponds to a surface brightness level of  $\mu = 26.0 \text{ mag/arcsec}^2$ . Three tidal features are clearly visible in the image. One extends towards the North-West (lower right) and is above the  $3\sigma$  level for all its extension with a small  $5\sigma$  peak in its middle. The tidal feature extending towards East (top) is enclosed by the  $2\sigma$  isophote with a  $3\sigma$  peak in the middle. On the northern side of the object (to the right) there are also clear distortions in the isophote shape visible which are around  $250 \text{ pc}$  in extent at the  $5\sigma$  level, and even the  $10\sigma$  isophote is clearly distorted. The two large tidal tails if measured from the center of the UCD have an apparent extension of  $\sim 350 \text{ pc}$  at  $\mu = 26.0 \text{ mag/arcsec}^2$ . The white arrow shows the direction towards the center of NGC 1399.



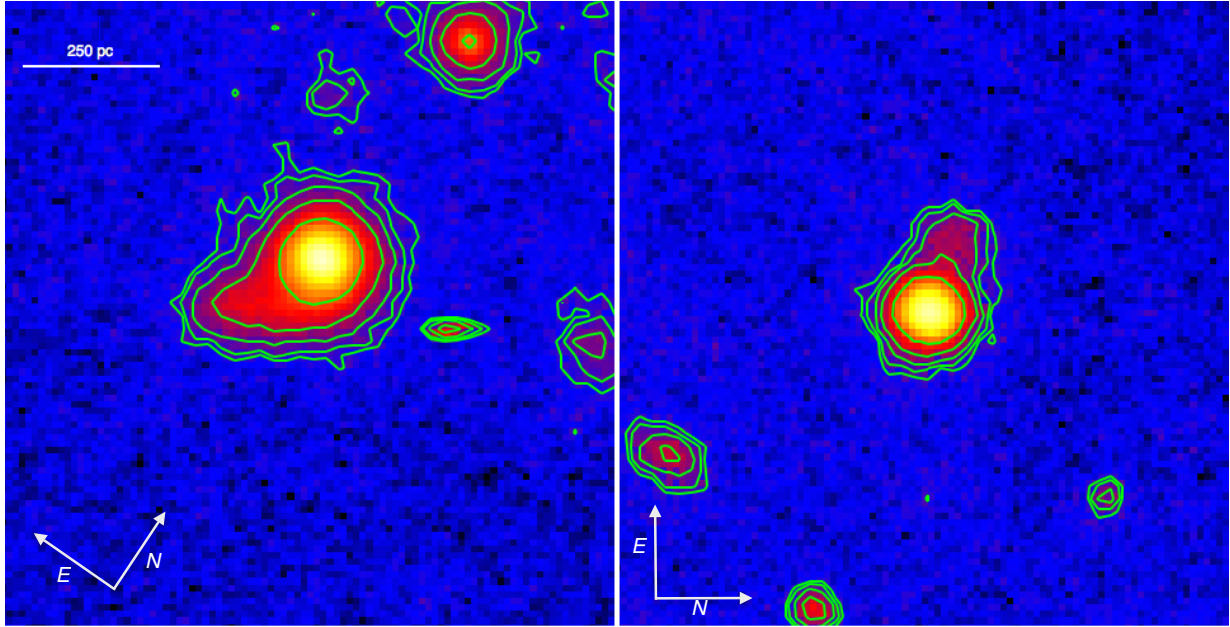


Figure 2.7: Left image shows the  $R$ -band image of UCD-FORS94. In the right panel UCD-FORS7 is shown. Both are overlaid with green isophote contours of constant surface brightness levels. The density levels correspond to 2, 3, 5, 10, and  $30\sigma$  with the lowest contour corresponding to a surface brightness level of  $\mu = 26.01 \text{ mag/arcsec}^2$ .

is possible that we see a background object in projection. Spectroscopy or high-resolution imaging are needed to clarify the nature of this apparent UCD extension.

The feature we detect at UCD-FORS7 toward the northeast has a much lower surface brightness level and a smaller extension than that of UCD-FORS94. The full extent of the  $5\sigma$  contour along the tail-like feature is 175 pc. This might be a true tidal tail, but spectroscopic confirmation is needed for this target as well.

In the following we estimate the probability of by-chance superpositions of low surface brightness background galaxies on our UCD sample. For simplicity we assume a Poisson distribution of UCDs and background galaxies. Within the surface area of our FORS fields we have  $N_1 = 97$  confirmed UCDs. We determined the amount of extended galaxies that could be confused as tidal tails if perfectly aligned by running SExtractor (Bertin & Arnouts 1996) on our FORS observations. We restricted the SExtractor output to objects with an ellipticity ( $\epsilon = 1 - \frac{B}{A}$ ) of  $0.2 < \epsilon < 1.0$  to retain only objects that have a significant elongation. We also set the requirement that the CLASS\_STAR (CS) parameter is  $CS < 0.5$  to obtain only objects that have been classified as galaxy-like objects. We set the detection threshold to  $2 - \sigma$  above the background with a minimum of ten contiguous pixels above this threshold. In total we extracted 1205 objects that could mimic a tidal tail when projected on a UCD-like object. As a minimum distance within which such a projection might be confused with a tidal tail, we assume  $r = 2'' = 0.184 \text{ kpc}$ . The combined surface of our FORS fields is  $\Omega = 35.595 \cdot 10^3 \text{ kpc}^2$ . The probability to find



one such close overlap in our sample is given as

$$P(R < r) = N_1 \cdot N_2 \frac{\pi \cdot r^2}{\Omega} = 0.349. \quad (2.7)$$

Thus, the probability of 34.9% for one superposition is not negligible. However, the probability that all eleven detected tail candidates are random superpositions is much lower. Calculating the binomial probability for two or more random superpositions within our sample of 97 UCDs is already  $P=5.09\%$ . For three and four or more random overlaps among our eleven candidates the probability goes down to  $P=0.53\%$  and  $0.04\%$ , respectively. The probability that all eleven detections among the 97 UCDs are random overlaps is  $P=7.25 \cdot 10^{-14}$ . Thus, it is virtually impossible that all detected tails are just random overlaps and it is very likely that the majority of our objects are detections of true tails around UCDs.

### 2.4.2 Globular clusters around UCDs

Another feature we detected frequently in the images of our UCDs are faint GC candidates, which are located very close to the main object. In the following, we investigate the frequency of close companions within 300 pc radius around each UCD. This radial size is motivated by the tidal radius of a  $M = 10^6 M_\odot$  UCD at a pericenter distance of 30 kpc from a host galaxy with  $M = 10^{12} M_\odot$ , i.e.

$$r_{tidal} = R \cdot \left( \frac{m}{M} \right)^{\frac{1}{3}}. \quad (2.8)$$

In total, we found 19 UCDs with a faint companion source that is closer than 300 pc in projection. This is  $\sim 20\%$  of our total UCD sample. Notably, four of these objects with companions belong to those with extended sizes above the resolution limit of 23 pc (UCDs in panels a, d, g, and q in Fig. 2.2). For some cases, the object is so close that it blends into the surface brightness profile of the main UCD, which makes the object appear skewed and elongated (see, e.g., UCDs in the panels a, c, m, n, and p in Fig. 2.2). Fitting a symmetric profile to these objects and then investigating the residuals shows that there is clearly a faint point source underneath and that the UCD is not just elongated in one direction. The second type are those UCDs where the faint source is well separated from the UCD and the two sources are clearly distinguishable.

All UCDs from our sample have radial velocities that confirm them as Fornax cluster members. As there are no measurements of radial velocities of their faint companion sources we take a statistical approach to determine whether these are potential globular clusters that are associated with the UCDs. To accomplish this, we measured the magnitude of the point sources on the residual images, where the light of the main UCD was subtracted. Then we assumed that these objects lie at the distance of Fornax at  $(m - M) = 31.39$ . In Fig. 2.8 the histogram of the absolute magnitude distribution of the UCDs is shown in blue and their companion sources in black. The distribution of companion sources peaks at  $M_V \simeq -7.0$ . The Gaussian fit to globular cluster luminosity function of GCs around

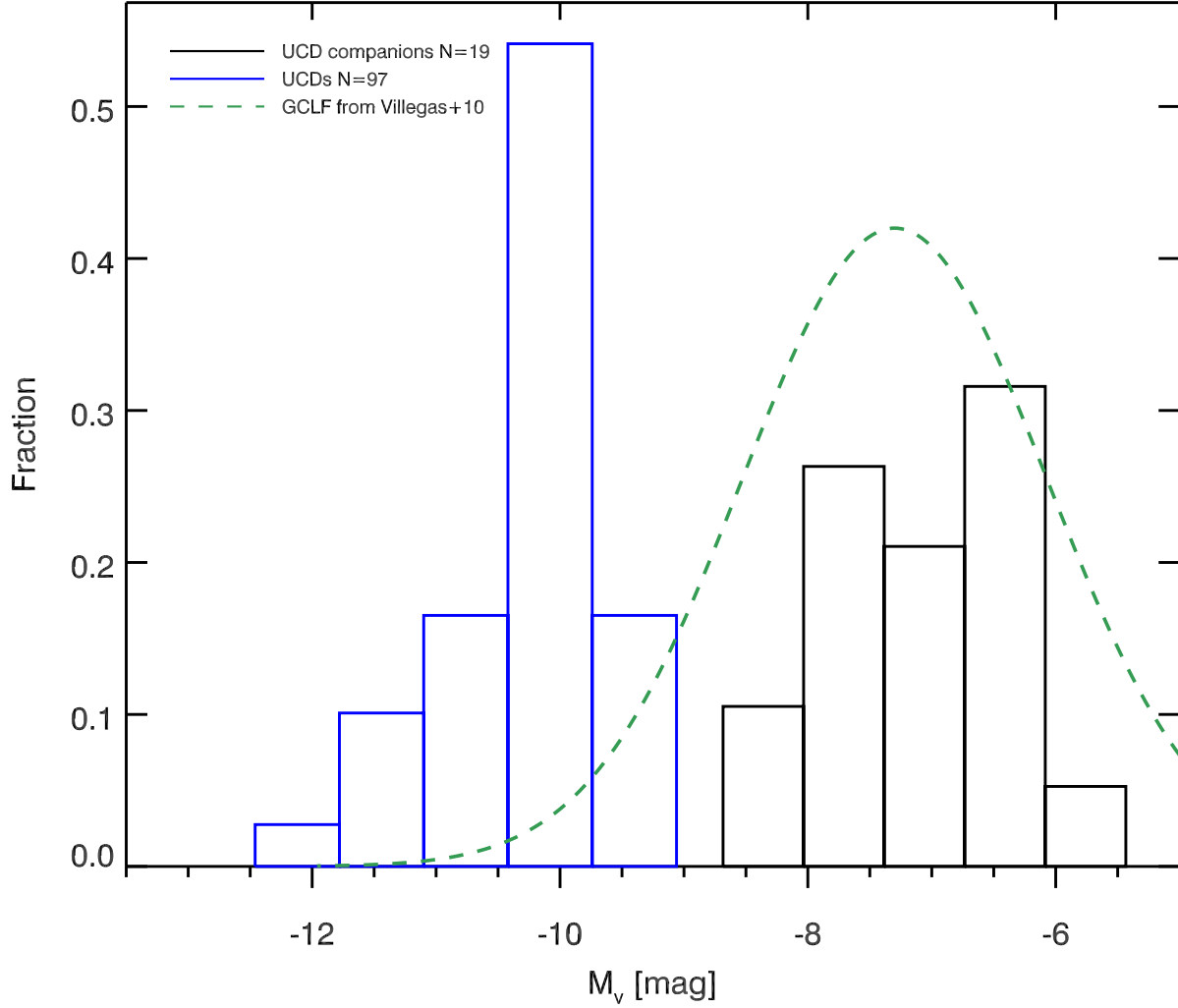


Figure 2.8: Histogram of absolute magnitudes of the 97 UCDs in the FORS field is shown in blue. Histogram of the 19 point sources we detected within a radius of 300 pc around the UCDs is shown in black, if we assume they lie at the distance of the Fornax cluster. The dashed green line is a Gaussian with peak magnitude  $M_V = -7.3$  mag and a dispersion  $\sigma = 1.23$  mag, as measured for the globular cluster luminosity function of NGC 1399 in [Villegas et al. \(2010\)](#). The NGC 1399 GCLF is normalized to the number counts of the companions in the magnitude bin at  $M_V \simeq -6.5$  mag. The average luminosity of the measured companion sources is  $M_V = -7.04$ .

NGC 1399 is overplotted as a green dashed line, as derived by Villegas et al. (2010). The Gaussian has a peak magnitude of  $M_V = -7.3$  and a dispersion of  $\sigma = 1.23$ .

All properties of the UCDs and their companions are listed in Table A.1 in the appendix. We also estimated the tidal radius for each UCD in this sample (column  $r_{\text{tidal}}$  in Table A.1) based on their projected distance from the center of NGC 1399 and their magnitudes, with Eq. 2.8 given above. We then checked whether our possible companions would lie within the tidal radius of their host UCD. To accomplish that, we took the ratio between  $\text{dist}_{\text{comp}}/r_{\text{tidal}}$  (see column 9 in Table A.1), which denotes at which fraction of the tidal radius of this object the companion is located. For 16 out of 19 objects this fraction is below 1.0, which means the companion candidates are well within the tidal radius. The companions are actually outside of the predicted tidal radius for only three objects (b, j, l). Thus, if these companions are associated with the UCD it is likely that they are still bound to it.

We also checked whether any of the companion GC candidates were detected by the Dirsch et al. (2003) observations. We found that the GC candidate from panel b) at the bottom of the frame was indeed detected and has a color of  $C - T_1 = 1.60$ . In the color magnitude space this puts it at the border between "blue" and "red" GCs at  $C - T_1 = 1.55$ .

## 2.5 Spatial clustering of GCs around UCDs in the halo of NGC 1399

### 2.5.1 The globular cluster system around NGC 1399

To study the statistics of globular cluster clustering around UCDs, we use the catalog of globular clusters around NGC 1399 by Dirsch et al. (2003). The catalog contains 10457 point sources. It was obtained using wide-field Washington photometry. We defined GCs as point sources in the color range  $1.0 < C - T_1 < 2.3$ . To avoid any incompleteness, we further restricted the GC sample to point sources of  $T_1 < 23.5$  for which the data are still complete. Since the completeness depends on the object's color, an additional color dependent magnitude cut was applied similar to the original work, given as

$$T_{\text{cut}} < -0.935 \cdot (C - T_1) + 24.69. \quad (2.9)$$

In order to avoid any duplications with the UCDs, we exclude all objects that have masses above  $M = 10^6 M_\odot$ . For the mass calculation of the GC candidates, we applied the same simple stellar population models (SSP) from Maraston (2005) as used in Sect. 2.3.1 for the UCDs to their Washington photometry, assuming an age of 13 Gyr, a Kroupa (2001) initial mass function (IMF) and a red horizontal branch.

Applying all selection criteria leaves us with a total of 2884 globular cluster candidates. In Fig. 2.12 we show the central area of the Fornax cluster with the spatial distribution of these GCs (black dots) and the UCDs (red), respectively.

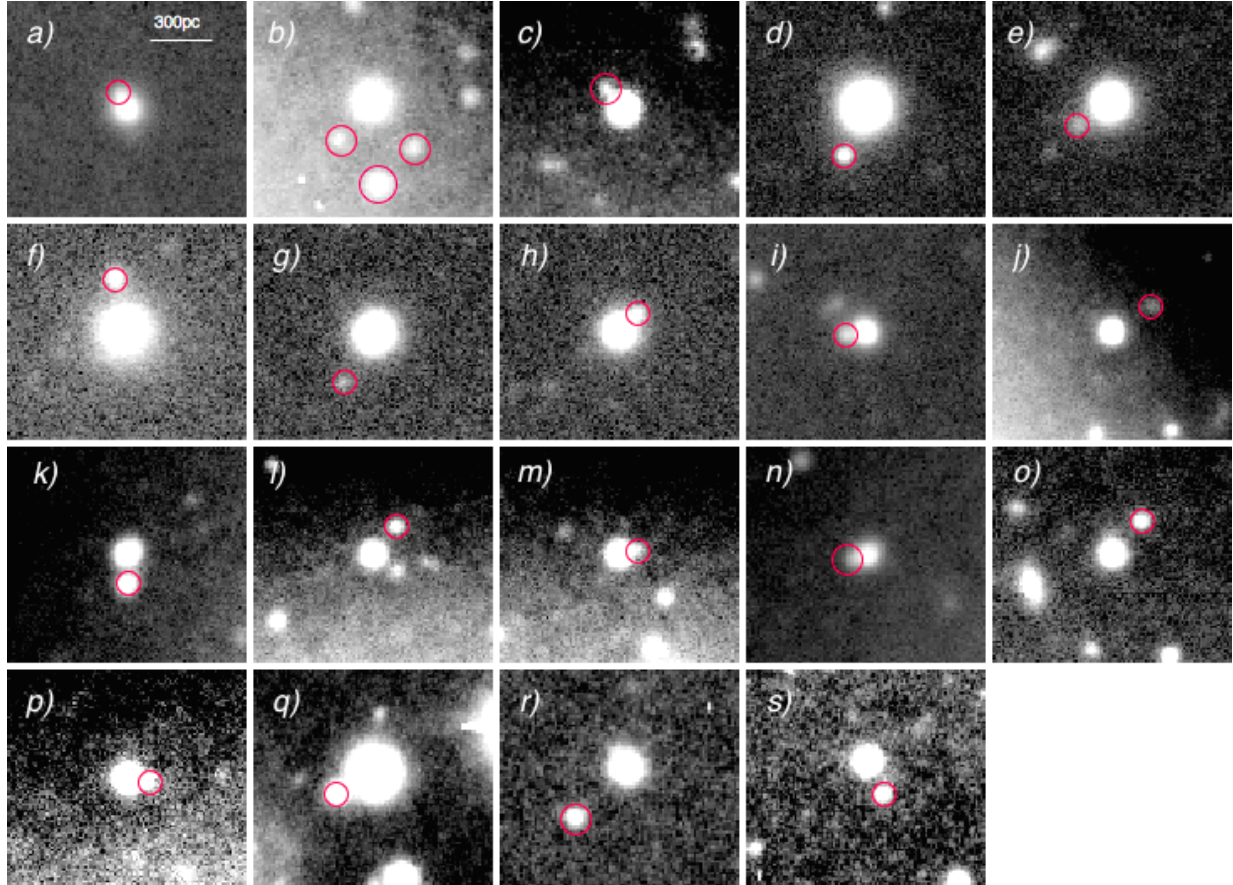


Figure 2.9: Cutout images of the 19 UCDs that have companion point sources (red circles) within a radius of  $r < 300$  pc. As the cutout images have varying background levels, the contrast used for display can slightly vary between the images to enhance the visibility of the companion.

We need to take into account the incomplete areas of the wide-field imaging in our statistical analysis on the spatial distribution of the GCs. In Fig. 2.12 the borders of incomplete areas and gap regions are shown as dashed lines. For any statistical analysis we have created a spatial incompleteness mask that determines which fraction of any given surface area is in the incomplete area. Thus we can statistically correct the number of GCs per surface unit. The green areas around the center of NGC 1399 are also masked out because of the incompleteness of the GC sample so close to the center of the main galaxy. For the two neighboring galaxies, NGC 1404 and NGC 1387, the green masking boxes are chosen generously to avoid any contamination of the radial distribution of NGC 1399 GCs by the GC populations of these neighboring galaxies.

The final incompleteness mask combined with the dataset makes it possible to apply very accurate geometrical incompleteness corrections to the number of objects contained in each annulus.

We analyze the projected surface number density of globular clusters (black dots) around NGC 1399 as a function of their galactocentric distance to NGC 1399. To accomplish that, we adopt bins between 10 and 110 kpc with a spacing of 3 kpc. At radial distances  $r < 10$  kpc, the density profile of the GCs flattens out (see black points in Fig. 2.10) as a result of incompleteness caused by the very bright center of NGC 1399. At distances of  $r > 110$  kpc, the number counts are too low and there is contamination by background objects and GCs of neighboring galaxies. The number of GCs in each bin was corrected for geometrical incompleteness as explained above. The completeness corrected number of GCs is then divided by the surface area in physical units of  $\text{kpc}^2$  to obtain the projected surface density  $\Sigma(r)$  of globular clusters, which is plotted in Fig. 2.10. The same procedure has also been done for the UCD sample located in the same wide-field and is shown as blue data points in Fig. 2.10. As the absolute surface density of UCDs is an order of magnitude smaller, the absolute density values of the UCDs (green) in Fig. 2.10 were scaled by a factor 10. This makes it easier to compare the slopes of both populations.

The radial surface density distribution of GCs was then fitted with a power law, given as:  $\Sigma(R) = (R/a_0)^n$ , where  $\Sigma$  is the number of GCs per square kpc and  $R$  is the radial distance in kpc. The fit was restricted to  $10 < R < 110$  kpc in galactocentric distance as shown by the two dashed vertical lines in Fig. 2.10.

The resulting power-law fit is shown in Fig. 2.10 as a red line with the measured density values shown as black dots. The central value of our power-law fit is  $a_0 = 10.25$  whereas the index we derive is  $n = -1.36$ , which is shallower than the  $n = -1.61$  derived by Bassino et al. (2006). This is not surprising since Bassino et al. (2006) defined the slope after subtracting background counts.

We also derived the radial surface density distribution for the blue,  $1.0 < C - T_1 < 1.55$ , and red,  $1.55 < C - T_1 < 2.3$ , GCs of our sample as shown in Fig. 2.11. The squares in red and blue show the measured surface density for each radial bin with their corresponding Poisson errors, respectively. We choose  $C - T_1 = 1.55$  as limit for splitting the GCs into a red and blue subpopulation, as Bassino et al. (2006) have shown that there is a dip in the bimodal color distribution at this color.

It is clearly visible from Fig. 2.11 that the red GC population has a steeper density

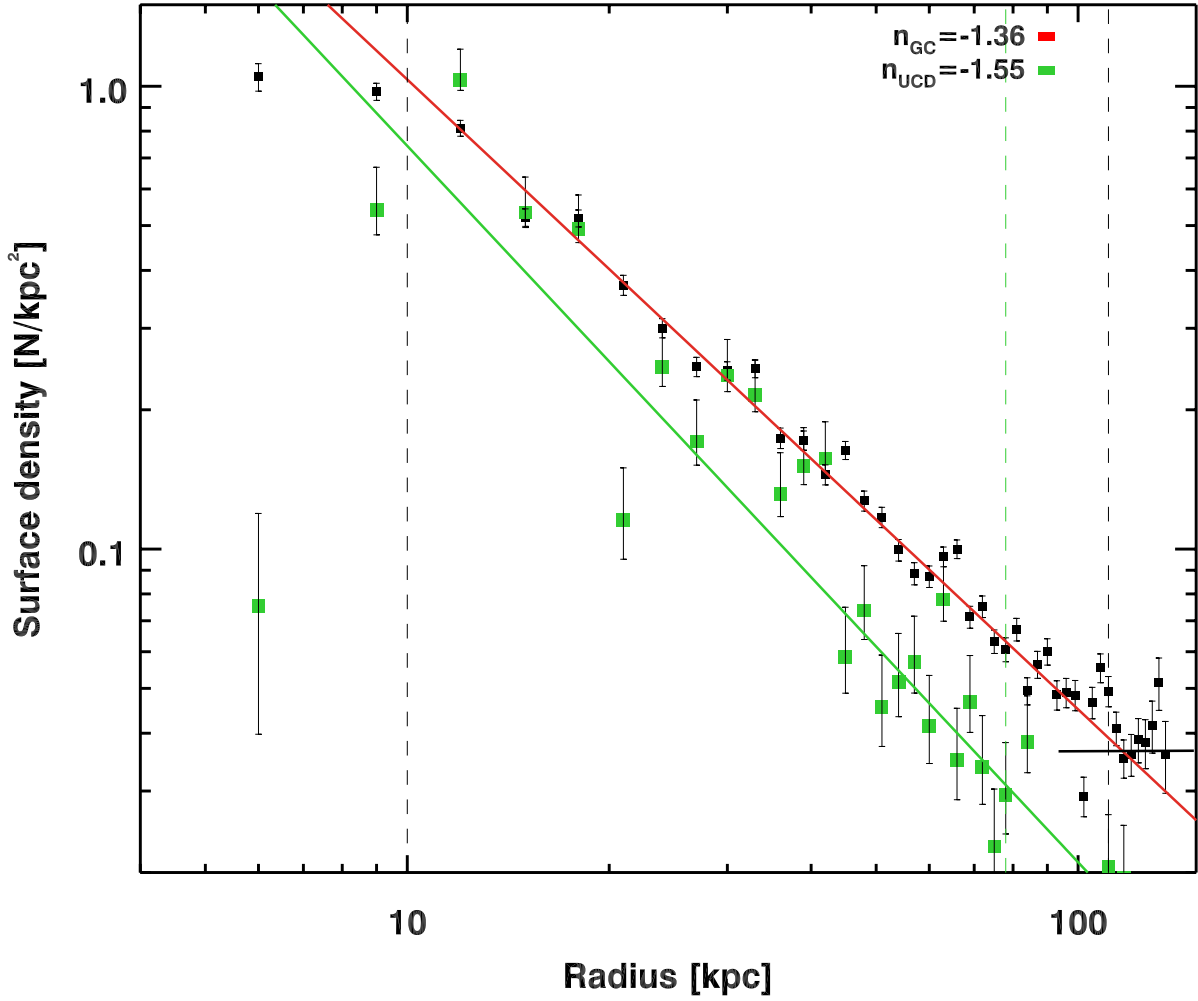


Figure 2.10: Projected surface density distribution of GCs and UCDs as a function of their galactocentric distance to NGC 1399. The red line shows the best power-law fit with an exponent of  $n = -1.36$ . The background level was labeled with a black horizontal line. The vertical dashed black lines show the radial interval to which we restricted our fit. The radial distribution of the confirmed UCDs is shown in green. As their absolute radial density is an order of magnitude smaller than the GCs, their density is scaled up by a factor of 10 for better visibility in the plot.

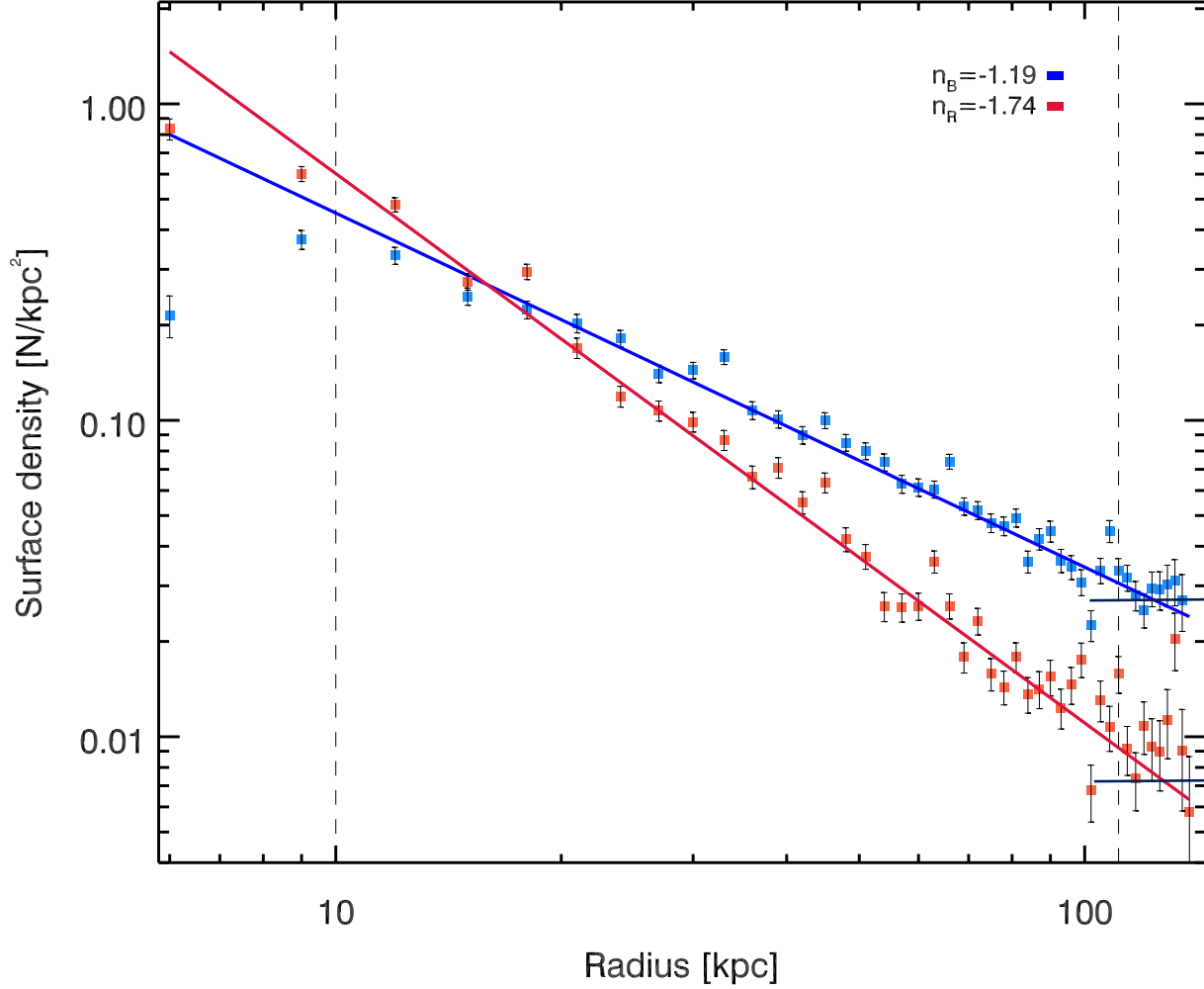


Figure 2.11: Projected surface density distribution of all selected globular clusters as function of their galactocentric distance to NGC 1399. The red line shows the best-fit power law to the red globular clusters with an exponent of  $n = -1.74$  whereas the blue line shows the best-fit power law to the blue GC population, which has a more shallow slope of  $n = -1.12$ . The two short horizontal lines show the respective background levels used for the statistical correction of our signal. The dashed black lines show the radial interval to which we restricted our fit.



profile than the blue GCs. The slope of the red GCs is  $n_R = -1.74$  whereas the blue GCs follow a power law with  $n_B = -1.19$ . The shallow profile of blue GCs and the stronger radial concentration of the red GC population in NGC 1399 is in agreement with what has been shown in [Bassino et al. \(2006\)](#).

### 2.5.2 Spatial correlation of GCs with UCDs

In this section we explain the search for spatial correlations of GCs around UCDs. A positive correlation might be expected if UCDs originate either from stripped nuclei of galaxies with their own globular cluster systems or from merged star cluster complexes with remnant clusters around them.

The stripped nuclei scenario is a viable formation channel in galaxy clusters as has been shown by [Pfeffer et al. \(2014\)](#). The reasoning for finding correlation signatures is the following: luminous dwarf galaxies, and in particular nucleated dwarf galaxies, are known to host their own GC system (e.g., [Lotz et al. 2004](#); [Georgiev et al. 2009](#)). When a dwarf galaxy falls into a large cluster of galaxies it starts to experience tidal forces and its tidal radius shrinks.

Through the tidal interaction with the cluster, the GCs residing outside the shrinking tidal radius are lost and dispersed into the general GC population of the central cluster galaxy, whereas GCs inside the tidal radius can remain bound to the core of the dwarf galaxy for a long time ([Muzzio 1986](#)).

One of the scenarios suggested for the formation of nuclear star clusters (NSCs) is that massive globular clusters merge toward the center of their host galaxy via dynamical friction in less than a Hubble time. ([Tremaine et al. 1975](#); [Capuzzo-Dolcetta 1993](#)). This process is especially efficient in dwarf galaxies. Recently, [Arca-Sedda & Capuzzo-Dolcetta \(2014\)](#) have computed, via a statistical approach, the number of surviving clusters around a galaxy and their mean mass, after a full Hubble time of dynamical friction. For dwarf galaxies with  $M = 10^9 M_\odot$  one expects 80% of the original globular cluster population to have merged with the nucleus via dynamical friction, and the mean mass of the remaining GC population is  $M = 10^5 M_\odot$ .

Recent mergers of star clusters in star cluster complexes can host a variety of substructures in the form of faint envelopes, tidal tails, and nonmerged companion GCs (e.g., [Brüns et al. 2011](#); [Fellhauer & Kroupa 2005](#); [Brüns et al. 2009](#)). Whereas in some simulations of UCD-like objects the surrounding GC companions have merged into the central object within the first Gyr ([Brüns et al. 2011](#)), and thus the merging process is finished. Other simulations of lower mass star cluster complexes suggest that some member star clusters still can be identified as substructures up to 5 Gyr after the onset of merging. Thus, depending on the initial conditions of the merging star cluster complex, we might expect to find companions around it for several Gyr after its formation.

In the following we test whether there is a statistical overabundance of globular clusters in close proximity of UCDs, as we expect such a signal for the inward migration of GCs within a disrupting nucleated dwarf galaxy as well as for a merged super star cluster complex. The main discriminator between both cases is the age of the UCD, as substructure



in star cluster complexes has only been shown for ages of 5 Gyrs.

We can use the radial GC density of NGC 1399, which we determined in the previous section as proxy for the GC density we expect at any given radial distance to the main galaxy. We then determine the local GC density around the UCDs and compare it with the expected value from the global distribution. This derived density ratio between expected and measured density shows whether we have any significant clustering of GCs around UCDs for single objects and the full sample.

In our statistical study we include 206 UCDs from the original sample, which lie within the Washington photometry area and are more massive than  $M > 10^6 M_\odot$ . Their spatial distribution is compared to the 2884 GC candidates from the Washington photometry sample, which have masses less than  $M < 10^6 M_\odot$  and also fulfill the color selection criteria for GCs (see previous section). The green areas in Fig. 2.12 are excluded for being too close to a bright center of a galaxy, and the chip gap areas, indicated with dashed black lines, are also excluded.

We used the same method as for the large scale distribution to determine the local density of GCs around UCDs. We determined the GC surface density for eight radial bins from 0.5 kpc up to 4 kpc with a spacing of 0.5 kpc in the ring-shaped apertures around the UCDs. The surface area of each annulus is completeness corrected if a part of it lies in the area that is masked out. The measured surface density  $\Sigma_{\text{measured}}$  of GCs around each UCD in each radial bin is then compared to the density we would expect at this position of the UCD from the derived large-scale GC distribution (see Figs. 2.10 and 2.11). The expected and measured GC density distribution are both statistically background corrected before the clustering signal is calculated. For the full population and the red and blue subpopulation we derive the following background GC densities from Fig. 2.11:  $\Sigma_0(\text{All}) = 0.026 \text{ kpc}^{-2}$ ,  $\Sigma_0(\text{Blue}) = 0.026 \text{ kpc}^{-2}$  and  $\Sigma_0(\text{Red}) = 0.0073 \text{ kpc}^{-2}$ .

After deriving the clustering ratio  $\Sigma_{\text{measured}}/\Sigma_{\text{expected}}$  for each single UCD, we average the clustering ratios for our full sample at each radial bin. The errorbars refer to the standard deviation of the clustering signals, divided by the square root of the number of UCDs we averaged. The same statistical procedure was applied to the blue and red GC subpopulations separately, where the expected GC surface density was taken from the color separated profiles shown in Fig. 2.11.

The two black circles in Fig. 2.12 show the area between 10 and 110 kpc of galactocentric distance to which we restrict the positions of the UCDs for which we carry out the statistical clustering study. This is the radial range within which the measured radial GC density profiles do not deviate much from the power law (see Fig. 2.10). At larger radial distances the noise in the surface density of the global distribution is too high and in the central areas below 10 kpc the surface density profile flattens out because of observational incompleteness caused mainly by the bright central parts of NGC 1399.

In the top panel of Fig. 2.13, the clustering results are shown for all the 206 UCDs that we included in the statistical sample. As we do not expect all UCDs to have a remnant GC nearby we also studied the subset of UCDs that have an object within 1 kpc. In total, 100 UCDs, which is close to half of the studied sample, have a GC candidate within 1 kpc of radius. The clustering results of those UCDs are shown in the lower panel of Fig. 2.13.

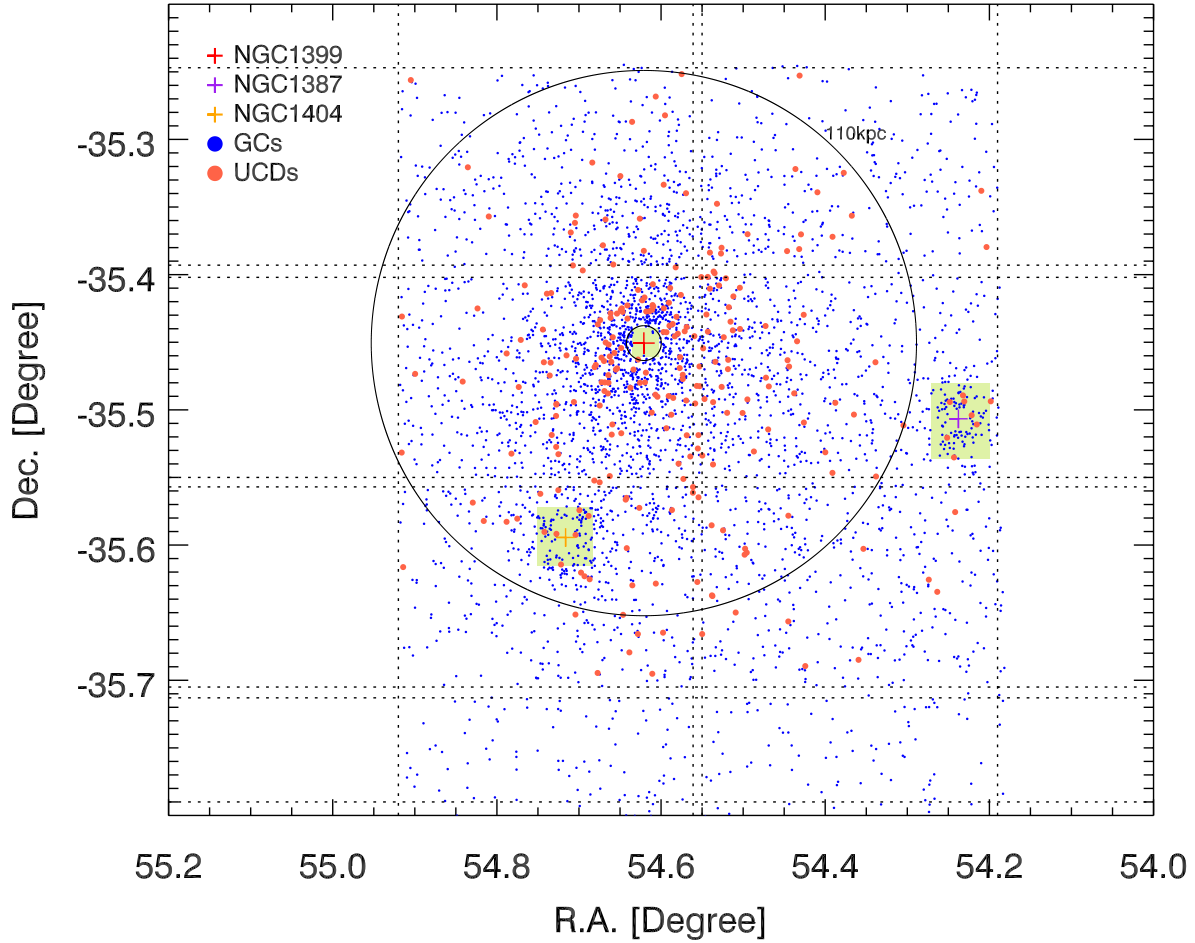


Figure 2.12: Central area of the Fornax cluster is shown. The globular clusters are denoted as blue dots, UCDs as red dots, and NGC 1399 and two neighboring galaxies are shown as colored plus signs. The dashed black lines denote the borders of the CCD chips and gap areas of the globular cluster sample. For our statistical studies, these are masked out. The green areas are also be masked out in the final study because they host their own GC population. The small green circle locates the position of the UCD with four neighboring GC candidates, which is shown in Fig. 2.14 in close up.

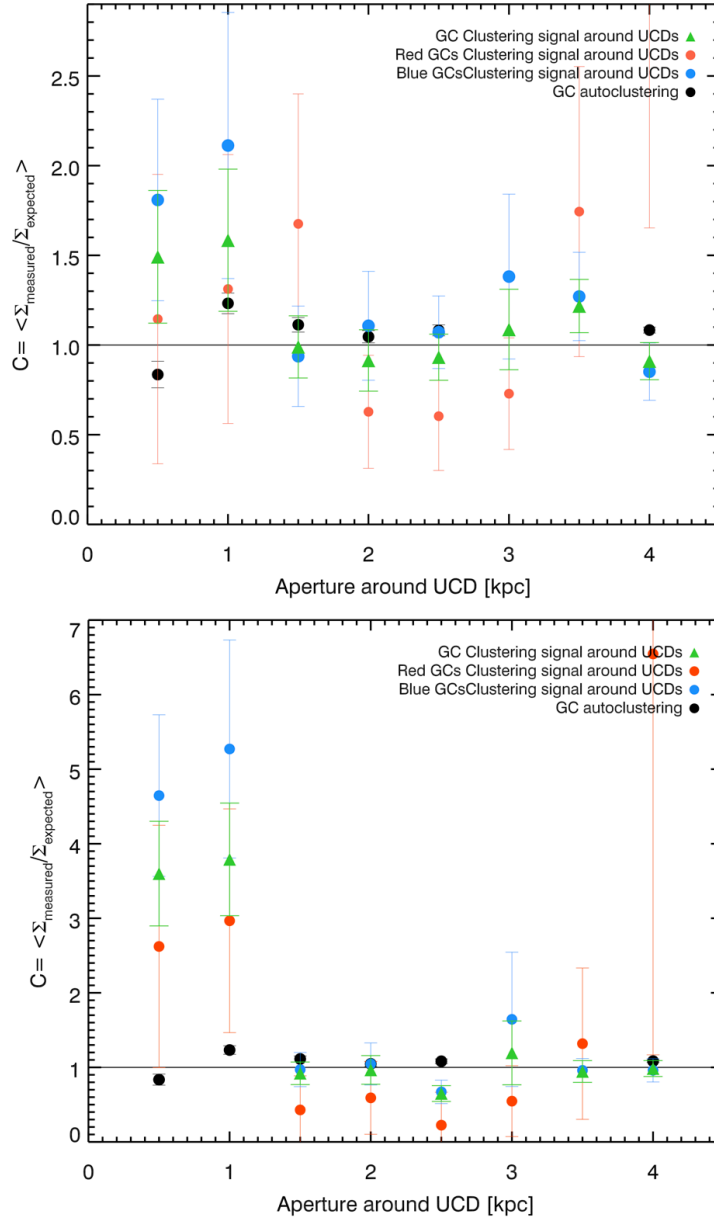


Figure 2.13: In the top panel, the average clustering of GCs around UCDs at different radial bins from the UCDs for the full GC population (green) and the red and blue subpopulations are shown. The black data points are the comparison with autoclustering of the GCs with themselves as a baseline. The clustering signal at each radial bin is the ratio between measured surface density and expected surface density of globular clusters from the large scale distribution, at different radial distances from the UCDs. The black line denotes the null level at which we have no clustering signal compared to what we expect. We averaged the clustering signal for each respective radial bin over the full probed sample of 206 UCDs. Bottom panel: the same plot for the 100 UCDs for which we found a GC candidate within  $r < 1$  kpc. The two y-axis has different scaling.

Table 2.3: Summary of the clustering signals of GCs around UCDs for the 100 UCDs that have a GC candidate within 1 kpc. The clustering check has also been subdivided into red and blue GCs.

Radial bin [kpc]	$C$	$\sigma$	$C_{\text{red}}$	$\sigma_{\text{red}}$	$C_{\text{blue}}$	$\sigma_{\text{blue}}$
0.5	$3.60 \pm 0.70$	3.70	$2.62 \pm 1.62$	0.99	$4.64 \pm 1.08$	3.36
1.0	$3.79 \pm 0.76$	3.69	$2.97 \pm 1.50$	1.31	$5.27 \pm 1.46$	2.92
1.5	$0.92 \pm 0.15$	-0.53	$0.43 \pm 0.46$	-1.24	$0.97 \pm 0.23$	-0.13
2.0	$0.96 \pm 0.19$	-0.18	$0.59 \pm 0.49$	-0.84	$1.05 \pm 0.28$	0.16
2.5	$0.64 \pm 0.10$	-3.31	$0.22 \pm 0.44$	-1.75	$0.67 \pm 0.16$	-2.09
3.0	$1.19 \pm 0.43$	-0.45	$0.55 \pm 0.48$	-0.95	$1.64 \pm 0.90$	0.71
3.5	$0.94 \pm 0.15$	-0.38	$1.32 \pm 1.01$	0.31	$0.96 \pm 0.16$	-0.25
4.0	$0.98 \pm 0.10$	-0.15	$6.54 \pm 5.37$	1.03	$0.96 \pm 0.16$	-0.26

In both panels of this figure, the average clustering signal  $C$  for the full GC population is shown with green triangles, and the results for red and blue GC subpopulations are indicated in their respective colors. The numeric results of the bottom panel are also summarized in Table 2.3, showing the average clustering signal for each population with their errorbars as well as the sigma significance of this signal. As a comparison, the spatial autoclustering of the 2884 GCs is shown with black data points in Fig. 2.13.

For the clustering signal of all UCDs, we find an increasing overdensity of GCs toward smaller distances below 1 kpc. At the smallest radial bin we find that the average UCD has 1.5 times more GCs within 500 pc than we would expect from the underlying distribution. Owing to the high scatter in this average, this results in a  $2\sigma$  statistical significance for the smallest bin. The color separated clustering signals show that for the red GCs  $C$  is compatible with 1, which implies no particular overabundance with respect to the expected values. However, the high scatter is an indication that although some individual UCDs have clustered red GCs, this is not the case on average. The blue (metal-poor) GCs show a higher abundance around UCDs than their red counterparts in the two inner bins. The statistical significance at 1.0 kpc is  $1.5\sigma$ .

Looking at the clustering signal of the 100 UCDs with a GC candidate within 1 kpc (bottom panel of Fig. 2.13), we see a clear clustering signal that distinguishes this UCD population from the autoclustering signal of GCs (black dots) at a very high significance. For the 0.5 and 1 kpc radial bins of this sample we find the clearest clustering signal. The detected overabundance of GCs around these UCDs has a statistical significance of  $3.7\sigma$  for the two smallest bins (see green triangles in bottom panel of Fig. 2.13 and Table 2.3). This clustering signal increases for the blue GCs and decreases for the red GCs, if we compare the clustering of the red and blue subpopulations separately. The blue subpopulation shows an even higher clustering of  $C = 4.64$  at 0.5 kpc compared to the red population with  $C = 2.62$ . In other words, blue, and thus most probably metal-poor GCs, are on average 4.6 times more abundant within 0.5 kpc of a UCD than what we would expect if the blue GCs were randomly distributed. Also, for the blue GCs the significance of the clustering is at  $3.36\sigma$ . Red GCs are also on average more abundant around UCDs up to

1 kpc, but only half as much as the blue GCs, and as a result of the small number statistics for the red subpopulation their numbers have significantly larger errors and much lower sigma values. All the statistics for the bottom panel are also summarized in Table 2.3. We do not find any significant clustering signals in the radial bins larger than 1 kpc.

We emphasize that this is an average clustering value for all UCDs. Single objects can be still located within local over- or underdensities of GCs, but if the averaged ratio is significantly higher than 1.0, this means that there is a systematic deviation of the surface density of GCs in the vicinity of UCDs from what we would expect from the large-scale distribution around NGC 1399.

We also checked for significant GC clustering at large radii. For statistical studies, the noise in the radial GC distribution (see Fig. 2.10) can dilute an average signal, but for single UCDs highly significant clustering can still be detected. We found one UCD (blue circle in Fig. 2.14) with four GC candidates (green circles) within 1 kpc radius (red circle). This UCD is located at RA= 03:38:30.768 and Dec = -35:39:56.88, 85 kpc south of NGC1399. All four GC candidates lie well within the estimated tidal radius from Eq. 2.8 given as  $r_{\text{tidal}}=1.36\text{kpc}$ , which is shown as red circle. The GC density around this UCD is  $\Sigma = 1.27\text{kpc}^{-2}$ , although we only expect  $\sim 0.04\text{kpc}^{-2}$  at these radial distances. Thus this is larger by a factor of  $\sim 32$  than what would be expected from a simple radial distribution of GCs in the halo of NGC 1399. In addition, all four GC candidates would belong to the blue (metal-poor) GC population if they are Fornax members, with an average of  $C - T_1 = 1.37$ . The UCD itself has a red color of  $C - T_1 = 1.82$ . This is in good agreement with our finding for the UCDs within 110 kpc, for which the blue GCs are more clustered around UCDs than the red GCs (see Fig. 2.13). The position of this UCD in the outskirts of the halo of NGC 1399 and its associated blue GC population make it a prime target for an infalling, nucleated dwarf galaxy in its early stages of disruption, where the original GC system might still be partially intact. However, it is very puzzling that no faint stellar envelope of tidal features have been found around this UCD. We come back to this in the discussion.

## 2.6 Discussion

### 2.6.1 Surface brightness profiles of UCDs and their scaling relations

One of the possible theories of UCD formation is that some of them are the remnant nuclei of larger dwarf ellipticals, which are stripped of their stellar envelope through tidal interactions (e.g., Bekki et al. 2003; Drinkwater et al. 2003). In Pfeffer & Baumgardt (2013), the trajectories from simulations in the size-mass plane of such a process are shown. After being tidally stripped, they end up with sizes and magnitudes of UCDs, effectively having to cross the empty region in between the galaxy and star cluster branch. Although it is noteworthy that these are idealized simulations that do not include a dark matter halo for the satellite galaxy, and thus apply only to galaxies that have already lost the

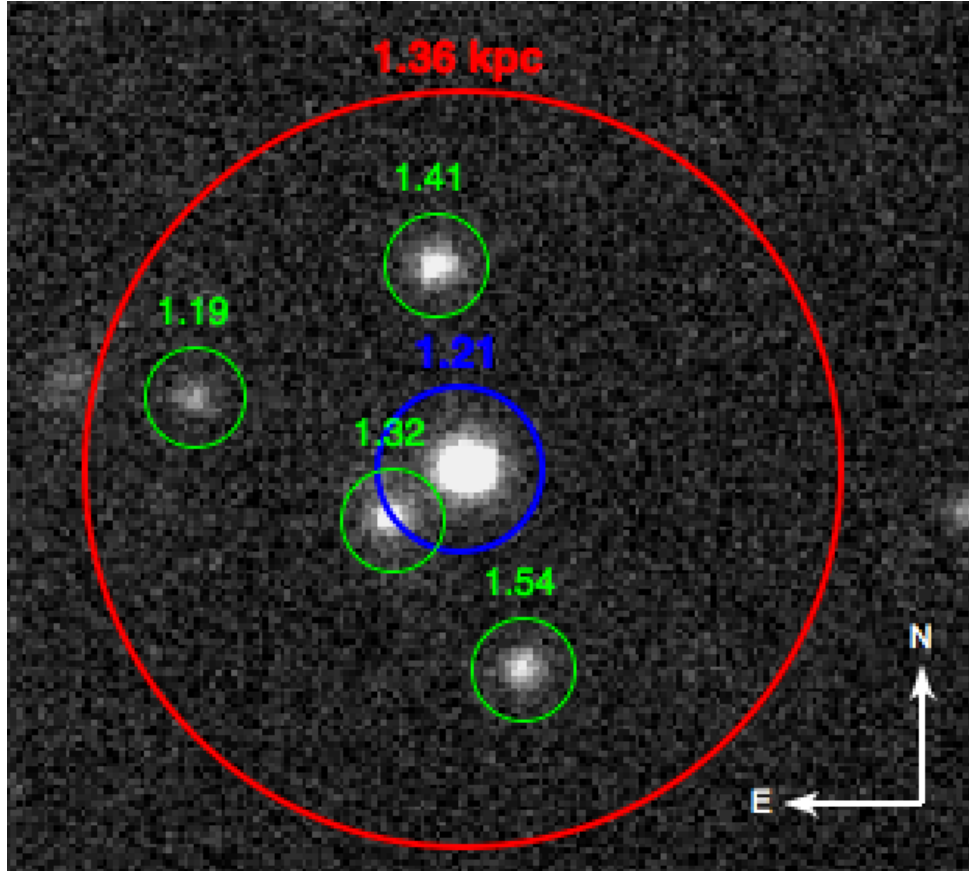


Figure 2.14: Blue circle indicates the UCD with the original name Y4289 ([Richtler et al. 2008](#)), which is a confirmed member of Fornax. The UCD itself has an absolute magnitude of  $M_V = -10.3$  and a color of  $(V - I) = 1.21 \pm 0.05$ . The four surrounding GC candidates ([Dirsch et al. 2003](#)) are shown with green circles and they are labeled with their respective  $C - T_1$  colors. A circle with a radius of 1.36 kpc, centered on the UCD, is shown in red. This circle denotes the estimated tidal radius from Eq. 2.8. The cutout has been taken from the wide-field VST Fornax survey imaging ([Iodice et al. in prep.](#))

majority of their dark matter. In Sect. 2.3.4 we posed the question why we do not see more objects in between both branches currently transformed if these objects are formed by tidal stripping? The predicted timescales of 2-3 Gyrs for this kind of stripping process are not too short compared to a Hubble time to observe a certain fraction of these stripped galaxies during the process. This, of course, depends on the number of nucleated dEs available that are on the right disruptive trajectories within the galaxy cluster and on the timing of disruption events. Most probably, the majority of accretion events happened during the violent early phases of the galaxy cluster assembly.

In any case, for those UCDs that are the remnants of tidally stripped dwarf galaxies, we expect that the overall size and luminosity of the disrupting dwarf galaxy is decreased by the stripping of the faint stellar envelope that is left around the nuclear cluster. Most surface brightness distributions of the UCDs we found are well fitted with a Sérsic index between  $2 < n < 6$ . Most dEs obey an exponential  $n = 1$  surface brightness profile (when excluding the nuclear star cluster), whereas compact ellipticals and giant ellipticals usually require more centrally concentrated profiles with  $n = 4$ . One explanation for this central concentration of the UCD profiles could be that we see a superposition of the centrally concentrated nuclear star cluster (NSC) and the remains of the stellar envelope. While the stellar envelope is getting fainter and fainter during stripping, the luminosity from the NSC starts to dominate the profile more and more, and thus causes a more centrally concentrated light profile.

Another possibility is that the merging of star cluster complexes into one extended UCD could cause the appearance of faint envelopes around UCDs. In Brüns et al. (2011), it has been shown with a numerical model that the products of such mergers at large galactocentric distances can have effective radii up to 80 pc. In Fellhauer & Kroupa (2005), the evolution of the surface brightness profiles of merging stellar superclusters are shown. Within the first 500 Myrs this kind of star cluster complex can exhibit faint halo-like features up to a few hundred pc of distance. In their work they also followed the evolution of two super star cluster over 10 Gyrs. The initially relatively bright halos at 25-26 mag/arcsec<sup>-2</sup> decrease quickly in size and surface brightness. After 10 Gyrs the faint envelope components have decreased to a surface brightness of 28-32 mag/arcsec<sup>-2</sup> at the maximum extension of  $\sim 100$  pc. In addition, Fellhauer & Kroupa (2005) showed that after evolving for 10 Gyr these merged star cluster complexes are rather resembling the faint fuzzy star clusters than UCDs. Thus the origin of these faint envelopes from merged star clusters is rather unlikely, as none of our UCDs with envelopes show any signs of very young ages ( $< 1$  Gyr) where a super star cluster envelope would still be bright enough to be detected. The predicted envelope magnitudes at 28-32 mag/arcsec<sup>-2</sup> for a 10 Gyr old star cluster complex are several orders of magnitude fainter than the  $\mu = 26$  mag/arcsec<sup>-2</sup> envelopes we found. Of course, this does not exclude that several of the UCDs without detectable envelopes originated from merged star cluster complexes.

When we decomposed the UCD light profiles in a King core component and a Sérsic envelope we found that the Sérsic index of the envelopes takes values of  $n < 2$ , which resembles more closely what is found for surface brightness profiles of dwarf ellipticals. In the size-magnitude diagram these remnant envelopes, if regarded as isolated components,



are located in the empty area between the galaxy and star cluster branch, which exactly is the transition area [Pfeffer & Baumgardt \(2013\)](#) predict for dEs that are being stripped.

An argument against UCDs being the nuclei of stripped dwarf galaxies is the location of the red extended UCDs on the color magnitude diagram. While blue extended UCDs agree well with the established nuclei locations in the CMD, red UCDs are significantly fainter than what is expected from a galaxy nucleus.

The stripping scenario is also supported by the three works that found double profiles for individual UCDs ([Evstigneeva et al. 2007](#); [Chilingarian et al. 2008](#); [Strader et al. 2013](#)). Their core components resemble the scaling relations of nuclear star clusters, whereas the envelopes lie in the previously empty transition area between the galaxy and star cluster branch. As mentioned before, however, envelopes are also a transient feature of merged star cluster complexes.

### 2.6.2 Tidal features

We examined our sample of confirmed UCDs for direct observational evidence of ongoing tidal stripping as possible proof for the transformation of a dE galaxy into a UCD or the tidal disruption of a super star cluster. We found extended features around eleven UCDs with apparent sizes between 100 and 350 pc. UCD-FORS 2 shows the clearest evidence for a tidal feature, with two tails detected at the  $3\sigma$  level above the background, which have an apparent extent of 350 pc. The theoretical tidal radius for this object is given as 444 pc for its distance of 33.34 pc to NGC 1399, and is thus only slightly larger than the observed tidal features. For an object of this luminosity a tidal radius of 130 pc would be reached at a pericenter distance of 10 kpc. The eleven UCDs with extended features account for 11.3% of the total population we analyzed in detail.

In [Pfeffer et al. \(2014\)](#), the number of stripped nuclei within  $R < 83$  kpc and masses  $M > 2 \cdot 10^6 M_\odot$  for the central parts of the Fornax cluster is predicted to be  $n_{\text{nuclei}} = 11.6^{+5.7}_{-4.9}$ . When we scale this value to the total surface of our three FORS fields we get a prediction of  $n_{\text{nuclei}} = 19.07^{+9.4}_{-8.1}$  stripped nuclei in our observing fields. This is marginally consistent with our eleven UCDs with possibly direct evidence for tidal features. However, there are several factors to be considered when comparing those two numbers: 1) Some of our detections might be by-chance superpositions of low surface brightness background galaxies, although the calculated probability for that is very low. 2) Because tidal features are of low surface brightness, the number of UCDs with stripping evidence would rise if we were able to observe deeper. Our observations were able to detect tails down to a limiting surface brightness of  $\mu = 26$  mag/arcsec<sup>2</sup>. In [Pfeffer & Baumgardt \(2013\)](#), the simulated envelopes reach this magnitude level after being stripped for 700 Myrs. Thus we miss stripping events that started more than  $\sim 1$  Gyr ago. In fact, the surface brightness levels of the envelopes can act as sort of clock for the disruption processes, which hints at the age since the tidal disruption started. In this respect, our determined fraction of nuclei remnants puts a lower limit on the contribution of the tidal stripping as formation channel for UCDs. 3) Tidal tails only occur during the actual stripping period, which lasts on the order 2-3 Gyr. In combination with our surface brightness limits this implies that the tidal tails are only



observable during a very short time window of the stripping process. Since disruption events are distributed all over the galaxy cluster evolution time, and probably were more common during the main galaxy cluster assembly several Gyr ago, one currently expects to see only a small fraction of ongoing disruption events. Pfeffer et al. (2014) estimate that about 5% of the available stripped nuclei candidates started stripping less than 2 Gyr ago, which would mean that only one event should be seen within our FORS fields. Maybe UCD-FORS2 is the 'lucky' smoking-gun.

Taken all factors together we can only state that the low number of observed tidal features at the given surface brightness limit, <11 out of 97 UCDs, is not in contradiction with the expected number of stripped nuclei from simulations. In terms of contamination it is an upper limit for recently stripped dEs, in terms of the total number of stripped nuclei it is a lower limit.

An alternative explanation for the appearance of the tail-like structures around UCD-FORS2 is that this object is a high mass globular cluster or a merged super star cluster that is currently being disrupted. The Galactic GCs Palomar 14 (Sollima et al. 2011) and Palomar 5 (Odenkirchen et al. 2001) show tidal features of comparable size and symmetry to our object. However, both Palomar clusters have masses of  $M \simeq 10^4 M_\odot$ , whereas our object is by a factor of 1000 more massive ( $\sim 10^7 M_\odot$ ) at a comparable half-light radius. To strip stellar material from this kind of an compact object requires a much stronger tidal field. The intermediate-age stellar populations detected in UCD-FORS2 (Richtler et al. 2005) might be hint that this UCD originated from a super star cluster complex that was formed a few Gyrs ago. On the other hand, a youngish age would also be expected for a nuclear star cluster that was built up by recurrent star formation from infalling gas.

Based on our evidence we cannot clearly distinguish if this object is a massive globular cluster being stripped or the remnant of a nucleated galaxy. Although the high stellar density makes direct stripping very difficult, the Balmer lines and metallicity detected for this object in Richtler et al. (2005) point to the presence of a younger stellar population, which agrees well with a stripped GC complex. In any case, this is the first time that a significant tidal tail has been discovered around a UCD-like object of this magnitude.

### 2.6.3 Spatial correlation of UCDs with globular clusters

In our statistical search for signatures of spatial clustering of GCs around UCDs within 10 to 110 kpc from NGC 1399, we found a local overabundance of GCs on scales of 0.5 to 1 kpc around UCDs when compared to the global abundance of GCs in the halo. In total 48.5% of our UCDs have an overdensity of globular clusters around them within 1 kpc. Thus, it appears that UCDs can be divided into two distinct populations: 1) UCDs that harbor a population of close-by satellite points sources, most probably low mass star clusters; 2) UCDs that have the same statistical clustering properties as so-called normal globular clusters.

One possible explanation for the clustering signal of GCs around UCDs could be that UCDs formed as nuclei of a dwarf galaxy that harbored its own GC system. What we see is the remnant GC population of the ancestor galaxy before it was stripped to its nucleus.

The observed clustering is expected in a scenario in which globular clusters merge toward the center of the galaxy via dynamical friction in less than a Hubble time. In particular, the dynamical friction timescale is shortest for the most massive globular clusters of a dwarf galaxy. Thus in a migratory-merger model, high mass GCs would spiral into the nucleus first as they have dynamical friction timescales of  $\tau < 10$  Gyrs. Evidence of this process is provided in Lotz et al. (2001), who found a deficit of bright GCs in the central parts of dE galaxies. Their sample of dwarf galaxies between  $-12 > M_V > -16$  have their own GC population between 0-25 GCs per dwarf galaxy. This low number of observed GCs in a dwarf elliptical combined with the models of Arca-Sedda & Capuzzo-Dolcetta (2014) leads to the prediction that a galaxy of  $M = 10^9 M_\odot$  mass loses 80% of its GC population over a Hubble time via dynamical friction, thus the observed number of GCs in old and potentially stripped objects should be fairly low, between 0-5 GCs. Even considering that a galaxy, which experienced strong mass loss after tidal stripping, has lost 95% of its original mass, the remaining 5% are still enough to harbor the NC, a companion GC, and a faint remnant envelope.

In the literature, there are some examples of nucleated dwarf galaxies that possess only a few GCs (Georgiev et al. 2009, 2010). Recently, Karachentsev et al. (2015) discovered a faint dwarf spheroidal,  $M_B = -10.8$ , which contains a central globular cluster with an extended faint stellar halo around it. These objects might be the progenitors of the extended UCDs we find. The globular clusters around dwarf galaxies are in majority metal-poor and old, thus are blue ( $V-I$ ). Since the observed clustering signal is strongest for the blue GC subpopulation, this strengthens the view that some UCDs with blue companions are the stripped nuclei of metal-poor (dwarf) galaxies. This notion is also supported by object Y4289 for which we found four very blue (probably metal-poor) GCs within a radius of 1 kpc and a red central UCD. The position of this UCD in the outskirts of the halo of NGC 1399 and its associated blue GC population make it a prime target for an infalling, nucleated dwarf galaxy where the original GC system might still be partially intact. The large color difference between the red nucleus and the blue GCs shows that the more metal-rich nucleus must have been metal-enriched through several SF episodes and most likely did not form similar to its surrounding metal-poor GCs. Alternatively, if this object is the result of a merger of a super star cluster complex, the blue colors of the surrounding GCs could be interpreted as youngish ages. But then one would expect that the central merged object (UCD) has the same color, except it had been enriched in metals during the violent formation in the central part of the super star cluster complex. Nevertheless it is puzzling that, assuming these are the remnant GCs of a disrupting dwarf galaxy, we do not see a remnant stellar envelope. In our search for stellar envelopes, we have a surface brightness limit of  $26 \text{ mag/arcsec}^{-2}$  and potential envelopes could be well below our detection limit, although bright dEs would have surface brightness of  $\sim 23\text{-}25 \text{ mag/arcsec}^{-2}$ .

A very different explanation for GC clustering around UCDs could be the temporary capture and focusing of GCs by the potential well of a UCD that is moving through the halo of a large galaxy. The typical tidal radii for a  $10^6 M_\odot$  UCD in a galaxy like NGC 1399 is given as 300 pc, 700 pc, and 900 pc for distances of 30, 50, and 70 kpc to the center of the galaxy, respectively. In this scenario, UCDs can keep objects bound for a considerable

time if their pericenter passage is not too close to the central galaxy and if they move in a similar phase space as the surrounding GCs, which would be the situation for a super star cluster complex with others cluster formation around it. In the outskirts of a halo, such as NGC1399, the tidal radius of an UCD can grow up to 1 kpc or larger and is in good agreement with the radial scale on which we find the clustering signal.

An alternative explanation for the clustering of GCs around UCDs could be that those UCDs initially formed in a star cluster complex that then subsequently merged to create a UCD (see, e.g., [Fellhauer & Kroupa 2002](#); [Brüns et al. 2009, 2011](#)). Massive star cluster complexes are common in gas-rich mergers (e.g., The Antennae, [Whitmore et al. 1999](#)). The overdensities of star clusters around the merged super star cluster then are the remnants of this process. In the simulations of [Brüns et al. \(2011, 2009\)](#), they predict that these kind of star cluster complexes would merge within 1 Gyr, although in some cases substructure can last up to 5 Gyr in their simulations. Thus, the UCD and its surrounding GCs must have rather young ages and probably a high metallicity to be able to detect a remaining GC of this complex that has not merged yet. Currently, spectroscopic observations of UCDs and GCs in Fornax indicate that most of them have an age older than 8 Gyr ([Mieske et al. 2006](#)). Some Fornax UCDs ([Chilingarian et al. 2011](#); [Chilingarian et al. 2008](#); [Richtler et al. 2005](#)), however, show intermediate ages, which could resemble a recently merged super star cluster complex. In contrast to the star cluster scenario, the majority of the companion GCs around UCDs are most probably metal-poor (see above), which points to a dwarf galaxy origin. Thus, we consider both the cluster complex merger scenario and the tidally stripped nucleated galaxy scenario as viable formation channels for Fornax UCDs with companion objects, and to discriminate between them one has to carefully compare the metallicities and ages of the nuclei and the companions.

In conclusion, we interpret the structural parameters of the studied UCDs and their faint envelopes as well as the discovered tidal features as an indication that the stripping of a dwarf galaxy is a viable formation channel of at least a fraction of UCDs. Homogeneous and deep observations that target finding and confirming the tidal features and improving the sample of UCDs with detailed structural parameters are necessary to draw definite conclusions about their origins and the contribution of each formation channel to the number counts of UCDs.

For the clustering of GCs around UCDs, it is important to confirm our finding with larger datasets in other galaxy clusters. The association of UCDs and their companion GCs can be probed by radial velocity and stellar population measurements. This is one of the key observations to distinguish whether these objects are, in fact, the remnants of disrupted galaxies or the remnants of merging star clusters.



# Chapter 3

## Probing the boundary between star clusters and dwarf galaxies: A MUSE view on the dynamics of Crater/Laevens I

This work has been published as Voggel, K., Hilker, M., Baumgardt, H., Collins, M. L. M., Grebel, E. K., Husemann, B., Richtler, T., Frank, M. J.; MNRAS, 2016, 460, 3384V;

*"Probing the boundary between star clusters and dwarf galaxies: A MUSE view on the dynamics of Crater/Laevens I"*

### 3.1 Introduction

The recent discovery of ultra-faint dwarf spheroidals and extended star clusters has changed our view on small stellar systems. A decade ago, globular clusters and dwarf galaxies were well separated in size-luminosity parameter space (Gilmore et al. 2007), and thus could easily be distinguished from each other. A multitude of new objects has been gradually filling the gap at the faint end of the radius-magnitude scaling relation, between dwarf spheroidal galaxies and star clusters (e.g. Misgeld & Hilker 2011; McConnachie 2012; Willman et al. 2005a; Huxor et al. 2005; Zucker et al. 2006b,a; Belokurov et al. 2007, 2008; Laevens et al. 2015a; Martin et al. 2016b).

With magnitudes of  $M_V > -6$  and sizes between 10-100 pc their structural parameters alone do not allow us to infer their nature. To distinguish the nature of ultra-faint objects one has to study their chemical and dynamical properties in greater detail. Some attempts have been made to clarify what a galaxy is apart from its size, e.g., Willman & Strader (2012), conclude that star formation that lasted for hundreds of Myr and the presence of dark matter are the main discriminators between star clusters and dwarf galaxies in the boundary region.

For several newly discovered objects in the boundary region spectroscopic follow-up observations were carried out to explore their nature with kinematical data of their stellar populations (e.g. Martin et al. 2016a, 2015; Kirby et al. 2015).

The dwarf galaxies with the lowest baryon content are expected to be extremely dark matter dominated and to show highly elevated mass-to-light ratios ( $M/L_V$ ), whereas globular clusters seem to be dark-matter-free. While the small sizes of globular clusters (a few pc compared to the typically much more extended dwarf spheroidal galaxies) and the impact of the tidal field of the host galaxy make the detection of dynamical signatures of dark matter harder, detailed velocity dispersion profiles of remote outer halo globular clusters, which are less affected by Galactic tides, suggest that mass follows light (e.g. [Jordi et al. 2009](#); [Frank et al. 2012](#)).

Crater/Laevens I<sup>1</sup> is an ultra faint object, independently discovered by [Belokurov et al. \(2014\)](#) and [Laevens et al. \(2014\)](#) in the outermost halo of the Milky Way. Before the discovery by professional astronomers Crater was already identified by the amateur astronomer Pascal Le Dû in the January 2014 issue of the magazine *L'Astronomie*<sup>2</sup>. [Belokurov et al. \(2014\)](#) discovered Crater in observations from the ESO VST ATLAS survey. According to their studies, Crater's half-light radius is  $r_h = 30$  pc and the absolute magnitude is  $M_V = -5.5$ , placing it right at the boundary between extended star clusters and the faintest dwarf galaxies in terms of size and magnitude. Crater's heliocentric distance of 170 kpc locates it farther than any other previously known Milky Way globular cluster, but well among dwarf galaxy distances.

The groundbased colour-magnitude diagram of Crater shows that the majority of the stellar population is old (between 7 and 10 Gyr) and metal-poor, except for a handful of possible luminous "blue loop" stars. These blue loop stars could be as young as 400 Myr, and if confirmed as members, would indicate a recent episode of star formation. As an extended star formation history is a diagnostic of dwarf galaxies (e.g. [Willman & Strader 2012](#)), [Belokurov et al. 2014](#) concluded this newly discovered object must be a dwarf galaxy.

Simultaneously, this faint object was also discovered in the Pan-STARRS1 survey by [Laevens et al. \(2014\)](#). They measured a slightly fainter absolute magnitude of  $M_V = -4.3 \pm 0.2$  and a slightly smaller heliocentric distance of  $145 \pm 17$  kpc, which also results in a smaller half-light radius of  $r_h = 20 \pm 2$  pc. They conclude that Crater consists of a stellar population that is 8-10 Gyr old and metal-poor with  $-2.3 \text{ dex} < [\text{Fe}/\text{H}] < -1.5 \text{ dex}$ . In their work the tentative blue loop stars were detected as well, but they argue that these are not part of the system. Combined with their slightly smaller structural parameters they conclude that this object has the typical properties of a young outer halo globular cluster, and thus classify it as such naming it Laevens I.

[Kirby et al. \(2015\)](#) presented spectra of 14 potential member stars of Crater, which were taken with DEIMOS on Keck II. They find a heliocentric velocity of  $v_{\text{sys}} = 149.3 \pm 1.2 \text{ km s}^{-1}$  for the 10 sample stars that they consider to be member stars. They derive a velocity dispersion of  $\sigma_v < 4.8 \text{ km s}^{-1}$  at a confidence level of 95%. Considering the membership status of the tentative blue loop stars, they find that two of them are not members and a third one is an ambiguous case. This blue star is within their  $2.58\sigma$  radial velocity

<sup>1</sup>For continuity with other recently published work, we will use Crater as naming convention for this paper

<sup>2</sup>[http://www.cielocean.fr/uploads/images/FichiersPDF/L-Astronomie-\\_Janvier2014.pdf](http://www.cielocean.fr/uploads/images/FichiersPDF/L-Astronomie-_Janvier2014.pdf)

membership criterion, but it is excluded as a member based on its position in the CMD. In this work it was also concluded that this object is most likely an outer halo GC.

Another attempt to clarify the nature of Crater was performed by [Bonifacio et al. \(2015\)](#) with X-SHOOTER spectra of two red giant stars in the system. They derive a radial velocity of  $V_1 = 144.3 \pm 4.0 \text{ km s}^{-1}$  for the first and  $V_2 = 134.1 \pm 4.0 \text{ km s}^{-1}$  for the second probed star. They conclude that both stars are probable members of the stellar system, and that their velocity difference implies a dispersion of  $\sigma_v > 3.7 \text{ km s}^{-1}$  at 95% confidence level, if one ignores the errors on the stellar velocities. If these errors are taken into account, their measurement is, however, consistent with a velocity dispersion of 0. They determine metallicities of  $[\text{Fe}/\text{H}] = -1.73$  dex and  $[\text{Fe}/\text{H}] = -1.67$  dex for the two stars. Their spectral and photometric data are consistent with an age of 7 Gyr for the majority of Crater’s stellar population, and the blue stars can be interpreted as a population with the same metallicity but an age of only 2.2 Gyr. Thus, in this work it was concluded that Crater is more likely to be a dwarf galaxy.

Recently, a new deep HST photometric study of the CMD of Crater ([Weisz et al. 2015](#)) revealed that its stellar population is well described by a single age of 7.5 Gyr with a metallicity of  $[\text{M}/\text{H}] \sim -1.65$  dex. Similar to [Bonifacio et al. \(2015\)](#) they also detect the blue stars just above the main sequence turnoff. They conclude that the most likely explanation for this sparse population are blue stragglers and not an intermediate age second generation of stars. This result would imply that Crater is a globular cluster, although the majority of intermediate-age star clusters are more metal-rich than Crater.

One outlier to this trend of shigher metallicities with ages is Lindsay 38 in the SMC, an intermediate age star cluster that is relatively similar to Crater in size and metallicity. It has a measured metallicity of -1.6 dex and an age of 6.5 Gyr ([Glatt et al. 2008](#)). Lindsay 38 is also comparable in structural parameters to Crater. The half-light radius measured by [Weisz et al. 2015](#) of Crater is  $r_h = 19.4 \text{ pc}$  while Lindsay 38 has a half-light radius of  $r_h = 20.93 \text{ pc}$  ([Glatt et al. 2009](#)).

The ongoing controversy on the nature of this object, even after spectroscopic follow-up, shows how unclear and blurry the distinction between dwarf galaxies and globular clusters is when we get to the boundary regions where they are not distinguishable any longer by their structural parameters. The location of Crater in the outer Milky Way halo means that the presence of dark matter in this object can be tested, as the tidal field of the galaxy has a much reduced influence at such distances, minimising the tidal effects on the stellar velocities ([Baumgardt et al. 2005](#)). With seven times the physical size of a typical GC and at the largest galactocentric distance of any GC in the MW halo, it is a unique system to study the formation and evolution mechanisms of ultra-faint dwarfs or intermediate-age, extended globular clusters at low metallicities.

In this paper, we present new radial velocity measurements of stars in Crater using the new IFU instrument MUSE on the VLT. We perform a detailed study of Craters stellar dynamics by increasing the sample size of likely member stars to 26. Simultaneously, the IFU data will allow us to characterise the chemical composition of the system, by analysing the abundances of absorption features in their spectra. This analysis of the chemistry of Crater will be published in a second work on this object. Throughout the paper we adopt



a distance to Crater of  $d = 145$  kpc, a magnitude of  $M_V = -5.3$  and a half-light radius of  $r_h = 19.4$  pc, unless otherwise noted. All these values are taken from the HST study of [Weisz et al. \(2015\)](#).

## 3.2 MUSE Observations

Crater was observed with MUSE ([Bacon et al. 2010](#)) mounted on UT4 of the VLT, during the night of March 13th 2015, under ESO programme Nr. 094.D-0880 (PI: Hilker). MUSE is an integral field spectrograph with a spatial sampling of  $0.2''$  and a spectral resolution between  $R=1500-3000$  along its wavelength coverage. We used the nominal mode of MUSE which covers the wavelength range of  $4750 - 9300$ . Three (out of four planned) pointings centered around Crater ( $R.A.[J2000] = 11:36:17.965$ ,  $\delta[J2000] = -10:52:04.80$ ), with  $2 \times 1400$  s each, were observed with the  $1 \text{ arcmin}^2$  field-of-view of MUSE. Each FOV covers Crater out to a spatial extent of roughly one half-light radius. Thus, the three observed pointings cover three quarters of the area within the half-light radius of Crater. In each observation the position angle of the spectrograph was rotated by  $90^\circ$  after the first 1400 s exposure. A dedicated sky field of 100s was taken after each observing block.

### 3.2.1 Data reduction process

The MUSE raw data were processed using version 1.0 of the provided ESO pipeline ([Weilbacher et al. 2012](#)). A master-bias, master-flatfield and a wavelength calibration were generated using the bias, flat and arc-lamp calibrations taken in the same night. The wavelength dependent line spread function was obtained from the calibration files.

Each exposure was bias subtracted and divided by the flatfield. The generated trace tables and the static geometric calibration, as well as the wavelength calibration, were then applied to the data cube. This calibrates the spectra to physical units of wavelength. The results of each basic reduction were then stored in separate *pixtables*, an intermediate product of the pipeline. These were then processed with the `muse_scipost` recipe. This recipe applies the on-sky calibrations to the *pixtables*. The astrometric calibrations of the two dimensional positions were applied, the sky was removed and the flux calibration was carried out in this step. This recipe stores one fully reduced *pixtable* for each of our 6 observations.

The 6 reduced *pixtables* were then merged into the final datacube using the MUSE `exp_combine` recipe of the pipeline. For this recipe the offsets of each exposure were provided manually, as the pipeline is not able to correct slight positional offsets automatically when the observations involve a position angle rotation of  $90^\circ$ . The position cross-correlations between exposures were provided by fitting the 5 brightest point sources in the FOV of each exposure with a Gaussian function. We then used the weighted mean of the position offsets as the geometric shifts provided to the pipeline. This recipe delivered a final three dimensional datacube with the science data in the first extension of the fits file, and an estimate of the noise in the second extension. The final MUSE cube, collapsed



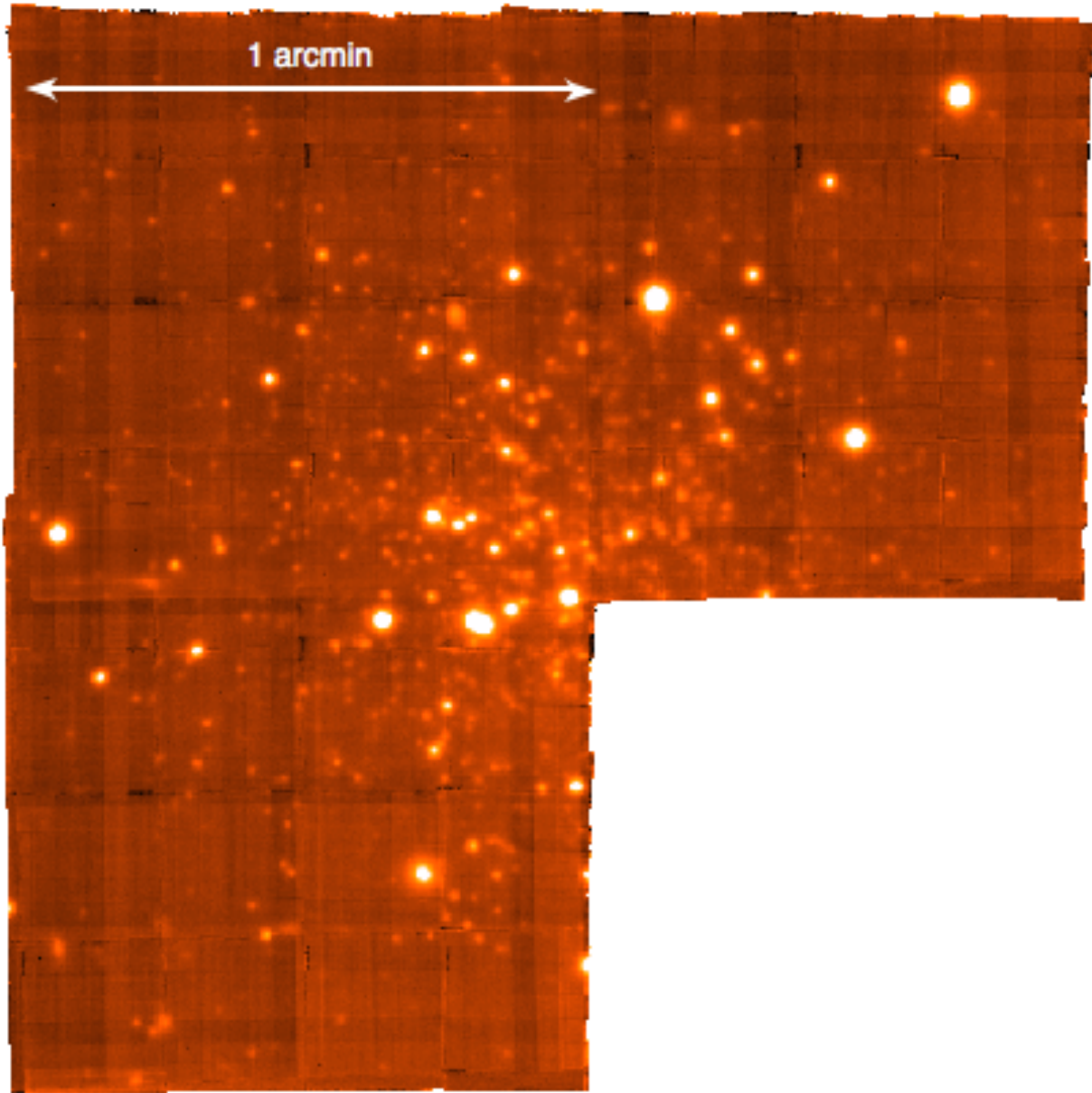


Figure 3.1: White light image of the final Crater MUSE cube for which all 6 observations have been combined. The cube is collapsed along its spectral axis. The image is oriented with north oriented towards the top and east towards the left.

along its spectral axis, is shown in Fig. 3.1.

### 3.2.2 Absolute velocity calibration

The wavelength calibration for MUSE cubes is performed directly by the pipeline using the provided arc lamp spectra. The pipeline corrects for systematic wavelength shifts between the arclamp lines and the observed sky lines by using the strong sky lines at 5577 Å and 6300 Å. This correction is propagated linearly to the rest of the spectrum, as to get rid of the wavelength dependency of this correction. It is unknown how well this linear propagation of the corrections holds in the Ca triplet wavelength range.

As we use the near infrared Ca II triplet to measure the radial velocities, and the velocity calibration of the pipeline was done at another wavelength range, we perform our own calibration to get rid of any leftover wavelength dependencies of the correction. For this precise velocity calibration we used a set of bright OH sky lines, located at the same wavelength range as the Ca II triplet.

For that we generated a MUSE cube similar to the original reduction except for not subtracting any sky and turning off the heliocentric velocity correction. From this cube we extracted the same spaxels corresponding to the position of our stars and co-added them, in the same fashion as was done for the science spectra. These sky spectra at the positions of our sources are then fitted with a model of the brightest OH sky-lines in that wavelength range. We brought the model OH spectra to the same resolution as the MUSE spectra. The precise restframe wavelengths of the OH line model was taken from the UVES sky emission catalog (Hanuschik 2003). An example of the combined model of 13 OH lines is shown in blue in the top panel of Fig. 3.2. As MUSE spectra are undersampled with a FWHM of 2.4 and a sampling of 1.25/pix of the spectral axis, our model includes several sky lines, which are then simultaneously fitted to the spectra, in order to be not affected by the undersampling of a single line. Thus the only free parameter of the final fit is the wavelength shift.

The velocity calibration of the MUSE spectra can vary from spaxel-to-spaxel across the entire field of view of the instrument. This variance of the sky line velocities is plotted in the bottom panel in Fig. 3.2. It illustrates why we cannot assume one absolute velocity calibration for all our stars. The analysis of the separate spaxels of the sky cube has been done in the same way as outlined above, shifting the sky model in wavelength direction. Due to the variance across the FOV we co-add the spaxels at the position of our sources and then derive the velocity calibration from those spectra. The velocity correction factors for the stars have a mean of  $\langle v \rangle = 0.8835 \text{ km s}^{-1}$ .

Above we outlined how we estimated the velocity correction factor. The pattern across the field is of systematic nature caused by applying a wavelength solution taken during day calibrations at different times/temperatures of the instrument. The measurement and application of the velocity correction factor assumes implicitly that the original wavelength solution has no uncertainty in the first place. However, this is not the case and there are always some deviations in the wavelength solution, which we need to determine from the arc lamp exposure itself. This is the final systematic velocity error since we took the velocity

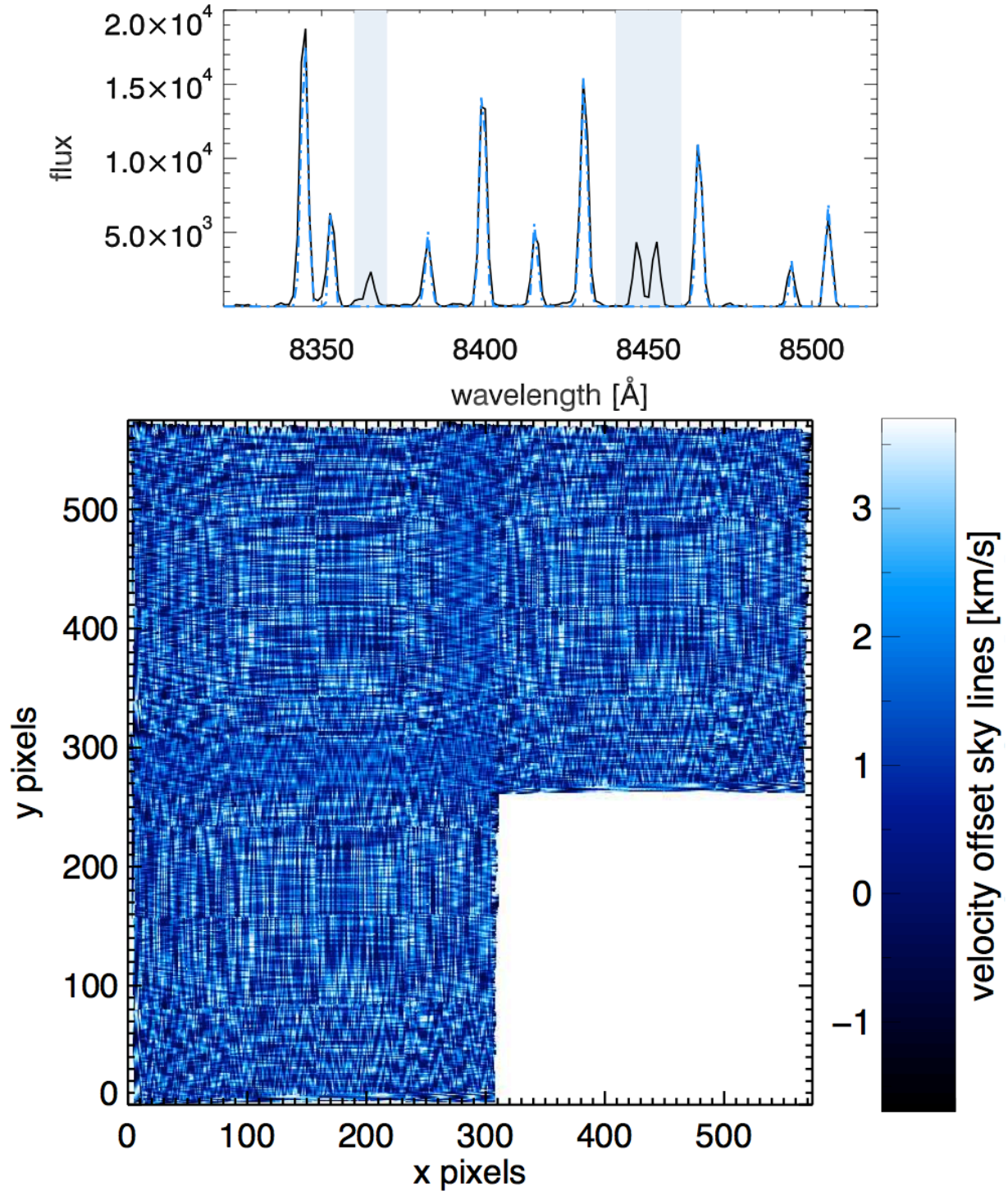


Figure 3.2: Top panel: The spectrum of the sky emission lines in the Ca triplet wavelength region for the co-added spaxels of the position of star 2. The shifted sky line model is shown in blue. The two shaded regions are excluded from the fit. Bottom panel: The observed MUSE FOV with a colour coding for the velocity corrections. The velocity offset is inferred from the sky lines and determined for each spaxel separately.

offsets into account that occur when applying the wavelength solution to the science data taken at different conditions.

To constrain the systematic errors we used a MUSE observation of a neon arc lamp, for which we applied a self-calibration by reducing it as a science frame. No radial velocity offset needs to be taken into account since calibration and data are matched in time and conditions. This reduced arc lamp frame was then analysed using a similar method which was used to measure the final radial velocities. We use 7 lines in the neon spectrum in the same wavelength range as the NIR Ca II triplet (see top panel Fig. 3.3). This neon model is then fitted to the spectra of each of the  $314 \times 304$  spaxels in the MUSE cube. An example for one such fit is given in the top panel of Fig. 3.3. The histogram of this procedure is shown in the bottom panel of Fig. 3.3. We fitted a Gaussian distribution to the histogram. The sigma of the Gaussian is  $\sigma = 2.27 \text{ km s}^{-1}$ . This width of the distribution of the systematic velocity error is the intrinsic accuracy of the wavelength solution and also represents the uncertainty for the velocity correction factor. This error is therefore our final instrumental velocity uncertainty which is quadratically added to the error deduced from the signal-to-noise of the spectra.

### 3.2.3 Extraction of stellar spectra

As a first step we need to extract the spectra of each star from the three dimensional cube for further analysis. Within a crowded field we have to locate the sources and deblend them if they overlap. To extract the spectra of a point source in an IFU we have to select the spaxels that correspond to a point source and co-add them into a one dimensional spectrum. To do this in an optimal way we have to take into account that the point spread function (PSF) changes with wavelength and is smaller at larger wavelengths.

For that we use the PAMPELMUSE software package (Kamann et al. 2013). This software is optimised to analyse integral-field spectroscopy data of stellar fields, by modelling the wavelength dependence of the PSF and then extracting and co-adding spaxels into one dimensional spectra. To run PAMPELMUSE an input catalogue of source positions and an estimate of their initial magnitudes is required, for which we used the photometry of Belokurov et al. (2014). As a first step, PAMPELMUSE identifies sources from the initial catalogue for which it can extract spectra and cross correlates their catalogue positions with the most likely positions within the MUSE field-of-view. The results of this correlation are displayed interactively, and after investigation the user can redo or accept the positions of the detected point sources.

After a successful position cross correlation, the pipeline continues with the actual source selection. Only those sources above the limiting photometric magnitude, with a  $S/N > 3$  and a minimum separation of  $0.3 \text{ FWHM}$  widths from other bright sources are extracted as single sources. The faint sources that are below the  $S/N \sim 3$  limit are also extracted, and co-added into one combined "unresolved" spectrum.

The extraction of accurate point source spectra from IFS data cubes including the wavelength dependent size is done by the CUBEFIT routine in PAMPELMUSE. It fits an analytic Gaussian or Moffat profile to each wavelength slice of the data cube for the

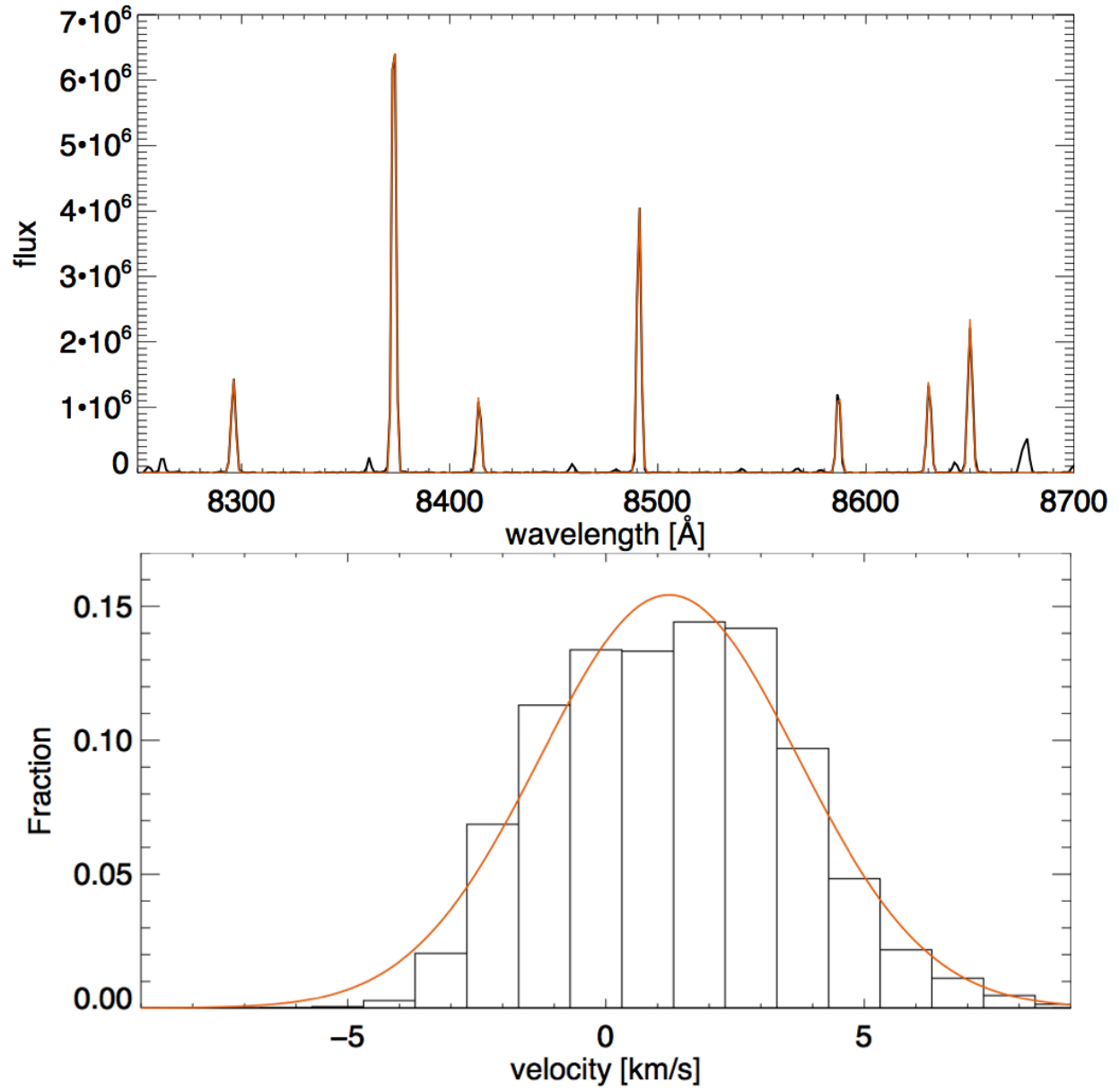


Figure 3.3: Top panel: The spectrum of the neon arc lamp in the Ca II triplet wavelength region, for one example spaxel. The fitted arc line model is shown in red. Bottom panel: The histogram of the arc lamp velocity measurements in each of the spaxels of the MUSE arc lamp cube. Overplotted in red is the best fit Gaussian model with a width of  $\sigma = 2.27 \text{ km s}^{-1}$



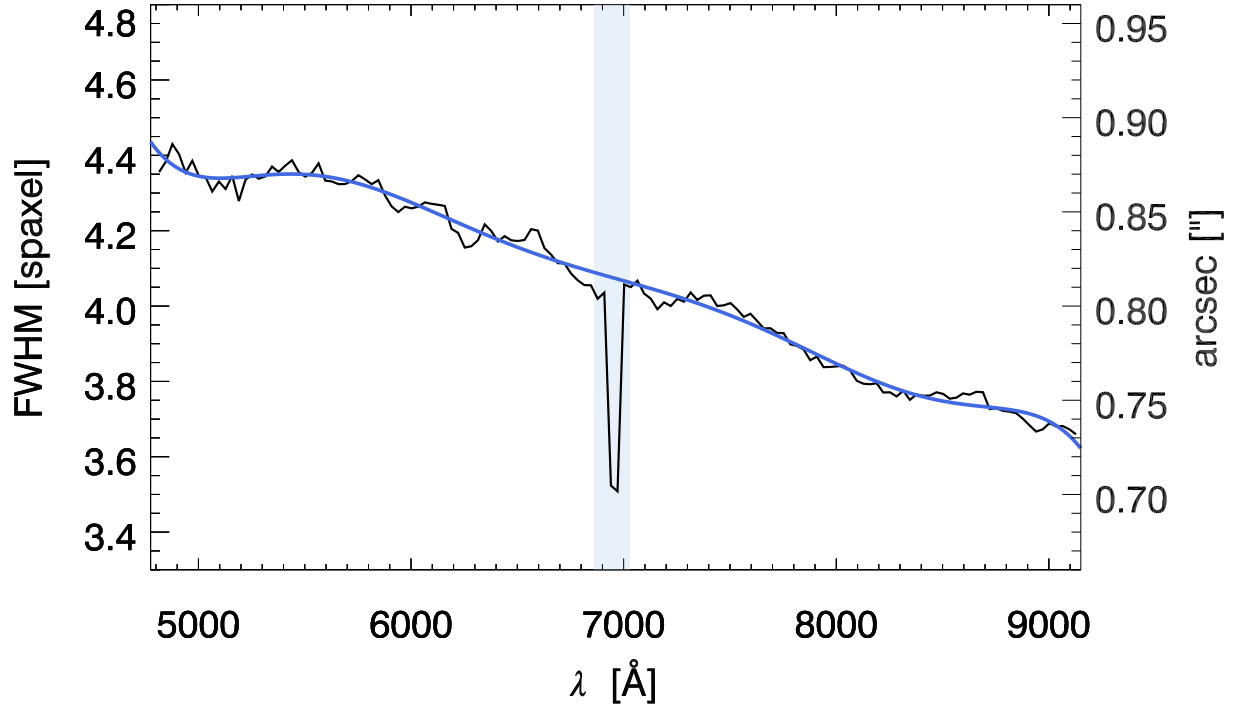


Figure 3.4: FWHM of the point spread function for each wavelength slice in the MUSE cube. The FWHM value was determined using a Moffat fit to the brightest stars in the field as determined by PAMPELMUSE. In blue a Hermite Polynomial of 7-th order fitted to the data is shown. The shaded region is an area of strong telluric absorption and was excluded from the fit.

brightest stars in the field of view. As a Gaussian PSF profile can underestimate the wings of the PSF, we chose a Moffat profile for our modelling.

The wavelength dependent FWHM of the PSF at each slice of the wavelength range is plotted in Fig. 3.4 as a black line. It was then fitted with a Hermite polynomial of 7th order, which is plotted in blue in Fig 3.4. The blue shaded wavelength region is a strong telluric absorption band. It was excluded from the polynomial fit. In a last step PAMPELMUSE stores each extracted one dimensional spectrum and the corresponding noise spectrum in a separate fits file that can be further analysed. We extracted a total of 41 spectra above the  $S/N > 3$  cut-off and one co-added spectrum of the unresolved sources. The position, magnitude, and colour of these point sources are shown in table B.1. We extracted spectra in a magnitude range from  $i = 17.3$  mag down to  $i = 22.1$  mag.

### 3.2.4 Radial velocity measurements

We measure the radial velocities using the three strong and prominent absorption lines of the Ca II triplet in the NIR part of the spectra. These lines at 8498, 8542, and 8662 Å are excellent for determining the velocity of our stars, as they are strong features that are well

resolved by medium resolution spectroscopy.

We measure the most likely velocities of our stars by using a model Ca II triplet spectrum at rest wavelength, which is then fit to the observed spectrum by shifting in radial velocity. The model Ca II spectrum was constructed using a MILES Ca II spectrum (Cenarro et al. 2001) with the properties  $T_{\text{eff}} = 4750$  K,  $\log(g) = 1.25$ ,  $[\text{Fe}/\text{H}] = -1.7$  dex with a spectral sampling of  $1.25 \text{ \AA}$ , and a spectral resolution FWHM of  $2.4 \text{ \AA}$ , similar to the MUSE instrumental values. We fitted the full Ca II MILES library to the spectrum of star 2, to determine a best fit model. The stellar parameters of the best fit model comparable well to those found for Crater stars in Bonifacio et al. (2015). The final model spectrum was constructed by fitting three Gaussian absorption lines to the original MILES spectra simultaneously, while the centre of the lines was fixed to the precise velocity of the Ca II features.

To have robust estimates of the velocity errors introduced by the noise of the spectrum, we ran a Monte Carlo procedure where each stellar spectrum is resampled 400 times using the uncertainty of the spectrum. These resampled spectra are then each again fitted with the model Ca triplet spectrum. The distribution of the determined radial velocities of each star was then fitted with a Gaussian function to determine its  $1\text{-}\sigma$  errorbar. An example of such a Gaussian function for star number 2 is shown in figure 3.5. The spectra were already corrected to the heliocentric rest frame by the reduction pipeline, and they were continuum normalised by dividing them with the best-fit third degree polynomial. The polynomial fit was carried out for each spectrum in the wavelength range between  $8350 \text{ \AA}$  and  $8900 \text{ \AA}$ . We applied a  $2.5\sigma$  clipping to our spectra in order to identify those wavelength regions dominated by continuum emission (as opposed to absorption lines). We then approximated the continuum by fitting a polynomial.

The derived noise uncertainty takes into account the error introduced by the noise of the spectrum, but not the error introduced by the systematics of the instrument, the undersampling or the local fitting process. The precision to which we can determine velocities with MUSE was determined in section 3.2.2. Using an arc lamp frame we found that the error introduced by the systematics, and thus the maximum precision of velocities derived from our MUSE data, is  $2.27 \text{ km s}^{-1}$ . As the error of the noise and the systematic error are independent from each other, we quadratically add the systematics and S/N errors of each extracted spectrum to arrive at a total uncertainty estimate. The typical uncertainties of our velocities are in the range of  $2.3 - 5 \text{ km s}^{-1}$  for the brightest stars with  $m_I < 20.0$  and between  $5 - 15 \text{ km s}^{-1}$  for the fainter stars. A complete list of every star, its position, magnitude, colour and radial velocity is given in Table B.1 in the appendix.

In Figure 3.6 the two dimensional position distribution of the stellar velocities is shown. Stars with a velocity between  $125$  and  $175 \text{ km s}^{-1}$  are colour coded according to their velocity. Stars with measured velocities outside this velocity range are plotted in dark black. Photometric measurements of stars in the FOV of Crater from the catalogue of Belokurov et al. (2014) in the magnitude range  $17.0 < I_{\text{mag}} < 26.0$  are shown as grey dots. The size of the coloured circles is a representation of their velocity uncertainty. One visible feature in the spatial distribution of the stars is the agglomeration of many stars close to the centre of Crater (marked by the black plus sign) with velocities close to the systemic

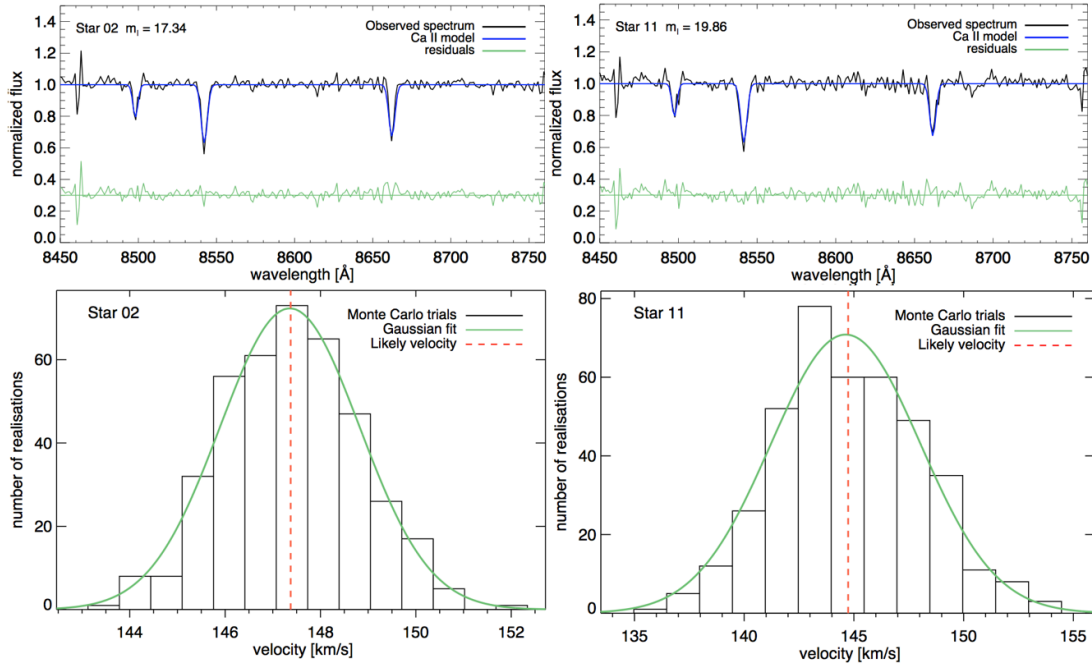


Figure 3.5: **Top left:** Continuum normalised spectrum of the Ca II region of star 2. The velocity shifted Ca II template spectrum is shown in blue, and in green the residuals of the fit are shown (offset by 0.3 for visibility). **Top right:** Same as the left panel but for star 11 which is 2.5 magnitudes fainter than star 2. **Bottom left:** The black velocity histogram shows the realisation of 400 Monte Carlo trials for star 2, when we added noise to the spectrum and then refitted the template. The green line is the best fit Gaussian, and the red dashed vertical line marks the most likely velocity, derived from the fit to the original spectrum. **Bottom right:** Same as the left panel but for star 11.



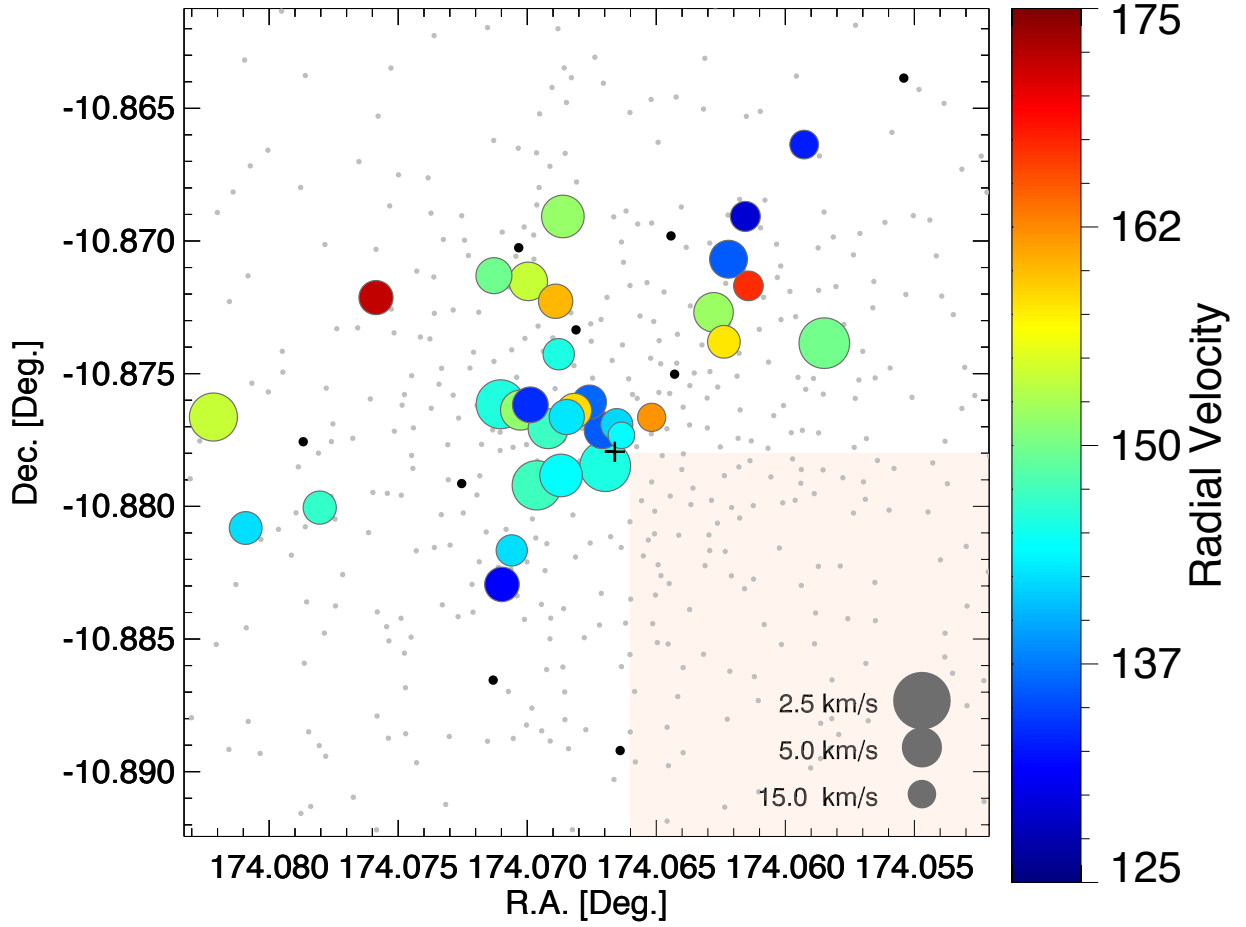


Figure 3.6: Position distribution of Crater stars with a measured velocity. The coloured circles represent the extracted stars, colour coded according to their radial velocity between  $125$  and  $175 \text{ km s}^{-1}$ . Stars that have a measured velocity below or above the colour coding limits are shown as black points. The larger the size of the coloured circles, the lower the derived uncertainty of the velocity measurement. The small grey dots represent all other stars in the Crater region between  $17.0 < I_{mag} < 26.0$  from [Belokurov et al. \(2014\)](#). The shaded region marks the area that was not observed with MUSE

Table 3.1: Stellar radial velocities compared to those in the literature.

	velocity this work (km s <sup>-1</sup> )	Index Kirby et al.	velocity Kirby (km s <sup>-1</sup> )	Index Bonifacio et al.	velocity Bonifacio et al. (km s <sup>-1</sup> )
2	147.37 ± 2.63	1710	143.6 ± 4.5	-	-
5	149.94 ± 2.43	420	149.8 ± 1.5	J113615-105227	144.3 ± 4.0
7	154.17 ± 2.83	399	155.3 ± 1.8	-	-
8	145.64 ± 2.40	93	147.2 ± 1.6	J113615-105244	134.1 ± 4.0
19	146.56 ± 8.14	1684	150.9 ± 3.1	-	-

This table lists the identifier of our work, the RA and DEC, the radial velocity from our sample and its errors. In column 3 the identifier from Kirby et al. (2015) is listed, and column 4 lists their velocities with errors. Column 5 and 6 list the respective values for the two stars from the Bonifacio et al. (2015) sample.

velocity of Crater. It is notable that stars located farther away from Crater show larger differences to the systemic velocity, but their measurement errors are also larger.

### 3.2.5 Comparison to other velocity measurements of Crater stars

In this section we compare our velocity measurements for Crater stars with the two existing samples in the literature. In Fig. 3.7 the radial velocities from the literature are plotted against the values we measure in this work. In total, 5 member stars from our sample are also present in Kirby et al. (2015). Both stars that were measured in Bonifacio et al. (2015) are present in all three samples. As is easily visible from the plot, our measurements are in overall very good agreement with the values given in the Kirby et al. 2015 sample. Interestingly, for star 7, which is the blue star with ambiguous membership, the independent measurement and our value are in excellent agreement. Therefore it is likely that the radial velocity of this star is genuinely high.

The two original velocities from the Bonifacio et al. 2015 sample (filled orange circles Fig. 3.7) are outliers compared to our measurements. They are systematically lower than our values as well as those from Kirby et al. 2015. Our velocity of star 5, which is in all three samples, agrees very well with the Kirby et al. 2015 value, but not with the Bonifacio et al. 2015 value, which is significantly lower. This is also true for star 8 from of our sample which was also measured by both previous spectroscopic studies. While the Kirby et al. 2015 value is consistent with ours, the Bonifacio et al. 2015 value is a 3 –  $\sigma$  outlier to both measurements. The radial velocities of stars that appear in our sample and the literature are summarised in table B.1.

The large discrepancy of the two Bonifacio et al. values could also be due to a systematic

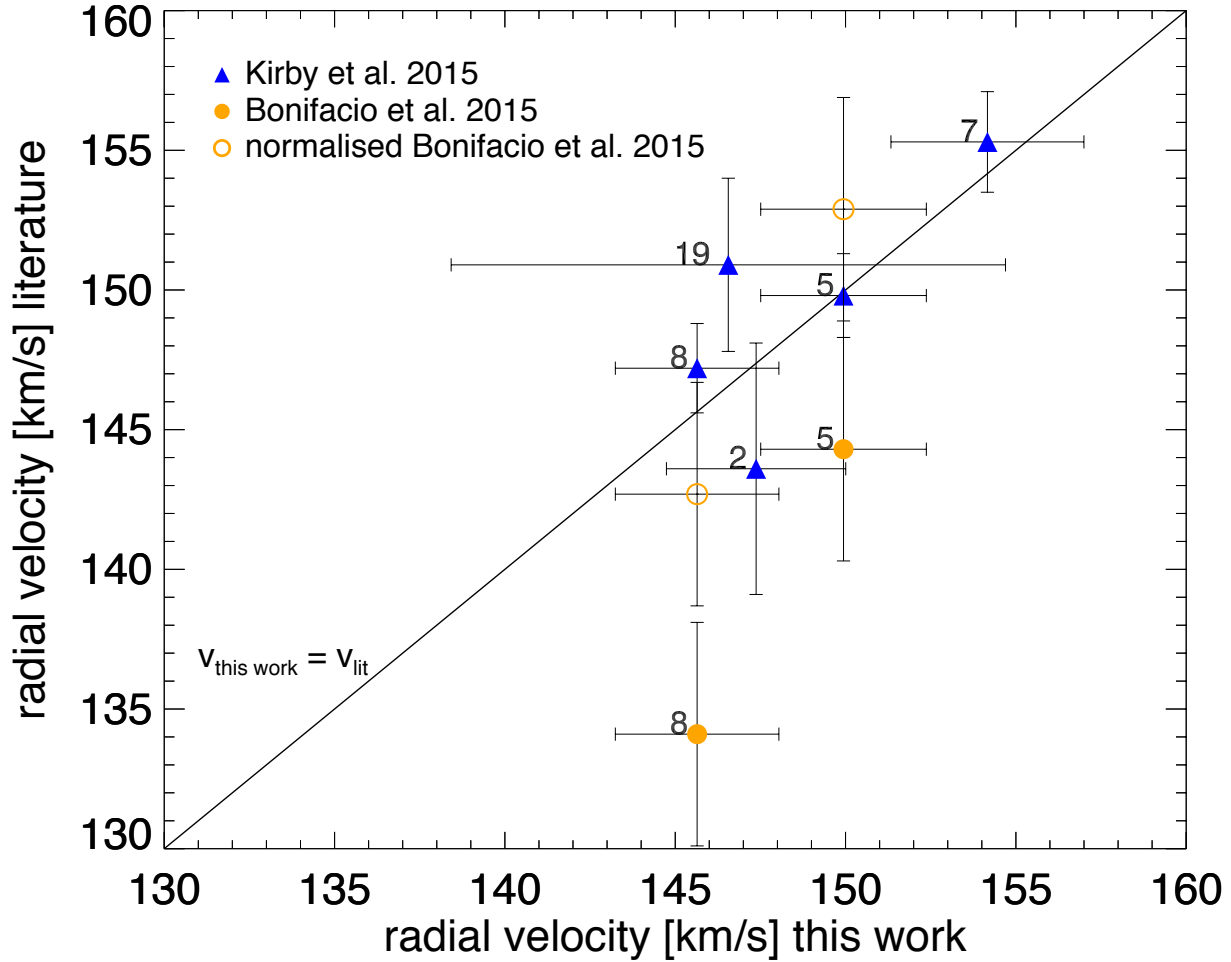


Figure 3.7: Comparison of stellar radial velocities with existing literature samples. On the x-axis our measurements are denoted and on the y-axis those from the literature. Blue triangles represent the values for the stars that were also measured in Kirby et al. (2015), and filled orange circles denote the two stars measured in Bonifacio et al. (2015). The numbers next to the data points are the identification numbers from our sample (see Table B.1 in the appendix). As there might be a systematic velocity offset in the Bonifacio sample, we also plot the open orange circles, which are the shifted Bonifacio velocities. They are shifted in such a way that they have the same mean velocities as stars 5 and 8 from our dataset. Stars 5 and 8 have velocity measurements in all three datasets.

velocity offset compared to our sample. Thus we renormalised the average velocity of both stars to the average velocity of those stars in our sample (open orange circles in Fig. 3.7). While the corrected velocities are now less significant outliers, the velocity difference between star 5 and 8 of  $10 \text{ km s}^{-1}$  remains much larger than the difference of  $4 \text{ km s}^{-1}$  in our sample and  $2.5 \text{ km s}^{-1}$  in the Kirby sample.

We also investigated when these observations were taken to determine if this could be radial velocity variations due to a binary star. Our observations were taken on March 13th 2015, the ones of Kirby on March 23rd 2015 and the ones of Bonifacio on March 22nd 2015 (as listed in the ESO Archive). Therefore we can exclude a real radial velocity variation, as the time delay between the Kirby et al. and Bonifacio et al. observation is a single day, and the difference to ours are 9 days. A binary is expected to have radial velocity variations on the order of a year. Thus we conclude that the most likely velocity of star 8 is consistent with the systemic velocity of Crater, and it is not a velocity outlier. Hence we suggest that the 95% confidence level lower velocity dispersion limit of  $\sigma > 3.9 \text{ km s}^{-1}$  by Bonifacio et al. based on the velocities of two stars only is likely wrong.

### 3.3 Probability based analysis of membership

#### 3.3.1 Membership probability

To determine which stars are members of Crater we have to distinguish them from foreground or background contaminants using our velocity, spatial, and colour information. Instead of making hard cuts for velocity, position, and CMD values we decided to follow a probabilistic method to statistically assess which stars are likely members. We base our method on what has been described in Collins et al. (2013) who investigated radial velocity measurements for 18 dwarf galaxies in Andromeda. The probability of each star to be a member is given as:

$$P_n = P_{\text{vel}} \cdot P_{\text{dis}} \quad (3.1)$$

where  $P_{\text{vel}}$  denotes the probability of membership based on the radial velocity of each star, whereas  $P_{\text{dis}}$  is the term that denotes the probability of membership based on the distance to Crater's centre. In contrast to what has been done in Collins et al. (2013) we do not include a term  $P_{\text{CMD}}$  which penalises the probability of stars that are far from the red giant branch of the cluster CMD. This is done to avoid that the potential blue member stars are penalised, as they do not lie on the RGB.

The  $P_{\text{dis}}$  term of our probability function is based on the known radial profile of Crater. We model the probability with a normalised Plummer profile with a half-light radius  $r_h = 0.46'$  (Weisz et al. 2015). The posterior probability term  $P_{\text{dis}}$  can be written as:

$$P_{\text{dis}} = \frac{1}{\pi \cdot r_h^2 [1 + (r/r_h)^2]^2} \quad (3.2)$$

The probability term  $P_{\text{vel}}$  is determined by assessing how probable it is that a star is either part of the foreground Galactic contamination or a member of Crater. For this we

use the velocity histogram of our measured velocities and model a Gaussian to Craters velocity peak as well as to the foreground distribution. As we have only a very sparse sampling of the foreground stellar population, we use the Besançon galaxy model (Robin et al. 2003) to determine the expected shape of the velocity distribution of the Galactic foreground at the Galactic longitude and latitude of Crater. We retrieved the Galactic foreground velocity distribution from the Besançon model for a FOV 10 times the size of the MUSE field, then normalise it to the same area. With this we ensure to have reliable number statistics on the foreground distribution. We choose to approximate the Besançon foreground distribution with a broad Gaussian model. The central velocity and the width of the foreground distribution, as derived from the Besançon model, are then used as fixed parameters of the foreground model when we decompose the observed data in foreground and Crater component. The systemic velocity of the Galactic contamination (red histogram in Fig. 3.8) is found to be  $v_{r,gal} = 153.1 \text{ km s}^{-1}$  with a velocity dispersion of  $\sigma_{v,gal} = 131.3 \text{ km s}^{-1}$ .

The measured velocities (blue histogram in Fig. 3.8) were then fitted with the sum of two Gaussians, one for the Crater velocity and one for the Galactic foreground. Although the Galactic foreground has its central velocity close to the Crater peak velocity, the level of Galactic contamination of 0.3 stars per velocity bin is small. The kinematic peak of Crater is clearly visible as a spike at  $v_r = 148 \text{ km s}^{-1}$  on top of the Galactic foreground. The probability of each star to be a member of the Crater system is then given as:

$$P_{n,crater} = a_{0,crater} \cdot \exp \left[ -\frac{1}{2} \frac{(v_n - v_{r,crater})^2}{\sigma_{v,crater}^2 + v_{n,err}^2} \right] \quad (3.3)$$

where the fitting of the double Gaussian has found the systemic velocity to be  $v_{r,crater} = 147.9 \text{ km s}^{-1}$  and a dispersion of  $\sigma_{v,crater} = 4.47 \text{ km s}^{-1}$ . To calculate the probabilities of membership of the single stars we also take into account the velocity error of each single star adding the  $v_{n,err}^2$  term to the Gaussian. The galactic foreground component was modelled as:

$$P_{n,gal} = a_{0,gal} \cdot \exp \left[ -\frac{1}{2} \left( \frac{v_n - v_{r,gal}}{\sigma_{v,gal}} \right)^2 \right] \quad (3.4)$$

where the systemic velocity of the foreground is given as  $v_{r,gal} = 153.1 \text{ km s}^{-1}$  with a broad width of the Gaussian distribution of  $\sigma_{v,gal} = 131.3 \text{ km s}^{-1}$  and a central height of the Gaussian of  $a_{0,gal} = 0.38$ .

With the results from fitting a double Gaussian distribution to our data, each star can then be assigned a probability  $P_{vel}$  to be a member of Crater by dividing the probability to be a member of Crater by the sum of probabilities to belong to the galactic foreground or to Crater:

$$P_{vel,n} = \frac{P_{n,crater}}{P_{n,crater} + P_{n,gal}} \quad (3.5)$$

The assigned membership probabilities for all stars with a MUSE spectrum are displayed in Fig. 3.9 as colour coding in the colour magnitude diagram (CMD). The *i*-band magnitude and *g* – *i* colour photometry are based on data from Belokurov et al. (2014).

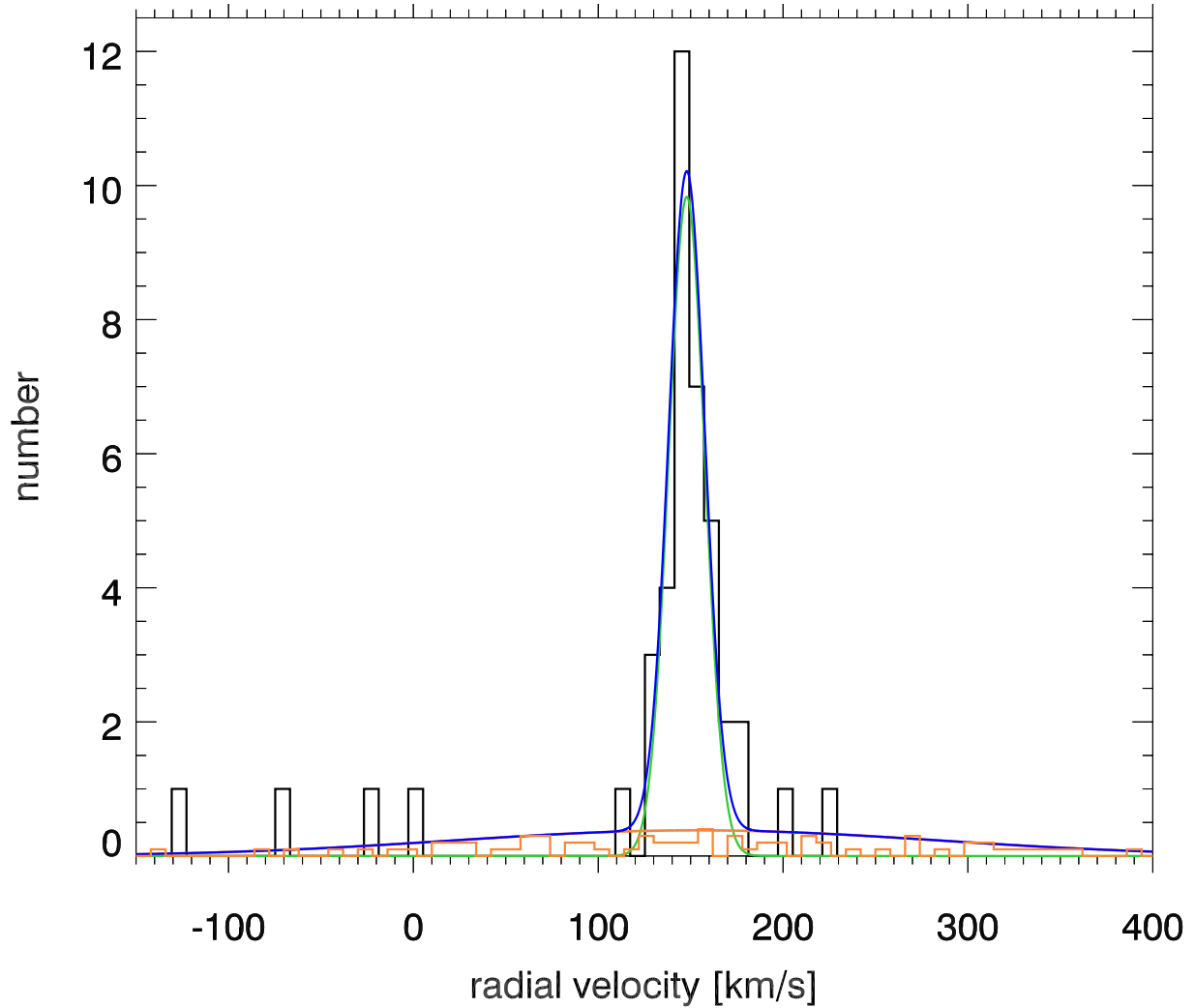


Figure 3.8: The velocity histogram for all observed stars in the MUSE field of view is shown in black. The strong peak of stars at  $v=148$  km/s is the systemic velocity of Crater, which clearly dominates our histogram. There are only few obvious foreground and background stars. The Besançon foreground stars are shown as orange histogram. The simultaneous double Gaussian fit is shown as a blue curve and the results for the Crater population and foreground population are shown as green and orange Gaussian curves, respectively.

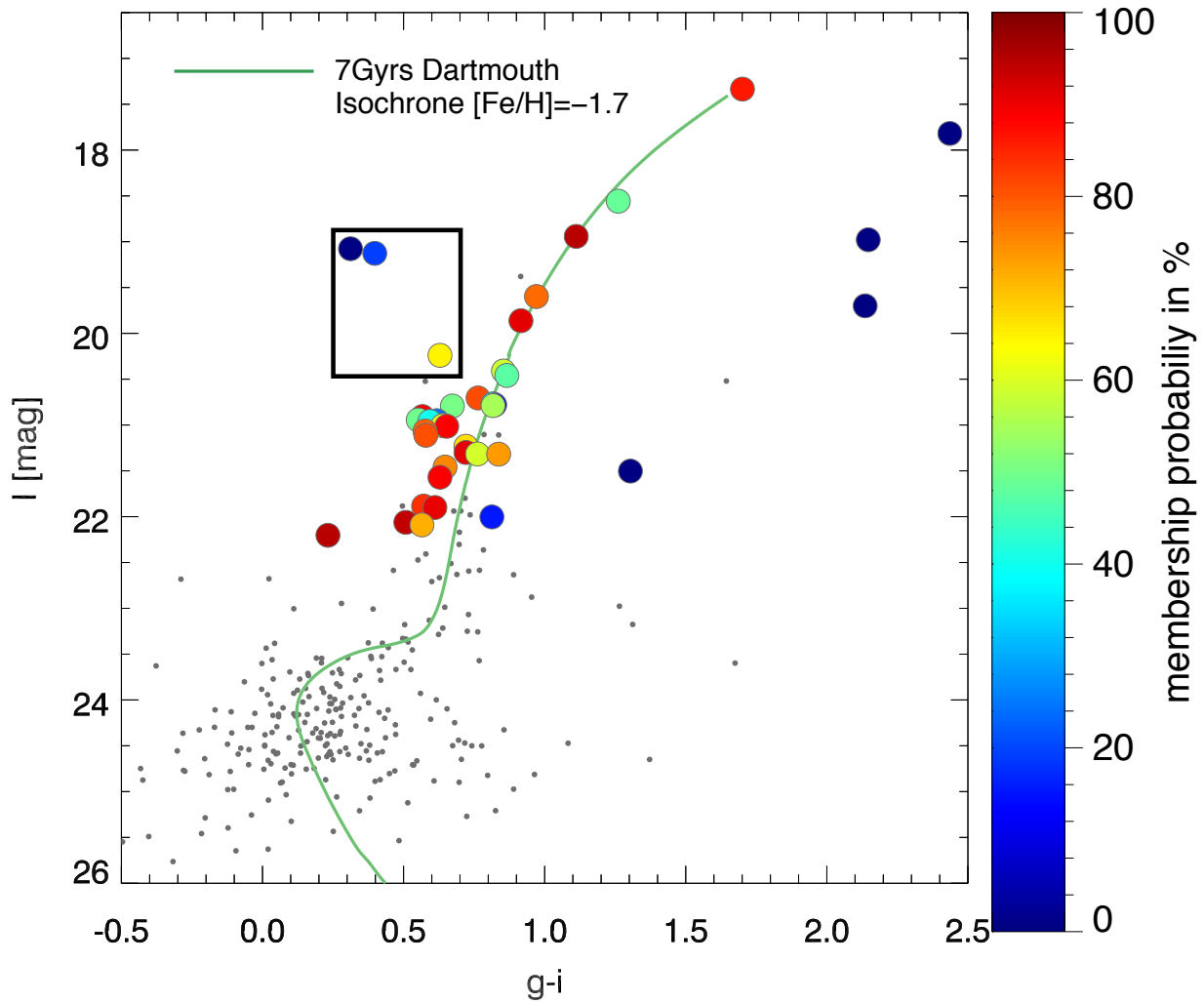


Figure 3.9: Crater CMD with stars for which we have a MUSE spectrum plotted as coloured points. All other stars are plotted as grey dots. The stars are colour coded according to their total membership probability. A Dartmouth isochrone with an age of 7 Gyr and  $[Fe/H]=-1.7$  dex is plotted as green curve.

In the CMD it is clearly visible that the probability method works reasonably well, assigning very low probabilities to clear non-members in the CMD, e.g. stars offset from the RGB. The red giant branch (RGB) and the red clump are well populated with stars with a high membership probability. Notably, there are four stars above the red clump and blue-wards of the RGB, for which three have a spectrum and thus an assigned probability (CMD area marked with a black box). These have been noted as a potential intermediate age population in [Belokurov et al. \(2014\)](#). The star marked in dark blue has  $P_n = 10^{-17}$  due to its velocity of  $v = 222.3 \pm 3.67 \text{ km s}^{-1}$  and is thus a clear non-member. For the two other stars the case is less clear. Right next to the non-member star in the box, star 7 is marked with a lighter shade of blue. It has a membership probability of  $P_n = 0.20$ . This relatively low probability is caused by its spatial position at one half-light radius from the centre and by the radial velocity of  $v_r = 154.17 \pm 2.8 \text{ km s}^{-1}$  that is a  $2\sigma$  outlier from the systemic velocity of Crater. Therefore, it seems possible that this star with a relative velocity of  $\Delta v = 6.5 \text{ km s}^{-1}$  is bound to Crater. Considering its position at roughly one half-light radius,  $52''$  from the centre, it is also possible that this is an unbound star that was recently stripped from the system. The third blue star with uncertain membership is star 13 marked by the yellow point within the black box in Fig. 3.9. It has a probability of 64.9% to be a member of Crater. With its radial velocity of  $v_r = 151.6 \pm 4.8 \text{ km s}^{-1}$  it is consistent within  $1\sigma$  of Crater's systemic velocity and its location at roughly half of the half-light radius makes it likely that it is a member star. Another notable feature is the blue faint star at  $g - i = 0.23$ , located above the expected main sequence turn-off in the expected blue straggler region. Although this is the faintest star, for which we were still able to extract a spectrum, and thus its radial velocity measurement has a high uncertainty, it has a very high membership probability of  $P=95\%$  making it a likely member.

### 3.3.2 Likelihood analysis

To determine the systemic velocity and the velocity dispersion of Crater, we follow the Bayesian maximum likelihood technique as used in [Collins et al. \(2013\)](#) and established in [Martin et al. \(2007\)](#). For this we use the posterior probability of each star being a member of Crater as a weight in the likelihood function. To determine which set of  $[v_r, \sigma_v]$  parameters maximises the likelihood function, we sample a fine grid in parameter space. The  $1000 \times 1000$  grid covers a range of  $0\text{--}14 \text{ km s}^{-1}$  for the velocity dispersion and  $135\text{--}160 \text{ km s}^{-1}$  for the systemic velocity. The log likelihood function that we are maximising can be written as:

$$\log(\mathcal{L}(v_r, \sigma_v)) = - \sum_{n=0}^N \left[ P_n \log \sigma_{\text{tot}} + \frac{1}{2} P_n \left( \frac{v_r - v_n}{\sigma_{\text{tot}}} \right)^2 + P_n \log(2\pi) \right] \quad (3.6)$$

Here  $N$  is given by the total number of stars for which we measured a radial velocity,  $v_n$  is the radial velocity of each star, and  $P_n$  is the posterior probability of the  $n$ -th star to be a member. The term  $\sigma_{\text{tot}} = \sqrt{\sigma_v^2 + v_{n,\text{err}}^2}$  includes the velocity error for each star. With this way of measuring the intrinsic velocity and dispersion we can discriminate the intrinsic



velocity dispersion of the object from the one introduced by the errors of the single velocity measurements. The errors of the velocity measurements are the quadratically added signal-to-noise errors and the systematic uncertainty of  $2.27 \text{ km s}^{-1}$ .

## 3.4 The kinematics of Crater

### 3.4.1 Velocity dispersion and M/L

We applied the previously described maximum likelihood analysis to our sample stars, using the posterior probabilities from Sec. 3.3.1 as weights for the individual stars. We applied a two dimensional grid of the systemic velocity  $v_{\text{sys}}$  and the velocity dispersion  $\sigma_v$  to determine the parameter set that maximises our likelihood function  $\mathcal{L}(v_r, \sigma_v)$ .

The two dimensional distribution of the normalised likelihood for the grid of  $\sigma_v$  and the systemic velocity  $v_{\text{sys}}$  is shown in the left panel of 3.10. The coloured sigma contours are the likelihood levels corresponding to the sigma levels of the systemic velocity, which has an almost symmetric likelihood distribution. We use the mean of the lower and upper velocity error, which is  $1.11 \text{ km s}^{-1}$  to trace the likelihood levels that correspond to the noted 0.5, 1.0, 1.5, 2.0, 3.0 and  $5.0\sigma$  levels. The explicit likelihood levels that are traced by this method are 0.9641, 0.8640, 0.7196, 0.5571, 0.4009, 0.2682 and 0.0258 in increasing order of sigma contours. The marginalised one dimensional likelihood distributions for both values are shown in the two right-handed panels. The most likely values are indicated with a vertical line, as well as their  $1\sigma$  uncertainties with dashed lines.

The set of values that maximises the likelihood is given as:  $v_{\text{sys}} = 148.18_{-1.15}^{+1.07} \text{ km s}^{-1}$  and  $\sigma_v = 2.04_{-1.06}^{+2.19} \text{ km s}^{-1}$ . We are able to resolve the velocity dispersion with our full sample and a dispersion of 0 is excluded with a confidence of almost  $2\sigma$  at the lower end. Also we can exclude a velocity dispersion of  $\sigma_v > 6 \text{ km s}^{-1}$  with 2 sigma confidence. The larger uncertainty of the dispersion towards higher values is due to several stars that are velocity outliers and have medium or low probability to be members and thus their contribution to the likelihood function does not vanish.

We tested how robustly our routine handles velocities with large uncertainties, of which we have several in our sample. Thus we reran the determination of the velocity dispersion, limiting our sample to stars with  $v_{\text{err}} < 15 \text{ km s}^{-1}$ ,  $v_{\text{err}} < 10 \text{ km s}^{-1}$  and  $v_{\text{err}} < 7 \text{ km s}^{-1}$ . The systemic velocity and the dispersion of Crater change only marginally when excluding low S/N stars. The values are all compatible with the values for the full sample within their uncertainties. The derived velocity dispersions and the amount of included stars are:

- $\sigma_{\text{err} < 15 \text{ km/s}} = 2.06_{-1.06}^{+2.2} \text{ km s}^{-1} \quad \text{N}=35$
- $\sigma_{\text{err} < 10 \text{ km/s}} = 2.06_{-1.05}^{+2.1} \text{ km s}^{-1} \quad \text{N}=29$
- $\sigma_{\text{err} < 7 \text{ km/s}} = 2.16_{-1.03}^{+2.5} \text{ km s}^{-1} \quad \text{N}=20$

This shows that the determination of our systematic errors and the S/N errors using Monte Carlo resampling are a reliable estimate of our uncertainties, as the derived  $v_{\text{sys}}$  and  $\sigma_v$  are stable when including or excluding low S/N stars.

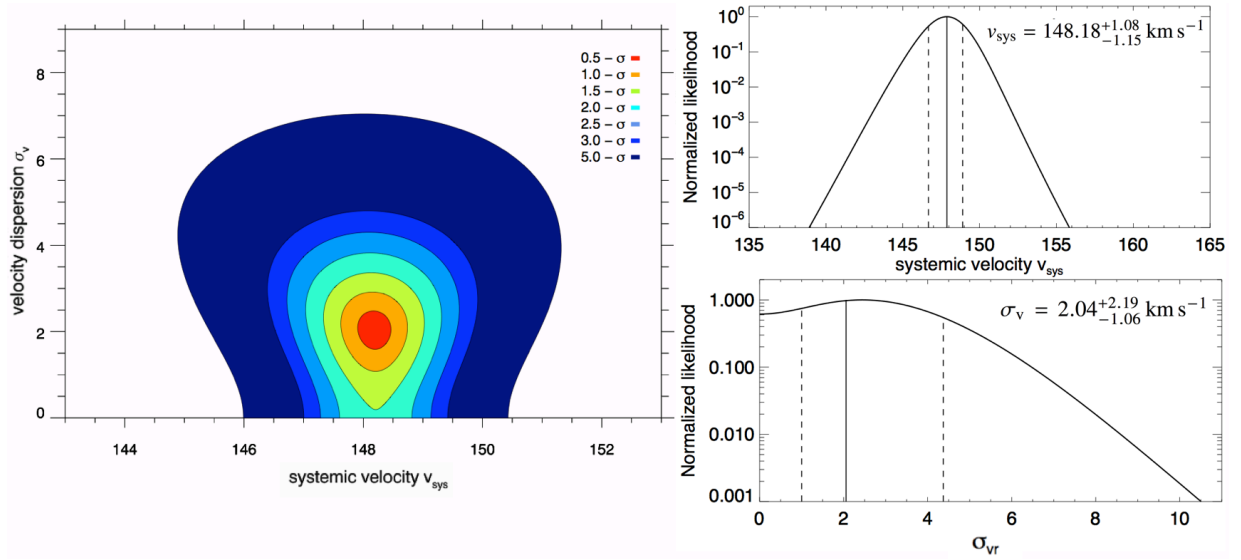


Figure 3.10: **Top left panel:** Two dimensional distribution of the normalised likelihood for the grid of systemic velocity and velocity dispersion. The colour coding of the likelihood ranges from 0.5-3.0  $\sigma$  levels in steps of 0.5 and an additional colour level for 5  $\sigma$ . **Top right panel:** The marginalised one dimensional likelihood distribution for the systemic velocity of Crater. The most likely value is noted with a solid line, whereas the  $1.0\sigma$  uncertainty levels are shown as dashed lines. **Lower right panel:** The marginalised one dimensional likelihood distribution of the velocity dispersion. The solid line denotes the most likely value and the dashed lines mark the  $1.0\sigma$  levels.

We reran the same exercise for different membership probability cut-off limits.

- $\sigma_{p \geq 0.2} = 2.00^{+2.3}_{-1.03} \text{ km s}^{-1}$     N=33
- $\sigma_{p \geq 0.5} = 1.43^{+2.1}_{-0.66} \text{ km s}^{-1}$     N=26

For the case where we limit our sample to stars with a membership probability of  $\geq 0.5$  we resolve a smaller dispersion but one that is still consistent within the errors with our other samples. From the spatial distributions of velocities in Fig. 3.6 it appears that the velocity dispersion of the central stars is lower than that of the outer stars. To test the isotropy of the velocity dispersion, we reran our Monte Carlo analysis for stars located within a radial distance of  $r < 35$  arcsec. For the 24 stars in this sample we derive a likely systemic velocity of  $v_{\text{sys}} = 147.17^{+1.3}_{-1.3} \text{ km s}^{-1}$  and a velocity dispersion of  $\sigma_v = 1.57^{+3.66}_{-0.54} \text{ km s}^{-1}$ . Thus the velocity dispersion is lower when only considering the central regions. Still, within the error bars, the values are largely consistent with the full sample values.

Assuming Crater is in dynamical equilibrium, we use the formula for deriving the dynamical mass of stellar dispersion supported systems of Wolf et al. (2010) to estimate its half-mass:

$$M_{1/2} = \frac{4}{G} \sigma_v^2 \cdot R_e \quad (3.7)$$

$R_e$  is the half-light radius of the system,  $\sigma_v$  the two dimensional velocity dispersion and  $G$  the gravitational constant. For  $R_e$  we use the value of 19.4 pc given in Weisz et al. (2015). We derive a dynamical half-mass of Crater of  $M_{1/2} = 7.51^{+24.7}_{-5.8} \cdot 10^4 M_\odot$ , assuming that it is a dispersion supported system in equilibrium. The mass-to-light ratio of Crater can then be calculated using the half-light luminosity  $L_v = 8.8 \cdot 10^3 L_\odot$  converted from the values given in Weisz et al. (2015). We derive  $M/L_v = 8.52^{+28.0}_{-6.5} M_\odot/L_\odot$ . For the second case, when restricting the measurement to the inner 35 arcsec, we derive a mass of  $M_{1/2} = 4.45^{+44.9}_{-2.53} \cdot 10^4 M_\odot$  which translates to a mass-to-light ratio of  $M/L_v = 5.05^{+50.9}_{-2.88} M_\odot/L_\odot$ .

The effects of dynamical equilibrium and spherical symmetry assumptions on the accuracy of the Wolf et al. (2010) mass estimator was examined recently by Campbell et al. (2016). They find that there exists no systematic biases, but an intrinsic 25% 1- $\sigma$  scatter in the masses determined with this estimator. This effect is mainly due to the unknown 3D distribution of the stellar mass. This intrinsic scatter can increase the errors on our measurement further.

We use population synthesis models to compare predicted mass-to-light ratios of a purely baryonic stellar system to the measured M/L of Crater. These models need the age and metallicity of the cluster as input parameters. We adopt the best fit age of 7.5 Gyr and a metallicity of  $[M/H] = -1.66$  as derived from HST photometry in Weisz et al. (2015). For this age and metallicity the SSP model of Maraston (2005) predicts  $M/L_v = 2.2 M_\odot/L_\odot$  for a Salpeter IMF and  $M/L_v = 1.5 M_\odot/L_\odot$  for a Kroupa IMF. Both values are clearly lower than what we derive for Crater. The Salpeter IMF prediction lies within the  $1\sigma$  uncertainty of the measured Crater M/L of the full sample, which has a lower limit of 2.17. The Kroupa IMF prediction is a slightly larger outlier. Thus we conclude that the measured M/L ratio of Crater is consistent with M/L predictions for a purely stellar

system. Even with the assumption of a Kroupa mass function, the stellar contribution is maximised.

Mass functions flatter than Kroupa or Salpeter with correspondingly lower M/L-values are still possible (Paust et al. 2010; Sollima et al. 2012). Of course, all of this analysis is based on the assumption of dynamical equilibrium, which we will investigate further in the next section. If we just use the sample of stars within 35 arcsec, the prediction for the M/L becomes a bit lower with 5.05, and its lower  $1\sigma$  level is  $M/L_V = 1.97 M_\odot/L_\odot$ , which is in good agreement with a stellar system following a Salpeter IMF. The upper limit for the dispersion and thus the M/L<sub>V</sub> ratio of Crater is less tightly constrained and reflects the existence of several velocity outlier stars (such as star 7 with  $154 \text{ km s}^{-1}$ ) with a non-negligible membership probability.

### 3.4.2 Radial distribution of stellar velocities, cluster rotation and velocity gradient

As the presence of rotational support, tidal distortions or binary stars can inflate the velocity dispersion significantly we test our sample as to whether we can find evidence for such a behaviour.

The distribution of stellar radial velocities as a function of distance to Crater is shown in Fig. 3.11. In the top panel, only stars in the FOV that have a velocity uncertainty of less than  $7 \text{ km s}^{-1}$  are included, in the bottom panel all stars for which we measure velocities are shown. In the top panel, it is visible that most stars are consistent within the  $\pm 1\sigma_v$  shaded area (darkest shade of blue) of the measured intrinsic dispersion of  $2.05 \text{ km s}^{-1}$ . There appears to be a subset of stars at larger and lower velocities whose errorbars are not consistent with the  $3\sigma$  region of the intrinsic velocity dispersion. The star at the largest radial distance of 55 arcsec is star 7, one of the potential blue stars of our dataset. It is within  $2\sigma$  of the intrinsic dispersion of the system. The stars with good velocity measurements in the top panel of 3.11 appear to follow a radial trend towards higher velocities for increasing distance to Crater. However, this behavior is not statistically significant, and we might be biased by the small number statistics of bright stars for which we have precise velocity measurements.

Our large sample of likely member stars enables us to test also for potential signatures of rotation in Crater. For this we plot the stars and their radial velocities as a function of their position angle in Fig. 3.12. Here the position angle (PA) is defined as PA=0 in western direction and as +90 degrees towards the south. Thus, the first 90 degrees of the rotation plot are empty because they lie in the unobserved quadrant. In the top panel the position angle of all stars in the sample between  $130 < v_{\text{rad}} < 175 \text{ km s}^{-1}$  are plotted. The plot indicates that there might be a radial velocity increase with position angle. To test if this increase is significant we used bins of  $30^\circ$  and calculated the weighted mean radial velocity in each bin. The results are shown in the bottom panel of Fig. 3.12.

The error-weighted mean velocities appear to depend on the position angle. As our data do not cover the full Crater position angles, and our velocities have relatively large

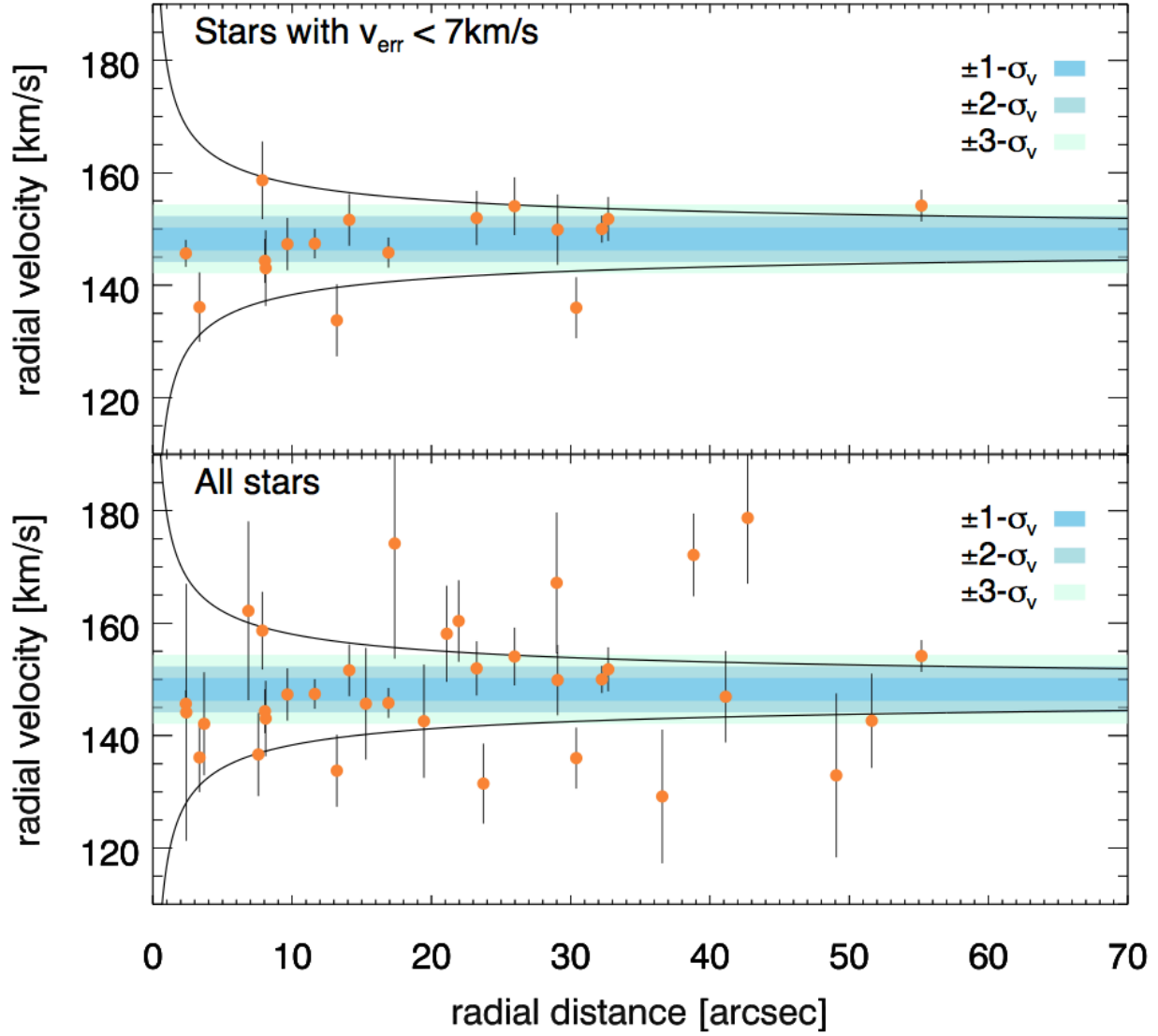


Figure 3.11: Stars with radial velocities as function of their distance to the centre of Crater. Shaded regions correspond to the velocity areas within  $\pm 1\sigma_v$ ,  $\pm 2\sigma_v$  and  $\pm 3\sigma_v$  of the systemic velocity of Crater. The top panel shows only velocities with  $v_{\text{err}} < 7 \text{ km s}^{-1}$  and the bottom panel shows all stars with velocities in the displayed range. The black lines in both panels represent the radial dependence of the escape velocity of the system if we assume a total dynamical mass of  $M_{\text{tot}} = 1.5 \cdot 10^5 M_{\odot}$ .

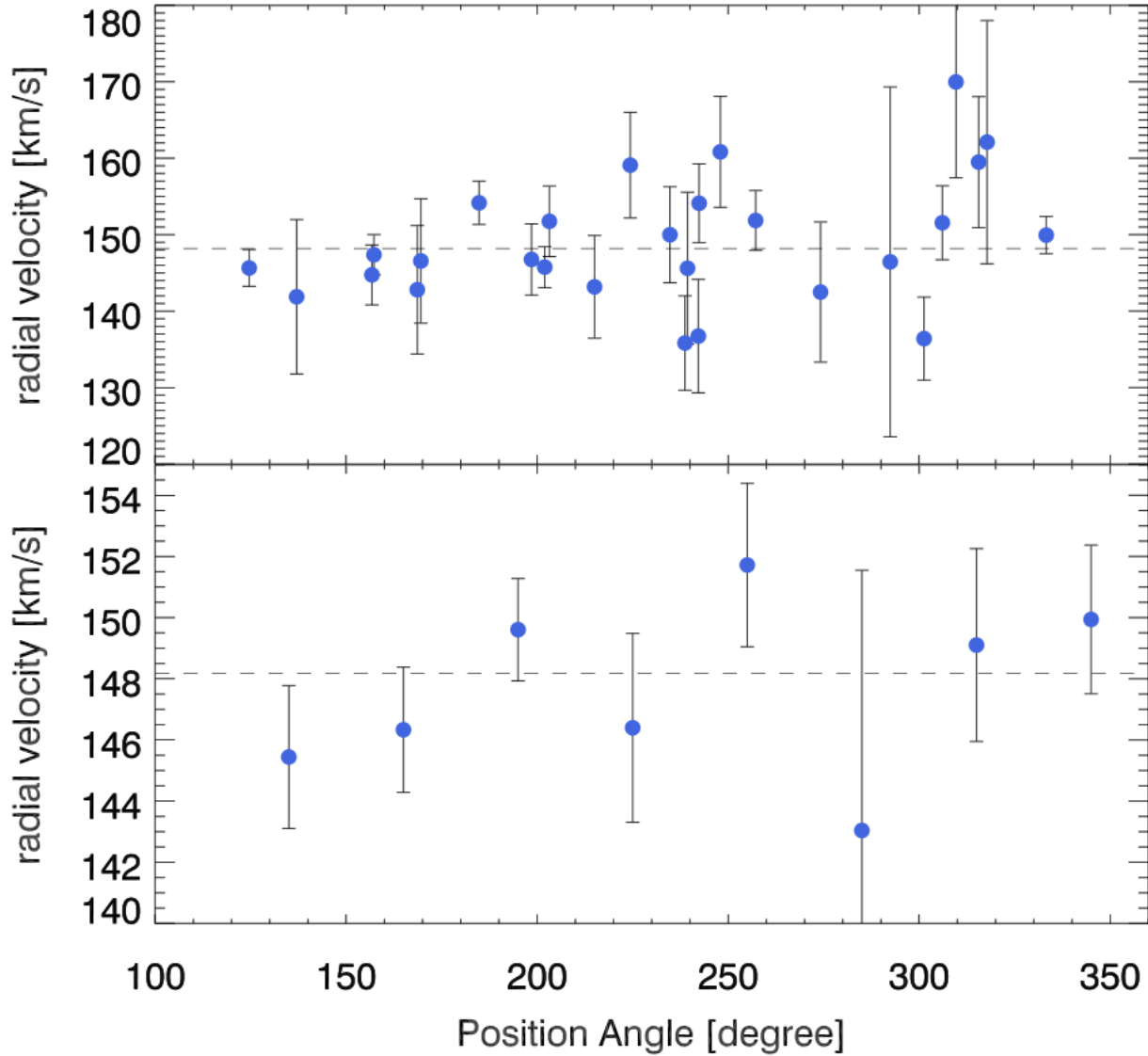


Figure 3.12: **Top panel:** The velocity of Crater stars as a function of the position angle (0 deg West, +90 deg South). Included are all stars with velocities between  $130 < v_{\text{rad}} < 175 \text{ km s}^{-1}$ . The dashed horizontal line in both panels indicates the systemic velocity of Crater. **Bottom panel:** The weighted mean of the radial velocities as a function of the position angle of the stars. The bin size is  $30^\circ$ . Note the different scaling of the y-axis in the two panels.

errors, it is not possible to draw a firm conclusion on a rotational amplitude by fitting a sinusoidal curve to the data. Nevertheless, we see that the weighted mean of the bin at PA=135° is  $v = 145.44 \pm 2.34 \text{ km s}^{-1}$  and at a PA=345° it rises to  $v = 149.94 \pm 2.43 \text{ km s}^{-1}$ . Assuming these two values would represent the amplitude of a rotational support in Crater, the difference of  $4.5 \text{ km s}^{-1}$  would imply an rotational amplitude of the order of  $2.25 \text{ km s}^{-1}$ . To determine if Crater is rotationally supported more and more precise radial velocities will be necessary. Alternatively, our data could also indicate that there is a velocity gradient from the south to the north, which would hint at previous tidal distortions of Crater's stellar population.

## 3.5 Discussion

### 3.5.1 Dynamical state of Crater

The dynamical mass-to-light ratio of Crater is consistent with predictions for baryonic globular cluster SSP models with a Salpeter IMF within its errorbars. Our derived total dynamical mass is  $M_{\text{tot}} = 1.50^{+4.9}_{-1.2} \cdot 10^5 M_{\odot}$  and translates into a mass-to-light ratio of  $M/L_V = 8.52^{+28.0}_{-6.5} M_{\odot}/L_{\odot}$ . This is consistent at the lower limit within  $1 \sigma$  with the  $M/L_V = 2.2 M_{\odot}/L_{\odot}$  predictions from SSP models of [Maraston \(2005\)](#) for a stellar system of 7 Gyr.

One explanation for an elevated dynamical mass-to-light ratio can be anisotropies in the velocity dispersion. Anisotropies such as rotational support or velocity gradients can inflate the observed velocity dispersion and elevate the M/L ratio. The (though not significant) hints for rotational support in Crater, as well as the observed dependence of radial velocities on the distance to Crater, suggests that Crater might not be in dynamical equilibrium.

If we assume that Crater is not in dynamical equilibrium because it is tidally disturbed, the velocity outlier stars might have been recently stripped and are thus unbound stars that are still in the vicinity of Crater. In [Küpper et al. \(2011\)](#) it was suggested that during the phase near the apocenter, tidal debris can be orbitally compressed and already unbound stars can appear to be close enough to be bound to the object. Thus, an object affected by tidal compression can appear dynamically hotter than it actually is, which will inflate the derived M/L ratios and can mimic the dynamical effects of a dark matter halo.

Binary blue stragglers and other binary stars can inflate the velocity dispersion of clusters as they are observed at random times of their orbits ([McConnachie & Côté 2010](#); [Frank et al. 2012](#)). One faint blue star at I=22 mag just above the main-sequence turn-off is a very likely member of Crater and located exactly where we would expect blue stragglers in the CMD. In addition its velocity is consistent with the systemic velocity of Crater. Its location at the very centre of the cluster at a distance of merely 6 arcsec is consistent with predictions for blue stragglers to migrate towards the cluster centre over time ([Ferraro et al. 2012](#)).

In [Milone et al. \(2012\)](#) it was found that lower mass and less concentrated GCs have on average a higher binary fraction. This is attributed to the fact that dense stellar environments are more efficient in destroying binaries. As Crater has a low stellar content and is



extended it should have a higher binary fraction than higher mass clusters. Assuming that Crater formed with its size and mass this means that we expect a high fraction of binaries in its stellar population that can then increase our velocity dispersion measurement.

In [Frank et al. \(2012\)](#) the effect of binaries on the measured velocity dispersion was simulated for the low-mass GC Pal 4. They conclude that a high binary fraction in a low-mass clusters can result in estimating too high dynamical masses for a given cluster. They suggest that the velocity dispersion can be overestimated by 20% assuming a high binary fraction within the cluster.

Crater's  $M/L$  ratio is not in agreement with what we expect for a dwarf galaxy of this mass, having mass-to-light ratios of  $M/L > 100$ . At face value, Crater's  $M/L$  ratio could nevertheless be interpreted as presence of dark matter. As we will discuss later, most arguments are in favour of Crater being a globular cluster, and the existence of dark matter in globular clusters has not been proven so far, although it was proposed several times in the past (e.g.: [Peebles 1984](#); [Padoan et al. 1997](#)).

Another explanation for the elevated dynamical mass of Crater might be that its dynamics does not follow Newton's laws but is non-Newtonian. In the case of MODified Newtonian Dynamics (MOND, [Milgrom 1983](#)) one would expect a velocity dispersion of 2.2 km/s, which is in good agreement with our measured value. The MONDian velocity dispersion was calculated using eq. 6 in [Baumgardt et al. \(2005\)](#), assuming that the cluster is in the deep MOND regime and that the internal acceleration dominates over the external one. We note, however, that other similarly remote clusters located in the low acceleration regime, like Pal 14, Pal 4, and NGC 2419, do not show evidence for MONDian dynamics ([Jordi et al. 2009](#); [Frank et al. 2012](#); [Ibata et al. 2011](#)).

In [Baumgardt et al. \(2010\)](#) two distinct populations of outer halo Milky Way star clusters were identified based on to which extent they fill their Jacobi radius  $r_J$  in comparison to their half mass radius  $r_h$ . On the one hand, there is a group of compact, tidally under-filling clusters with  $r_h/r_J < 0.05$ . On the other hand, there exists a second population of tidally filling clusters  $0.1 < r_h/r_J < 0.3$  that are likely in the stage of dissolution. Thus we can use this estimator to test if Crater is a dissolving GC. We use equation 1 from [Baumgardt et al. \(2010\)](#) to determine the Jacobi radius:

$$r_J = \left( \frac{GM_c}{2 \cdot V_G^2} \right)^{1/3} R_{GC}^{2/3} \quad (3.8)$$

We use a dynamical total mass of  $M_{\text{tot}} = 1.5 \cdot 10^5 M_\odot$  as the cluster mass,  $V_G = 220$  km/s as circular velocity of the Milky Way, and a Galactocentric distance for Crater of  $d = 145$  kpc (taken from [Weisz et al. 2015](#)). Using a deprojected radius of  $r_h = 1.33 \cdot r_{\text{halfight}}$  as defined in [Baumgardt et al. \(2010\)](#), we derive a ratio of  $r_t/r_J = 0.114$ . This is consistent with a dissolving globular cluster in the tidally filling regime. Due to its unusual metallicity, age, and distance, it has been already speculated that Crater formed as GC of another dwarf galaxy that was then accreted onto the Milky Way. In this scenario Crater must have already been subjected to strong tidal forces during a pericenter passage in order to be efficiently stripped from its parent dwarf galaxy, and thus might currently be in the phase of dissolution.

### 3.5.2 Is Crater a former member of a dwarf galaxy?

It was noted by [Belokurov et al. \(2014\)](#) that Crater is aligned on a common great circle with Leo IV and Leo V, which also have comparable radial velocities. Thus a potential association of Crater with Leo IV and Leo V, with a common origin of these objects, has been suggested. Recently, a new dwarf galaxy, Crater II, was discovered in the vicinity of Crater, aligned with the same great circle as the other three objects ([Torrealba et al. 2016](#)). This dwarf galaxy is very extended,  $R_e = 1.1$  kpc, considering its relatively faint magnitude of  $M_v = -8$ . Its apparent angular separation from Crater is only  $\sim 8^\circ$ , which is equivalent to a distance of 20 kpc at a distance of 145 kpc. In addition, the derived metallicity of  $-1.7$  dex for the Crater II dwarf from [Torrealba et al. \(2016\)](#) is consistent with the values derived for Crater, giving further reason to speculate that Crater 2 is the dwarf galaxy that has potentially hosted Crater, and what we see now are the leftovers of a satellite group that forms a narrow tidal debris stream.

The hypothesis that Crater was stripped from a dwarf galaxy is further supported by the existence of extended GCs in other dwarf galaxies (e.g. [Georgiev et al. 2009](#); [Da Costa et al. 2009](#)), in addition to their presence in the outer Milky Way and M31 (e.g. [Huxor et al. 2005](#)). The extended cluster in the dwarf elliptical Sc22 in the Sculptor group has a half-light radius of 22 pc making it one of the largest known GCs that is associated with a dwarf galaxy ([Da Costa et al. 2009](#)). In addition, its metallicity was found to be  $[\text{Fe}/\text{H}] = -1.7$  dex making it similarly metal-poor as Crater. In this work, it is suggested that GCs in dwarf galaxies can form in two modes, one "normal" mode and an extended mode with half-light radii of larger than 10 pc. It is suggested that an environment with low stellar density is the requirement for the formation of clusters in the extended mode, which supports the view that Crater originated in another dwarf galaxy and has been stripped from it.

### 3.5.3 Crater among Milky Way halo GCs and dwarf galaxies

In the Milky Way halo, globular clusters that are at larger galactocentric distances than 100 kpc are extremely rare. Only six Milky Way GCs can be found further out than 50 kpc, and of those two lie at distances larger than 100 kpc ([Harris 1996](#)). The population of globular clusters in the outer Milky Way halo is on average younger and has a lower central stellar density than the inner halo GCs ([Dotter et al. 2010](#)). But among those "young" outer halo GCs, with an age of 7 Gyr, Crater is still considerably younger than any other GC at galactocentric distances larger than 100 kpc, which all have ages of 10 Gyr or larger. Several authors have suggested that these young outer halo GCs were accreted onto the Milky Way along with their dwarf galaxy hosts, whereas the inner globular clusters formed via direct early collapse of the inner halo ([Côté et al. 2000](#); [Lee et al. 2007](#); [Forbes & Bridges 2010](#)). As already mentioned, it was suggested in [Weisz et al. \(2015\)](#) that Crater was accreted onto the Milky Way as a GC within a dwarf galaxy, from which it was later stripped, consistent with the proposed origin of the other outer halo GCs.

While Crater's  $M/L$  is elevated compared to models of a purely baryonic stellar system,

there are cases in the literature where higher dynamical M/L ratios were derived for objects that are clearly GCs and not dwarf galaxies. One comparable object is the globular cluster NGC 2257 in the Large Magellanic Cloud, which has a high dynamical mass-to-light ratio of 10.4 (McLaughlin & van der Marel 2005), similar to what we measure for Crater. This GC was also measured to be metal-poor with  $[\text{Fe}/\text{H}] = -1.59$  dex. This is comparable to what we measure for Crater. The reason for the elevated mass-to-light ratio of NGC 2257 is still unknown.

Another intriguing cluster that exhibits similar properties as Crater is Lindsay 38 (Glatt et al. 2008), one of the most remote clusters of the SMC with a distance of 68 kpc to the SMC. With an age of 6.5 Gyr and a metallicity of  $[\text{Fe}/\text{H}] = -1.59$  dex it is an intermediate age and metal-poor cluster. Its remote distance, size, age and metallicity are all similar to Crater's properties.

The most similar objects to Crater are thus the intermediate-age extended clusters of the LMC/SMC. Therefore, the possibility that Crater was formed as a member of the LMC/SMC and later stripped from them appears also like a viable formation channel. Crater's position in the all-sky plot is close enough to the LMC-SMC orbit to be in principle consistent with a stripping scenario (see e.g. Fig. 1 Pawlowski et al. 2015). Nevertheless, the LMC-SMC orbit is oriented among the Vast Polar Structure of satellite galaxies of the Milky Way, and thus we expect many satellite objects to be aligned with this plane. Crater's true, deprojected position is  $\sim 150$  kpc away from the LMC, which makes a stripping origin from the LMC relatively unlikely if we assume the LMC is only on its first perigalactic passage (e.g. Besla et al. 2007; Kallivayalil et al. 2013).

In Jethwa et al. (2016) the distribution of the satellites of the Magellanic Clouds was modelled dynamically. In their likelihood distribution, Crater would be located just at the border of their projected satellite likelihood distribution. Thus Crater's position is consistent with this model, although the probability is relatively low. Deason et al. (2015) use dark matter simulations to predict the fraction of Milky Way satellites at a certain distance that were once satellites bound to the LMC. According to their simulations, the fraction of satellites that were bound to the LMC would amount to  $\sim 10\%$  at a present-day distance of 150 kpc. In summary, current models of the LMC-SMC satellite distributions cannot exclude that Crater originated from either LMC or SMC, but dynamical models predict a low probability for a LMC-SMC origin of Crater. However, until proper motion measurements will be conducted, no firm conclusions can be reached on its connection to the Magellanic System.

### 3.6 Summary

Our MUSE observations of Crater revealed that it has a systemic radial velocity of  $v_{\text{sys}} = 148.18^{+1.08}_{-1.15} \text{ km s}^{-1}$ . Its most likely velocity dispersion is  $\sigma_v = 2.04^{+2.19}_{-1.06} \text{ km s}^{-1}$ , which leads to a total dynamical mass of the system, assuming dynamical equilibrium, of  $M_{\text{tot}} = 1.50^{+4.9}_{-1.2} \cdot 10^5 M_{\odot}$ . This dynamical mass implies a mass-to-light ratio of  $M/L_V = 8.52^{+28.0}_{-6.5} M_{\odot}/L_{\odot}$ , which is consistent with a purely baryonic stellar population within its errors and no sig-

nificant evidence for the presence dark matter is found.

We conclude that our MUSE results, as well as the results of the other recent work on Crater ([Weisz et al. 2015](#); [Kirby et al. 2015](#)), all strongly support Crater to be a globular cluster and not a dwarf galaxy. Especially the deep, high-quality CMD of [Weisz et al. \(2015\)](#) shows no evidence of more recent star formation. Our spectroscopy excludes membership of two of the luminous blue stars, and the data as well as the position of the third blue star make its membership quite unlikely. Even if this blue star were a genuine member it is difficult to explain why there would be only one clearly identifiable, luminous star left over from a more recent episode of star-formation. The comparatively young age of Crater makes it a direct counterpart of the intermediate-age clusters in the SMC, many of which are located at large distances from the SMC's centre and could be stripped relatively easily from the SMC during an interaction.

The young age - with no obvious presence of an old population - is another argument against a dwarf galaxy. All dwarf galaxies that are sufficiently close to be resolved into stars have been found to contain old populations, without exception ([Grebel & Gallagher 2004](#)). The ultrafaint dwarf spheroidals may have had their star formation truncated by reionization and never recovered their gas to undergo more recent star-formation. Assuming that Crater formed as an isolated dwarf galaxy, the question remains, how such a low-mass object would have managed to avoid SF at early times and to have been able to retain its gas to have only one single burst of star-formation 7 Gyr ago, well after reionization? In addition, its dynamical M/L is much lower than that of any other dSph of that luminosity (e.g. [McConnachie 2012](#)). Although these are not definitive exclusion arguments, they show that, if Crater had formed as a genuine dwarf galaxy, it would defy our understanding of dSphs and of dwarf galaxies in general. Thus we conclude that our findings strongly support that Crater is a faint intermediate-age outer halo globular cluster and not a dwarf galaxy.



# Chapter 4

## The metallicity of the stars in the outer halo globular cluster Crater as seen by MUSE

### 4.1 Introduction

Globular clusters are notably homogenous in their iron abundance. Their masses are not high enough to retain the heavy elements ejected by supernova explosions, and they are formed in very short single starburst events (Gratton et al. 2004; Carretta et al. 2009a; Willman & Strader 2012). The intrinsic spread of iron in most globular clusters is extremely small. For a sample of 19 globular clusters, based on high resolution spectroscopy, the iron spreads are smaller than 0.05 dex (Carretta et al. 2009a).

Exceptions to this rule mainly exist for GCs brighter than  $M_v = -10$  mag, where significant iron spreads were identified. The classic example for a massive GC with a known iron abundance spread is  $\omega$  Cen. It has been studied extensively and its iron abundance ranges from  $-2.2 < [\text{Fe}/\text{H}] < -0.5$  with a peak at  $[\text{Fe}/\text{H}] = -1.7$  (e.g.: Norris & Da Costa 1995; Hilker & Richtler 2000; Sollima et al. 2005). This large range of iron abundance has been associated to the self-enrichment from multiple star formation episodes (e.g.: Ikuta & Arimoto 2000; Marcolini et al. 2007). Another explanation for the presence of multiple episodes of star formation is that GCs with large iron abundance spreads have formed as nuclear star clusters of galaxies, which are known to host multiple generations of stellar populations (e.g.: Seth et al. 2006; Walcher et al. 2006; Rossa et al. 2006). If these GCs are the former nuclei of dwarfs they must have been stripped from their previous host galaxy (Freeman 1993). Dynamical models (e.g. Bekki & Freeman 2003) have shown that the stripped nucleus formation channel for  $\omega$  Cen is a viable possibility. It was proposed in Da Costa (2015), that every globular clusters which harbours an iron spread must have formed as the nucleus of a stripped dwarf galaxy.

Sarajedini & Layden (1995) showed that the stellar population of M 54, a GC within the Sagittarius dwarf galaxy, exhibits a spread in iron abundance of  $\sigma_{[\text{Fe}/\text{H}]} = 0.16$  dex. This result was further confirmed by Bellazzini et al. (2008), who determined in a spectroscopic study of 321 member stars of M 54 an intrinsic iron spread of 0.14 dex. As M 54 lies very close to the photometric centre of Sagittarius, it was suggested that M 54 is not only a GC

of the dwarf galaxy, but its nuclear star cluster (Sarajedini & Layden 1995; Ibata et al. 1995).

A similar intrinsic spread in heavy elements was measured in M 22 by Da Costa et al. (2009) who studied 41 RGB stars, similar to the 0.14 dex dispersion determined by Marino et al. (2009). With a magnitude of  $M_V = -8.5$ , M 22 is the faintest cluster for which a significant spread in heavy elements is observed.

An iron spread of 0.17 dex was also detected in NGC 6273 (Yong et al. 2016). Another intriguing GC with chemical anomalies is NGC 2419 in the outer Milky Way halo. It lies at a distance of 90 kpc (Harris et al. 1997), and thus is besides Crater one of the most distant GCs of the Milky Way, and with  $M_V = -9.5$  one of its brightest GCs. Among other chemical peculiarities, an intrinsic spread of 0.2 dex in Calcium but no spread in iron was found (Cohen et al. 2010; Cohen & Kirby 2012). Similarly to M 54 and  $\omega$  Cen, also these clusters are interpreted as candidates of former nuclear star clusters of dwarf galaxies.

One explanation for the spread in iron abundance within massive GCs is that they did not form as nuclear star clusters, but have a spread in iron abundance due to self-enrichment (Ikuta & Arimoto 2000; Marcolini et al. 2007; Carretta et al. 2009b; Murray 2009). For self-enrichment GCs need to have a potential well that is deep enough to keep the ejected heavy elements from supernova explosions within their gravitational potential.

The spread in iron abundance  $\sigma_{[\text{Fe}/\text{H}]}$  has been suggested as diagnostic to distinguish dwarf galaxies from globular clusters in cases where the dynamics of the objects give ambiguous results (Willman & Strader 2012). Stars in dwarf galaxies exhibit a large spread in metallicities that is due to their continuous star formation episodes over several Gyrs (Grebel et al. 2003). During this process the gas supply for the next generations of stars gets enriched in heavy elements. Such subsequent populations will thus be significantly more metal-rich than the older populations.

For the magnitude range of Crater there are several dwarf galaxies with measured iron dispersions. The Hercules dwarf galaxy with  $M_V = -6.2$  shows an intrinsic iron spread of  $\sigma_{[\text{Fe}/\text{H}]} = 0.51$ , derived in the spectroscopic study of Kirby et al. (2008). The Ursa Major I dwarf galaxy ( $M_V = -5.5$ ) has an iron spread of 0.54 dex, and the Leo IV dwarf galaxy ( $M_V = -5.5$ ) a spread of 0.75 dex (Kirby et al. 2008). For the magnitude range  $-7 < M_V < -4$ , all dwarf galaxies with measured spectroscopic iron spreads have  $\sigma_{[\text{Fe}/\text{H}]} > 0.55$  (see summary in Willman & Strader 2012). Therefore, in this magnitude regime, iron spreads of  $\sigma_{[\text{Fe}/\text{H}]} > 0.55$  dex indicate dwarf galaxies, whereas spreads smaller than 0.1 dex are the signature of classical globular clusters.

This distinction in metallicity dispersion is very clear for objects that are fainter than  $M_V = -10$ . However for GCs and dwarfs brighter than  $M_V = -10$  the difference in heavy element spread between them becomes much smaller (see e.g. Fig. 1 in Willman & Strader 2012). Therefore, the iron dispersion is a good classification criterion for objects fainter than  $M_V = -10$ . The iron dispersion is already used as a second diagnostic tool in the study of dwarf galaxies, which is independent of the dynamical measurements, such as the mass-to-light ratios (e.g. Martin et al. 2007; Willman et al. 2011).

The dynamical analysis of the MUSE data we obtained on Crater was presented in



chapter 3 (published in [Voggel et al. 2016](#)). In this chapter we will use the obtained spectra for a detailed account on the metallicity of the stellar population of Crater. We will use this analysis as a second independent way to investigate the nature of Crater.

## 4.2 Observation, reduction and extraction of spectra

The detailed account of the data reduction of the MUSE cube was presented in section ??, but is summarised here for completeness. Crater was observed with the new integral field instrument MUSE ([Bacon et al. 2010](#)) on the VLT (ESO programme Nr. 094.D-0880, PI: Hilker). The broad spectral range of MUSE covers the wavelength region from 4750-9300 Å with a moderate resolution of  $R = 1500\text{-}3000$ , which is combined it with a large 1'' field-of-view.

We mapped the extent of Crater using three pointings around Crater (R.A. = 11:36:17.965,  $\delta = -10:52:04.80$ ) with  $2 \times 1400\text{ s}$  each. The six raw MUSE cubes were reduced with version 1.0 of the standard ESO pipeline ([Weilbacher et al. 2012](#)). All the standard reduction steps such as the bias correction, subtracting the flatfield and a calibration of the wavelength grid was performed on each individual IFU in each of the 6 observed cubes. These were stored in so-called pixtables and subsequently combined into one final data cube. An image of the collapsed white-light cube is shown in Fig.3.1.

The spectra are extracted from the IFU cube using the PAMPELMUSE software package from [Kamann et al. \(2013\)](#). This routine models the wavelength dependence of the point-spread function and then extracts and co-adds the IFU spaxels into one dimensional spectra, one per point source.

## 4.3 Analysis

We analyse the metallicity of Craters stars using a fitting routine that compares the Göttingen stellar library of [Husser et al. \(2013\)](#) to the observed MUSE spectra. This stellar library provides synthetic spectra based on the PHOENIX code of stellar atmospheres. The advantage of this library is that, due to its broad wavelength coverage from 500 to  $5.5\mu\text{m}$  and high resolution, model spectra that cover the full MUSE wavelength range and have the same spectral resolution can easily be generated. The models cover a very broad parameter space from  $2300\text{ K} < T_{\text{eff}} < 12000\text{ K}$  in effective temperature and from  $0 < \log(g) < 6.0$  in surface gravity. Most importantly for this work, the models also extend to low metallicity ranges of  $[\text{Fe}/\text{H}] = -4.0$ , which many other models do not reach. The final models to which we compare our observations are a weighted combination of several PHOENIX models, and thus a fine sampling in  $T_{\text{eff}}$ , metallicity phase space and surface gravity is possible.

In [Husser et al. \(2016\)](#) a detailed explanation of the analysis method is presented. We briefly summarise the fitting routine of the spectra here.

As a start point for the fitting routine we use the best fit Dartmouth isochrone (see

Fig. 4.5) and derive the closest point on the isochrone to each star in the CMD. The isochrone model thus provides us with a starting value of  $\log(g)$  and  $T_{\text{eff}}$  for each star. The code then runs a cross correlation between the model and observed spectra, and obtains a best fit model spectrum. The free parameters in this fit are  $T_{\text{eff}}$ ,  $[\text{Fe}/\text{H}]$ ,  $\log(g)$  and the radial velocity  $v_r$ . A major advantage of this method is that the full spectral range is fitted simultaneously and that the routine includes a model for the telluric absorption. The best fit model and the residual of one example spectrum of the RGB star No. 5 is shown in Figure 4.1. The observed spectrum is shown in black and the best fit model in blue in the top panel. The second panel shows the residuals to the fit and in the bottom panel the telluric absorption model is plotted in green.

In a first run all the parameters are kept fixed and only the radial velocity is allowed to vary. This derived radial velocity is then used as a starting value for the second iteration. In the second run, all parameters, except  $\log(g)$  are allowed to vary. A test fit including  $[\alpha/\text{Fe}]$  as free parameters derives an average  $[\alpha/\text{Fe}]=0.4$ , to which we fix our alpha abundance in the other iterations. This value is consistent with the fact that most GCs are enriched in alpha elements. Fixing this parameter to a sensible value avoids that the parameter space becomes too large. We also include a model for the telluric absorption features. The starting values for the next iterations are the previously derived radial velocity and the surface gravity  $\log(g)$  that was taken from its closest isochrone position.

We now run a free  $\log(g)$  fit and one where the  $\log(g)$  values are fixed to their isochrone values. The iterations with a fixed  $\log(g)$  implicitly assume that stars are members of Crater and lie on the isochrone. Evidently, assuming a  $\log(g)$  based on the isochrone position, is problematic for stars offset from the isochrone. We will use the results from the free  $\log(g)$  fit in cases where the star is offset by more than 0.3 mag from the isochrone in  $g-i$  colour.

Keeping the surface gravities fixed was already used in Husser et al. (2016) due to the sensitivity of  $\log(g)$  to the exact shape of the absorption lines. For MUSE data, the line shapes depend somewhat on the exact line spread function (LSF) of MUSE, which is known to vary among IFUs as well as across the spectral range. Thus fixing  $\log(g)$  to their photometric values avoids this problem entirely.

The reliability of the uncertainties provided by the pipeline for  $T_{\text{eff}}$  and  $[\text{Fe}/\text{H}]$  values were analysed by Husser et al. (2016). They found that the uncertainties of  $T_{\text{eff}}$  need to be multiplied with a factor of 1.5 and the metallicity uncertainties of  $[\text{Fe}/\text{H}]$  with a factor 1.24. We also multiply our  $T_{\text{eff}}$  and  $[\text{Fe}/\text{H}]$  errorbars from the pipeline with these factors to retain reliable uncertainties.

## 4.4 Results

### 4.4.1 Stellar parameters

The final stellar parameters of each star in Crater are listed in table 4.1. We show the results from the fixed  $\log(g)$  iterations, for all stars that are within  $\Delta(g-i) < 0.3$  mag

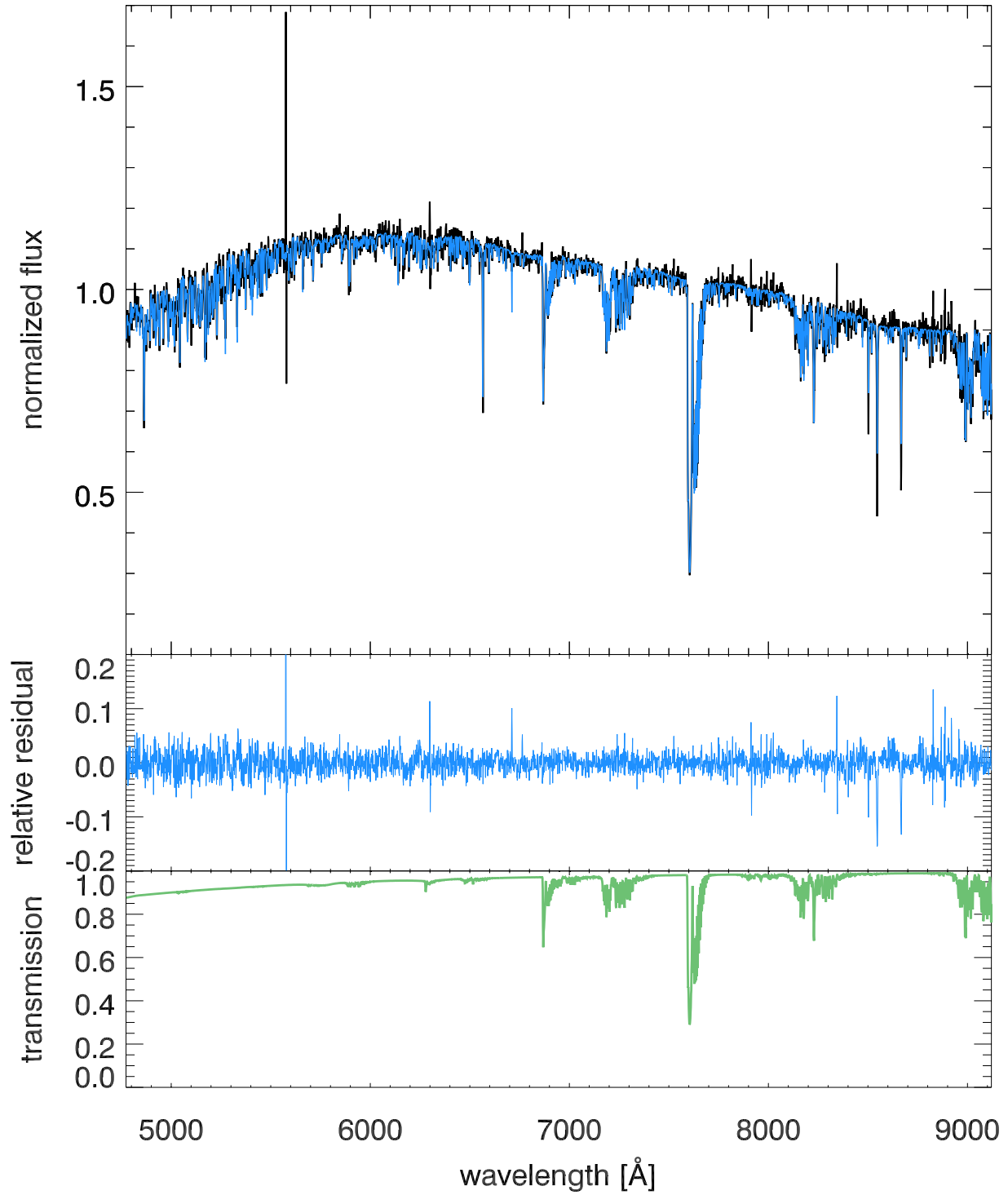


Figure 4.1: In the top panel, the observed spectrum of star 5 is shown in black, and the best fit model is plotted in blue. Model and spectrum both still contain the telluric absorption lines. The second panel displays the residuals between model and spectra. And in the last panel the modelled telluric transmission spectrum is shown in green.

of the isochrones colour at a given magnitude. For stars that do not lie on the isochrone, the assumption of the isochrone  $\log(g)$  is not appropriate. We adopt the parameters of fits where  $\log(g)$  is allowed to vary. For the  $\log(g)$  values, we only included errorbars for those stars where we used a free  $\log(g)$  fit. All other  $\log(g)$  values are derived from the comparison with the isochrone. Apart from the effective stellar temperature and the metallicity  $[\text{Fe}/\text{H}]$  we also tabulate the membership probabilities as reported in chapter 3.

We can generally derive the effective temperatures of our stars with an uncertainty of 15-80 K for the brightest stars and 200-300 K for the fainter ones. Our metallicity uncertainties for the brightest stars are of the order of 0.05 dex, whereas for the fainter stars, that are harder to model, we still are able to obtain metallicity estimates with errors of 0.2-0.4 dex. When considering only those 26 stars with a membership probability of  $p > 0.5$ , the error-weighted mean stellar metallicity is  $[\text{Fe}/\text{H}] = -1.76 \pm 0.17$  dex. This is in good agreement with the  $[\text{Fe}/\text{H}] = -1.7$  dex derived with the best fit isochrone to the HST CMD (Weisz et al. 2015).

The broad spectral range of MUSE is very beneficial, as it covers many iron and other metal lines in the blue part of the spectrum. Most low resolution studies of metallicities in RGB stars of stellar clusters have to infer the iron abundances using only one, or very few strong absorption features, such as the Ca II triplet in the infrared.

In figures 4.2, 4.3 and 4.4 we show the detailed spectral features of the stars 5, 8 and 17 as examples of our data. Both, stars 5 and 8, are relatively bright stars, with  $m_I = 18.6$  and 18.9 respectively, whereas star 17 is much fainter at  $m_I = 20.7$ . Each plot has four different panels, in which different parts of the spectrum are shown in greater detail. In each panel, the blue line corresponds to the observed spectrum, whereas the best fit model is shown in red. We also show the corresponding residual below each panel. The top panel is zoomed onto the  $\text{H}\beta$  line, the Mg-b lines and several iron lines, whose positions are indicated with dashed vertical lines. The left middle panel is focused on the region of the sodium doublet, whereas the middle right panel displays the  $\text{H}\alpha$  absorption line. In the bottom panel the region around the Ca II triplet absorption feature is shown in detail.

For the two bright stars, the agreement of the model with the observed spectrum is excellent for the top panel. The  $\text{H}\beta$  line and the iron and magnesium lines are all very well fitted and no large systematic effects are visible in the residuals of both stars. For star 17 the spectrum is more noisy, but our routine is still able to identify the positions of the major hydrogen, magnesium and iron lines. From the residuals in the top panel of star 5 it is visible that several iron lines (e.g.  $\text{Fe}[5270]$ ,  $\text{Fe}[5406]$ ) are slightly too abundant in the model.

For both bright stars, 5 and 8, the sodium doublet is well detected (left middle panel), and well fitted by the stellar models. Only for the third noisy spectrum of star 17, the doublet is not detected. The strong  $\text{H}\alpha$  absorption line is shown in the middle panel on the right. It is also fitted well in all three stellar spectra, even if the central depth of the model is somewhat shallower than the observed spectrum. Even in the noisy spectrum of star 17 this feature is still very well fitted.

In the bottom panel the fit results of the Calcium triplet are shown for each star. The models do not reach the depth of the observed Ca II abundance for the central pixel of

the line in all three models, although the shape of the line is generally well fitted in the model. As the  $[\alpha/\text{Fe}]$  abundance was fixed to 0.4, the typical value of a globular cluster, it is unlikely that the models lack in calcium abundance. The same lack in depth in the central pixel was noted by [Husser et al. \(2016\)](#), but as the other lines are very well fitted, the lack of depth in the central pixel should not influence the final metallicities too much.

The three example spectra illustrate how well our models fit the stellar spectra even for weak absorption features. This is especially true in the blue parts of the spectrum. As the pipeline calculates the metallicity of the stars using the full spectral range with a large number of individual lines that are useful for the fit, it provides robust estimates of the iron abundances.

Table 4.1: This table summarises the stellar parameters of Crater stars. The first column lists the identifier, the second the  $I$  magnitude, the third column the  $\log(g)$  values, then the effective stellar temperatures, the iron abundances and the last column gives the membership probability for each star taken from chapter 3.

Index	$I_{\text{mag}}$ (mag)	$\log(g)$	$T_{\text{eff}}$ (K)	$[\text{Fe}/\text{H}]$ (dex)	membership probability
2	17.34	0.53	$4766 \pm 80$	$-2.21 \pm 0.06$	0.86
3	17.44	$5.02 \pm 0.05$	$3562 \pm 15$	$-0.59 \pm 0.04$	0.00
4	17.82	$4.56 \pm 0.04$	$3717 \pm 16$	$-0.73 \pm 0.04$	0.00
5	18.56	1.22	$4809 \pm 43$	$-1.58 \pm 0.04$	0.50
6	19.08	$4.41 \pm 0.09$	$6474 \pm 23$	$-2.47 \pm 0.11$	0.00
7	19.13	$4.45 \pm 0.09$	$6114 \pm 24$	$-1.74 \pm 0.04$	0.20
8	18.94	1.45	$4908 \pm 35$	$-1.64 \pm 0.04$	0.95
9	18.98	$3.81 \pm 0.10$	$3651 \pm 36$	$-0.97 \pm 0.08$	0.0
10	19.60	1.79	$5011 \pm 55$	$-1.76 \pm 0.05$	0.78
11	19.86	1.92	$5067 \pm 84$	$-1.76 \pm 0.07$	0.91
13	20.24	$3.80 \pm 0.34$	$5660 \pm 97$	$-1.78 \pm 0.11$	0.65
14	20.41	2.18	$5017 \pm 126$	$-2.04 \pm 0.12$	0.59
15	20.46	2.19	$5097 \pm 95$	$-1.63 \pm 0.09$	0.48
17	20.71	2.35	$5267 \pm 89$	$-1.78 \pm 0.10$	0.81
18	20.79	2.44	$5456 \pm 155$	$-2.05 \pm 0.20$	0.51
19	20.77	2.34	$4984 \pm 187$	$-2.02 \pm 0.21$	0.36
20	20.78	2.35	$5222 \pm 148$	$-1.91 \pm 0.17$	0.11
21	20.79	2.35	$5160 \pm 156$	$-1.95 \pm 0.16$	0.55
22	20.91	2.57	$5508 \pm 187$	$-2.06 \pm 0.24$	0.89
23	20.95	2.59	$5717 \pm 170$	$-1.81 \pm 0.23$	0.50

24	20.96	2.57	$5412 \pm 273$	$-1.74 \pm 0.26$	0.41
25	20.95	2.54	$5523 \pm 185$	$-2.04 \pm 0.22$	0.24
26	21.01	2.56	$5403 \pm 171$	$-1.88 \pm 0.16$	0.62
27	21.01	2.54	$5456 \pm 101$	$-1.88 \pm 0.11$	0.89
28	21.00	2.54	$5171 \pm 208$	$-2.15 \pm 0.20$	0.26
29	21.07	2.63	$5382 \pm 122$	$-1.93 \pm 0.15$	0.79
30	21.11	2.64	$5521 \pm 236$	$-2.18 \pm 0.25$	0.81
33	21.23	2.59	$5042 \pm 268$	$-2.06 \pm 0.27$	0.67
34	21.30	2.62	$5415 \pm 236$	$-1.95 \pm 0.23$	0.91
35	21.32	2.60	$5555 \pm 187$	$-1.82 \pm 0.25$	0.60
36	21.32	2.55	$4957 \pm 293$	$-2.13 \pm 0.36$	0.73
37	21.46	2.73	$5570 \pm 245$	$-1.66 \pm 0.31$	0.75
38	21.57	2.79	$5440 \pm 156$	$-1.63 \pm 0.16$	0.89
39	21.89	2.96	$5665 \pm 210$	$-1.42 \pm 0.23$	0.84
40	21.90	2.94	$5132 \pm 331$	$-2.18 \pm 0.36$	0.91
48	22.20	3.32	$6500 \pm 262$	$-2.58 \pm 1.00$	0.95
49	22.06	3.07	$5370 \pm 306$	$-1.87 \pm 0.33$	0.94
50	22.09	3.04	$6102 \pm 257$	$-1.22 \pm 0.32$	0.71
51	22.00	2.84	$4592 \pm 344$	$-2.35 \pm 0.40$	0.15

#### 4.4.2 Colour magnitude diagram and metallicity

In figure 4.5 we show the colour-magnitude diagram of Craters stellar population, based on the  $g$ ,  $i$  photometry provided by Belokurov et al. (2014). The colour coding indicates the metallicity  $[\text{Fe}/\text{H}]$  as derived by the fitting routine. In the left panel the metallicities derived with the free surface gravity parameter routine are shown and in the right panel the version with fixed  $\log(g)$  values. In both panels, the Dartmouth isochrone with an age of 7 Gyr and  $[\text{Fe}/\text{H}] = -1.7$  is displayed in green and stars, for which we have no spectra, are marked as grey dots.

For both fitting versions we see a dependence of the metallicity on the luminosity of the red giant branch (RGB) stars. The metallicity for brighter stars is higher than for their faint counterparts. This effect is less pronounced for the fixed  $\log(g)$  version. The effect of the metallicity depending on the position on the RGB branch has already been noted by Husser et al. (2016) in the analysis of the metallicity of 12 000 stars in the globular cluster NGC 6397. They found an increase of the average metallicity along the RGB of 0.25 dex.

This effect is most pronounced for stars above  $I_{\text{mag}} < 19.5$  in the fixed  $\log(g)$  version. For red clump stars and fainter RGB stars, that have been determined as likely members of Crater, the metallicity is more homogenous. The largest difference between both panels are the stars that are offset from the isochrone. E.g. the two very red stars at  $g - i > 2.0$  are found to be rather metal-rich when we leave their  $\log(g)$  free and become much more metal-

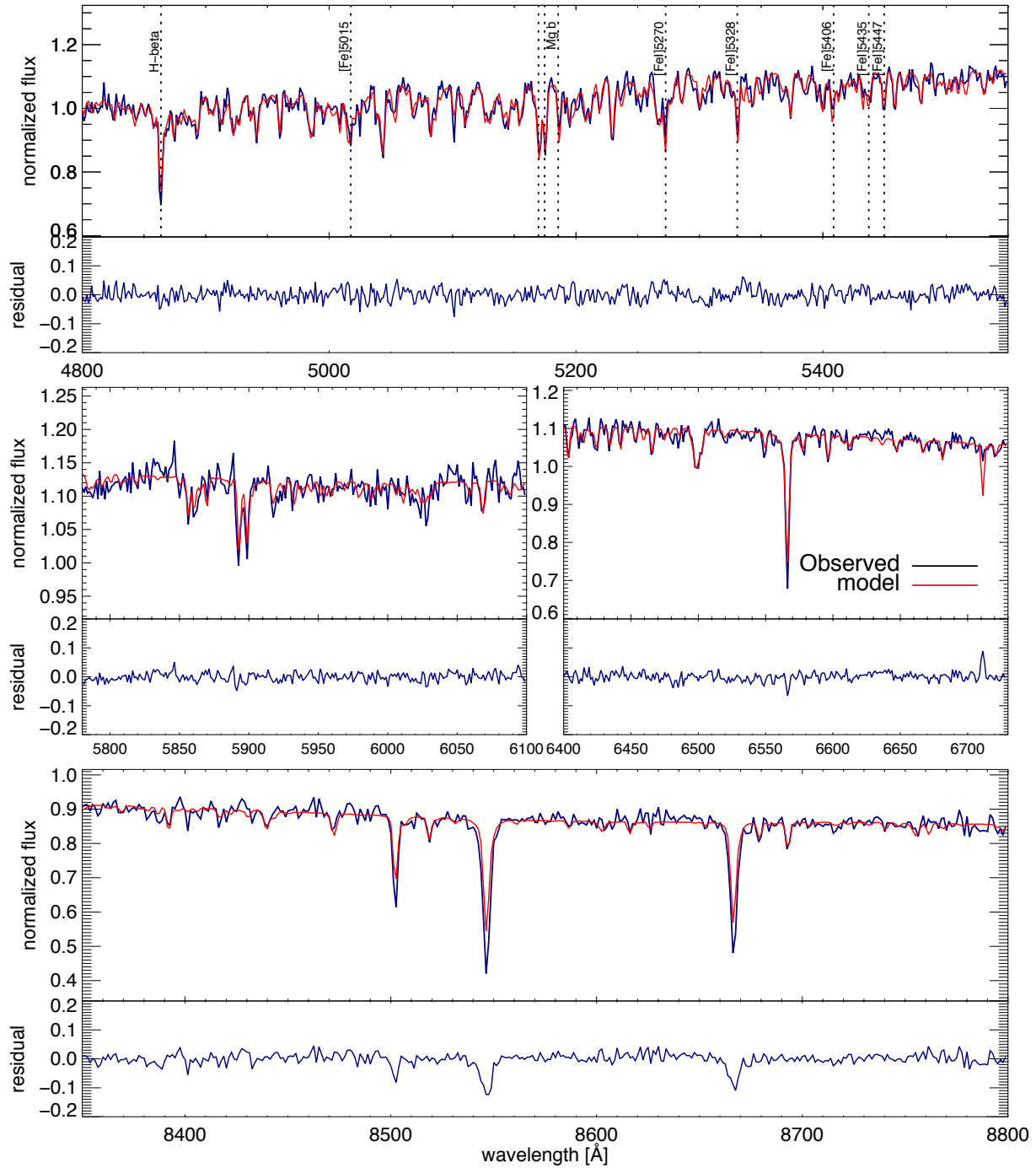


Figure 4.2: In this figure, the four main panels display different wavelength ranges of the spectrum of star 5. Each top panel displays the observed spectrum (blue) and the best-fit model in red. The corresponding lower sub-panel displays the residuals between model and spectra.



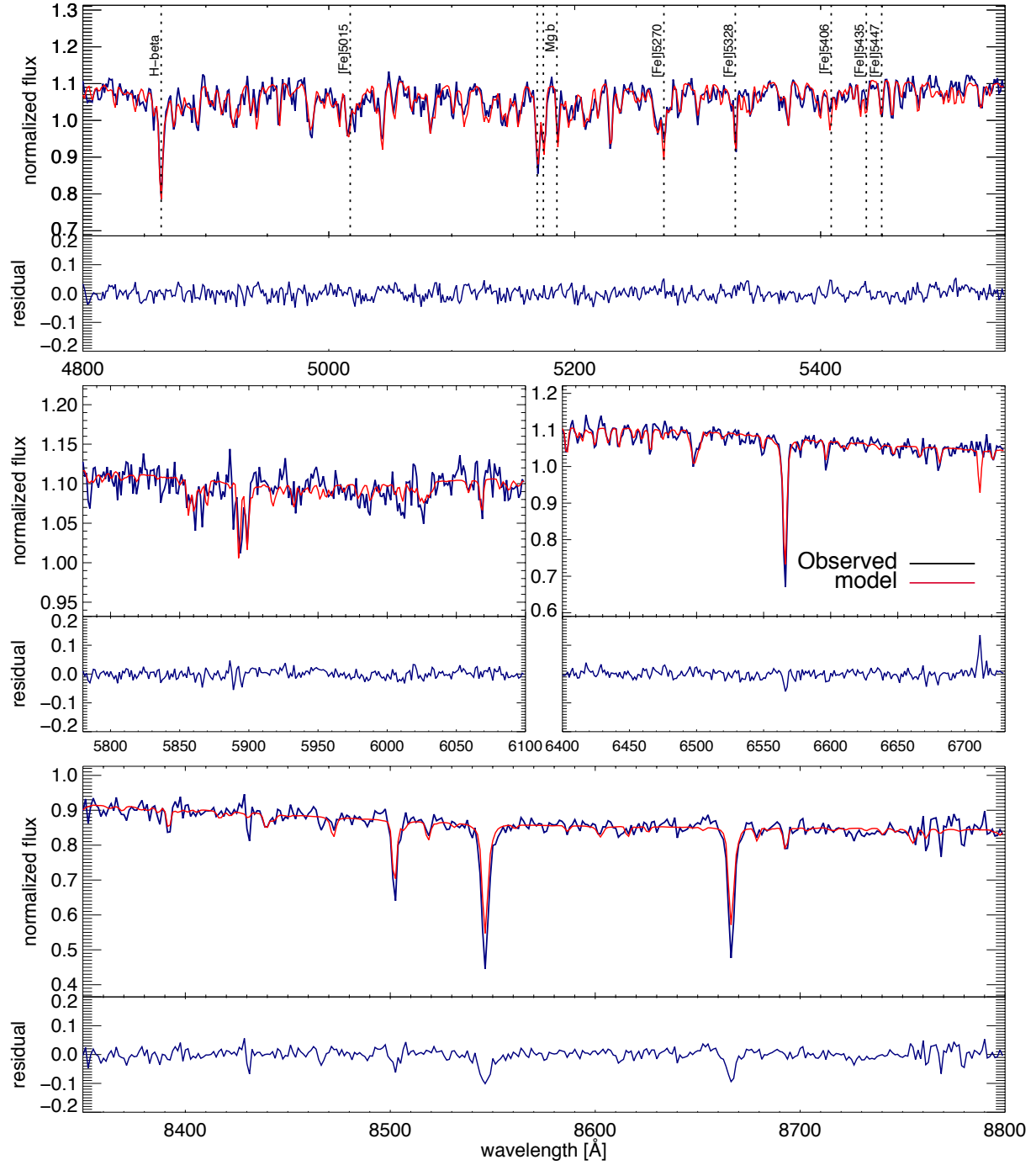


Figure 4.3: In this figure, the four main panels display different wavelength ranges of the spectrum of star 8. Each top panel displays the observed spectrum (blue) and the best-fit model in red. The corresponding lower sub-panel displays the residuals between model and spectra.

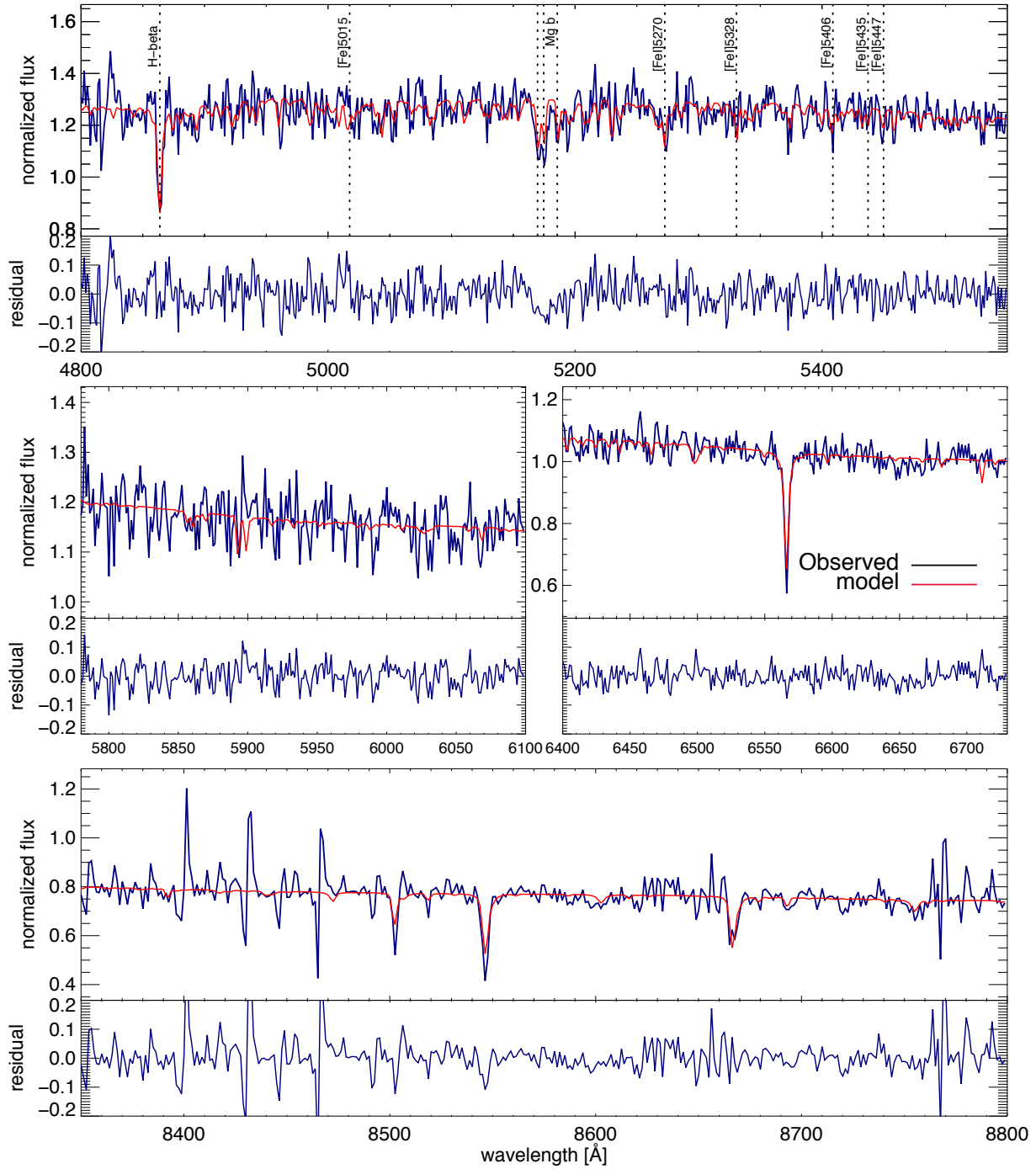


Figure 4.4: In this figure, the four main panels display different wavelength ranges of the spectrum of star 17. Each top panel displays the observed spectrum (blue) and the best-fit model in red. The corresponding lower sub-panel displays the residuals between model and spectra.

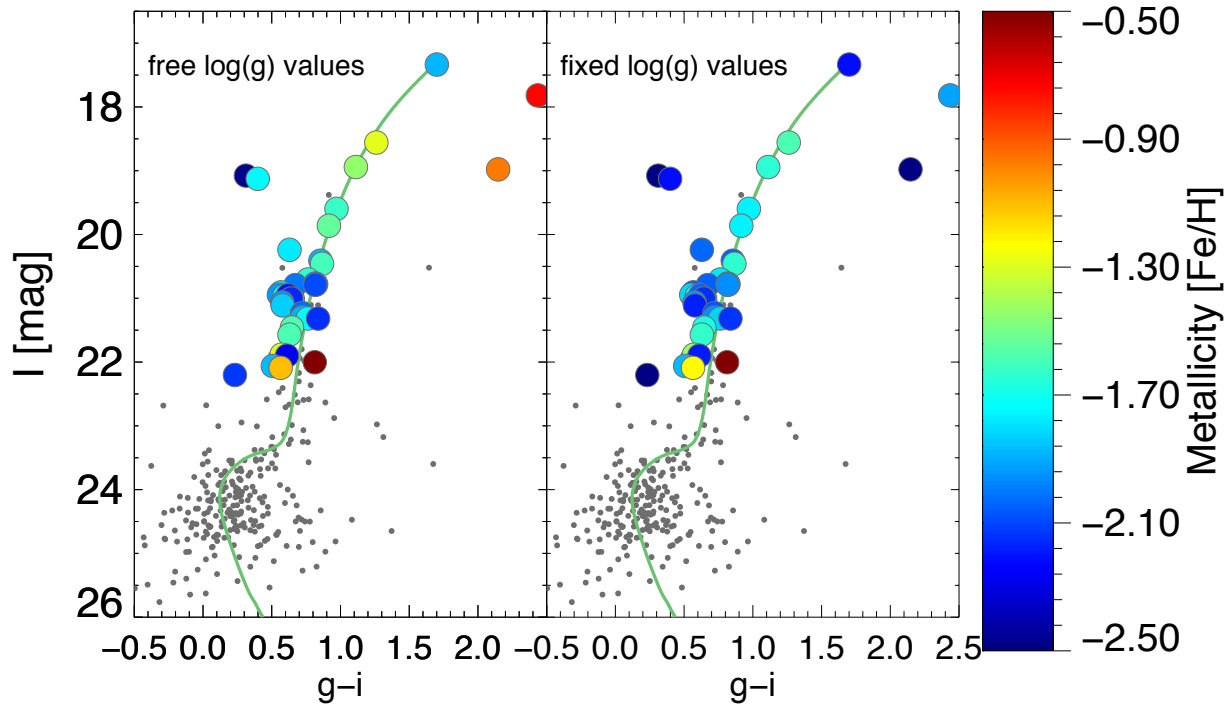


Figure 4.5: In both panels, the colour magnitude diagram of Crater stars is shown. In the left panel the colour-coding are the metallicity of the stars from the fitting routine that allowed the  $\log(g)$  values to vary. In the right panel, the colour-coding are the metallicities that are derived when fixing the surface gravities to the values given by the theoretical best-fit isochrone. The Dartmouth 7 Gyr isochrone with  $[\text{Fe}/\text{H}] = -1.7$  is displayed in green. Stars for which we have no spectrum are plotted as grey dots.

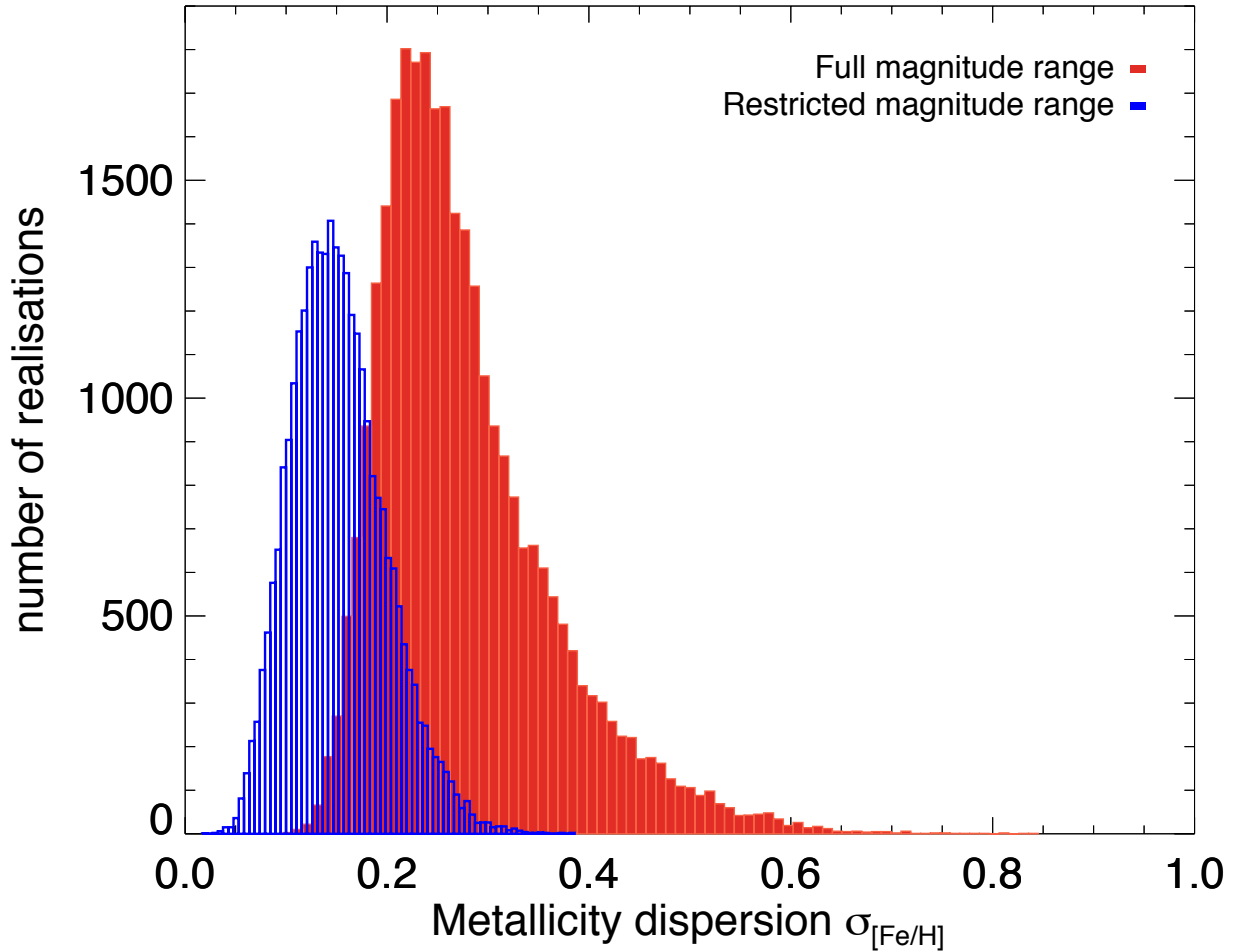


Figure 4.6: The two histograms show the distribution of the Monte Carlo realisations for the iron dispersion of stars with membership probabilities of  $p > 0.5$ . The red histogram uses the full magnitude range of possible member stars. For the blue histogram we restricted the magnitude range to  $19 < M_I < 21$  mag.

poor when we fix the  $\log(g)$  values to the isochrone values. Assuming a fixed isochrone  $\log(g)$  for stars that lie very far from the assumed isochrone is not meaningful. Therefore, for stars that are offset by more than 0.3 mag in colour from their nearest isochrone (stars No. 3, 4, 6, 7, 9, 13), we use the fit results with free  $\log(g)$  parameters. The parameters in terms of  $T_{\text{eff}}$ ,  $[\text{Fe}/\text{H}]$  and  $\log(g)$  for all stars with a spectrum, are summarized in table 4.1.

#### 4.4.3 Iron spread

We use the stars with a membership probability of larger than 0.5 (from chapter 3) to determine if there is a significant iron spread present in Crater. An iron spread of  $\sigma_{[\text{Fe}/\text{H}]} > 0.5$  dex generally indicates a dwarf galaxy, whereas iron spreads that are smaller than

0.1 dex usually indicate a globular cluster. To determine the iron spread of Crater stars we ran a Monte Carlo routine that takes into account the individual errors on the measured metallicities.

For each of the member stars, we draw a random number from a gaussian distribution with the width of its corresponding errorbar. This is repeated for each star in the sample and then the dispersion is calculated for this set of metallicities. This is repeated for 30000 trials. A Monte Carlo routine is an easy way to check the dispersion distribution for values with different errorbars. In Fig.4.6 the histogram of iron spreads  $\sigma_{[\text{Fe}/\text{H}]}$  from the Monte Carlo trials for all stars is shown as the red histogram. Using the cumulative normalised distribution of the realisations, we can determine the median value and the  $1-\sigma$  intervals of this intrinsically non-symmetric distribution of realisations. We derive a dispersion for the iron abundance of Crater member stars of  $\sigma_{[\text{Fe}/\text{H}]} = 0.25^{+0.10}_{-0.05}$ . The errorbars represent the width of the Monte Carlo trials distribution which is asymmetric.

In Fig.4.5 it is visible that the metallicity of Craters stars depends on the position along the red-giant branch. Brighter stars are more metal-rich than their fainter counterparts. This systematic effect has to be taken into account when determining the intrinsic iron spread. To test if there is a significant dependence of metallicity on the brightness of the star we plotted the iron abundance vs. luminosity in Figure 4.7. Here the stars with a membership probability of  $p > 0.5$  are shown as blue triangles, and the other stars in the sample as red points. In black we display the average metallicity of the likely members, for 7 bins in magnitude. Due to the small number of stars at bright magnitudes we use a bin size of one magnitude from 18-20 magnitude and after that we use half magnitude bins. We see a clear dependence of metallicity with magnitude. The average metallicity for stars between 18 and 20 magnitude is  $[\text{Fe}/\text{H}] = -1.68$ , for the following three bins the average is  $[\text{Fe}/\text{H}] = -1.88$ . For the faintest two magnitude bins, this average rises again to  $[\text{Fe}/\text{H}] = -1.60$ , but measured values in these bins possess large errorbars due to the low S/N in this regime. Within 18 to 21 magnitude, there is an amplitude of 0.2 dex for the metallicity distribution of Crater stars. This systematic trend influences the iron spread we calculate from the stellar population. A dependence on luminosity is not expected for the intrinsic iron spread in the stellar population of a GC.

Therefore, we rerun our original Monte Carlo realisation for a restricted luminosity range between  $19 < M_V < 21$ . We do not include the faintest stars as their metallicities are derived from low signal-to-noise spectra, and therefore have a large intrinsic scatter. We do not include the stars brighter than 19 mag as we have a clear systematic trend towards higher metallicities among brighter stars in figure 4.7. In restricting the range we aim to estimate the true intrinsic spread for a less systematically biased sample. The realisation of the Monte Carlo routine with the restricted magnitude range is shown as the blue histogram in Fig. 4.6. It shows a lower iron spread than the histogram for the full magnitude range. The dispersion obtained from the restricted magnitude range (blue histogram) is  $\sigma_{[\text{Fe}/\text{H}]} = 0.15 \pm 0.05$  dex.

The iron spread from the restricted magnitude range is consistent at the lower limit with the maximum spread of 0.1 dex for globular clusters. In Figure 4.12 the literature values for iron dispersions are plotted together with the result for Crater. It is visible that

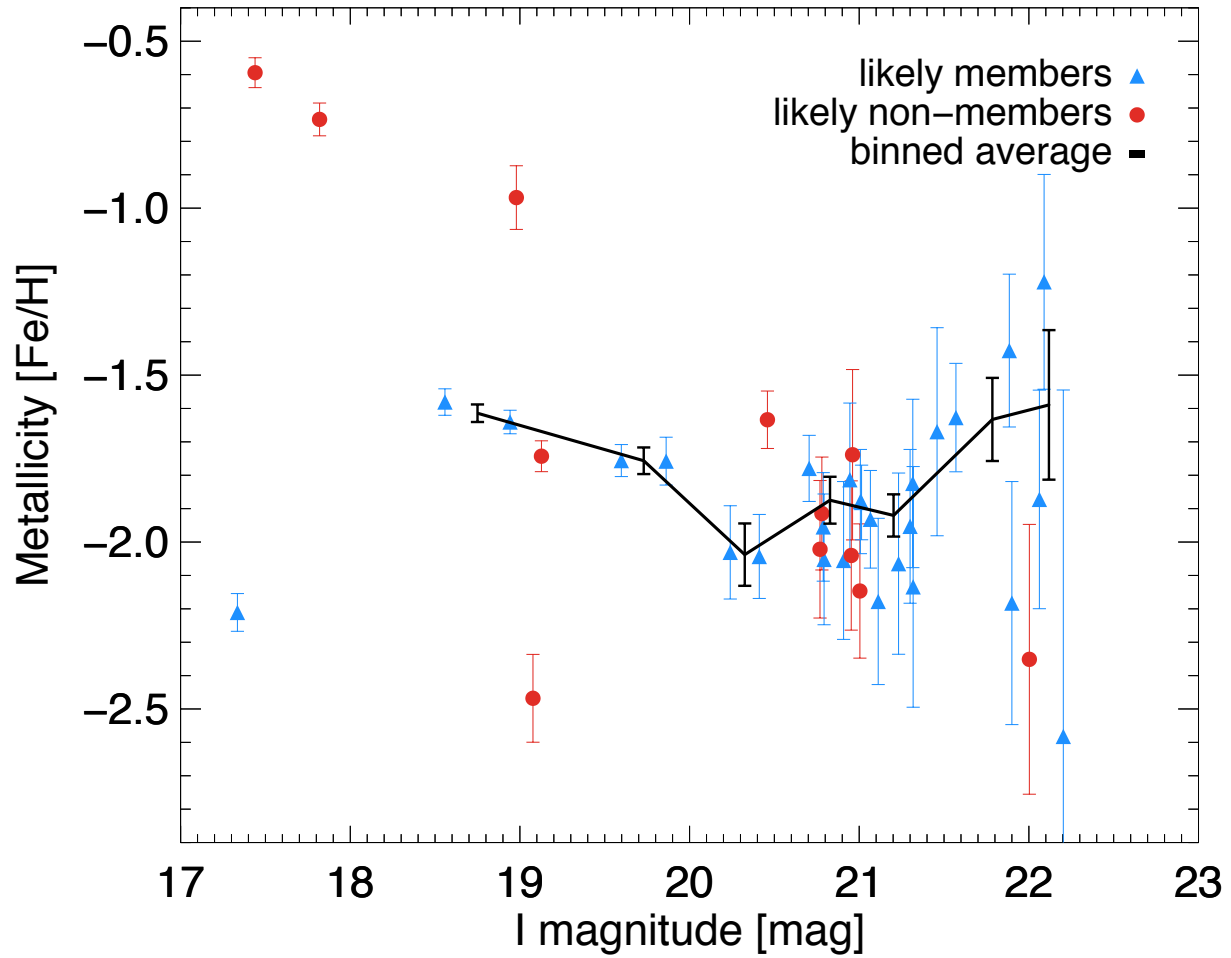


Figure 4.7: Here the metallicity distribution as function of the magnitude of the stellar population of Crater is shown. Blue triangles show stars with a membership probability of  $p > 0.5$ , and stars with smaller membership probabilities are shown as red points. A binned average of the metallicities of the probable member stars is marked in black. The bins have sizes of one magnitude between 18 and 20, and at fainter magnitudes are divided in half magnitude bins.

Crater is much closer in its dispersion value to GCs than to typical dwarf galaxies at the same magnitude. However, the iron spread is still higher than the 0.05 dex that one would expect for an average globular cluster of Craters brightness.

#### 4.4.4 Metallicity-velocity distribution

The distribution of the metallicity of Crater stars as function of the radial velocities is shown in the top panel of Figure 4.8. The radial velocities are taken from chapter 3. Those stars that have a membership probability of  $p < 0.5$  are plotted in red, whereas the blue points mark stars with  $p > 0.5$ . The bottom panel shows the  $[\text{Fe}/\text{H}]$  metallicity histogram of those two distributions. Most of the stars are clustered around Craters systemic velocity of  $v_{\text{sys}} = 148.2 \text{ km s}^{-1}$  and its average metallicity  $[\text{Fe}/\text{H}] = -1.76 \text{ dex}$ . The likely foreground stars have often significantly higher or lower velocities than Crater and are clear outliers to the main accumulation of stars in the metallicity velocity plane. The three radial velocity confirmed foreground stars with  $v < 110 \text{ km s}^{-1}$  are the stars with high metallicities close to solar abundance, which is expected for the foreground distribution. We also find two stars that have higher radial velocities and much lower metallicities than the bulk of Craters member stars. Those are likely halo field stars.

The histogram of likely members (blue) in the bottom panel shows that the Crater stars are clustered around the mean  $[\text{Fe}/\text{H}] = -1.76 \text{ dex}$ . The metallicity histogram of the foreground stars is a relatively flat distribution (red histogram) that does have some excess at Craters peak metallicity distribution, suggesting that some of the medium probability stars between 0.25-0.5 might also be members of Crater.

#### 4.4.5 Hertzsprung-Russel diagram

Figure 4.9 shows the Hertzsprung-Russel diagram of Craters stars. The derived effective temperature  $T_{\text{eff}}$  of our best-fit models is plotted against the stellar luminosity. We plot the results for the fitting routine where we kept the  $\log(g)$  values fixed to their respective values derived from the isochrone (blue points) together with the results of the fit where  $\log(g)$  is a free parameter in the fit. In red, a Dartmouth isochrone (Dotter et al. 2008) with an age of 7 Gyr and a metallicity of  $[\text{Fe}/\text{H}] = -1.7 \text{ dex}$  is plotted. This is the same isochrone as shown in Fig. 4.5.

For the results of the fixed isochrones fits (blue data points) it is visible that the effective temperatures of Craters stars agree well with the isochrone position below a luminosity of  $L_{\odot} = 100$ . For the free  $\log(g)$  fits, the effective temperatures are offset roughly by 300 K to hotter temperatures, and their positions are in less good agreement with the theoretical RGB isochrone.

Stars brighter than  $L_{\odot} > 100$  on the RGB are significantly offset from the isochrone. Both datasets are shifted towards higher temperatures than what is predicted by the theoretical Dartmouth isochrone plotted in red. This effect is larger for the free  $\log(g)$  fits (orange triangles) and smaller for the case when we fix to isochrone surface gravity values.



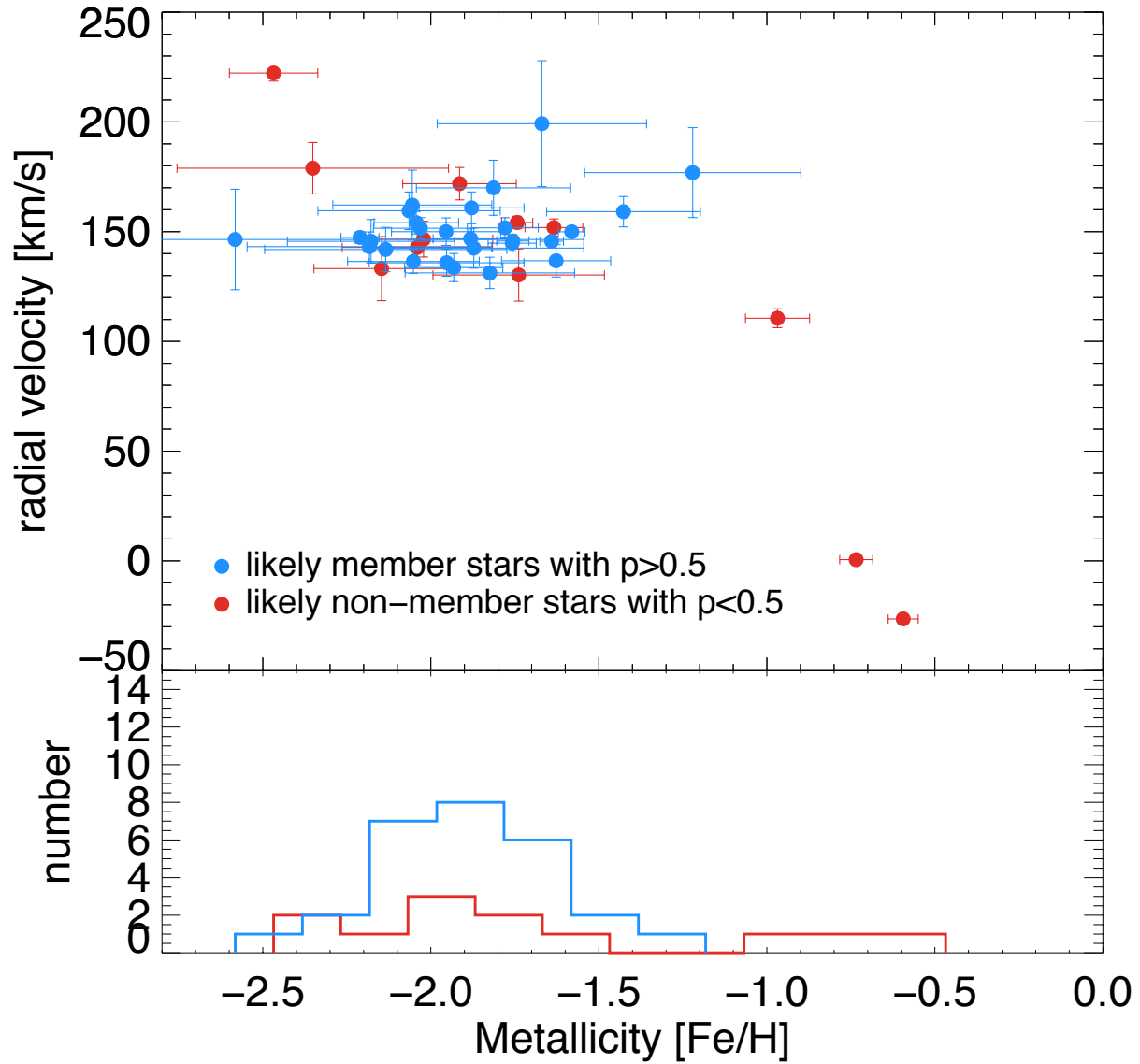


Figure 4.8: **Top panel:** The radial velocity of Craters stars are plotted against the metallicity [Fe/H]. Blue symbols mark stars with a membership probability larger than 0.5. The membership probability is taken from table 4.1. The likely non-members with a membership probability of 0.5 or less are shown as red points. **Bottom panel:** The metallicity histogram is shown with the same colour coding as in the top panel.

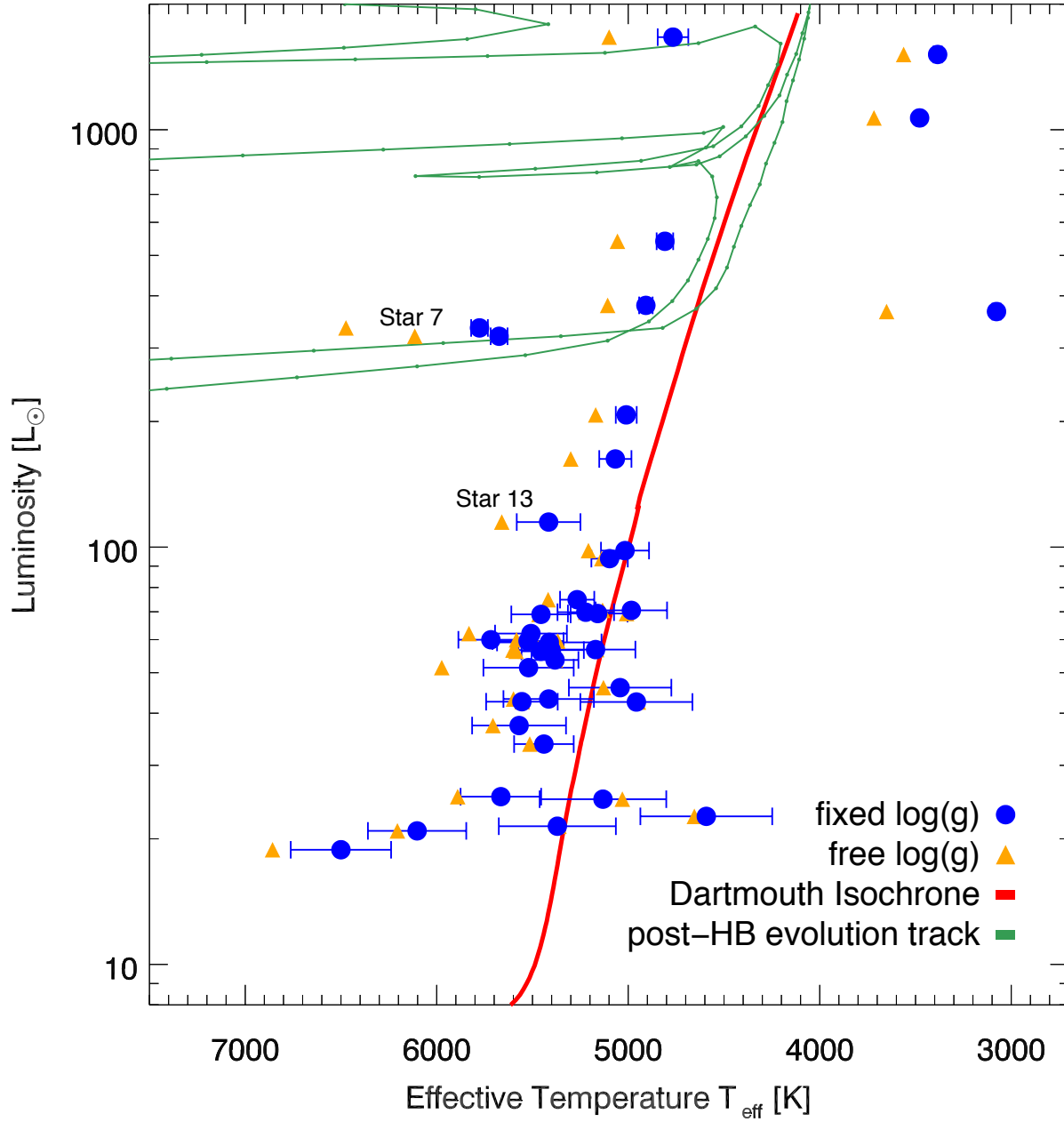


Figure 4.9: The Hertzsprung-Russel diagram of Crater stars. Luminosity is plotted against the effective temperature  $T_{\text{eff}}$  derived from the full spectral fits. The blue points mark the results for the fits with fixed  $\log(g)$ , and the orange triangles show the free  $\log(g)$  fits. The red line is the RGB part of the 7 Gyrs Dartmouth isochrone (Dotter et al. 2008), similar to the one plotted in figure 4.5. The green lines are the post horizontal branch evolution tracks of the Dorman et al. (1993) models.

The errorbars on the  $T_{\text{eff}}$  values are of the order of 15–60 K and not large enough to explain the offsets in the derived temperature.

For the two bright blue stars, we use the results from the free  $\log(g)$  fits (orange triangles) as a reference result. The fitting method derives a temperature of  $T_{\text{eff}} = 6114$  K for star 7, which locates it blue-wards of the red giant branch, in agreement with its position in the CMD (Fig. 4.5). The method similarly is able to detect the low stellar effective temperature  $\sim 3500$  K of the three foreground stars, that have been confirmed as such in chapter 3 using radial velocities.

The location of star 7 is of great interest, as its radial velocity is only a  $2\sigma$  outlier to Craters systemic velocity and it has a derived metallicity of  $[\text{Fe}/\text{H}] = -1.74$  which is in full agreement with Craters average metallicity. Its position in the Hertzsprung-Russel diagram is not easily explained. Compared with a normal horizontal branch star, it is 2.5 magnitudes brighter than expected. However star 7 might be in a post-horizontal branch stage of evolution.

Therefore, we compare the position of star 7 in the HRD to post-HB stellar evolution models from Dorman et al. (1993). In Fig. 4.9 we plot the post-HB evolutionary track of a  $M = 0.52 M_{\odot}$  star with a metallicity of  $[\text{Fe}/\text{H}] = -1.48$  in green. This was the available model with the closest metallicity compared to Craters. This evolutionary phase is predicted to last for 130 Myr in the model. Although this stage of evolution is short, the position of star 7 in the HRD is located very close to this evolution track. This makes it plausible that this star is a genuine Crater member star that is currently evolving off the HB.

The presence of blue stragglers in Crater, as indicated by the HST CMD, shows that this cluster has a significant fraction of binary stars. We also see a well populated red clump region. These are stars that move down to the HB and stay in the red clump for most of their core helium burning stage, due to their massive envelopes. Stars with smaller envelope masses move to the bluer and hotter parts of the horizontal branch, which is where star 7 must have come from if it is in a post-HB evolution stage. Therefore, star 7 has probably lost a significant fraction of its original envelope due to binary interaction, and thus lived its HB lifetime blue-wards of the red clump. The Dorman et al. (1993) models predict a surface gravity of 4.3 at the start of the evolution off the HB and at  $t=130$  Myr it has  $\log(g)=4.6$ . The  $\log(g)$  found by the free  $\log(g)$  fitting routine is  $\log(g) = 4.45 \pm 0.10$  for star 7, in good agreement with the expectations from the theoretical models. In the next section we will compare the spectra of star 7 and also star 13 to model spectra with several fixed  $\log(g)$  values, to test how solid these parameters are.

#### 4.4.6 The blue stars

The two blue stars (No. 7 and 13) are two special cases in the stellar population of Crater. As they do not lie on the RGB, but are offset towards the blue we did not use the fixed isochrone  $\log(g)$  values but let them vary for our initial fits. These initial fits derive a  $\log(g) = 4.45 \pm 0.1$  for star 7 and a  $\log(g) = 3.8 \pm 0.34$ . To test how solid these values are and if there are any degeneracies, we rerun our fitting analysis for several  $\log(g)$  values

log(g)	Red. $\chi^2$	[Fe/H] dex	$T_{\text{eff}}$ [K]
Star 7	S/N= 55.4		
1	3.40	$-2.71 \pm 0.06$	$5505 \pm 19$
2	3.25	$-2.22 \pm 0.05$	$5674 \pm 29$
3	3.08	$-1.89 \pm 0.04$	$5887 \pm 22$
4	2.94	$-1.73 \pm 0.04$	$6072 \pm 24$
Star 13	S/N=20.93		
1	2.49	$-2.39 \pm 0.12$	$5286 \pm 60$
2	2.48	$-2.13 \pm 0.15$	$5390 \pm 103$
3	2.47	$-1.82 \pm 0.09$	$5614 \pm 54$
4	2.47	$-1.78 \pm 0.10$	$5721 \pm 67$

Table 4.2: This table lists the stellar parameters of the fits to the two blue stars No. 7 and 13. Four fixed  $\log(g)$  values were tested. The first column shows the adopted fixed  $\log(g)$  values, the second column the reduced  $\chi^2$  of the spectral fit, the third column the resulting [Fe/H] values and the last column the effective temperature of the best-fit model.

ranging from the typical values for a red giant star, down to values of dwarf stars. We ran four fits with fixed  $\log(g) = 1, 2, 3, 4$ . These fits can then be compared to the actual observed spectrum. The details of all eight fits, with the reduced  $\chi^2$ , [Fe/H] and  $T_{\text{eff}}$  parameters are listed in table 4.2.

In figures 4.10 and 4.11 we plot three panels, which focus on different sections of the spectrum of star 7 and 13 in greater detail. The observed spectrum is shown in black and the four models with fixed  $\log(g)$  as coloured curves. The red line represents  $\log(g)=1$ , the orange line  $\log(g)=2$ , the green line  $\log(g)=3$  and the blue line  $\log(g)=4$ . For each panel we also show the residual between model and observations, right underneath with the same colour coding. As one can see in table 4.2, the reduced  $\chi^2$  decreases for models with higher  $\log(g)$  values. From  $\chi^2=3.40$  for the  $\log(g)=1$  models down to  $\chi^2=2.94$  for the  $\log(g)=4$  fit. Therefore, higher  $\log(g)$  values appear to better fit our spectra, which is mirrored in Fig. 4.10. For star 13 the  $\chi^2$  decreases only marginally by 0.02 towards higher  $\log(g)$  values and thus we are not able to discriminate between different  $\log(g)$  with much certainty.

In the top panels of Fig. 4.10 and 4.11 we display the H- $\beta$ -line and the surrounding metal lines. The different coloured lines indicate models with different  $\log(g)$  values. For both stars, all four models provide a reasonably good fit to the spectrum. However it is noticeable for both stars that the red and orange residuals are clearly larger for most absorption lines. These are the models with surface gravities of  $\log(g)=1$  and 2 similar to RGB stars.

The middle panel in Fig.4.10 and ?? is zoomed on the H- $\alpha$  line, with the four  $\log(g)$  model overplotted in different colours. This strong absorption line is most sensitive to  $\log(g)$  effects, as we are able to resolve the broad wings of the line with high signal-to-noise. For the high S/N spectrum of star 7 in Fig.4.10 the wings of the line are matched best by the  $\log(g)=4$  model in blue. The other models significantly underestimate the width of the line. For star 13 in Fig. 4.11 the shape of the H- $\alpha$  line cannot discriminate between the different model  $\log(g)$  due to the lower S/N of the spectrum.

The bottom panel focuses on the Ca II-triplet lines and the surrounding metal lines. Although this region of the spectrum is noisier, the differences between models of the different  $\log(g)$  values are large. This is in a large part due to the changing metallicity for the different  $\log(g)$  fits. For the  $\log(g)=1$  model, the measured metallicity is  $[\text{Fe}/\text{H}] = -2.71$  and for the  $\log(g)=4$  model it is determined as  $[\text{Fe}/\text{H}] = -1.73$ . The three Calcium lines are not deep enough for the red and orange models as they have a very low metallicity. In addition, the absorption lines in between the main Ca lines, e.g. at 8605 Å, are overestimated in the small  $\log(g)$  models. Therefore it is apparent that our spectrum of star 7 agrees best with models for a large  $\log(g) = 4$ . The metallicity of the  $\log(g)=4$  fit is derived as  $-1.73$  dex and is in very good agreement with the average metallicity of the other Crater stars of  $[\text{Fe}/\text{H}] = -1.76$  dex.

These results confirm that the surface gravities determined by the free  $\log(g)$  fits in the previous section are reliable and not influenced heavily by some degeneracies in the models or fitting routine.

## 4.5 Discussion

### 4.5.1 Metallicity and iron spread

We measure that Craters stars have an average metallicity of  $[\text{Fe}/\text{H}] = -1.76 \pm 0.17$  dex. This is consistent with the average abundance  $[\text{Fe}/\text{H}] = -1.68 \pm 0.05$  dex of the stars studied in Kirby et al. (2015). Metallicity measurements of Crater stars in the literature from Kirby et al. (2015) and Bonifacio et al. (2015) are listed in table 4.5.1. All three listed stars are in excellent agreement with the  $[\text{Fe}/\text{H}]$  values from Kirby et al. (2015). Star 8 is also consistent with the measurement of Bonifacio et al. (2015), whereas the metallicity of star 5 is a little lower in their work. In general however, our agreement with the three available literature measurements is excellent and shows that our metallicities are reliable estimates of the abundances.

We derive that Crater has a spread in iron abundance of  $\sigma_{[\text{Fe}/\text{H}]} = 0.15 \pm 0.05$  dex when only considering stars between  $19 < I < 21$  mag. This restriction is necessary since the metallicity of RGB stars increases with decreasing magnitude. Stars fainter than  $I = 21$  dex have large uncertainties in the measurements, due to low S/N. The derived iron spread is consistent, at the lower limit, with the maximum spreads of 0.1 dex in  $[\text{Fe}/\text{H}]$  among globular clusters. Although this iron spread is elevated compared to most globular clusters which have generally 0.05 dex, it also does not meet the criteria for an iron spread

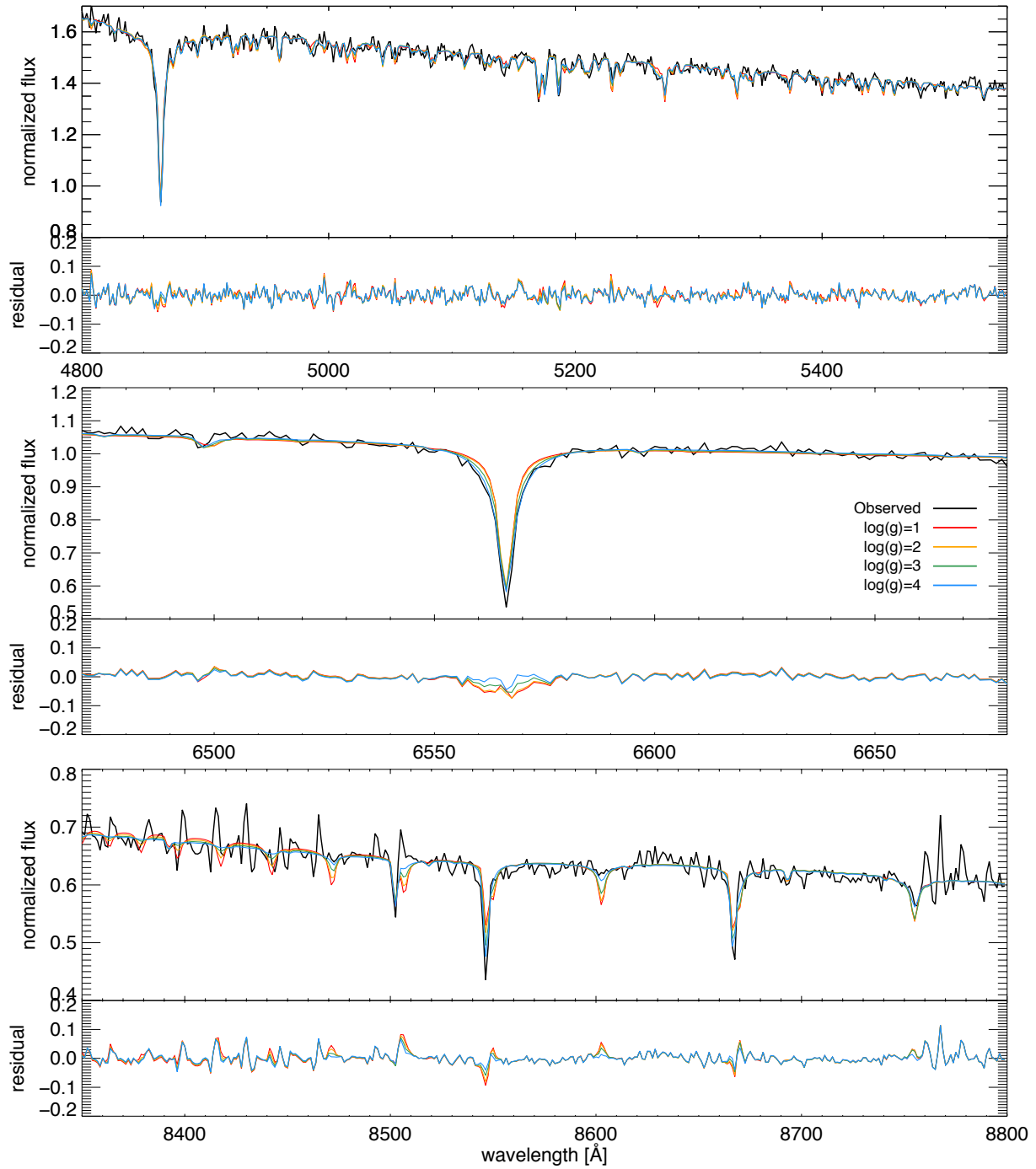


Figure 4.10: Three detailed parts of the spectrum of star 7 are shown as black line, with the residual in the panel to the bottom of each spectrum. In all three panels, the observed (black) spectrum is compared to the four stellar models plotted as coloured lines, as explained in the legend of the middle panel

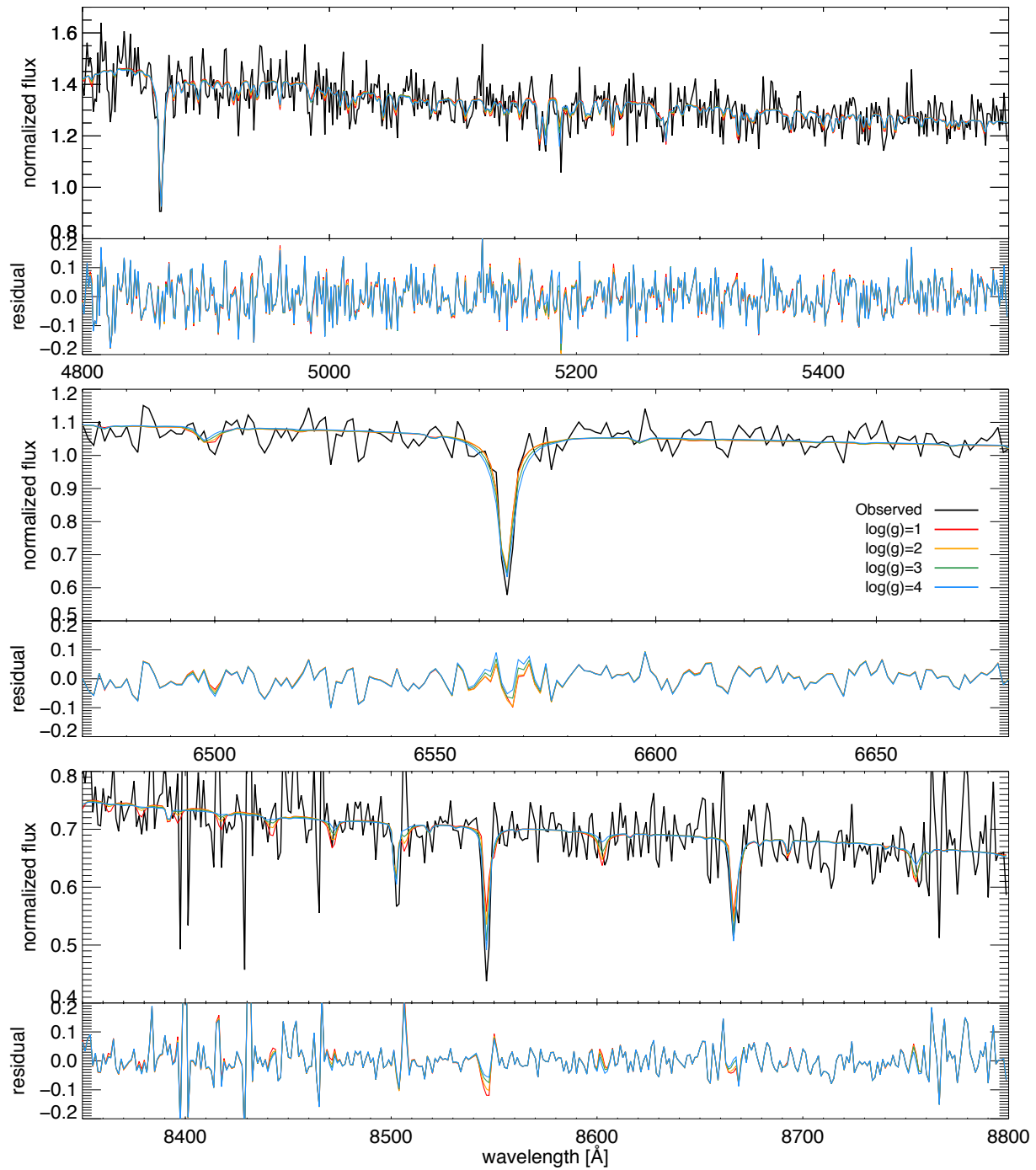


Figure 4.11: Three detailed parts of the spectrum of star 13 are shown as black line, with the residual in the panel to the bottom of each spectrum. In all three panels, the observed (black) spectrum is compared to the four stellar models plotted as coloured lines, as explained in the legend of the middle panel



Star No	This work dex	Kirby et al. dex	Bonifacio et al. dex
5	$-1.58 \pm 0.04$	$-1.55 \pm 0.11$	$-1.73$
8	$-1.64 \pm 0.04$	$-1.65 \pm 0.11$	$-1.67$
19	$-2.02 \pm 0.21$	$-2.10 \pm 0.21$	-

Table 4.3: This table lists the metallicity of the stars that also have literature values. The first column lists the identifier and the second column the values measured in this work. The third column lists the values from Kirby et al. (2015) and the last column the values from Bonifacio et al. (2015).

that is typical for dwarf galaxies in this magnitude range, for which one would expect a spread  $\sigma_{[\text{Fe}/\text{H}]} > 0.55$ .

In Figure 4.12 the literature values for the iron dispersions in GCs and dwarf galaxies are plotted together with the result for Crater. It is evident that Crater is much closer in its dispersion value to GCs than to the typical dwarf galaxies at its magnitude. However, if our errorbars are reliable, it is not as homogenous as one would expect for a cluster of Craters brightness, as these have spreads that are usually smaller than 0.05 dex. Craters spread in iron abundance is significant at  $0.15 \pm 0.05$  dex. The findings are consistent within  $2\sigma$  with a standard globular cluster iron spread, and consistent within  $1\sigma$  with GCs such as M 22 and M 54 which have spreads of  $\sim 0.1 - 0.2$  dex. The dwarf galaxies at this magnitude have iron spreads of larger than 0.55 dex, which is a  $6\sigma$  outlier to our findings for Crater. As Crater is much more similar to GCs and their abundance patterns, this is in agreement with the confusion drawn from the dynamical study in chapter 3.

Heavy element enriched globular clusters are currently only observed in clusters that are much brighter and massive than Crater. With  $M_V = -8.5$  the GC M 22 is currently the faintest one to exhibit a spread in heavy elements. With its magnitude of  $M_V = -5.5$  Crater is fainter by three magnitudes than M 22. The dynamical mass of  $M = 1.5 \times 10^5 M_\odot$  that we derived in chapter 3 would not be enough for self-enrichment scenarios to allow Crater to retain some of its supernova ejecta. If we assume that the iron spread is due to self-enrichment that would lead to the expectation, that Crater must have been much more massive in the past and has lost a substantial amount of its initial mass.

We also found that the average metallicity of brighter stars on the RGB is higher by 0.2 dex than for their fainter counterparts. This dependence of metallicity on magnitude was already observed in NGC 6397 by Husser et al. (2016). One explanation of the increase in metallicity of RGB stars is the assumption of a local thermo-dynamic equilibrium (LTE) in most stellar models that might not hold for RGB stars anymore. However, in Bergemann et al. (2012) the systematic uncertainty of LTE models was compared to those including non-LTE effects and the maximum difference was found to be 0.1 dex. Thus NLTE effects are not large enough to explain the observed differences.

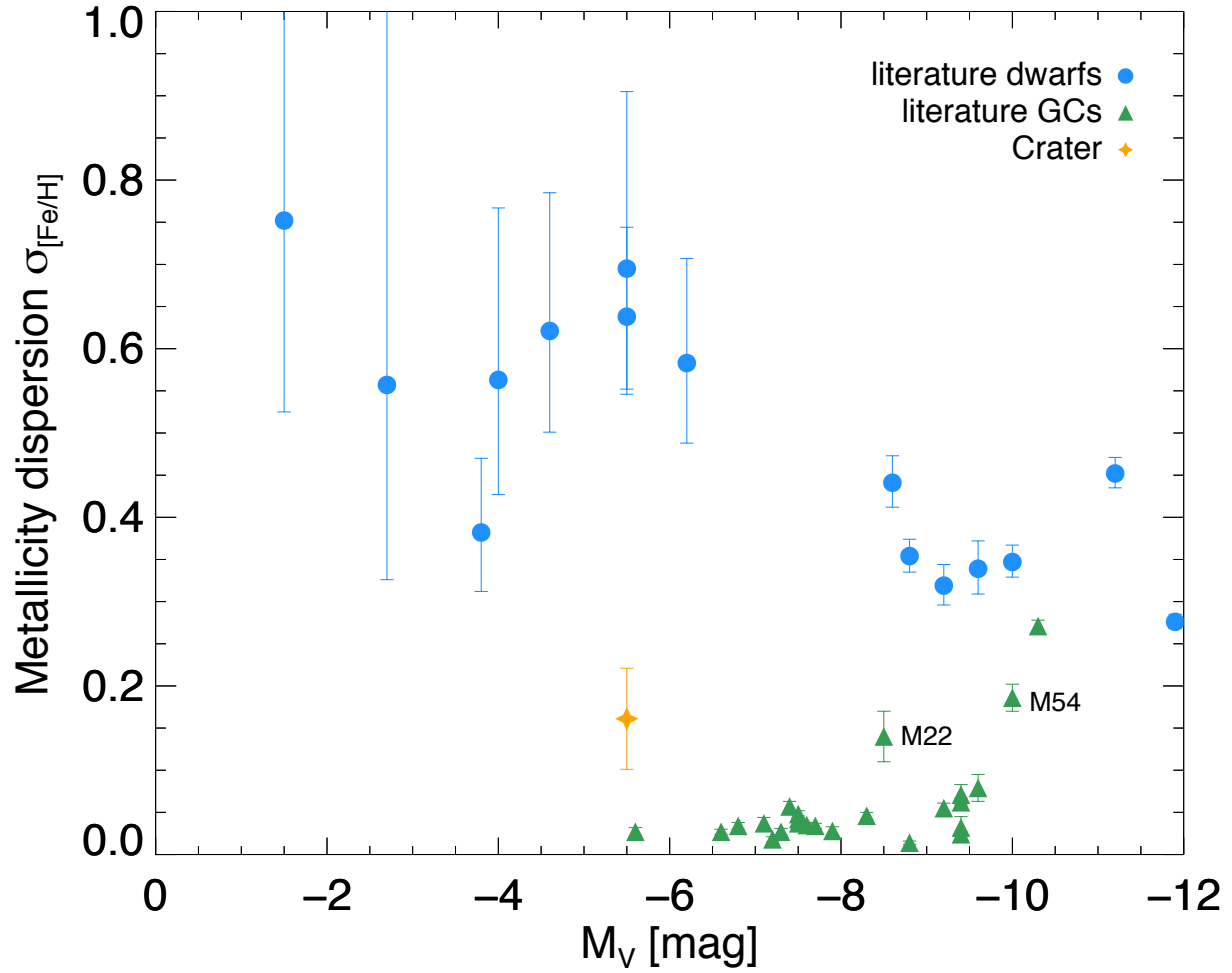


Figure 4.12: The dispersion in iron abundance  $\sigma_{[Fe/H]}$  is plotted against the absolute magnitude of the objects. The blue points mark objects that have been classified as dwarf galaxies, whereas the objects known as globular clusters are shown as green triangles. Crater is plotted as an orange star symbol. The literature values are all taken from [Willman & Strader \(2012\)](#), except for the value for M 22, which is taken from [Carretta et al. \(2009b\)](#).

### 4.5.2 What is the nature of the blue stars?

From our metallicity analysis using free  $\log(g)$  values, we find that star 7 has an iron abundance of  $[\text{Fe}/\text{H}] = -1.73 \pm 0.04$  dex, which is fully consistent with the weighted average metallicity of Craters stars of  $[\text{Fe}/\text{H}] = -1.76$  dex. Star 13 with  $[\text{Fe}/\text{H}] = -1.78 \pm 0.11$  dex is also consistent with the overall metallicity of Crater within its errorbars. In Chapter 3 it was found that star 7 is a  $2\sigma$  outlier from Craters systemic velocity and star 13 is fully compatible with the systemic velocity of Crater. Considering the velocity and metallicity results for these two blue stars it becomes apparent that at similar velocities and metallicities, they are likely members of the system. The chances of foreground stars from the Milky Way being at the same location, velocity and metallicity as Crater are extremely small. Thus we conclude that stars 7 and 13 must be members of Craters stellar population.

Nevertheless, if these stars are members of Craters stellar system, the question remains: How can we explain the existence of the blue stars? The location of star 7 in the colour magnitude diagram is too far offset from the RGB towards the blue to be a red giant. Nor does it agree with the location of normal horizontal branch stars, as we expect the horizontal branch of Craters to be located at  $21 < I < 22$  mag, which is 2 magnitudes fainter than the observed magnitude of star 7.

Therefore, we compared the position of star 7 with post horizontal branch evolution models from Dorman et al. (1993). We find that the location of star 7 in the CMD agrees very well with what is predicted for the post-HB evolution of a  $M = 0.52M_{\odot}$  star with a metallicity of  $[\text{Fe}/\text{H}] = -1.48$  dex. In order to be located at such a blue colour in its post-HB evolution phase, the star must have lost a significant fraction of its stellar envelope. The colour of a horizontal branch star strongly depends on the amount of envelope mass they can retain after the RGB phase (e.g. Iben & Rood 1970). Because HB stars with low envelope masses occupy the blue parts of the HB branch. When these stars move onto the HB and ignite the core helium burning phase, their envelopes collapse.

Therefore, in order for star 7 to have become a hot HB star, it must have lost a significant fraction of its envelope mass in the RGB phase. Stars with more massive envelopes move down to the HB but stay all their core helium burning lifespans in the red part of the HB at the red clump. That star 13 is a red HB star appears very likely, as it is located only at slightly brighter magnitude than the bulk of the red clump stars.

One way of how star 7 could have lost its envelope mass is binary interaction with another star. Many blue stragglers were found in the HST study of Craters CMD (Weisz et al. 2015), pointing to a large abundance of binary stars in Craters stellar populations. It also has been found that clusters with lower stellar density, e.g. like Crater, have a higher binary fraction compared to their denser counterparts, due to the lower destruction rate of binary systems, thus increasing the plausibility of this scenario.

One argument against this scenario is the short lifetime of the post-HB evolution phase. The models of Dorman et al. (1993) predict a post-HB timespan of only 130 Myrs for this phase, making the occurrence of such a star quite unlikely, but it appears to be the only plausible explanation for its existence. In fact the existence of such stars has been

known since the work of [Zinn et al. \(1972\)](#), in which a systematic search within 27 GCs has revealed many member stars lying above the horizontal branch but blue-wards of the RGB. Populations of post-HB stars were detected in clusters. For example, in  $\omega$  Cen it was observed that 30 % of all horizontal branch stars are post-HB stars which are lying above the HB in terms of magnitude ([D’Cruz et al. 2000](#)).

The predicted  $\log(g)$  value of the HB model of [Dorman et al. \(1993\)](#) for a post-HB star is  $\log(g)=4.6$ , which is in good agreement with the measured surface gravity for the free fit of  $\log(g)=4.45 \pm 0.1$ . The tests with four different, but fixed  $\log(g)$  values, showed clearly that the shape of the various measured absorption lines is best fitted with a high surface gravity, essentially showing that the  $\log(g)=4.45$  and  $3.80$  values for stars 7 and 13 are not the result of a degeneracy in the method.

## 4.6 Conclusion

We conclude that our metallicity results combined with the dynamical study strongly reinforce the notion that Crater is a globular cluster and not a dwarf galaxy. Our metallicity analysis shows that although there is a detectable spread in heavy elements it is much closer to the normal GC abundance patterns. Albeit its measured spread of  $0.15 \text{ dex}$  in iron abundance, Crater it is consistent within  $2\sigma$  with the uniform iron abundance of a GC and a  $6\sigma$  outlier to the large spreads observed in dwarf galaxies at this magnitude. This strongly supports our findings from the dynamical study in chapter 3, where we find Crater to be consistent with a purely baryonic stellar system.

The two blue stars have metallicities that are consistent with the rest of the stellar population of Crater. Therefore, considering their position, velocity and metallicity we conclude that they must be members of Crater. They are not young stars, left over from a recent burst of star formation in Crater, but rather they currently are in the post horizontal branch stage of their stellar evolution.



# Chapter 5

## Summary and Outlook

This thesis studies the properties of diffuse star clusters/ultra-faint dwarf galaxies and ultra-compact dwarf galaxies (UCDs), to establish their nature and provide insights into their formation mechanisms. In terms of their sizes and magnitudes these objects are located in the gap region between classical dwarf galaxies and globular clusters, which challenged many previous definitions of what constitutes a star cluster and what is the definition of a galaxy. Such objects have only been discovered in the last 15 years and their formation and evolution is not yet understood.

The first part of this thesis consists of an observational study of deep photometric data on UCDs in the Fornax cluster. I decomposed the radial surface-brightness profiles of the UCDs into two components and discovered several UCDs with low surface brightness envelopes around their central compact component. These envelopes are the likely remnants of the dwarf galaxy that was stripped, and the remaining nucleus is the UCD. Moreover, this study also discovered for the first time significant tidal tails around some UCDs. In particular, UCD-FORS 2, which exhibits two large tails of 300 pc in size, is the most convincing "smoking gun" example of a UCD that has been possibly caught during the late phases of the stripping process.

In the first chapter of this thesis, I developed new ways of statistically constraining the contribution of different UCD formation channels to the total UCD population in the centre of the Fornax cluster. The signatures that provide evidence for the nature of UCDs, such as supermassive black holes and extended star-formation histories, are currently the only measured properties for individual UCDs and remain rare as they are observationally expensive. Thus, I developed a new method that tests if GCs are more abundant in the vicinity of UCDs than what is expected from their global distribution in the halo of NGC 1399 in the Fornax cluster. Indeed, local overabundance of GCs was found around UCDs on a scale of 0.5-1 kpc compared to the large-scale GC distribution. This clustering effect is stronger for the metal-poor blue GCs and weaker for the red GCs. Hence, I showed that UCDs harbour a population of close-by satellite point sources, which is consistent with left-over GCs of a dwarf galaxy in the stripping scenario.

In the second chapter of this thesis, I performed an observational study of Crater/Laevens I, a faint object that was discovered in the outer halo of the Milky Way. It has a controversial nature, as it was claimed by different studies to be an extended GC or an ultra-faint dwarf galaxy. The classification of Crater as a dwarf is based on evidence for a young blue population of stars. To determine if this object genuinely hosts multiple

stellar populations and if it contains dark matter, it was observed with the integral field spectroscopic instrument MUSE on the VLT. MUSE covers a large spectral range, has a wide field of view for an integral-field spectrograph and combines this with a high spatial sampling, ideally suited for extended objects.

Using radial velocity measurements in the Calcium triplet region, 26 stars of Crater were spectroscopically confirmed as members of Crater. Using a maximum likelihood analysis, the data reveal that Crater has a dynamical mass-to-light ratio of  $M/L_V = 8.52^{+28.0}_{-6.5} M_\odot/L_\odot$  which implies that it is consistent with a baryonic dominated stellar system, and there is no large amount of dark matter. The findings from the dynamical study strongly support that Crater is a faint intermediate-age outer halo globular cluster and not a dwarf galaxy. Surprisingly, the two blue stars that are not on the 7 Gyr isochrone have similar velocities as the main system. Their existence is very puzzling if they belong to the same population as all Crater member stars.

In the third chapter, I compared the MUSE spectra of each star over the full wavelength range with a synthetic stellar atmosphere library, to determine the metallicities of Crater's stars. In particular, the metallicity analysis shows that although there is a detectable spread in heavy elements of  $\sigma = 0.15 \pm 0.05$ , it is consistent within  $2\sigma$  with the standard 0.05 dex iron dispersion pattern of a GC, and it is a  $6\sigma$  outlier to the large spreads observed in dwarf galaxies at this magnitude. This finding gives further support to the notion that Crater is a GC and not a dwarf galaxy. This is consistent with the findings from the dynamical study where no strong evidence for the presence of dark matter was found.

The spectroscopy shows that two of the very blue stars have metallicities that are consistent with the rest of the stellar population of Crater. Therefore, taking into account that the velocity and metallicity of the two blue stars are consistent with the average population, they most probably are member stars of the system. The detailed comparison of their spectra with the models revealed that they have high surface gravities of  $\log(g) \sim 4$  and positions in the CMD that are consistent with evolution models for post-horizontal branch stars. Therefore it is concluded that these peculiar blue stars are not young stars left over from a recent burst of star formation, but that the most plausible explanation is that they are currently in the post-horizontal branch stage of their stellar evolution.

## 5.1 Future prospects

### 5.1.1 Ultra-compact dwarf galaxies

The research that has been conducted in this thesis can be advanced and developed in several ways that I will discuss in this section.

The UCDs with tidal tails are prime targets for future studies testing UCD formation theories. Spectroscopic follow-up observations will be able to confirm if the tidal tail UCDs are actually stripped nuclear star clusters from a dwarf galaxy. A study of the stellar population of bright UCDs with tidal tails is possible up to the distance of Virgo/Fornax. An instrument such as X-SHOOTER on the VLT would be able to provide crucial information



on their internal composition. Such detailed follow-up spectroscopy can determine if these UCDs have an extended star formation history, have a spread in metallicity or host a central black hole, all signatures of nuclear star clusters. In order to detect black holes in the centres of UCDs, adaptive optics assisted IFU observations are needed. Such observations will be possible with future upgrades such as the upcoming narrow field adaptive optics mode on MUSE. The tidal tail UCDs are the best candidates to improve our understanding of the tidal stripping UCD formation channel. Combined with the photometric evidence for tidal interactions from this work, follow-up work can provide the missing evolutionary link between dwarf galaxies and UCDs.

In models of tidal stripping for UCD formation, the newly discovered envelopes surrounding them are predicted when a dwarf galaxy is stripped down to its nucleus. The envelopes serve as an intermediate step in the morphological sequence that connects nucleated dwarf galaxies with UCDs. I have shown in this work that, for the first time, such envelopes can be detected with very good seeing ground-based imaging, and not only space-based imaging. A prospect is, therefore, to extend deep, wide-field photometric surveys in good seeing conditions that enable the envelopes to be resolved from ground-based imaging to more clusters and different environments. Such complete and homogenous surveys will provide an assessment of the presence and statistical abundance of envelopes around UCDs in a more complete manner than was possible in the first studies that have been carried out. This is necessary to establish the comprehensive fraction of UCDs that are stripped dwarf nuclei, and whether they depend on their environment. The frequency and structure of envelope components surrounding UCDs will provide important constraints on the evolution timescales and efficiency of tidal stripping of UCDs. This will be useful to model the evolution of UCDs in further depth.

The newly developed GC clustering approach to study an entire population of UCDs in a statistical manner provides a way forward in UCD studies. So far, they mainly consist of either photometric studies of large numbers of UCDs or very detailed studies of individual UCDs. This statistical approach can provide the link between the features of individual UCDs and their large-scale distribution, to bring them together into one homogenous picture. One way to accomplish this is to investigate whether the clustering of GCs around UCDs is an actual physical connection.

For this, it is necessary to perform large spectroscopic surveys that provide radial velocities for UCDs and the fainter GCs in galaxy clusters. Obtaining precise radial velocities of candidate GCs in the close vicinity of UCDs to determine if they share the same radial velocity is thus the natural next step. If such associations can be confirmed, this would be evidence that these UCDs formed as nuclei, and what we see is the remnant GC population of their ancestor galaxy. Using the data from large spectroscopic surveys to map the spatial and velocity phase space of UCDs and GCs would provide crucial information on the existence of other GC substructures, such as streams that are leftovers from the infall and stripping history of the dwarf galaxies. Doing this with UCDs provides the advantage that GCs are point source tracers, and visible to much larger distances than low-surface brightness stellar streams.

### 5.1.2 Ultra-faint dwarf galaxies and extended star clusters

Several large imaging surveys such as SDSS, Pan-STARRS or VST ATLAS have discovered new ultra-faint dwarf galaxies (UFDs) and extended star clusters, and the sample of known ultra faint objects in the Milky Way halo and the Local Group has increased significantly in recent years. New surveys extending to fainter magnitudes and covering further parts of the sky will expand the sample size of ultra-faint objects even further. To settle the nature and formation of UFDs and extended star clusters, extended datasets measuring precise radial velocities and metallicities for the stars of every object will be required to improve our general picture of ultra-faint objects.

Because of the extremely low stellar content, UFDs are the main targets when searching for the dynamical effects of dark matter. Their kinematic behaviour will help to settle their nature and improve our understanding of galaxy formation and dark matter clustering on the smallest known scale. The small-scale study of dark matter clustering is currently confined to the dwarfs in the proximity of the Local Group, where individual stars can be resolved. Thus the Local Group dwarf satellites are the prime targets to study their precise dynamics from the stars themselves, as tracers of the gravitational potential.

To extend the work on ultra-faint dwarf galaxies, it will be necessary to increase the number of studied dwarf galaxies, while at the same time covering a larger number of stars that extend beyond the half-light radius in each dwarf galaxy. Measuring not only the central velocity dispersion, but extending the kinematic studies to more distant stars of the dwarf galaxy, and going deeper in the CMD to faint stars, will help to identify the shape of dark matter profiles. Such new precision measurements of large numbers of stars in each dwarf galaxy will provide a less biased picture of dwarf galaxy dynamics than what can be measured with small numbers of central and bright RGB stars. New integral field instruments like MUSE can contribute tremendously, as their wide field of view allows to study the resolved stellar populations without pre-selecting the target stars, thus providing a more complete and unbiased picture.

Very distant outer halo globular clusters are widely believed to have been stripped from accreted dwarf galaxies. Intriguingly, Crater is aligned on one great circle with the neighbouring dwarf galaxies Leo IV and LeoV, and also shares similar radial velocity with them. A physical association of Crater with Leo IV and LeoV due to a common origin of these objects has been suggested. By measuring its detailed chemistry, we can compare them to the stars of potential former host galaxies, and determine if their properties match. To find the progenitor it will also be crucial to do a precise proper motion study of Crater and its surrounding dwarf galaxies with HST or in the future JWST. A physical association of those objects would provide important constraints for the dynamical models that study the hierarchical assembly history of the Milky Way.

The new method to constrain the systematic instrumental velocity uncertainty of MUSE spectra that was developed in this work also has many future follow-up applications. As integral field studies of stellar populations become more common, so does the need to do an absolute velocity offset correction and determine the intrinsic instrumental uncertainties. The method was already applied to several other MUSE cubes of globular clusters. The

principle of the two-dimensional velocity corrections is essential when performing precision IFU studies close to the velocity resolution of the instrument. This method is also applicable to future IFU instruments and other datasets.

Crater is an important precedent for future studies of the formation of extended star clusters. Extended clusters with half-light radii of more than 10 pc were found in the Milky Way, within dwarf galaxies (such as Sc22 in the Sculptor group), and in Andromeda. We currently do not understand how extended star clusters form. Do they have large radii due to tidal interactions that increases their sizes? Or does GC formation occur in two intrinsically distinct modes, one "normal" compact mode and an extended mode with large half-light radii? In the two-modes picture, the extended GCs form naturally with larger sizes within the low stellar density environment of a dwarf galaxy. As a result of the controversy about Craters nature and its proximity, it is one of the best studied extended clusters and will provide further insights into extended cluster formation. Detailed studies of the internal properties of large samples of extended clusters in dwarf galaxies are necessary to understand if GC formation depends on the environment they were formed in.



# Appendix A

## Tables of UCD properties

Table A.1: UCD and companion properties of all 19 objects for which a faint point source was found within  $r < 300$  pc (see figure 2.9). In column 1 the reference used in figure 2.9 is shown. In column 2 and 3 the name used in this paper and the original name are shown, respectively. Column 4 and 5 give their positions in R.A. and Dec. In column 6 and 7 the V magnitude and color of the UCD are shown. In column 8 the magnitude of the possible companion is given. In column 9 the distance of the companion to the UCD is given in pc. The distance of the UCD to the center of NCG1399 is given in column 10. In column 11 we show the estimate of the tidal radius of this UCD for it's specific position using the formula given in 2.8. The second to last column gives the fraction between  $dist_{comp}/r_{tidal}$ . Thus if this fraction is smaller than 1.0 the companion lies within the tidal radius of the UCD host object, which is the case for 16 out of our 19 UCDs.

Ref.	Name	Name <sub>alt</sub>	R.A. (h:m:s)	DEC. (°:':")	$V_{UCD}$ (mag)	$(V - I)$ (mag)	$V_{comp.}$ (mag)	$dist_{comp}$ (pc)	$dist_{NCG1399}$ (kpc)	$r_{tid}$ pc	$dis_{co}/r_{tid}$	$v$ (km s <sup>-1</sup> )
a)	UCD-FORS 1	1_0630	3:38:56.14	-35:24:49.0	20.35	1.02	25.21	108	32.86	590	0.18	666 ± 48
b)	UCD-FORS 13	Y446	3:38:33.82	-35:25:57.0	21.01	1.03	25.01	211	8.07	119	1.77	1224 ± 221
c)	UCD-FORS 13	Y446	3:38:33.82	-35:25:57.0	21.01	1.03	23.80	307	8.07	119	2.58	1224 ± 221
d)	UCD-FORS 13	Y446	3:38:33.82	-35:25:57.0	21.01	1.03	24.59	241	8.07	119	2.03	1224 ± 221
e)	UCD-FORS 20	77.002	3:38:38.11	-35:26:46.7	21.02	1.03	24.81	119	10.32	151	0.79	1788 ± 58
f)	UCD-FORS 32	UCD6	3:38:05.04	-35:24:09.7	18.93	1.13	23.20	263	31.30	985	0.27	1220 ± 45
g)	UCD-FORS 33	NTT414	3:38:09.72	-35:23:01.2	19.61	0.99	23.78	206	31.03	686	0.30	1607 ± 141
h)	UCD-FORS 35	UCD32	3:38:16.70	-35:20:23.1	20.09	0.99	23.64	278	39.24	748	0.37	1439 ± 23
i)	UCD-FORS 36	UCDm	3:38:06.48	-35:23:03.8	20.01	1.0	25.12	283	33.53	659	0.43	1442 ± 123
j)	UCD-FORS 37	UCD36	3:38:23.23	-35:20:00.6	20.22	1.12	24.62	139	39.35	820	0.17	1347 ± 61
k)	UCD-FORS 52	2_2127	3:38:11.69	-35:27:16.2	20.93	1.16	23.77	154	19.53	349	0.44	1443 ± 131
l)	UCD-FORS 57	Y3905	3:38:23.28	-35:26:32.7	21.27	1.09	24.62	224	7.01	101	2.22	1504 ± 12
m)	UCD-FORS 64	K1042m	3:38:36.88	-35:25:43.8	21.37	1.23	22.71	151	11.43	193	0.78	1328 ± 90
n)	UCD-FORS 69	Y9410	3:38:27.35	-35:25:37.5	21.30	1.16	25.08	174	8.02	127	1.37	1392 ± 32
o)	UCD-FORS 70	Y4081	3:38:26.63	-35:25:34.0	21.39	1.22	25.50	100	8.56	143	0.70	1442 ± 22
p)	UCD-FORS 71	Y10048	3:38:35.23	-35:25:39.2	21.57	1.09	25.11	63	10.34	136	0.46	1602 ± 30
q)	UCD-FORS 76	80.039	3:38:21.34	-35:24:35.6	21.63	1.13	23.93	211	16.03	220	0.96	900 ± 66
r)	UCD-FORS 80	K1040	3:38:28.84	-35:25:00.7	21.93	1.17	24.92	124	11.18	149	0.83	1481 ± 57
s)	UCD-FORS 81	UCD2	3:38:06.29	-35:28:58.8	19.31	1.13	24.47	193	27.71	776	0.24	1249 ± 37
t)	UCD-FORS 92	Y7623	3:38:16.65	-35:29:35.2	21.59	1.05	24.22	177	19.77	248	0.71	1676 ± 50
u)	UCD-FORS 96	89.038	3:38:11.93	-35:32:01.7	21.45	0.97	23.72	291	33.58	417	0.70	1350 ± 78

A. Tables of UCD properties

Table A.2: Here those UCDs from the original sample of 97 in the FORS fields are shown, which are not yet listed in Table 2.1 or as a companion hosting UCD in Table A.1. Column 1 gives their running name in our notation, column 2 their alternative name from the literature, which follows the same convention as explained in Table 2.1. Columns 3 and 4 give the R.A. and Dec. of the UCDs. In Columns 5 and 6 the V magnitudes as well as V-I colors are shown.

Name	Name <sub>alt</sub>	R.A. (h:m:s)	DEC. (°:':")	$V_{UCD}$ (mag)	$(V - I)$ (mag)
UCD-FORS 3	1_2103	3:38:57.38	-35:24:50.8	$20.82 \pm 0.11$	$1.14 \pm 0.07$
UCD-FORS 5	1_064	3:38:49.78	-35:23:35.5	$20.99 \pm 0.08$	$1.18 \pm 0.05$
UCD-FORS 6	76.059	3:38:46.90	-35:23:48.8	$21.10 \pm 0.08$	$1.01 \pm 0.08$
UCD-FORS 7	75.085	3:38:50.40	-35:22:07.7	$21.46 \pm 0.08$	$1.23 \pm 0.08$
UCD-FORS 8	Y5100	3:38:48.93	-35:21:22.6	$21.73 \pm 0.10$	$1.36 \pm 0.05$
UCD-FORS 9	78.070	3:38:42.48	-35:26:12.5	$21.88 \pm 0.09$	$1.20 \pm 0.05$
UCD-FORS 10	UCD41	3:38:29.04	-35:22:56.6	$19.98 \pm 0.07$	$1.16 \pm 0.04$
UCD-FORS 11	0_2030	3:38:28.34	-35:25:38.3	$20.08 \pm 0.11$	$1.10 \pm 0.05$
UCD-FORS 12	Y446	3:38:30.72	-35:24:40.7	$21.01 \pm 0.10$	$1.03 \pm 0.06$
UCD-FORS 14	1_058	3:38:39.31	-35:27:06.5	$20.72 \pm 0.15$	$1.08 \pm 0.13$
UCD-FORS 15	AAT38	3:38:37.97	-35:23:33.0	$20.90 \pm 0.10$	$1.19 \pm 0.13$
UCD-FORS 16	0_2074	3:38:35.66	-35:27:15.5	$21.03 \pm 0.12$	$1.11 \pm 0.07$
UCD-FORS 17	76.080	3:38:40.99	-35:22:41.9	$21.27 \pm 0.08$	$1.15 \pm 0.07$
UCD-FORS 18	Y4735	3:38:40.24	-35:21:33.2	$21.48 \pm 0.15$	$1.15 \pm 0.07$
UCD-FORS 19	K1044a	3:38:40.20	-35:27:00.7	$21.30 \pm 0.08$	$0.89 \pm 0.05$
UCD-FORS 21	Y4654	3:38:38.75	-35:25:42.9	$21.64 \pm 0.04$	$1.17 \pm 0.06$
UCD-FORS 22	UCD27	3:38:10.34	-35:24:06.1	$19.70 \pm 0.11$	$1.10 \pm 0.06$
UCD-FORS 23	Y99071	3:38:08.64	-35:23:51.8	$22.02 \pm 0.10$	$4.89 \pm 0.04$
UCD-FORS 24	80.056	3:38:19.73	-35:23:40.6	$20.66 \pm 0.09$	$0.97 \pm 0.08$
UCD-FORS 25	0_2032	3:38:30.22	-35:21:31.0	$20.86 \pm 0.08$	$1.04 \pm 0.08$
UCD-FORS 26	81.049	3:38:08.35	-35:23:56.0	$22.12 \pm 0.53$	$1.02 \pm 0.24$
UCD-FORS 27	81.041	3:38:07.06	-35:24:28.8	$21.60 \pm 0.08$	$1.26 \pm 0.06$
UCD-FORS 28	81.098	3:38:07.66	-35:20:51.4	$21.93 \pm 0.07$	$0.94 \pm 0.05$
UCD-FORS 29	81.066	3:38:06.31	-35:22:48.4	$21.85 \pm 0.08$	$0.94 \pm 0.05$
UCD-FORS 30	0_2030	3:38:28.34	-35:25:38.3	$20.08 \pm 0.11$	$1.10 \pm 0.05$
UCD-FORS 31	NTT407	3:38:04.17	-35:25:26.6	$20.24 \pm 0.17$	$0.91 \pm 0.11$
UCD-FORS 34	Y446	3:38:30.72	-35:24:40.7	$21.01 \pm 0.10$	$1.03 \pm 0.06$
UCD-FORS 38	0_2063	3:38:19.08	-35:26:37.3	$20.87 \pm 0.05$	$1.06 \pm 0.05$
UCD-FORS 39	0_2027	3:38:19.49	-35:25:52.3	$21.08 \pm 0.09$	$1.25 \pm 0.06$
UCD-FORS 40	0_2089	3:38:17.09	-35:26:30.8	$21.00 \pm 0.13$	$1.13 \pm 0.04$

Table A.2: continued.

Name	Name <sub>alt</sub>	R.A. (h:m:s)	DEC. (°:′:″)	$V_{UCD}$ (mag)	$(V - I)$ (mag)
UCD-FORS 41	K1026	3:38:14.25	-35:26:43.9	$20.91 \pm 0.08$	$1.11 \pm 0.06$
UCD-FORS 42	80.028	3:38:26.47	-35:25:21.0	$21.31 \pm 0.09$	$1.08 \pm 0.06$
UCD-FORS 43	Y7797	3:38:26.40	-35:24:25.6	$21.31 \pm 0.06$	$1.08 \pm 0.05$
UCD-FORS 44	Y4222	3:38:29.52	-35:25:08.5	$21.31 \pm 0.10$	$1.21 \pm 0.06$
UCD-FORS 46	Y9320	3:38:19.99	-35:26:44.0	$21.29 \pm 0.10$	$1.08 \pm 0.06$
UCD-FORS 47	80.027	3:38:26.28	-35:25:25.0	$21.38 \pm 0.08$	$1.24 \pm 0.05$
UCD-FORS 49	80.035	3:38:18.22	-35:24:54.0	$21.30 \pm 0.09$	$1.08 \pm 0.06$
UCD-FORS 51	82.040	3:38:10.32	-35:26:31.9	$21.86 \pm 0.38$	$1.22 \pm 0.19$
UCD-FORS 53	Y4507	3:38:35.48	-35:25:29.6	$21.41 \pm 0.04$	$1.18 \pm 0.05$
UCD-FORS 54	82.029	3:38:05.66	-35:26:46.7	$22.04 \pm 0.41$	$1.22 \pm 0.09$
UCD-FORS 55	Y3866	3:38:22.41	-35:26:33.2	$21.15 \pm 0.11$	$1.10 \pm 0.07$
UCD-FORS 58	Y7698	3:38:20.60	-35:26:11.3	$21.62 \pm 0.06$	$1.15 \pm 0.05$
UCD-FORS 59	Y7967	3:38:35.78	-35:25:34.1	$21.62 \pm 0.02$	$1.01 \pm 0.04$
UCD-FORS 60	Y7935	3:38:33.86	-35:25:21.9	$21.72 \pm 0.25$	$0.83 \pm 0.05$
UCD-FORS 61	Y9354	3:38:23.21	-35:25:29.7	$21.94 \pm 0.07$	$1.32 \pm 0.13$
UCD-FORS 62	K1031	3:38:21.54	-35:26:16.1	$21.89 \pm 0.08$	$1.01 \pm 0.04$
UCD-FORS 63	K1032a	3:38:21.69	-35:25:14.9	$21.92 \pm 0.08$	$1.20 \pm 0.04$
UCD-FORS 65	80.045	3:38:22.85	-35:24:23.0	$22.18 \pm 0.13$	$0.78 \pm 0.27$
UCD-FORS 66	UCD33	3:38:17.47	-35:33:04.0	$20.40 \pm 0.06$	$0.99 \pm 0.05$
UCD-FORS 67	0_2023	3:38:12.70	-35:28:57.0	$20.85 \pm 0.08$	$1.10 \pm 0.08$
UCD-FORS 68	0_2026	3:38:18.89	-35:32:23.3	$20.98 \pm 0.09$	$1.11 \pm 0.07$
UCD-FORS 72	2_089	3:38:14.02	-35:29:43.1	$20.96 \pm 0.08$	$1.04 \pm 0.06$
UCD-FORS 73	Y3786	3:38:20.81	-35:34:26.9	$21.06 \pm 0.03$	$0.96 \pm 0.04$
UCD-FORS 74	2_2100	3:38:00.17	-35:30:08.3	$21.12 \pm 0.09$	$1.05 \pm 0.07$
UCD-FORS 75	91.113	3:38:08.16	-35:27:52.2	$21.08 \pm 0.09$	$1.01 \pm 0.05$
UCD-FORS 77	89.055	3:38:22.44	-35:30:49.0	$21.14 \pm 0.10$	$0.96 \pm 0.06$
UCD-FORS 78	Y7523	3:38:08.80	-35:32:25.5	$21.53 \pm 0.03$	$1.80 \pm 0.03$
UCD-FORS 79	90.074	3:38:08.78	-35:29:39.5	$21.17 \pm 0.07$	$0.95 \pm 0.05$
UCD-FORS 82	92.060	3:38:04.68	-35:30:07.9	$21.17 \pm 0.08$	$1.16 \pm 0.05$
UCD-FORS 83	AAT21	3:38:13.07	-35:31:07.4	$21.11 \pm 0.11$	$1.09 \pm 0.12$
UCD-FORS 85	90.077	3:38:11.30	-35:29:31.2	$21.43 \pm 0.09$	$1.08 \pm 0.05$
UCD-FORS 86	90.015	3:38:14.66	-35:33:25.6	$21.31 \pm 0.08$	$1.22 \pm 0.05$
UCD-FORS 87	gc156	3:38:13.56	-35:28:56.3	$21.28 \pm 0.02$	$1.15 \pm 0.03$
UCD-FORS 88	91.083	3:37:58.75	-35:29:32.3	$21.43 \pm 0.08$	$1.04 \pm 0.06$
UCD-FORS 89	91.109	3:38:04.44	-35:28:11.6	$21.42 \pm 0.07$	$1.19 \pm 0.05$
UCD-FORS 90	89.037	3:38:15.46	-35:32:04.2	$21.43 \pm 0.08$	$1.04 \pm 0.05$
UCD-FORS 91	Y7703	3:38:20.99	-35:30:13.1	$21.55 \pm 0.11$	$1.03 \pm 0.05$
UCD-FORS 93	Y3603	3:38:16.49	-35:31:07.7	$21.59 \pm 0.10$	$1.01 \pm 0.04$
UCD-FORS 94	90.044	3:38:18.31	-35:31:34.7	$22.20 \pm 0.18$	$0.94 \pm 0.04$



Table A.2: continued.

Name	Name <sub>alt</sub>	R.A. (h:m:s)	DEC. (°:':")	$V_{UCD}$ (mag)	$(V - I)$ (mag)
UCD-FORS 95	89.042	3:38:13.25	-35:31:43.0	$21.85 \pm 0.08$	$0.86 \pm 0.13$
UCD-FORS 97	K1022	3:38:09.21	-35:35:07.3	$20.85 \pm 0.07$	$1.31 \pm 0.05$



# Appendix B

## Radial velocities and membership probabilities of Craters stars

This table lists the identifier, the R.A. and DEC, the  $I$  magnitude any  $g - i$  colour form [Belokurov et al. 2014](#) and the radial velocity and its uncertainty. The last column gives the membership probability for each star calculated in chapter 3.

Table B.1: Radial velocities of extracted stars

Index	R.A. (J2000)	Dec.(J2000)	$I_{\text{mag}}$ (mag)	$(g - i)$ (mag)	radial velocity (km s <sup>-1</sup> )	membership probability
2	174.06963	-10.879207	17.34	1.70	147.37 $\pm$ 2.63	0.86
3	174.06443	-10.869809	17.44	2.63	-26.43 $\pm$ 2.33	0.00
4	174.05541	-10.863862	17.82	2.44	0.58 $\pm$ 2.41	0.00
5	174.05849	-10.873851	18.56	1.26	149.94 $\pm$ 2.43	0.50
6	174.07254	-10.879141	19.08	0.31	222.26 $\pm$ 3.67	0.00
7	174.08216	-10.876634	19.13	0.40	154.17 $\pm$ 2.83	0.20
8	174.06698	-10.878484	18.94	1.11	145.64 $\pm$ 2.40	0.95
9	174.06640	-10.889202	18.98	2.15	110.56 $\pm$ 4.30	2.65e-05
10	174.07103	-10.876154	19.60	0.97	145.76 $\pm$ 2.68	0.78
11	174.06869	-10.878836	19.86	0.92	144.74 $\pm$ 3.92	0.91
12	174.07132	-10.886548	19.70	2.14	-73.73 $\pm$ 48.77	1.9e-4
13	174.06278	-10.872687	20.24	0.63	151.56 $\pm$ 4.83	0.65
14	174.06996	-10.871523	20.41	0.85	154.11 $\pm$ 5.14	0.59
15	174.06862	-10.869076	20.46	0.87	151.86 $\pm$ 3.92	0.48
17	174.07026	-10.876373	20.71	0.76	151.75 $\pm$ 4.62	0.81
18	174.06220	-10.870687	20.79	0.67	136.40 $\pm$ 5.43	0.51
19	174.07804	-10.880047	20.77	0.82	146.56 $\pm$ 8.14	0.36
20	174.07586	-10.872134	20.78	0.82	171.85 $\pm$ 7.37	0.11
21	174.07129	-10.871307	20.79	0.82	149.99 $\pm$ 6.27	0.55
22	174.06518	-10.876647	20.91	0.57	162.10 $\pm$ 15.91	0.89
23	174.06143	-10.871692	20.95	0.55	169.97 $\pm$ 12.53	0.50
24	174.06155	-10.869075	20.96	0.59	130.26 $\pm$ 11.89	0.41
25	174.08091	-10.880816	20.95	0.62	142.80 $\pm$ 8.40	0.24

---

26	174.06890	-10.872272	21.01	0.64	$160.83 \pm 7.26$	0.62
27	174.06919	-10.877074	21.01	0.65	$146.75 \pm 4.66$	0.89
28	174.05927	-10.866367	21.00	0.64	$133.17 \pm 14.59$	0.26
29	174.06988	-10.876175	21.07	0.58	$133.64 \pm 6.42$	0.79
30	174.06878	-10.874268	21.11	0.58	$145.61 \pm 9.94$	0.81
33	174.06238	-10.873799	21.23	0.72	$159.49 \pm 8.57$	0.67
34	174.06709	-10.877142	21.30	0.72	$135.83 \pm 6.17$	0.91
35	174.07098	-10.882941	21.32	0.76	$131.20 \pm 7.12$	0.60
36	174.07060	-10.881660	21.32	0.84	$141.87 \pm 10.09$	0.73
37	174.06429	-10.875020	21.46	0.65	$199.18 \pm 28.65$	0.75
38	174.06759	-10.876072	21.57	0.63	$136.73 \pm 7.42$	0.89
39	174.06818	-10.876399	21.89	0.57	$159.09 \pm 6.91$	0.84
40	174.06847	-10.876633	21.90	0.61	$143.17 \pm 6.72$	0.91
47	174.07033	-10.870255	21.50	1.30	$-131.02 \pm 10.62$	0.00
48	174.06635	-10.877323	22.20	0.23	$146.44 \pm 22.87$	0.95
49	174.06653	-10.876920	22.06	0.51	$142.49 \pm 9.17$	0.94
50	174.06811	-10.873349	22.09	0.57	$176.90 \pm 20.49$	0.71
51	174.07868	-10.877564	22.00	0.81	$178.90 \pm 11.70$	0.15

---

# Bibliography

- Ackermann, M., Albert, A., Anderson, B., et al. 2015, *Physical Review Letters*, 115, 231301
- Arca-Sedda, M. & Capuzzo-Dolcetta, R. 2014, *MNRAS*, 444, 3738
- Bacon, R., Accardo, M., Adjali, L., et al. 2010, in *Society of Photo-Optical Instrumentation Engineers (SPIE) Conference Series*, Vol. 7735, Society of Photo-Optical Instrumentation Engineers (SPIE) Conference Series, 8
- Bassino, L. P., Cellone, S. A., Forte, J. C., & Dirsch, B. 2003, *A&A*, 399, 489
- Bassino, L. P., Faifer, F. R., Forte, J. C., et al. 2006, *A&A*, 451, 789
- Baumgardt, H., Grebel, E. K., & Kroupa, P. 2005, *MNRAS*, 359, L1
- Baumgardt, H., Parmentier, G., Gieles, M., & Vesperini, E. 2010, *MNRAS*, 401, 1832
- Bekki, K., Couch, W. J., Drinkwater, M. J., & Shioya, Y. 2003, *MNRAS*, 344, 399
- Bekki, K. & Freeman, K. C. 2003, *MNRAS*, 346, L11
- Bellazzini, M., Ibata, R. A., Chapman, S. C., et al. 2008, *AJ*, 136, 1147
- Belokurov, V., Irwin, M. J., Koposov, S. E., et al. 2014, *MNRAS*, 441, 2124
- Belokurov, V., Walker, M. G., Evans, N. W., et al. 2008, *ApJL*, 686, L83
- Belokurov, V., Walker, M. G., Evans, N. W., et al. 2009, *MNRAS*, 397, 1748
- Belokurov, V., Zucker, D. B., Evans, N. W., et al. 2007, *ApJ*, 654, 897
- Belokurov, V., Zucker, D. B., Evans, N. W., et al. 2006, *ApJL*, 647, L111
- Bender, R., Burstein, D., & Faber, S. M. 1993, *ApJ*, 411, 153
- Bergemann, M., Lind, K., Collet, R., Magic, Z., & Asplund, M. 2012, *MNRAS*, 427, 27
- Bertin, E. & Arnouts, S. 1996, *A&AS*, 117, 393
- Besla, G., Kallivayalil, N., Hernquist, L., et al. 2007, *ApJ*, 668, 949
- Böker, T., Sarzi, M., McLaughlin, D. E., et al. 2004, *AJ*, 127, 105
- Bonifacio, P., Caffau, E., Zaggia, S., et al. 2015, *A&A*, 579, L6

- Brodie, J. P., Romanowsky, A. J., Strader, J., & Forbes, D. A. 2011, *AJ*, 142, 199
- Brüns, R. C., Kroupa, P., & Fellhauer, M. 2009, *ApJ*, 702, 1268
- Brüns, R. C., Kroupa, P., Fellhauer, M., Metz, M., & Assmann, P. 2011, *A&A*, 529, A138
- Bruzual, G. & Charlot, S. 2003, *MNRAS*, 344, 1000
- Campbell, D. J. R., Frenk, C. S., Jenkins, A., et al. 2016, *ArXiv e-prints*
- Cappellari, M., Emsellem, E., Krajnović, D., et al. 2011, *MNRAS*, 413, 813
- Capuzzo-Dolcetta, R. 1993, *ApJ*, 415, 616
- Carretta, E., Bragaglia, A., Gratton, R., D’Orazi, V., & Lucatello, S. 2009a, *A&A*, 508, 695
- Carretta, E., Bragaglia, A., Gratton, R. G., et al. 2009b, *A&A*, 505, 117
- Cenarro, A. J., Cardiel, N., Gorgas, J., et al. 2001, *MNRAS*, 326, 959
- Chandrasekhar, S. 1943, *ApJ*, 97, 255
- Chilingarian, I. V., Cayatte, V., & Bergond, G. 2008, *MNRAS*, 390, 906
- Chilingarian, I. V., Mieske, S., Hilker, M., & Infante, L. 2011, *MNRAS*, 412, 1627
- Ciotti, L. 1991, *A&A*, 249, 99
- Cohen, J. G. & Kirby, E. N. 2012, *ApJ*, 760, 86
- Cohen, J. G., Kirby, E. N., Simon, J. D., & Geha, M. 2010, *ApJ*, 725, 288
- Collins, M. L. M., Chapman, S. C., Rich, R. M., et al. 2013, *ApJ*, 768, 172
- Collins, M. L. M., Martin, N. F., Rich, R. M., et al. 2015, *ApJL*, 799, L13
- Côté, P., Marzke, R. O., West, M. J., & Minniti, D. 2000, *ApJ*, 533, 869
- Côté, P., Piatek, S., Ferrarese, L., et al. 2006, *ApJS*, 165, 57
- Da Costa, G. S. 2015, *ArXiv e-prints*
- Da Costa, G. S., Held, E. V., Saviane, I., & Gullieuszik, M. 2009, *ApJ*, 705, 1481
- Da Rocha, C., Mieske, S., Georgiev, I. Y., et al. 2011, *A&A*, 525, A86
- D’Cruz, N. L., O’Connell, R. W., Rood, R. T., et al. 2000, *ApJ*, 530, 352
- De Propriis, R., Phillipps, S., Drinkwater, M. J., et al. 2005, *ApJL*, 623, L105

- Deason, A. J., Wetzel, A. R., Garrison-Kimmel, S., & Belokurov, V. 2015, MNRAS, 453, 3568
- Dirsch, B., Richtler, T., Geisler, D., et al. 2003, AJ, 125, 1908
- Dirsch, B., Richtler, T., Geisler, D., et al. 2004, AJ, 127, 2114
- Dorman, B., Rood, R. T., & O’Connell, R. W. 1993, ApJ, 419, 596
- Dotter, A., Chaboyer, B., Jevremović, D., et al. 2008, ApJS, 178, 89
- Dotter, A., Sarajedini, A., Anderson, J., et al. 2010, ApJ, 708, 698
- Drinkwater, M. J., Gregg, M. D., Hilker, M., et al. 2003, Nature, 423, 519
- Drinkwater, M. J., Jones, J. B., Gregg, M. D., & Phillipps, S. 2000, PASA, 17, 227
- Evstigneeva, E. A., Drinkwater, M. J., Peng, C. Y., et al. 2008, AJ, 136, 461
- Evstigneeva, E. A., Gregg, M. D., Drinkwater, M. J., & Hilker, M. 2007, AJ, 133, 1722
- Fellhauer, M. & Kroupa, P. 2002, MNRAS, 330, 642
- Fellhauer, M. & Kroupa, P. 2005, ApJ, 630, 879
- Fensch, J., Mieske, S., Müller-Seidlitz, J., & Hilker, M. 2014, A&A, 567, A105
- Ferrarese, L., Côté, P., Jordán, A., et al. 2006, ApJS, 164, 334
- Ferraro, F. R., Lanzoni, B., Dalessandro, E., et al. 2012, Nature, 492, 393
- Firth, P., Drinkwater, M. J., Evstigneeva, E. A., et al. 2007, MNRAS, 382, 1342
- Forbes, D. A. & Bridges, T. 2010, MNRAS, 404, 1203
- Forbes, D. A., Pota, V., Usher, C., et al. 2013, MNRAS, 435, L6
- Frank, M. J., Hilker, M., Baumgardt, H., et al. 2012, MNRAS, 423, 2917
- Freedman, W. L., Madore, B. F., Gibson, B. K., et al. 2001, ApJ, 553, 47
- Freeman, K. C. 1993, in Astronomical Society of the Pacific Conference Series, Vol. 48, The Globular Cluster-Galaxy Connection, ed. G. H. Smith & J. P. Brodie, 608
- Georgiev, I. Y. & Böker, T. 2014, MNRAS, 441, 3570
- Georgiev, I. Y., Puzia, T. H., Goudfrooij, P., & Hilker, M. 2010, MNRAS, 406, 1967
- Georgiev, I. Y., Puzia, T. H., Hilker, M., & Goudfrooij, P. 2009, MNRAS, 392, 879
- Gilmore, G., Wilkinson, M. I., Wyse, R. F. G., et al. 2007, ApJ, 663, 948

- Glatt, K., Grebel, E. K., Gallagher, III, J. S., et al. 2009, AJ, 138, 1403
- Glatt, K., Grebel, E. K., Sabbi, E., et al. 2008, AJ, 136, 1703
- Gratton, R., Sneden, C., & Carretta, E. 2004, ARAA, 42, 385
- Grebel, E. K. & Gallagher, III, J. S. 2004, ApJL, 610, L89
- Grebel, E. K., Gallagher, III, J. S., & Harbeck, D. 2003, AJ, 125, 1926
- Gregg, M. D., Drinkwater, M. J., Evstigneeva, E., et al. 2009, AJ, 137, 498
- Grillmair, C. J. 2009, ApJ, 693, 1118
- Hasegan, M., Jordán, A., Côté, P., et al. 2005, ApJ, 627, 203
- Hanuschik, R. W. 2003, A&A, 407, 1157
- Harris, W. E. 1996, AJ, 112, 1487
- Harris, W. E., Bell, R. A., Vandenberg, D. A., et al. 1997, AJ, 114, 1030
- Hilker, M. 2006, ArXiv Astrophysics e-prints
- Hilker, M., Baumgardt, H., Infante, L., et al. 2007, A&A, 463, 119
- Hilker, M., Infante, L., Vieira, G., Kissler-Patig, M., & Richtler, T. 1999, A&AS, 134, 75
- Hilker, M. & Richtler, T. 2000, A&A, 362, 895
- Husser, T.-O., Kamann, S., Dreizler, S., et al. 2016, A&A, 588, A148
- Husser, T.-O., Wende-von Berg, S., Dreizler, S., et al. 2013, A&A, 553, A6
- Huxor, A. P., Tanvir, N. R., Irwin, M. J., et al. 2005, MNRAS, 360, 1007
- Ibata, R., Sollima, A., Nipoti, C., et al. 2011, ApJ, 738, 186
- Ibata, R. A., Gilmore, G., & Irwin, M. J. 1995, MNRAS, 277, 781
- Ibata, R. A., Lewis, G. F., Conn, A. R., et al. 2013, Nature, 493, 62
- Iben, Jr., I. & Rood, R. T. 1970, ApJ, 161, 587
- Ikuta, C. & Arimoto, N. 2000, A&A, 358, 535
- Irwin, M. J., Belokurov, V., Evans, N. W., et al. 2007, ApJL, 656, L13
- Janz, J., Forbes, D. A., Norris, M. A., et al. 2015, MNRAS, 449, 1716
- Jethwa, P., Erkal, D., & Belokurov, V. 2016, ArXiv e-prints



- Jordán, A., Blakeslee, J. P., Côté, P., et al. 2007, *ApJS*, 169, 213
- Jordán, A., Peng, E. W., Blakeslee, J. P., et al. 2009, *ApJS*, 180, 54
- Jordi, K., Grebel, E. K., Hilker, M., et al. 2009, *AJ*, 137, 4586
- Kallivayalil, N., van der Marel, R. P., Besla, G., Anderson, J., & Alcock, C. 2013, *ApJ*, 764, 161
- Kamann, S., Wisotzki, L., & Roth, M. M. 2013, *A&A*, 549, A71
- Karachentsev, I. D., Makarova, L. N., Makarov, D. I., Tully, R. B., & Rizzi, L. 2015, *MNRAS*, 447, L85
- Kim, D. & Jerjen, H. 2015, *ApJL*, 808, L39
- King, I. 1962, *AJ*, 67, 471
- Kirby, E. N., Guhathakurta, P., Simon, J. D., et al. 2010, *ApJS*, 191, 352
- Kirby, E. N., Simon, J. D., & Cohen, J. G. 2015, *ApJ*, 810, 56
- Kirby, E. N., Simon, J. D., Geha, M., Guhathakurta, P., & Frebel, A. 2008, *ApJL*, 685, L43
- Koposov, S. E., Belokurov, V., Torrealba, G., & Evans, N. W. 2015, *ApJ*, 805, 130
- Kroupa, P. 2001, *MNRAS*, 322, 231
- Kroupa, P., Theis, C., & Boily, C. M. 2005, *A&A*, 431, 517
- Küpper, A. H. W., Mieske, S., & Kroupa, P. 2011, *MNRAS*, 413, 863
- Laevens, B. P. M., Martin, N. F., Bernard, E. J., et al. 2015a, *ApJ*, 813, 44
- Laevens, B. P. M., Martin, N. F., Ibata, R. A., et al. 2015b, *ApJL*, 802, L18
- Laevens, B. P. M., Martin, N. F., Sesar, B., et al. 2014, *ApJL*, 786, L3
- Landsman, W. B. 1993, in *Astronomical Society of the Pacific Conference Series*, Vol. 52, *Astronomical Data Analysis Software and Systems II*, ed. R. J. Hanisch, R. J. V. Brissenden, & J. Barnes, 246
- Lee, Y.-W., Gim, H. B., & Casetti-Dinescu, D. I. 2007, *ApJL*, 661, L49
- Li, Y.-S. & Helmi, A. 2008, *MNRAS*, 385, 1365
- Lieder, S., Lisker, T., Hilker, M., Misgeld, I., & Durrell, P. 2012, *A&A*, 538, A69
- Lisker, T., Grebel, E. K., Binggeli, B., & Glatt, K. 2007, *ApJ*, 660, 1186

- Liu, C., Peng, E. W., Cote, P., et al. 2015a, ArXiv e-prints
- Liu, C., Peng, E. W., Toloba, E., et al. 2015b, ApJL, 812, L2
- Lotz, J. M., Miller, B. W., & Ferguson, H. C. 2004, ApJ, 613, 262
- Lotz, J. M., Telford, R., Ferguson, H. C., et al. 2001, ApJ, 552, 572
- Lynden-Bell, D. 1976, MNRAS, 174, 695
- Maraston, C. 2005, MNRAS, 362, 799
- Marcolini, A., Sollima, A., D’Ercole, A., Gibson, B. K., & Ferraro, F. R. 2007, MNRAS, 382, 443
- Marino, A. F., Milone, A. P., Piotto, G., et al. 2009, A&A, 505, 1099
- Martin, N. F., Geha, M., Ibata, R. A., et al. 2016a, MNRAS, 458, L59
- Martin, N. F., Ibata, R. A., Chapman, S. C., Irwin, M., & Lewis, G. F. 2007, MNRAS, 380, 281
- Martin, N. F., Ibata, R. A., Collins, M. L. M., et al. 2016b, ApJ, 818, 40
- Martin, N. F., Ibata, R. A., Irwin, M. J., et al. 2006, MNRAS, 371, 1983
- Martin, N. F., Nidever, D. L., Besla, G., et al. 2015, ApJL, 804, L5
- McConnachie, A. W. 2012, AJ, 144, 4
- McConnachie, A. W. & Côté, P. 2010, ApJL, 722, L209
- McLaughlin, D. E. & van der Marel, R. P. 2005, ApJS, 161, 304
- Metz, M. & Kroupa, P. 2007, MNRAS, 376, 387
- Metz, M., Kroupa, P., & Libeskind, N. I. 2008, ApJ, 680, 287
- Metz, M., Kroupa, P., Theis, C., Hensler, G., & Jerjen, H. 2009, ApJ, 697, 269
- Mieske, S., Hilker, M., & Infante, L. 2002, A&A, 383, 823
- Mieske, S., Hilker, M., & Infante, L. 2004, A&A, 418, 445
- Mieske, S., Hilker, M., Infante, L., & Jordán, A. 2006, AJ, 131, 2442
- Mieske, S., Hilker, M., Jordán, A., et al. 2008, A&A, 487, 921
- Mieske, S., Jordán, A., Côté, P., et al. 2010, ApJ, 710, 1672
- Milgrom, M. 1983, ApJ, 270, 365

- Milone, A. P., Piotto, G., Bedin, L. R., et al. 2012, *A&A*, 540, A16
- Minniti, D., Kissler-Patig, M., Goudfrooij, P., & Meylan, G. 1998, *AJ*, 115, 121
- Misgeld, I. & Hilker, M. 2011, *MNRAS*, 414, 3699
- Misgeld, I., Hilker, M., & Mieske, S. 2009a, *A&A*, 496, 683
- Misgeld, I., Hilker, M., & Mieske, S. 2009b, *A&A*, 496, 683
- Misgeld, I., Mieske, S., & Hilker, M. 2008a, *A&A*, 486, 697
- Misgeld, I., Mieske, S., & Hilker, M. 2008b, *A&A*, 486, 697
- Murray, N. 2009, *ApJ*, 691, 946
- Muzzio, J. C. 1986, *ApJ*, 306, 44
- Norris, J. E. & Da Costa, G. S. 1995, *ApJ*, 447, 680
- Norris, M. A., Escudero, C. G., Faifer, F. R., et al. 2015, *ArXiv e-prints*
- Norris, M. A. & Kannappan, S. J. 2011, *MNRAS*, 414, 739
- Norris, M. A., Kannappan, S. J., Forbes, D. A., et al. 2014, *MNRAS*, 443, 1151
- Odenkirchen, M., Grebel, E. K., Rockosi, C. M., et al. 2001, *ApJL*, 548, L165
- Padoan, P., Jimenez, R., & Jones, B. 1997, *MNRAS*, 285, 711
- Paust, N. E. Q., Reid, I. N., Piotto, G., et al. 2010, *AJ*, 139, 476
- Pawlowski, M. S., Famaey, B., Jerjen, H., et al. 2014, *MNRAS*, 442, 2362
- Pawlowski, M. S., Kroupa, P., Angus, G., et al. 2012, *MNRAS*, 424, 80
- Pawlowski, M. S., Kroupa, P., & de Boer, K. S. 2011, *A&A*, 532, A118
- Pawlowski, M. S., McGaugh, S. S., & Jerjen, H. 2015, *MNRAS*, 453, 1047
- Peacock, M. B., Maccarone, T. J., Waters, C. Z., et al. 2009, *MNRAS*, 392, L55
- Peebles, P. J. E. 1984, *ApJ*, 277, 470
- Peng, C. Y., Ho, L. C., Impey, C. D., & Rix, H.-W. 2002, *AJ*, 124, 266
- Pfeffer, J. & Baumgardt, H. 2013, *MNRAS*, 433, 1997
- Pfeffer, J., Griffen, B. F., Baumgardt, H., & Hilker, M. 2014, *MNRAS*, 444, 3670
- Phillipps, S., Drinkwater, M. J., Gregg, M. D., & Jones, J. B. 2001, *ApJ*, 560, 201

- Price, J., Phillipps, S., Huxor, A., et al. 2009, MNRAS, 397, 1816
- Richtler, T., Dirsch, B., Larsen, S., Hilker, M., & Infante, L. 2005, A&A, 439, 533
- Richtler, T., Schubert, Y., Hilker, M., et al. 2008, A&A, 478, L23
- Robin, A. C., Reyl  , C., Derri  re, S., & Picaud, S. 2003, A&A, 409, 523
- Rossa, J., van der Marel, R. P., B  ker, T., et al. 2006, AJ, 132, 1074
- Sakamoto, T. & Hasegawa, T. 2006, ApJL, 653, L29
- Sarajedini, A. & Layden, A. C. 1995, AJ, 109, 1086
- Schubert, Y., Richtler, T., Hilker, M., et al. 2010, A&A, 513, A52
- Seth, A. C., Dalcanton, J. J., Hodge, P. W., & Debattista, V. P. 2006, AJ, 132, 2539
- Seth, A. C., van den Bosch, R., Mieske, S., et al. 2014, Nature, 513, 398
- Sollima, A., Bellazzini, M., & Lee, J.-W. 2012, ApJ, 755, 156
- Sollima, A., Mart  nez-Delgado, D., Valls-Gabaud, D., & Pe  arrubia, J. 2011, ApJ, 726, 47
- Sollima, A., Pancino, E., Ferraro, F. R., et al. 2005, ApJ, 634, 332
- Strader, J., Seth, A. C., Forbes, D. A., et al. 2013, ApJL, 775, L6
- Torrealba, G., Koposov, S. E., Belokurov, V., & Irwin, M. 2016, ArXiv e-prints
- Tremaine, S. D., Ostriker, J. P., & Spitzer, Jr., L. 1975, ApJ, 196, 407
- Villegas, D., Jord  n, A., Peng, E. W., et al. 2010, ApJ, 717, 603
- Vogel, K., Hilker, M., Baumgardt, H., et al. 2016, ArXiv e-prints
- Walcher, C. J., B  ker, T., Charlot, S., et al. 2006, ApJ, 649, 692
- Walsh, S. M., Jerjen, H., & Willman, B. 2007, ApJL, 662, L83
- Weilbacher, P. M., Streicher, O., Urrutia, T., et al. 2012, in Proceedings SPIE, Vol. 8451, Software and Cyberinfrastructure for Astronomy II, 84510B
- Weisz, D. R., Koposov, S. E., Dolphin, A. E., et al. 2015, ArXiv e-prints
- White, S. D. M. & Rees, M. J. 1978, MNRAS, 183, 341
- Whitmore, B. C., Zhang, Q., Leitherer, C., et al. 1999, AJ, 118, 1551
- Willman, B., Blanton, M. R., West, A. A., et al. 2005a, AJ, 129, 2692

- Willman, B., Blanton, M. R., West, A. A., et al. 2005b, *AJ*, 129, 2692
- Willman, B., Geha, M., Strader, J., et al. 2011, *AJ*, 142, 128
- Willman, B. & Strader, J. 2012, *AJ*, 144, 76
- Wolf, J., Martinez, G. D., Bullock, J. S., et al. 2010, *MNRAS*, 406, 1220
- Yong, D., Da Costa, G. S., & Norris, J. E. 2016, *MNRAS*, 460, 1846
- York, D. G., Adelman, J., Anderson, Jr., J. E., et al. 2000, *AJ*, 120, 1579
- Zhang, H.-X., Peng, E. W., Côté, P., et al. 2015, *ApJ*, 802, 30
- Zinn, R. J., Newell, E. B., & Gibson, J. B. 1972, *A&A*, 18, 390
- Zucker, D. B., Belokurov, V., Evans, N. W., et al. 2006a, *ApJL*, 650, L41
- Zucker, D. B., Belokurov, V., Evans, N. W., et al. 2006b, *ApJL*, 643, L103
- Zucker, D. B., Kniazev, A. Y., Bell, E. F., et al. 2004, *ApJL*, 612, L121



# Acknowledgements

First and foremost I want to sincerely thank my supervisor Michael for his continuous support through my entire PhD. You taught me so many things about science and astronomy. I am very grateful for your encouragement, understanding and patience that helped me to grow as a scientist and made my PhD a rewarding experience. Thanks go also to my official supervisor Andreas Burkert for supporting this work.

I also want to acknowledge the support of Tom Richtler, you have been an invaluable source of support and wisdom and I am very glad you visited ESO a lot. I also want to express my sincere gratitude to my collaborators and all other people that contributed to my research in some way. In particular I am grateful to Bernd Husemann, Eva Grebel, Holger Baumgardt, Joel Pfeffer, Matthias Frank, Michelle Collins and Sebastian Kamann for the help, advice and the discussions. Special thanks go to Eric Takasugi and Dominic Brodelon for proofreading the language of several parts of this thesis.

Thanks also go to ESO and all my colleagues, that were part of the journey of this PhD and made it an unforgettable, inspiring time. I could not have asked for a more supportive and nice place to do my thesis. In particular, I am grateful that ESO provided the resources to give seminars and present my work at countless conferences all around the globe, and to have had the possibility to visit places such as Paranal and ALMA.

I want to thank Julian, the best officemate and best friend one can imagine. Your positive energy and support made the nice times even more enjoyable and helped me through the hard times. The memories we shared in office 524 and beyond won't be forgotten, and I am sure there are plenty more chapters in our friendship to come.

I want to thank all my friends in Munich, which made the three years here a truly fun experience. I already miss you all! Thanks for all the memories we shared, Alessia, Andra, Anna, Belinda, Chris, Claudia, Eliana, Eric, Florian, Jethro, Laura, Matias, Matteo, Phil, Siyi, Victor and all the others that were part of this journey.

Thanks go also to my family and specifically my parents who always supported me. You taught me to follow my passions in life and your sacrifices are the reason I made it so far. My upbringing has given me the strength to tackle the challenges that life might throw my way. Danke!

And last, but most importantly, I want to thank Matthieu. My time at ESO will always be precious, as this is the reason we met. Your encouragement, patience and love are the reason I made it so far. It makes me beyond grateful to have someone to share all the small and big adventures of life with. Merci!

**Dankeschön euch allen!**





# Lebenslauf

**Karina Theresia Voggel**

Geburtsdatum: 16.06.1989

Geboren in Sigmaringen

08/1999 - 08/2008    Gymnasium Mengen, Mengen

09/2008 - 08/2011    Bachelorstudium der Physik an der Universität Heidelberg

05/2011 - 08/2011    Bachelorarbeit Max-Planck-Institut für Astronomie (MPIA), Heidelberg

Betreuer: Dr. Arjen van der Wel, Prof. Dr. Hans-Walter Rix

09/2011 - 08/2013    Masterstudium der Physik an der Universität Heidelberg

10/2012 - 08/2013    Masterarbeit am Astronomischen Recheninstitut (ARI),  
Universität Heidelberg

Betreuer: Dr. Thorsten Lisker

09/2013 - 09/2016    Doktorarbeit am European Southern Observatory (ESO)

Garching bei München

Betreuer: Dr. Michael Hilker, Prof. Dr. Andreas Burkert

München, den 19 August 2016